Department of Physics
Indian Institute of Technology Guwahati
Ph.D. Thesis

Sandpile model under rotational constraint: Scaling, universality and crossover

Jahir Abbas Ahmed

Supervisor: Dr. S. B. Santra
June, 2012.

Sandpile model under rotational constraint: Scaling, universality and crossover

A thesis submitted by

Jahir Abbas Ahmed

to

Indian Institute of Technology Guwahati
in partial fulfillment of the requirements
for the award of the degree of
Doctor of Philosophy in Physics

Department of Physics
Indian Institute of Technology Guwahati
Guwahati - 781039, Assam, India

Statement

The work contained in the thesis entitled "*Sandpile model under rotational constraint: Scaling, universality and crossover*" has been carried out by me under the supervision of Dr. S. B. Santra, Associate Professor, Department of Physics, Indian Institute of Technology Guwahati. This work has not been submitted elsewhere for the award of any degree.

(Jahir Abbas Ahmed) June 14, 2012
Department of Physics
Indian Institute of Technology Guwahati
Guwahati - 781039


भारतीय प्रौद्योगिकी संस्थान गुवाहाटी
Indian Institute of Technology Guwahati

Certificate

It is certified that the work contained in the thesis entitled "*Sandpile model under rotational constraint: Scaling, universality and crossover*" by Mr. Jahir Abbas Ahmed, a Ph.D. student of the Department of Physics, Indian Institute of Technology Guwahati for the award of Doctor of Philosophy has been carried out under my supervision. This work has not been submitted elsewhere for the award of any degree.

(Dr. S. B. Santra)
Department of Physics
Indian Institute of Technology Guwahati
Guwahati - 781039

June 14, 2012

To my parents...

Acknowledgements

I am indebted to my supervisor Dr. Sitangshu Bikash Santra for his patient guidance, invaluable suggestions, constant encouragement and support throughout my research work. Despite his own busy schedule, he always gave time to me for discussion which immensely benefited me. During the period of work with Dr. Santra, for the first time I have realized that negative results which contradict the usual perception are worth-full if one finds out the reason behind it. I would like to thank him for removing the fear regarding Quantum Mechanics and Statistical Physics. I am also thankful to him for introducing me to many advanced subjects in physics like critical phenomena, percolation, self organized criticality, surface physics etc. I will remain ever grateful to him for his great assistance to make this thesis possible.

I would like to thank my doctoral committee members, Dr. S. Ghosh, Dr. S. Basu and Dr. B. Bose for valuable suggestions and critical comments during the course of my work and specially during the annual review. I am thankful to all other faculty members of Physics department for being helpful in all regards. My special thanks to Prof. Alika Khare and Prof. S. Ravi, for their timely help and support.

I wish to thank Department of Physics, Indian Institute of Technology Guwahati (IITG), to provide me with necessary computational facilities. I thank all the technical assistants of the department for their assistance in various ways during my research period. I would specially like to thank Mr. Basab Bijoy Purkayastha in this regard. My special thanks goes to my senior Dr. Santanu Sinha who helped me a lot when I just joined as a graduate student. I would also like to thank other seniors of our computational lab, Dr. Biswanath Dutta, Dr. Poulumi Dey, Dr. Kishore Dutta and Dr. Meera V. and all of my colleagues and juniors for their co-operation. I would like to thank Himangsu Bhaumik for his cooperation. Special thanks to Vindhyawasini, Abu, Supriya, Enamullah, Brahmananda, Apurba, Bappaditya Roy, Suresh, Onkar and Ubaidullah for entertaining discussions over evening tea sessions.

I am grateful to IITG for the financial support.

I have been fortunate to come across excellent friends who made my stay at IITG cheerful. My special thanks go to Khan Zaheer, Adeel, Ajmal, Shahnawaz, Abdul Gaffar, Bappa, Naseem, Nazmul, Raj, Masum, Kaimuzaman, Julfiqar, Faraz, Kaushik Da, Dr. Monowar Hussain, Dr. Musaweer Khan and Dr. Ahmad Ali for their timely help, support and encouragement. I will be always thankfull to Dr. Rafi Ahmed and his family members for their encouragement, help and support.

I am deeply indebted to my parents, brothers and sisters for their unconditional love, constant support and encouragement towards my thesis work. They always stood behind me during the ups and downs of my life.

Jahir

Abstract

Sandpile model introduced by Bak, Tang and Wiesenfeld (BTW) was taken as paradigm to study *Self Organized Criticality* (SOC), a phenomena of non-existence of any characteristic size or time of events in the non-equilibrium steady state of a class of slowly driven system. The effect of rotational constraint on the toppling dynamics of a sandpile model is studied here constructing a rotational sandpile model (RSM). RSM has deterministic toppling rule except the first toppling and develops internal stochasticity during time evolution. There exists a well defined prescription to study critical behaviour in equilibrium critical phenomena. However, non-equilibrium models generally lack such a well defined method. The critical properties of sandpile models are usually studied by calculating the probability distributions of different avalanche properties and performing moment analysis of them. In this thesis, the critical avalanche properties of RSM are studied not only by applying usual numerical techniques but also inventing several new techniques. RSM is found to belong to a new universality class different from that of a stochastic sandpile model (SSM) as well as that of the deterministic BTW model. It was known that the BTW model follows a complicated multi-scaling whereas the SSM follows finite size scaling (FSS). The finite size effect on the critical exponents of the RSM is verified performing moment analysis of the distribution functions. It is found that they follow usual FSS ansatz. Not only the RSM but different variants of the RSM constructed with changes in the toppling rule of RSM under the same rotational symmetry are found to belong to the same universality class of RSM. The RSM universality class seems to be a robust universality class which remains unaffected due to the change in the details of the toppling rule. The existence of such a robust universality class has been confirmed and analyzed further applying the newer techniques invented in this thesis. These newer techniques are based on a “microscopic” avalanche parameter namely the toppling number S_i, the number of times a site i toppled in an avalanche. The multifractal aspect of an avalanche is explored defining a multifractal measure, the toppling number density $\mu_i = S_i / \sum S_i$. Toppling number density is found to be mono-fractal for the BTW but it corresponds to different multifractal spectrum of exponents for the SSM and the RSM. A new entity, “toppling surface”, is defined in terms of S_i. The study of two point height difference correlation function reveals that the toppling surfaces of the BTW, the SSM and the RSM have widely different Hurst exponents H. The RSM and the SSM toppling surfaces are found to be multi-affine whereas that of BTW is a simple mono-affine surface. The roughness exponent χ of these surfaces are measured by studying the surface widths as a function of the system size. It is found that the scaling relation between H and χ follows usual Vicsek-Family scaling for the BTW model whereas for the other two models it follows a new anomalous scaling. A continuous phase transition, called “flooding transition”, in the toppling surfaces of RSM and SSM is found to occur when the toppling surfaces are flooded with water (say). In the flooding transition a path of water connecting the opposite sides of the toppling surface appears for the first time at a critical height of flooding (flooding threshold). Such a transition does not occur on the toppling surface of BTW model. Criticality of islands and their perimeters at the flooding threshold are found to depend on the Hurst exponent of toppling surfaces, the perimeter fractal dimension and the capacity dimension of the avalanche area. The universality class of flooding transition does not belong to the percolation universality class. All the critical exponents characterizing properties of islands and their perimeters in the flooding transition are found to be related with the avalanche size distribution exponents through the roughness exponent or the Hurst exponent of the toppling surfaces. Hence, the application of such new techniques to study the avalanche properties of different sandpile models not only classify their universality classes distinctly but also provide indepth information of the steady states of these dynamical systems. Finally, a continuous crossover from the RSM to the SSM universality class is demonstrated in a suitable parameter space controlling the fraction of sites with anti-clockwise rotational field in the RSM under clockwise rotational field.

Contents

Chapter 1

Introduction

Nature is complex. Complexity is usually attributed to the inability of capturing all the properties of a system by a single formalism. However, a large class of natural systems are found to share a common typical behaviour independent of the microscopic details of individual systems. For example, a pile of sand grains, an elastic network of springs, an ecosystem, the community of stock market dealers, etc., consist of many components that interact through some kind of exchange of forces or information. Time evolution of such systems under the influence of external forces along with the internal interaction forces lead to unexpected observations. Surprisingly, these dynamical systems are found to organize themselves without "tuning" of any of the system parameters from outside into a state with complex but rather general structure. Complexity in these systems corresponds to the non-existence of any single characteristic event size, time or length scale. On the other hand, in spite of the complexity, their general aspect is that all these physically measurable quantities demonstrate power law scaling behaviour at the steady state. Such a scale free power law scaling behaviour of observables are the demonstrating features of equilibrium critical phenomena [1,2,3] at a well defined critical point. However, in equilibrium critical phenomena, the critical point corresponding to a continuous phase transition is arrived by fine "tuning" of a system parameter, usually temperature. Bak, Tang and Wiesenfeld (BTW), in 1987, described the behaviour of organization to a critical state without fine tuning of any system parameter of a class of dynamical systems as *Self Organized Criticality* (SOC)[4].

Soon after the proposal of SOC, a large number of physical systems or processes were discovered whose time evolution dynamics exhibit SOC characteristics. A brief list of experiments as well as some natural phenomena that exhibit SOC is given here. In 1990, Held *et al.*[5] observed power law distribution of avalanche mass in experiments with different types of sand grains, though some initial experiments by Jaeger *et al.*[6,7] did not observe any power law distribution or critical behaviour. Power law distribution of avalanche mass were also observed in the experiments with elongated rough rice grains[8]. Plourde *et al.*[9] found a power law distribution of the droplet sizes when mist was sprayed inside a Plexiglas dome at a slow rate. In a chemical reaction of metals (Mg and Al) with aqueous $CuCl_2$, the distribution of chemo-magnetic field intensity generated by the electrochemical currents that appear due to the chemical reaction were also found to exhibit power law scaling behaviour[10]. The motion of vortexes in superconductors also exhibit scale invariant behaviour in both space and time[11,12,13]. The distribution of lifetimes and areas of discrete Barkhausen pulses in magnetic alloys follow power law distribution[14,15,16,17,18]. Power law distribution is also observed in the avalanches of neuronal activities in the networks of cortical neurones of a rat's brain[19,20]. Size distribution of power blackouts in power grid network of Norway and North America were recently observed to obey power law scaling behaviour[21]. Atmosphere which is constantly being pumped with evaporation energy of water vapours, relaxes its energy in the form of rainfall which also exhibit power law distribution of its size and frequencies[22,23]. The stresses between the tectonic plates that develops over the years are released in minutes in terms of earthquakes. The distribution of intensity and frequency of occurrence of earthquakes also show power law scaling behaviour[24]. The sudden release of magnetic energy due to rapid change in coronal magnetic field of solar corona induces radiative emission which is detected as solar flares. The probability distribution of these flare energies show a power law scaling behaviour[25,26,27].

Apart from the above mentioned physical and natural processes, there are several mathematical models, other than sandpile model introduced by BTW, that also demonstrate SOC. For example, Olami, Feder and Christensen (OFC) modeled earthquake in terms of sliding tectonic plates where local force or stress are taken as dynamical variable[28]. In their model, when a real dynamical variable E_i representing the energy or force associated with sites of a d dimensional cubic lattice becomes greater than or equal to some threshold value E_c, representing the sliding friction, the site releases all its energy. Out of the released energy E_i only $q\alpha E_i$ amount of energy is distributed equally to all the q nearest neighbours (NN) and $(1 - q\alpha)E_i$ energy is lost. The distribution of amount of energy released follow a power law scaling behaviour for $\alpha > \alpha_c$ where α_c is the critical level of conservation[29,30,31,32]. The second example is the lattice gas model for studying the fluctuation in vortex density of superconductor[33,34]. In this model particle in each cell of a d dimensional square lattice moves due to repulsive central force between (NN) sites and some additional driving forces. The power spectrum of fluctuation in number density of the particles with time show power law scaling behaviour. The third example is the forest fire model introduced by Drossel and Schwabl[35,36,37]. In this model the green trees grow with a probability p until they come in contact with nearest neighbouring burning tree or ignited by thunder with probability f. The distribution of the size of clusters formed by green trees exhibit power law scaling behaviour during the time evolution. This model was also successfully used to explain the temporal behaviour of number of people affected with measles in isolated Danish island of Bornholm as well as Faroe Islands[38]. The last example could be the model of biological evolution introduced by Bak and Sneppen[39]. In this model, the sudden extinction of certain species lead to change the fitness of other species which depend on the now-extinct species and may cause a chain of extinction event or avalanche. The distribution of number of extinct species during a certain burst of extinction and the duration of such an extinction follow a power law scaling behaviour.

It is observed that all these dynamical systems which are evolving into SOC state has a large separation of time scale between the external driving and the internal relaxation. Usually, the internal relaxation is much faster than the external drive. For example, the stress in the earth's crust is build up on the scale of years owing to the motion of the tectonic plates. However, the stress is subsequently released in a few seconds or minutes during an earthquake. Therefore, a class of systems, slowly driven from outside, evolves into a dynamical steady state at which the incoming flux of a physical quantity such as mass, energy, etc. remains the same as that of outgoing flux. The non-equilibrium steady state of these systems is found to be characterized by long range spatio-temporal correlations described by power law scaling[40,41,42,43,44,45].

1.1 Sandpile as prototypical model of SOC

BTW model: In 1987, BTW[4] introduced a simple cellular automata model, called BTW sandpile model, to study SOC. The model is defined on a two dimensional $(2d)$ square lattice. Each lattice site is assigned with a positive integer variable h, representing the height of the sand column of the respective lattice site. One starts with an empty lattice and keeps on adding sand grains, one at a time, to a randomly selected lattice site i. If the lattice site i receives a sand grain, the height of the sand column of the ith site is increased by one unit as $h_i \rightarrow h_i + 1$. The sand column of a lattice site becomes unstable or active when it's height h_i becomes equal or exceeds a predefined threshold value h_c. For a $2d$ square lattice, the critical height is taken as $h_c = 4$. If a site i becomes active it topples by loosing h_c amount of grains and they are distributed equally among the nearest neighbours (NNs). The toppling dynamics can be summarized by the following deterministic toppling rule

$$\begin{aligned} h_i &\rightarrow h_i - 4 \\ h_j &\rightarrow h_j + 1, \quad j = 1, 2, 3, 4 \end{aligned} \tag{1.1}$$

where $\{j\}$s are the NN sites of the site i.

After the introduction of BTW model a large number of its variant were introduced and studied. Only a few of them are mentioned below.

Zhang model: A continuous height model was introduced by Zhang[46]. In this model $h_c = 1$. The model was driven by adding certain amount of energy δ with $0 < \delta \leq 1$, to a randomly chosen lattice site i, and hence $h_i \rightarrow h_i + \delta$. The value of δ was kept fixed over the simulation. On a square lattice, the toppling rule is given as

$$\begin{aligned} h_i &\rightarrow 0, \\ h_j &\rightarrow h_j + h_i/4, \quad j = 1, 2, 3, 4 \end{aligned} \tag{1.2}$$

where the height of the toppled site is reduced to 0 and all the four neighboring sites $\{j\}$ gain $h_i/4$ amount of sand.

A generalized Zhang model was also introduced by Biham[47]. In this model, the amount of sand transfer to NNs after toppling is given by $ph_i/4$ where $0 \leq p \leq 1$. Thus, only a fraction p of the sands present in the unstable site i is distributed to its neighbours and the rest remain in i.

Manna model: In the above mentioned models, sand grains are distributed equally to the NN sites of the active site. However, such equal distribution of sand grains may not always occur for real sand grains with irregular shape and sizes. For sand grains with irregular shape and sizes, the NNs of the active site may receive different number of sand grains. In order to incorporate such irregularity in the shape and size of the sand grains, Manna developed a stochastic sandpile model[48,49]. In Manna's stochastic model (MSM), the critical height was chosen as $h_c = 2$ for the square lattice. During the time evolution, when the height of the sand column at the ith lattice site, $h_i \geq h_c$ the site becomes active and bursts into toppling activity. For each sand grain at the active site, a NN site was randomly chosen and the grain was transferred until the active site becomes empty.

Dhar model: This is a modified version of the Manna model. In Dhar model[50], the critical height was also taken as $h_c = 2$ for the square lattice. After toppling, the sand grains flow in two randomly selected directions out of four possible directions on a square lattice and reduces the height of the present site only by an amount equal to h_c and rest of the sand grains remain at the active site. The toppling rule can be summarized as:

$$h_i \rightarrow h_i - h_c, \quad h_j \rightarrow h_j + 1, \quad j = j1, j2 \tag{1.3}$$

where $j1, j2$ are the two randomly selected sites out of the four NN sites of the active site i on a square lattice. The modified Manna model or the Dhar model will be referred as SSM later on.

Directed sandpile model: The effect of external bias on sandpile models was studied by applying a global directed bias and the corresponding model is called directed sandpile model (DSM)[51]. The directness in a sandpile model physically correspond to a sandpile dynamics on an inclined plane. The model was defined on a $2d$ square lattice. Sand grains were added to the randomly selected sites on the top edge of the lattice. The global directed bias is applied along the direction top to bottom of the lattice. If the height of the sand column is greater than the critical height $h_c = 2$, it topples by releasing two sand grains and gives one each to the two downward neighbours of the toppled site.

All these models are mostly studied with open boundary condition where dissipation of sand grains occur at the boundary of the lattice or at the bottom edge of the lattice for the DSM. Toppling of an active site may make some of the neighbouring sites active and consequently cause a cascade of toppling activities which constitutes an avalanche. The avalanche stops when heights of all the sand columns become under critical. During the avalanche no sand grain is added in order to keep the time scale associated with the internal dynamics much smaller than the time scale associated with the external drive. As the sand grains are kept on adding, the system evolves on its own to a situation at which the average influx of the sand grains is equal

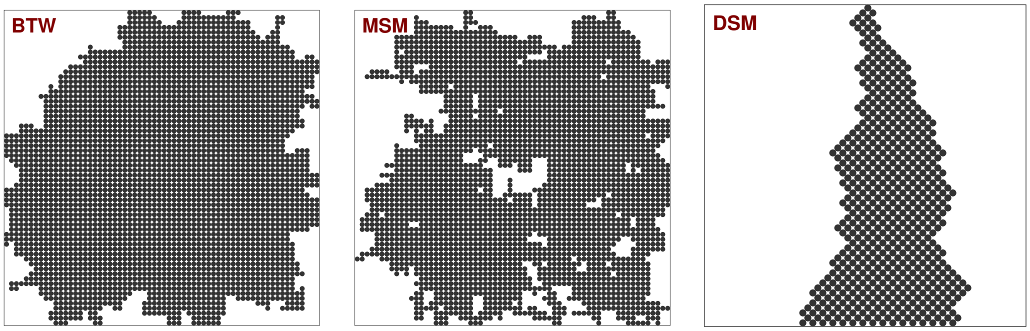

Figure 1.1: Typical avalanche cluster obtained at the steady state of the BTW, the MSM and the DSM on a 64×64 square lattice are shown. The avalanche clusters of both the BTW and the DSM are compact and do not contain any hole, whereas in MSM there are several holes of different sizes. Both the avalanche clusters of BTW and MSM are isotropic but for the DSM it is anisotropic.

to that of average outflux. This is called the non-equilibrium steady state of these systems.

These models have some salient features. Firstly, in a given time step during avalanche there could be more than one active sites. In the case of BTW, the final height configuration is found independent on the sequence at which the active sites are toppled. Whereas, in the case of Manna model, the final height configuration depends on the sequence at which the active sites are toppled. In abstract algebra, an Abelian group is a group in which the result of applying group operation to two group elements does not depend on their order. Following such a definition, the BTW model is identified as a deterministic Abelian sandpile model whereas the Zhang model is a deterministic non-Abelian model. The Manna model, MSM, is a stochastic non-Abelian model whereas the Dhar model, SSM, is a stochastic Abelian model. DSM is a deterministic Abelian model. Secondly, in the BTW model, if a site topples it gives away four sand grains to its neighbours. At the same time, if its neighbours topple once each they give back exactly four sand grains to the original site. This is called “complete toppling balance”. However, the other models described above do not have toppling balance.

In Fig.1.1, typical avalanche clusters obtained at the steady states of different sandpile models are shown. The avalanche clusters presented here by the black dots are the collection of distinct sites toppled during the avalanche. The avalanche clusters for the BTW and the MSM are isotropic in nature whereas it is anisotropic for the DSM due to the presence of global directed bias. The deterministic models like

BTW and DSM do not have any voids inside the avalanche clusters whereas there are some voids inside the avalanche cluster of MSM.

Apart from the above mentioned models, several other sandpile model were also introduced and studied extensively over last two decades. Some of those models are: sandpile model with stickiness[52], non-conservative sandpile models[53,54,55,56], sandpile model with spatial disorder[57], continuous Abelian sandpile[58], sandpile with bulk dissipation[59,60,61,62,63], Abelian and non-Abelian stochastic sandpile models[64,65,66] and many others.

1.2 Characterization of SOC

There exists a well defined prescription to study critical behaviour in equilibrium statistical mechanics[1,2,3,67]. In equilibrium critical phenomena, a quantitative change in the properties of a system occurs at a sharply defined parameter value, the critical point, if that parameter is changed continuously. In thermodynamic systems such a parameter is usually the temperature T. As $T \to T_c$, critical temperature, the system exhibits features called critical phenomena[1,2,3,67]. Thermodynamic quantities Q such as order parameter and response functions of the system, exhibit singularities $Q \sim |T - T_c|^{\pm\theta}$ as $T \to T_c$ where θ is called the critical exponent. Plus sign corresponds to branch point singularity and minus sign corresponds to divergence. The thermodynamic quantities can be estimated by taking different derivatives of the appropriate free energy function of the system. The free energy function is obtained by calculating the canonical partition function $Z(\mathcal{H})$ knowing the Hamiltonian $\mathcal{H}$ of the system. The free energy functions are found to be generalized homogeneous functions as $T \to T_c$. A generalized homogeneous function $F(x, y)$ can be written as

$$F(x, y) = x^a \mathsf{f}(y/x^b)$$

when both $x, y \to 0$. As a consequence of the thermodynamic potentials being generalized homogeneous functions: (i) all the critical exponents can be obtained in terms of a and b since, thermodynamic quantities are just different derivatives of thermodynamic potentials. Hence they are not all independent. (ii) data for different values of x and y should follow a single scaling function $\mathsf{f}(z) = F(x, y)/x^a$ where $z = y/x^b$ is a scaled variable. One often estimates the values of the critical exponents that describe the singularities of the thermodynamic quantities and verifies the scaling function forms. The set of critical exponents and the form of the scaling function determine the universality class of a system in the thermodynamic limit.

However, such a well defined prescription is often not available to study the systems at out of equilibrium. Most often one finds the Hamiltonian is too complex or it cannot be written. Moreover, one needs to identify appropriate response functions that could be measured. In the case of sandpile models, the response of the system to the external drive could be the total number of toppling or toppling size s in an avalanche, the number of distinct sites toppled in an avalanche or the avalanche area a, the number of parallel updates to make all the sites under critical or the lifetime t, and spatial extension l of an avalanche. The spatial extension l of an avalanche can be defined as $l^2 = 2\sum_{i=1}^{a}(\mathbf{r}_0 - \mathbf{r}_i)^2/a$ where $\mathbf{r}_0 = \sum_{i=1}^{a}\mathbf{r}_i/a$, $\mathbf{r}_i$ is the position vector of the distinct sites toppled. As the system evolves to the steady state, one needs to measure such quantities. However, these quantities are not independent. On the other hand, one can perhaps easily estimate the probability $P(s,a,t,l)$ of occurrence of an avalanche with toppling size s, area a, lifetime t and spatial extension l. Knowing $P(s,a,t,l)$, one may obtain the probability $P(x)$, $x \in \{s,a,t,l\}$ to find an avalanche with parameter value x irrespective of the values of the other parameters as

$$P(s) = \int\int\int P(s,a,t,l)dadtdl, \tag{1.4}$$

$$P(a) = \int\int\int P(s,a,t,l)dsdtdl, \tag{1.5}$$

$$P(t) = \int\int\int P(s,a,t,l)dsdadl, \tag{1.6}$$

$$P(l) = \int\int\int P(s,a,t,l)dsdadt. \tag{1.7}$$

In the equilibrium critical phenomena, the criticality corresponds to the appearance of fluctuation at all possible length scale or clusters of all possible sizes and consequently power law scaling becomes a signature of the criticality. Thus, the probability distribution functions defined here at the non-equilibrium steady state of a dynamical system are also expected to obey power law behaviour in order to demonstrate the criticality of the steady state. In the thermodynamic limit, the distributions are then given by

$$P(x) \sim x^{-\tau_x} \quad ; \quad x \in \{s, a, t, l\} \tag{1.8}$$

where τ_x is the critical exponent related to the quantity x.

Since the avalanche properties are related to each other, conditional expectation values can be defined appropriately[68]. The conditional expectation value of an avalanche property x when another property is exactly equal to y is defined as

$$\langle x(y) \rangle = \int_0^{x_{max}} xP(x|y)dx \tag{1.9}$$

where $P(x, y)$ is the probability to find a property x when the other property is exactly equal to y. In the steady state, the expectation values scale with its argument as

$$\langle x(y) \rangle \sim y^{\gamma_{xy}}, \tag{1.10}$$

where γ_{xy} is a critical exponent. Similarly, one can define other expectation values as

$$\langle x(z) \rangle \sim z^{\gamma_{xz}} \quad \text{and} \quad \langle y(z) \rangle \sim z^{\gamma_{yz}}. \tag{1.11}$$

According to these scaling function forms, the exponents should satisfy a scaling relation

$$\gamma_{xz} = \gamma_{xy}\gamma_{yz}. \tag{1.12}$$

A set of scaling relations between the probability distribution exponents τ_x and the exponents γ_{xy} can be obtained. Since the properties (s, a, t, l) are of the same avalanche, the conditional expectation values must satisfy the following identity:

$$\int \langle z(x) \rangle P(x)dx = \int \langle z(y) \rangle P(y)dy. \tag{1.13}$$

Such an identity would be satisfied by a set of any three stochastic variables out of (s, a, t, l). Following the above identity, one has

$$\int x^{\gamma_{zx}-\tau_x}dx = \int y^{\gamma_{zy}-\tau_y}dy. \tag{1.14}$$

Since, $\langle x(y) \rangle \sim y^{\gamma_{xy}}$,

$$\int x^{\gamma_{zx}-\tau_x}dx = \int x^{\gamma_{xy}(\gamma_{zy}-\tau_y)}.x^{\gamma_{xy}-1}dx = \int x^{\gamma_{zx}+\gamma_{xy}(1-\tau_y)-1}dx. \tag{1.15}$$

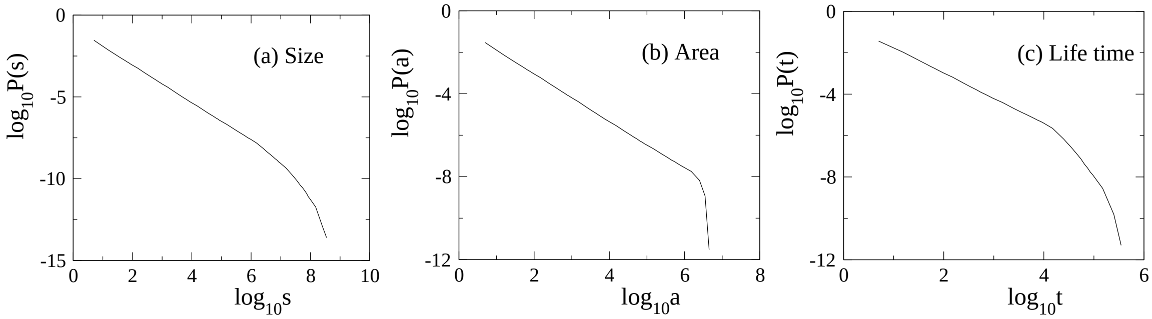

Figure 1.2: Probability distributions (a) $P(s)$, (b) $P(a)$ and (c) $P(t)$ are plotted against s, a and t respectively for system size $L = 2048$ for the BTW. Reasonable power law scaling is observed for all the distributions.

Integrating both sides one has,

$$\gamma_{xy} = \frac{\tau_y - 1}{\tau_x - 1}. \tag{1.16}$$

As in the equilibrium critical phenomena, one should now identify the power law scaling, estimate the values of the critical exponents, $\tau_x, \tau_y, \gamma_{xy}$ etc., and verify the scaling relations among them. Having the values of the critical exponents, one can determine the universality class of a sandpile model. In Fig. 1.2, the probability distributions of toppling size $P(s)$, area $P(a)$ and lifetime $P(t)$ of the avalanches of the BTW model obtained on a 2048×2048 square lattice are shown. It can be seen that avalanches with all possible toppling size, area and lifetime appear in the steady state and consequently all the response functions have power law distribution. The cut off values of these distributions are of course determined by finite system size. Numerical study of the probability distribution of avalanche related quantities in the steady state of not only the sandpile models but also other models of SOC reveals that the distribution functions follow power law scaling. The conditional expectation values of several quantities also found to follow the scaling given in Eq. 1.10. The values of critical exponents associated with probability distributions and conditional expectations are listed in Table 1.1 for some of the well known sandpile models. It can be seen that the exponent values of the BTW and the Zhang are almost the same and consequently these two models are believed to belong to the same universality class. It can be noticed that the values of the distribution exponents (τ_x) of the MSM are narrowly resolved to that of the BTW and it was initially believed that the BTW and the MSM belong to the same universality class[69,70,71,72,73]. Though SSM is an Abelian model and MSM is a non-Abelian model, the values of the critical exponents of these two models were found to be the same and consequently belong to the same universality class. Later stochastic sandpile models will be referred as SSM. However, measuring the exponents describing the conditional expectation, γ_{xy}s, it was shown that MSM belongs to a new universality class[74,75,76,77]. DSM, an anisotropic sandpile model, is exactly solved and the values of the critical exponents for this model are also given in Table 1.1. It can be seen that the DSM exponents are very different from those for the BTW or MSM (or SSM). DSM, therefore, belongs to a different universality class than that of both BTW and SSM (or MSM). A stochastic version of DSM, directed stochastic sandpile model (DSSM)[64,65], was studied later and its critical exponents are also reported in Table 1.1. It was found that DSSM belongs to a different universality class than DSM.

Model	τ_s	τ_a	τ_t	τ_l	γ_{sa}	γ_{al}	γ_{at}	γ_{tl}
BTW[47,75,76,77]	1.293	1.330	1.480	1.665	1.06	2.00	1.53	1.32
Zhang[46,47,78]	1.282	1.338	1.50	1.682	1.06	2.00	1.53	1.29
MSM[75,76,77]	1.275	1.373	1.493	1.743	1.23	2.00	1.35	1.49
DSM[51,64,75]	4/3	···	3/2	···	1.00	···	1.50	1
DSSM[64]	1.43	···	1.71	···	···	···	···	0.99

Table 1.1: Critical exponents associated with probability distributions and conditional expectations of different avalanche related quantities of BTW, Zhang, MSM, DSM and DSSM.

In order to understand the scaling behaviour of the distribution functions and to confirm the different universality classes of BTW and SSM, finite size scaling analysis of the distributions were performed using moment analysis[79,80,81,82] which will be discussed below.

1.3 Finite size scaling

In numerical simulations, the results are very often limited by the finite system size L. There is rounding and shifting of critical singularities in finite systems depending on the ratio of correlation length to the linear dimension L of a system. In order to obtain the behavior of a macroscopic system in the thermodynamic limit, the results of the finite systems are often extrapolated using finite-size scaling (FSS) ansatz[83]. Because of finite system size L, the probability distributions $P(x, L)$ are limited by the maximum value $x_{max}(L)$ of an avalanche related quantity x. The cutoff $x_{max}(L)$ is expected to increase with system size as $x_{max}(L) \sim L^{D_x}$, where D_x is called a capacity dimension. The probability distribution function of an avalanche-related quantity x at the steady state for a system size L can be written as

$$P(x, L) = x^{-\tau_x} \mathsf{f}_x(x/L^{D_x}) \tag{1.17}$$

where τ_x is the corresponding critical exponent and x stands for s, a, t and l and $\mathsf{f}(x/L^{D_x})$ is the finite size scaling function. In the $L \to \infty$ limit, the scaling function $\mathsf{f}(0)$ becomes a constant and the power law behavior given in Eq.1.17 can be approximated as $P(x) \sim x^{-\tau_x}$.

In order to verify whether the scaling functions obey FSS or not, the method of moment analysis was developed[79,80,81,82]. In this method, higher moments of an avalanche property are calculated and checked whether the scaling exponent varies proportionately with the order of the moment taken. The qth moment of a property x is defined as

$$\langle x^q \rangle = \int_0^{x_{max}} x^q P(x, L) dx = \int_0^{x_{max}} x^{q-\tau_x} \mathsf{f}(x/L^{D_x}) dx. \tag{1.18}$$

Defining a scaled variable $Z = x/L^{D_x}$, $\langle x^q \rangle$ can be written in terms of Z as

$$\langle x^q \rangle = L^{(q+1-\tau_x)D_x} \int_0^{Z_{max}} \mathsf{f}(Z) dZ \sim L^{\sigma_x(q)}. \tag{1.19}$$

Since the integration will contribute to a constant, $\sigma_x(q)$ can be written as

$$\sigma_x(q) = (q + 1 - \tau_x) D_x. \tag{1.20}$$

Thus, if the probability distributions obey FSS then the exponent $\sigma_x(q)$ should have a constant gap between two successive moments $\sigma_x(q+1) - \sigma_x(q) = D_x$. On the other hand, if they obey multiscaling, $\sigma_x(q+1) - \sigma_x(q)$ should have a continuous dependence on q. Thus the derivative $\partial\sigma_x(q)/\partial q$ should converge to D_x in the $q \to \infty$ limit. Knowing the capacity dimensions D_x, it is possible to check the scaling function form given in Eq. 1.17 studying the distribution functions for different system sizes L. Data for different system sizes L should collapse onto a single curve $\mathsf{f}(z)$, if a scaled distribution $P(x)L^{D_x\tau_x}$ is plotted against a scaled variable $z = x/L^{D_x}$ for $x \in \{s, a, t, l\}$.

FSS and moment analysis for the sandpile models were extensively studied in the literature[73,79,80,81,84,85]. It was found that the toppling size distribution function does not obey FSS in BTW rather follows a peculiar multiscaling[79,80,81] whereas the same distribution in the MSM and the SSM were found to obey FSS[73,79,80,81,84,85]. The FSS analysis was then able to confirm different universality classes of MSM (or SSM) and BTW. In order to understand the reason behind the unusual multiscaling behaviour in BTW and FSS in MSM, a coarse grained study of sandpile avalanches were performed decomposing the avalanches into waves of toppling[86,87,88]. The toppling wave time series were found to have a positive auto-correlation in BTW but a negative auto-correlation in MSM[89,90,91]. The presence of positive auto-correlation in toppling wave time series is believed to be the reason behind the multiscaling behaviour in BTW[89,90,91].

1.4 Absorbing state phase transition and interface growth

The non-equilibrium steady state of a sandpile model is reached without fine tuning of any control parameter. Such dynamical systems are also studied in a similar footing of equilibrium continuous phase transition taking the density of the sand grains ζ as a tunable parameter. The sandpile model was also studied with closed boundary and no dissipation. Such a sandpile model is known as fixed energy sandpile (FES) model. In FES, the density of the sand grains ζ was tuned to a critical value ζ_c from below and an absorbing to an active state phase transition was observed[84,92]. At $\zeta = \zeta_c$, an infinite avalanche occurs for the first time. For $\zeta < \zeta_c$, the toppling activity in the system always stops at a finite time but the activity sustains indefinitely for $\zeta \geq \zeta_c$. During the toppling activity, the number of toppling of a site upto time t defines an interface. In the active-absorbing state phase transition of sandpile models, the growth of the interface stops and becomes a pinned surface for $\zeta < \zeta_c$ but the it grows continuously for $\zeta \geq \zeta_c$. Thus the system undergoes a depinning transition at $\zeta = \zeta_c$. The growth dynamics of the interface was studied by several groups as mentioned in Ref.[93,94,95,96,97]. The width $W(t,L)$[98,99,100] of the interface at time t was found to follow the scaling given by

$$W(t,L) \sim \begin{cases} t^{\beta_W} & t \ll t_\times \\ L^\chi & t \gg t_\times \end{cases}$$

where β_w is the growth exponent, χ is the roughness exponent and $t_\times$ is the crossover time after which the interface width attains its saturation. $t_\times$ scales with L as

$t_\times \sim L^z$, where z is the dynamical exponent which is related to growth and roughness exponent as $\chi = \beta_w z$. The values of the critical exponents for BTW was found as $\chi = 1.01$, $\beta_W = 0.62$ and $z = 1.63$ where as for Manna model they were found as $\chi = 0.80$, $\beta_W = 0.51$ and $z = 1.57$[93]. The roughness exponent χ is related to the capacity dimension of avalanche size D_s as $D_s = 2 + \chi$[95,96]. In fact, mapping of avalanches of sandpile models to growing interfaces were first introduced by Paczuski and Boettcher[101] in the context of Oslo sandpile in $1d$ in 1996 and later studied extensively for BTW and SSM by Alava[95,96].

1.5 The problem:

In the last few sections, a number of sandpile models are introduced and several techniques to characterize these models including absorbing state phase transition are discussed. It is important to notice that the application of global directed bias on the sandpile dynamics (the DSM) leads to a non-trivial phenomenon. The avalanche cluster of this deterministic Abelian model is anisotropic and its properties are described by a new set of critical exponents than the other models. A stochastic version of DSM, DSM with stickiness[52], was found to belong to the same universality class of directed percolation[102]. The non-trivial effect of directed bias on the dynamical system at out of equilibrium was not surprising because the application of such a bias on several lattice statistical models in equilibrium critical phenomena were already found to produce non-trivial effects. For example, models like directed self-avoiding walks[103,104], directed lattice animal[105], directed percolation[102] exhibit different critical behaviour than their respective models without directed bias. In the equilibrium critical phenomena, the rotational bias was also found to have nontrivial effect on the critical behaviour of many lattice statistical models. Such as, spiral self-avoiding walks[106,107], spiral lattice animal[108,109], spiral percolation[110], directed spiral percolation[111,112] etc. belongs to new universality classes than their original counterpart in absence of rotational field. The rotational field does not destroy the isotropic nature of a system whereas the application of a directed bias always introduces anisotropy in the system. Moreover, the rotational field has broken mirror symmetry. It is then intriguing to explore the effect of rotational bias on the critical behaviour of sandpile models. Sandpile model under rotational bias may physically correspond to a sandpile dynamics on a horizontal disk rotating slowly about an axis perpendicular to the disk and passing through the center of the disk. In this thesis, a new sandpile model called rotational sandpile model (RSM)[113] is constructed applying rotational constraint on the toppling dynamics of a sandpile model. The rotational toppling rule is mostly deterministic except the first step and thus the model is a quasi-deterministic model. However, the rotational dynamics as evolved with time introduces certain stochasticity in the model. It is therefore important to investigate such a model and characterize the non-equilibrium steady state in order to identify the universality class of RSM. It is curious to observe whether RSM belongs to the BTW universality class or to that of the SSM. In RSM, it is possible to control the internal stochasticity by tuning the toppling rule. The tuning could lead the model to a more deterministic one or to a more stochastic one. The effect of such tuning of the toppling rule on the universality class of the model is then important to look at. Moreover, the universality class of a system is identified by the values of the critical exponents. On the other hand, the numerical values of the critical exponents obtained for different models through the measurement of power law distributions or moment analysis were found to be narrowly resolved in most of the cases. Therefore, it is also important to explore newer techniques or statistical methods which could classify the dynamical systems distinctly. In this thesis, several such techniques are developed and employed to different sandpile models. It is observed in equilibrium critical phenomena that the universality class of a system in the same spatial dimension is determined by the symmetry (number of components) in the order parameter. Is it possible to identify a similar prescription for the dynamical systems to identify different symmetries in the toppling rules corresponding to different universality classes of these systems? An attempt has been made to resolve such an issue at the end of the thesis. The possibility of crossing over from one universality class to that of another by controlling certain external parameter has also been explored. Finally, the application of a set of new techniques to study different sandpile models makes it possible to characterize them distinctly, the universality classes of these models are identified by the symmetries in their toppling rules and a crossover from RSM universality class to that of SSM is found possible.

The thesis is organized in the following way. In chapter 2, the rotational sandpile model (RSM) is introduced and the critical behaviour of the steady state is characterized by studying the probability distribution of avalanche properties as well as by performing FSS analysis. In chapter 3, two variants of RSM are introduced. In one variant of RSM, called RSM1, the toppling rule is more deterministic than RSM and in the other variant of RSM, called RSM2, the toppling rule is more stochastic than RSM. Usual techniques of measuring the critical exponents are employed and their universality classes are determined. In chapter 4, two new methods to analyze avalanche properties are introduced. Multifractal aspect of the avalanche cluster as well as multi-affine character of the toppling surface associated with an avalanche are explored. In chapter 5, a novel continuous phase transition called flooding transition through the toppling surface is studied and a set of new critical exponents are estimated. Chapter 6 contains the critical properties of the island perimeters at the threshold of flooding transition. The symmetries of different sandpile models and a crossover from RSM to SSM in a suitable parameter space are studied in chapter 7. A summary of the whole thesis and a discussion on the importance of the results obtained are given in chapter 8.

Chapter 2

Rotational sandpile model and its properties

A lattice statistical model is developed here to study the sandpile dynamics in 2-dimensions ($2d$) under rotational constraint. A common example of rotational motion is the motion of a charged particle in a plane in presence of a magnetic field applied perpendicular to the plane of motion. The sandpile model under rotational constraint will be called as rotational sandpile model or RSM. In order to implement rotational constraint on a lattice model, one needs to remember the direction along which a sand grain or a particle moves at every time step. If in a given time step, a particle has moved toward north then in the next time step it can move either toward north or toward east under a clockwise rotational field. Implementation of such a bias on a square lattice is demonstrated in Fig. 2.1. The motion of the particle under rotational constraint in a given time step depends on the direction of motion in the previous time step and could be different at one lattice point to another. Such a bias is called a local bias. Implementation of rotational bias in equilibrium lattice statistical models can be found in Ref.[108,109,110]. Below, the sandpile model is developed under such a local bias.

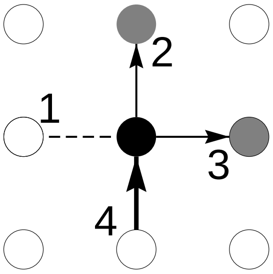

Figure 2.1: Four directions from a lattice site are marked as 1, 2, 3 and 4. Direction 1 corresponds the left, 2 corresponds the up, 3 corresponds the right and 4 corresponds the down from a site. The particle coming from 4 to the central black site can move to 2 or 3 under a clockwise rotational constraint.

2.1 The model: RSM

Consider a $2d$ square lattice of size $L \times L$. A positive integer variable h_i is assigned to each lattice site i which will represent the height of the sand column at the site i. Starting with an empty lattice where all h_is are zero, sand grains are added one at a time to randomly chosen lattice sites. The variable h_i is incremented to $h_i + 1$ if a sand grain is added to the ith site. A site becomes active or critical when the height of the site becomes greater than or equal to a predefined threshold value h_c. The value of h_c is taken as $h_c = 2$ for the $2d$ square lattice. While adding a sand grain if the site becomes active it will burst into a toppling activity by loosing h_c sand grains and distributing them to the nearest neighbours (NN) according to the toppling rule described below. On the very first toppling of the active site, two sand grains are given away to two randomly selected nearest neighbors out of four nearest neighbors on a square lattice. As soon as a site receives a sand grain, the direction d_i from which the grain was received is assigned to it besides incrementing the height of the sand column h_i by one unit. The value of d_i can change from 1 to 4 as there are four possible directions on a square lattice. The directions from an active site i are defined as $d_i = 1$ for left, $d_i = 2$ for up, $d_i = 3$ for right and $d_i = 4$ for down. As the avalanche propagates, the direction d_i and height h_i are updated on receiving a sand grain and the information from which direction the last sand grain was received is only kept. The next active sites with $h_i \geq h_c$ in the avalanche will topple following a deterministic rotational toppling rule. One of the two sand grains from an active site will flow in the forward direction, the direction from which the last grain was received, and the other will flow in a clockwise rotational direction with respect to the forward direction. The toppling rules for an active site i can be stated as:

For the first toppling only:

$$\begin{aligned} h_i &\to h_i - 2, \\ h_j &\to h_j + 1, \quad j = j1, j2 \end{aligned} \tag{2.1}$$

where $j1, j2$ are two randomly selected sites out of four NN sites of the active site i on a square lattice.

For the second toppling onward:

$$\begin{aligned} h_i &\to h_i - 2, \\ h_j &\to h_j + 1, \quad j = d_i \ \& \ d_i + 1 \end{aligned} \tag{2.2}$$

where d_i is the direction from which the last sand grain was received by the ith site.

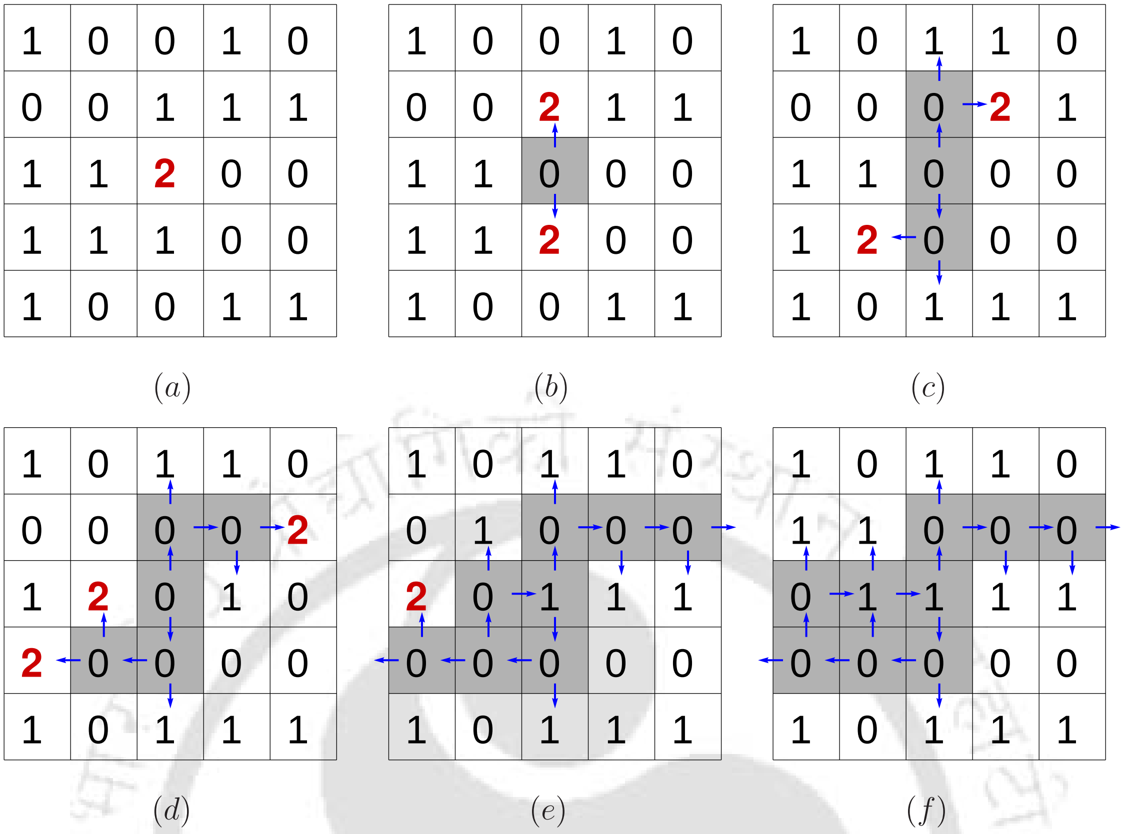

Figure 2.2: RSM is demonstrated on a 5 × 5 square lattice taking an arbitrary initial configuration with the central site as an active site. The active sites with height 2 are represented by bold letters in red. In the first toppling, the up and down NNs are randomly chosen for sand grain distribution. In later toppling, the sand grains from an active site flow in the forward direction and in a clockwise rotational direction. The sites in the avalanche cluster are represented by the grey shade. Five parallel updates were needed to make the system under critical. The avalanche has toppling size and area both equal to nine.

If the index j becomes greater than 4 it is taken to be 1.

Toppling of an active site may initiate a series of intermittent bursts which constitute an avalanche. Toppling of the first active site in an avalanche is taken as the first time step. At the end of the first time step, some of the NN sites become active. They are kept sequentially as they appear. In the second time step, all those active sites are toppled in the sequence as they are stored. This is called a parallel update. The sites that become active at the end of the second time step are relaxed by the next parallel update or third time step. The process of parallel update continues until an avalanche stops when the height of all the sand columns are less than h_c. The number of parallel updates required to make the system under critical is taken as the lifetime of an avalanche. During an avalanche no sand grain is added to keep the driving slow in comparison to the internal relaxation. The avalanche dynamics is studied with open boundary condition *i.e.*; loss of sand grain from the lattice is possible through the boundary of the lattice.

Toppling rule of RSM is demonstrated in Fig. 2.2 on a 5 × 5 square lattice taking an arbitrary initial configuration of the height of the sand columns. The numbers associated with the boxes in Fig. 2.2 represent the height of the sand columns at each lattice site. Upon adding one sand grain to the central site makes it an active site and it is represented by a bold faced digit 2 in red. The active site topples and it relaxes by releasing two sand grains. For the first time, they are distributed to two randomly selected NN sites following the toppling rule given in Eq. 2.1. As shown in Fig. 2.2(b), the two randomly selected sites are the top and the bottom NN sites. The directions from which the top and the bottom sites received sand grains are $d_i = 2$ and $d_i = 4$ respectively and they are indicated by arrows in Fig. 2.2(b). Both the top and the bottom NNs of the central site become active upon receiving a sand grain each. They topple simultaneously (parallel update of the active sites) in the next time step following clockwise toppling rule given in Eq. 2.2(b). As per the toppling rule given in Eq. 2.2(b), the sand grains of the top NN site will flow toward up and right whereas for the bottom NN site they will flow toward down and left. The flow of sand grains from these active sites are shown by arrows in Fig. 2.2(c). On receiving these sand grains, some sites again become active. The active sites produced in this time step are toppled simultaneously in the next time step and the cascade of toppling activities stop when all the site become under critical. In five time steps, the toppling activity stops and the final configuration is shown in Fig. 2.2 (f). At the end of the avalanche, it can be noticed from the arrows marked in Fig. 2.2 that the sand grains whirl in a clockwise rotational path during the toppling activity.

2.2 Salient features of RSM

Several salient features of this newly introduced model are discussed below.

Two states: Since the final state of a site is either occupied by a single sand grain or remains empty, the RSM is a two state model. Similarly, the MSM (or the SSM) is also a two state model but the BTW is a four state model.

Mass conservation: During toppling the sand grains released from an active site are not lost, instead they are distributed to the NN sites of the active site following

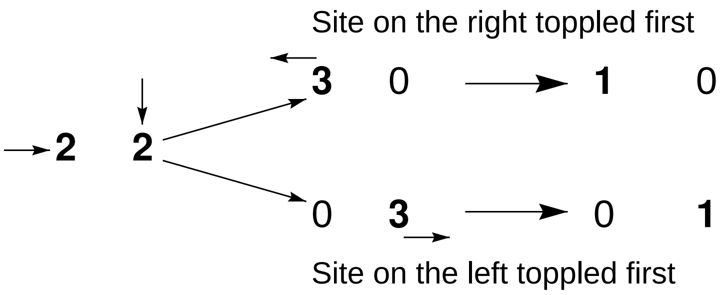

Figure 2.3: Two different final states are obtained interchanging the toppling sequence starting from the same initial state. The numbers represent the height of the sand column and the associated short arrows represent the direction from which the last sand grain was received.

the toppling rules of the RSM. In a non-conservative model, certain fraction of sand is lost at each toppling and rest are distributed to the NN sites following the toppling rule of that model[53,54,55,56]. Therefore, there is conservation of mass in the RSM.

Toppling imbalance: The number of sand grains outgoing from a site after toppling is not necessarily equal to the number of sand grains incoming to the same site after toppling of its NNs once each. Therefore, there is toppling imbalance in RSM. This is also the case in the MSM[82]. However, there is complete toppling balance in BTW[4,114,115] because toppling of a site gives away four sand grains and toppling of its four NNs once each gives back four sand grains. It can be noted that, imposition of rotational constraint is responsible for toppling imbalance in RSM whereas the toppling imbalance in SSM or MSM is due to randomness in grain distribution.

Non-Abelian: The final configuration in an avalanche depends on the sequence of toppling of the active sites due to the rotational toppling rules considered in the RSM. It is demonstrated in Fig. 2.3 considering two nearest neighbours at the critical state ($h = 2$) at the same time step. The numbers represent the height of the sand column at that site. The short arrows associated with the numbers represent the direction from which the last sand grain was received. It can be seen that reversing the order of toppling, two different final states are obtained. It has been verified for a larger lattice on $2d$ that the interchange of toppling sequence leads to different final configurations starting from the same initial configuration. Consequently, the model is non-Abelian. In the BTW model, however, the final configuration is independent of toppling sequence and it is an Abelian model. The original Manna model is non-Abelian but the modified Manna model (SSM) is an Abelian model.

Internal stocashticity: In RSM, it is important to notice that toppling of one site may change the present state (direction from which the last sand grain was received) of the nearest neighbours. Consequently, the sand grains will flow in different directions than it was expected before toppling of its neighbours. Apart from the initial stochastic step, the imposition of the rotational rule then also introduces some randomness in the model during time evolution. This can be considered as "internal stochasticity" in the model in contrast to the externally imposed stochasticity in SSM or MSM[48,49,50]. This inherent randomness makes the model not only non-Abelian but also "quasideterministic". It is also important to notice that because of the internal stochasticity in RSM, the local correlation in the rotational toppling rules then cannot propagate throughout the avalanche as in the BTW.

Thus, on one hand RSM has features of mass conservation, open boundary, local deterministicity in gain distribution after toppling as that of BTW while on the other hand, it has features like toppling imbalance, certain stochasticity as that of SSM and MSM as well as non-Abelianity as that of MSM. It is then important to characterize the critical behaviour of RSM which has microscopic features of both the BTW and the SSM or the MSM. Later on stochastic sandpile model will be referred as SSM if it is not mentioned specifically.

2.3 Steady state

Taking an empty square lattice of size 4096 × 4096, sand grains are added one at a time to randomly chosen sites. The system evolves following the RSM toppling rule. The non-equilibrium steady state of a sandpile model corresponds to constant current of the incoming and outgoing flux of sand grains. At this situation, average height of the sand columns remains constant with time. In order to identify the steady state of RSM, the average height of the sand columns

$$\langle h \rangle = \frac{1}{L^2} \sum_{i=1}^{L^2} h_i \tag{2.3}$$

is measured adding a large number of sand grains. The average height $\langle h \rangle$ is measured after every $10,000$ sand grains added. Measurement of $\langle h \rangle$ is always performed after the avalanche is completed. In Fig. 2.4(a), $\langle h \rangle$ is plotted against the number of sand grains added. Total number of sand grains added to the system of size $L = 4096$ is 15×10^6. It can be seen that a constant average height $\langle h \rangle$ is achieved

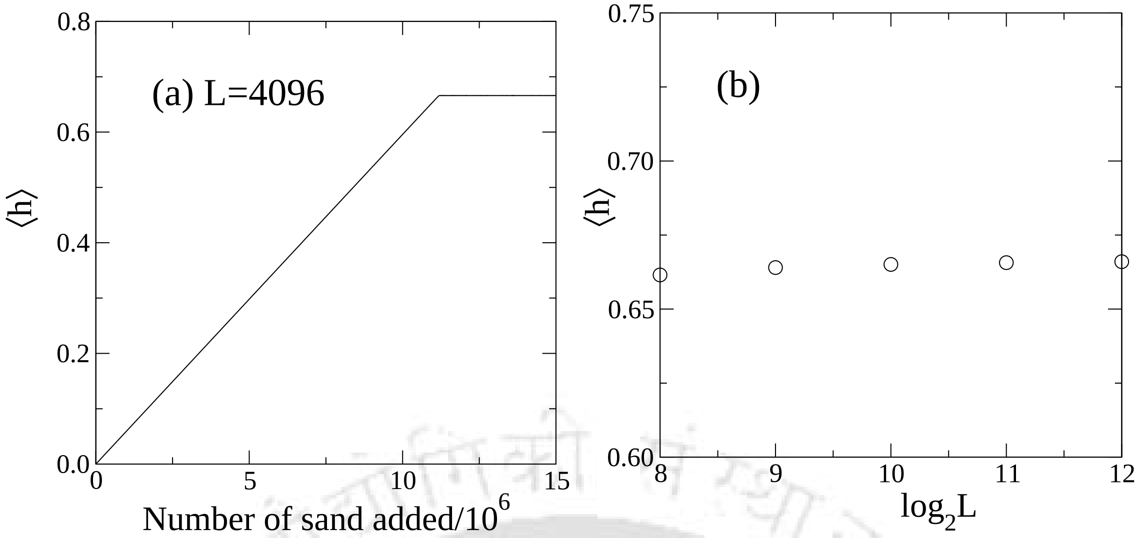

Figure 2.4: (a) Plot of average height $\langle h \rangle$ against the number of sand grains added. The value of $\langle h \rangle$ remains constant over a large number of sand grains added. (b) Dependence of the saturated average height $\langle h \rangle$ on the system size L. $\langle h \rangle$ remains almost constant with system size L.

after adding a sufficiently large number of sand grains. It was observed that about 10^6 avalanches occurred due to the addition of 15×10^6 sand grains into the system. Therefore, at least 10^6 initial avalanches are required to achieve the steady state for a system of size $L = 4096$. For smaller lattice sizes, the steady states are reached after a comparatively smaller number of avalanches than that of $L = 4096$. The values of $\langle h \rangle$ against the system size L is plotted in Fig. 2.4(b). It can be seen that the average height remains almost constant over the system sizes.

2.4 Avalanche cluster morphology

Before starting the estimation and analyzing the properties of RSM avalanches it is important to visualize the typical morphology of RSM avalanches. A typical large avalanche cluster of the RSM obtained in its steady state on a square lattice of size 128×128 is shown in Fig. 2.5(a). In an avalanche cluster the number of times a site toppled is called toppling number S_i of the site. Different colours correspond to different bands of toppling number in an avalanche. As mentioned in the caption of Fig. 2.5, white space inside the cluster corresponds to the sites that did not topple at all during the avalanche and the colours correspond to (●) for $1 \leq S_i \leq 14$, (●) for $15 \leq S_i \leq 28$, (●) for $29 \leq S_i \leq 42$, (●) for $43 \leq S_i \leq 56$, (●) for $57 \leq S_i \leq 70$, (●) for $71 \leq S_i \leq 84$, (●) for $S_i \geq 85$. Since the toppling rule of the RSM has features

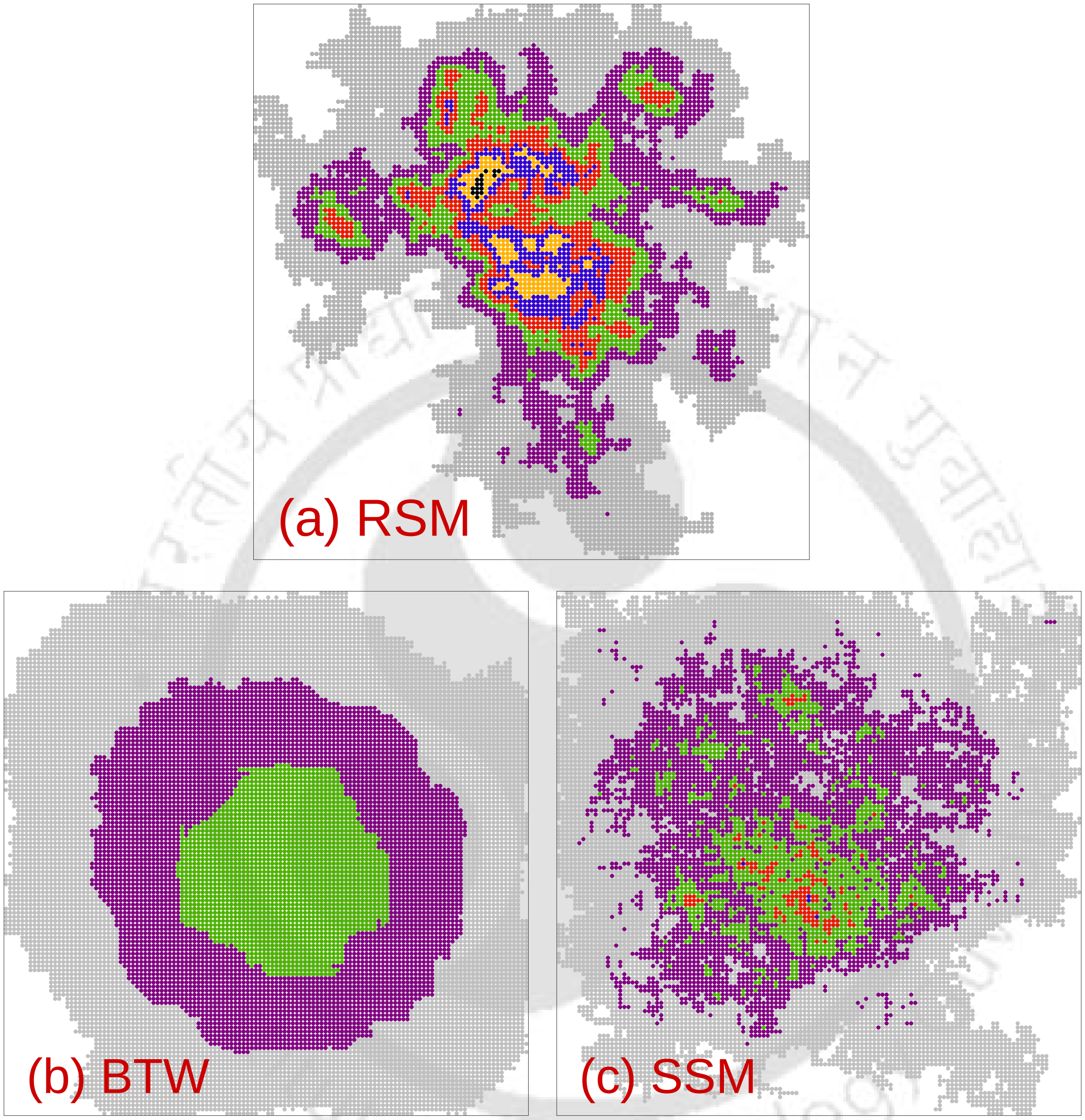

Figure 2.5: Typical avalanche clusters of (a) the RSM, (b) the BTW and (c) the SSM generated at their respective steady states on a square lattice of size 128×128 are shown. The white space inside the clusters corresponds to the sites that did not topple at all during the avalanche. Different colours represent toppling numbers in bins as (●) for $1 \leq S_i \leq 14$, (●) for $15 \leq S_i \leq 28$, (●) for $29 \leq S_i \leq 42$, (●) for $43 \leq S_i \leq 56$, (●) for $57 \leq S_i \leq 70$, (●) for $71 \leq S_i \leq 84$, (●) for $S_i \geq 85$.

of both the BTW and the SSM, it is interesting to compare the morphology of the RSM avalanche cluster with those of the BTW and SSM. The avalanche clusters of the BTW and the SSM obtained at their respective steady states on the square lattice of size $L = 128$ are given in Fig. 2.5(b) Fig. 2.5(c) respectively. The colours in these clusters correspond to the same width of toppling numbers as that of RSM. There are a number of things to notice. First, the avalanche cluster of RSM has the maximum number of colours whereas the BTW cluster has the minimum number of colours. The number of colours in a cluster corresponds to the maximum number of times a site toppled during the avalanche. The clusters shown here have the maximum number of toppling of a site as 108, 42 and 51 for the RSM, the BTW and the SSM respectively. It has been observed in an ensemble of avalanche clusters that in RSM, the maximum number of times a site toppled during the avalanche is larger in comparison to that of the other models. Second, the avalanche clusters in all three models are isotropic in nature. Anisotropic avalanche clusters were obtained only in the presence of a global bias in the model as in the DSM[51] and the directed fixed energy sandpile (DFES)[116]. Third, avalanche cluster morphology of the RSM is very different from that of both the BTW as well as the SSM. The BTW avalanche cluster consists of concentric zones of lower and lower number of toppling around a single maximal toppling zone[60,117,118] whereas avalanche cluster of the SSM is random in nature[75,77]. The RSM avalanche cluster neither fully consists of concentric zones as in the BTW nor it is totally random. It is important to note that the local correlation in rotational constraint does not lead to long range correlation generating the BTW like correlated structure. Fourth, there are more than one black zones (maximum number of toppling zones) in the avalanche cluster of the RSM. It is then possible to have several maximal toppling zones in an avalanche in the RSM like that of the SSM[60,75,77,117,118] whereas in the BTW always one maximal toppling zone appears[60,117,118]. The RSM avalanche looks like superimposition of several BTW type structures around different maximal toppling zones. Fifth, the maximal toppling zones appear at arbitrarily different places in RSM which does not correspond to the lattice site where the sand grain was added to initiate the avalanche. In the BTW, the maximal toppling zone appears at and around the site where the sand grain was added to initiate the avalanche[60,117,118]. Sixth, the BTW avalanche clusters are compact without holes or no toppling regions inside an avalanche. On the other hand, the avalanche clusters of the SSM consists of several holes inside the cluster due to the stochastic rule of sand distribution. The RSM avalanche cluster is almost compact with a few holes here and there.

The appearance of holes in RSM is due to the rotational rule of sand distribution. However, generation of a single sited hole should be forbidden by the rotational rule with rotation in a particular direction and without any randomness. It can be noted that holes of a single site also appear in the avalanche clusters of RSM. An avalanche in RSM can also be considered as a branching process as demonstrated for the SSM[119]. Single sited holes in the RSM avalanche cluster could only appear at the termination point of different branches of toppling.

The RSM avalanche cluster therefore has properties of both the deterministic BTW and the stochastic SSM. It is then expected that the critical avalanche properties in the steady state will show a mixed behaviour.

2.5 Avalanche properties in the steady state

In order to characterize the physical properties of the avalanches which occurred at the non-equilibrium steady state, extensive computer simulations have been performed on the square lattice of size $L = 4096$ in multiples of 2. Santra *et al.*[113] reported some numerical results considering lattice size upto $L = 2048$. In this thesis, the numerical computation is extended to higher lattice sizes and the results are verified. On the square lattice of size $L = 4096$, the first 10^6 avalanches were skipped to achieve the steady state. Ten height configurations on the steady state are saved. Each of these configurations is further evolved using different random number seeds. For each of these the steady state configurations, initial 10^5 avalanches are neglected again before collecting data. Averaging of data is made over 2×10^6 avalanches collecting from ten different steady state branches. It should be mentioned here that due to the rotational constraint the lifetime of an avalanche in RSM is much higher in comparison to that of other models. The generation of a large number of avalanches then requires huge computer time for RSM. For example in order to generate the steady state configurations from an empty lattice of size $L = 4096$ it takes 589 hours and 21 minutes in a single IBM machine. After reaching the steady state in order to generate a total of 2×10^6 avalanches from 10 branches, computation time about 90 hours per branch is required.

2.5.1 Probability distribution

In order to characterize different physical properties of the avalanches which occurred at the steady state, the following quantities such as toppling size s of an avalanche,

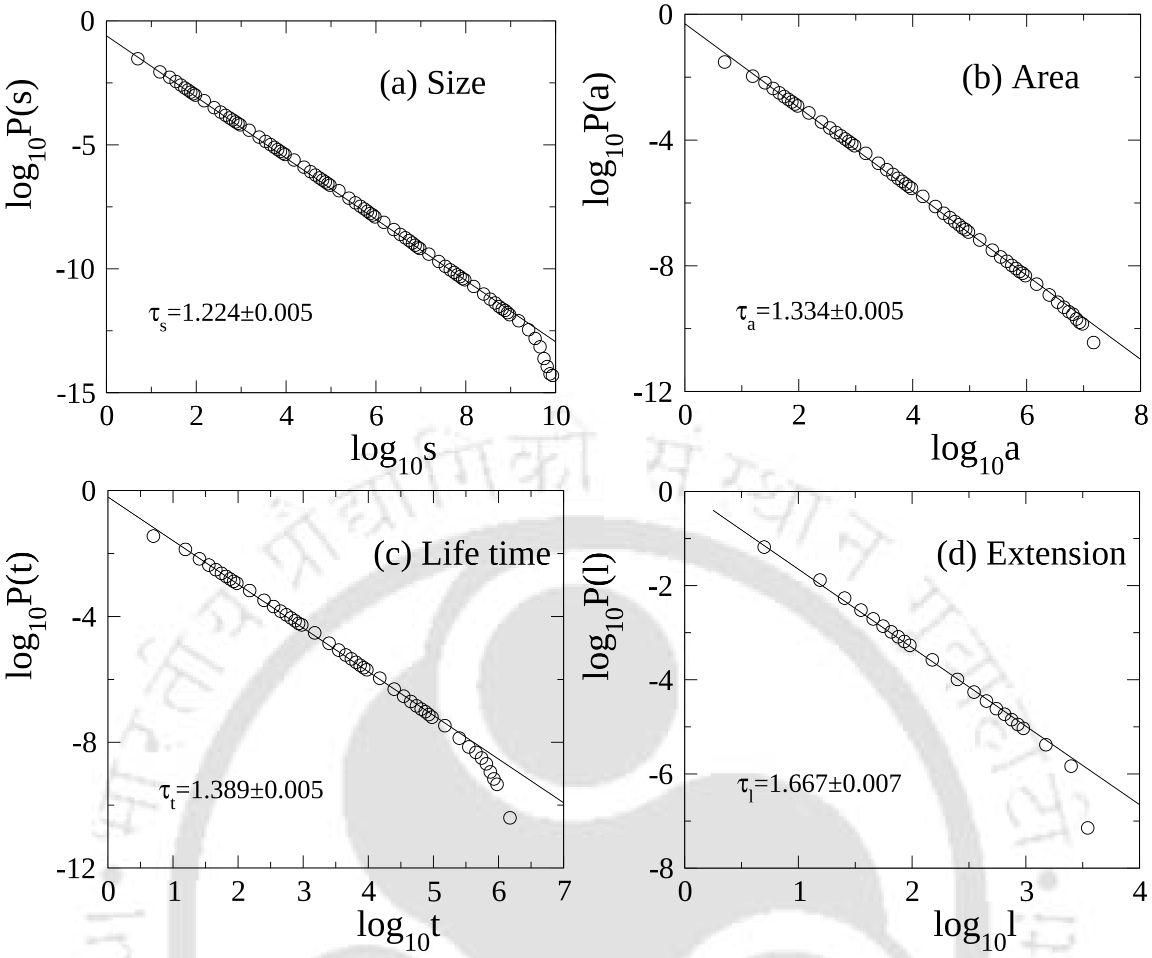

Figure 2.6: Probability distributions (a) $P(s)$, (b) $P(a)$, (c) $P(t)$, and (d) $P(l)$ are plotted against s, a, t and l respectively for system size $L = 4096$. The solid lines are best fitted lines through the linear part of the distributions.

avalanche area a, lifetime t, and spatial extension l are measured. Toppling size s is the total number of toppling that occurred in an avalanche. Area a is the number of distinct sites toppled. Lifetime t is the number of parallel updates to make all the sites under critical. The spatial extension l is given by $l^2 = 2\sum_{i=1}^{a}(\mathbf{r}_0 - \mathbf{r}_i)^2/a$ where $\mathbf{r}_0 = \sum_{i=1}^{a}\mathbf{r}_i/a$, $\mathbf{r}_i$ is the position vector of the distinct sites toppled. The probability distribution function of the avalanche related quantities s, a, t and l at the steady state of the RSM is expected to obey power law scaling behaviour given by

$$P(s) \sim s^{-\tau_s}, \quad P(a) \sim a^{-\tau_a}, \quad P(t) \sim t^{-\tau_t}, \quad P(l) \sim l^{-\tau_l} \tag{2.4}$$

where τ_s, τ_a, τ_t and τ_l are the corresponding critical exponent associated with for s, a, t and l. In order to obtain the probability distributions, data are collected in bins of intervals of 10s, 100s, 1000s and so on. Finally the data are normalized by the bin widths. The probability distribution $P(s)$ of the toppling size s, $P(a)$ of the area a, $P(t)$ of the lifetime t, $P(l)$ of the extension l are plotted in double logarithmic scale for the system of size $L = 4096$ in Figs. 2.6(a), (b), (c) and (d) respectively. It can be seen that the probability distributions of all four avalanche related quantities follow power law scaling behaviour as expected. The probability distributions are limited by the finite system size. For example, the maximum possible a and l of an avalanche are $L^2 \approx 10^6$ and $L \approx 10^3$ respectively for a system of size $L = 4096$ as it can be seen in Figs. 2.6 (b) and (d) respectively. Therefore, there is no characteristic size, area, lifetime and extension of the avalanches at the non-equilibrium steady state of RSM. Hence, RSM exhibits self-organized criticality. The probability distribution exponents τ_x for $x \in \{s, a, l, t\}$ are estimated from the slope of the best fitted straight line through the data points of the probability distributions in Fig. 2.6. The solid lines in Fig. 2.6 represent the best fitted straight line between the data points. The values of the exponents estimated are, $\tau_s = 1.224 \pm 0.005$, $\tau_a = 1.334 \pm 0.005$, $\tau_t = 1.389 \pm 0.005$ and $\tau_l = 1.667 \pm 0.007$. The errors are due to the least square fitting taking into account the statistical error of each data point. In the Table 2.1, the values of the critical exponents obtained for the RSM are listed and compared with those known for the BTW and the SSM. The values of the exponents for the BTW and the SSM are taken from Refs.[75,76,77]. The values of the critical exponents obtained for RSM on the system size $L = 4096$ are found consistent with those obtained previously on a smaller system size[113]. The toppling size exponent τ_s and the lifetime exponent τ_t are different whereas τ_a and τ_l are almost the same as that of the BTW. The disagreement of the toppling size and lifetime distribution exponents with the corresponding BTW exponents can be accounted by the fact that in the RSM the avalanche waves generally have a spiraling nature around several maximal toppling zones within the avalanche cluster and as a consequence it will take a longer time and a large number of toppling for an avalanche to die away than that in the BTW where a single maximal toppling zone occurs and the toppling wave propagates outwardly. On the other hand, in comparison to the SSM, most of the exponents are found different. Thus, from the point of view of power law correlations, some of the avalanche properties are similar to that of BTW but different from the SSM. Note that $\tau_s = 2 - 1/\tau_a$, conjectured by Majumder and Dhar[120], is satisfied in the case of the SSM but it is not valid for the BTW. It can be seen that the conjecture is just outside the error bar here in the case of the RSM. The expected value of τ_s in the RSM from the conjecture is ≈ 1.25 close to the obtained value 1.224 ± 0.005.

Exponent	Models		
	BTW	SSM	RSM
τ_s	1.293	1.275	1.224 ± 0.005
τ_a	1.330	1.373	1.334 ± 0.005
τ_t	1.480	1.493	1.389 ± 0.005
τ_l	1.665	1.743	1.667 ± 0.007
γ_{al}	2.00	2.00	2.002 ± 0.002
γ_{at}	1.53	1.35	1.167 ± 0.005
γ_{sa}	1.06	1.23	1.453 ± 0.003
γ_{tl}	1.32	1.49	1.715 ± 0.005

Table 2.1: Comparison of critical exponents obtained for the RSM with that of the BTW and the SSM. The values of the critical exponents for BTW and SSM are taken from Refs.[75,76,77]. Some of the exponents are close to that of BTW and most of them are different from that of SSM.

2.5.2 Conditional expectation values

Since the avalanche properties are related to each other, conditional expectation values are defined as introduced by Christensen *et al.*[121]. The conditional expectation value of different avalanche property is defined as

$$\langle a(l)\rangle = \int_0^{a_{max}} aP(a|l)da, \qquad \langle a(t)\rangle = \int_0^{a_{max}} aP(a|t)da$$
$$\langle s(a)\rangle = \int_0^{s_{max}} sP(s|a)ds, \qquad \langle t(l)\rangle = \int_0^{t_{max}} tP(t|l)dt \tag{2.5}$$

where $P(a|l)$ is the probability to find an avalanche of area a with extension exactly equal to l, $P(a|t)$ is the probability to find an avalanche of area a with lifetime exactly equal to t, $P(s|a)$ is the probability to find an avalanche of toppling size s with area exactly equal to a, and $P(t|l)$ is the probability to find an avalanche of lifetime t with extension exactly equal to l. In the steady state, the expectation values scale with its argument are as

$$\langle a(l)\rangle \sim l^{\gamma_{al}}, \quad \langle a(t)\rangle \sim t^{\gamma_{at}}, \quad \langle s(a)\rangle \sim a^{\gamma_{sa}}, \quad \langle t(l)\rangle \sim l^{\gamma_{tl}} \tag{2.6}$$

where $\gamma_{al}, \gamma_{at}, \gamma_{sa}$ and γ_{tl} are the critical exponents. Four expectation values $\langle a(l)\rangle$, $\langle a(t)\rangle$, $\langle s(a)\rangle$, and $\langle t(l)\rangle$ are calculated on a square lattice of size $L = 4096$ and their scaling behaviour are determined. In Fig. 2.7, the expectation values are plotted against their respective arguments in double logarithmic scale in order to estimate

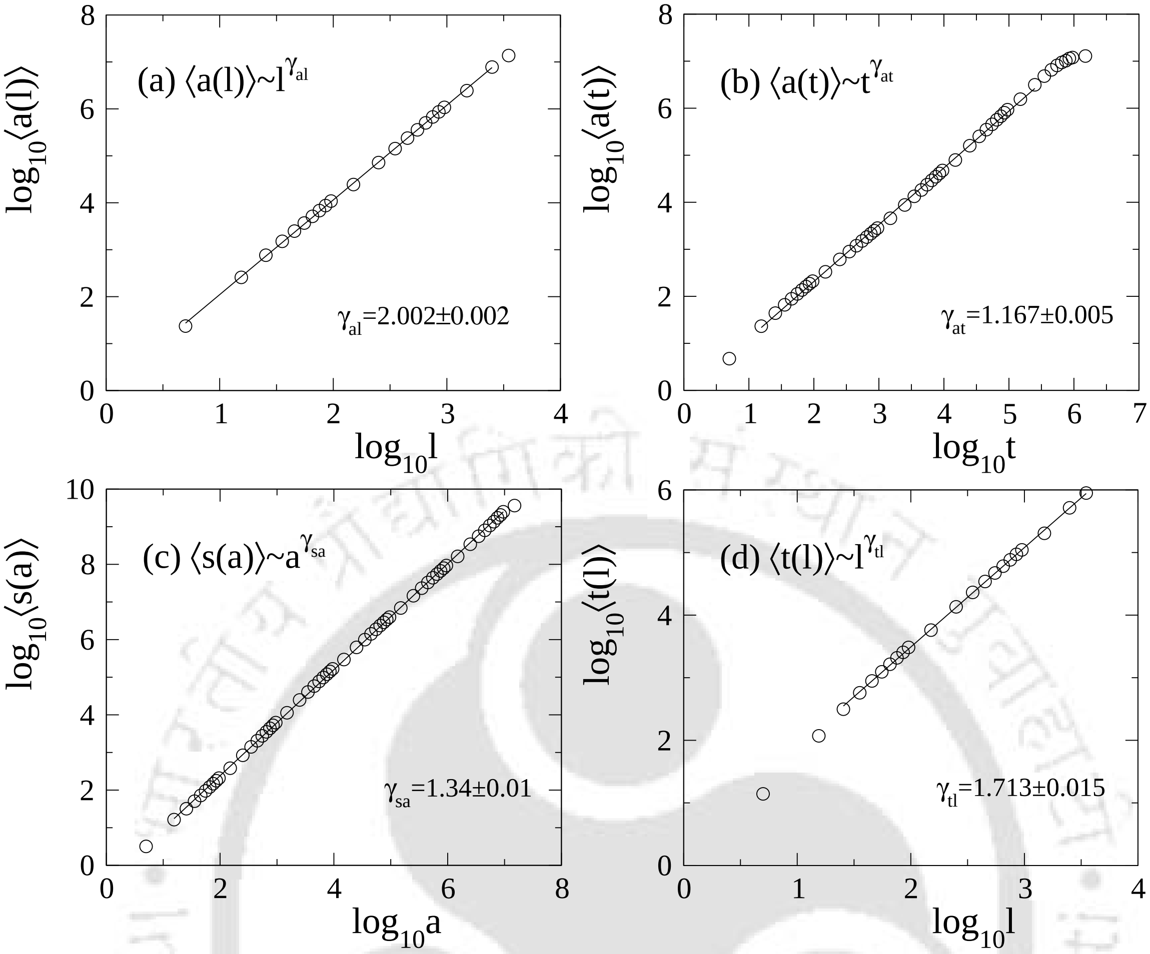

Figure 2.7: Plot of conditional expectations of avalanche properties: (a) area ($\langle a(l)\rangle$) versus extension (l), (b) area ($\langle a(t)\rangle$) versus time (t), (c) toppling size ($\langle s(a)\rangle$) versus area (a), and (d) time ($\langle t(l)\rangle$) versus length (l). The solid lines show the best fitted straight lines. Corresponding exponents are found as: $\gamma_{at} = 1.167 \pm 0.005$, $\gamma_{al} = 2.002 \pm 0.002$, $\gamma_{sa} = 1.34 \pm 0.01$ and $\gamma_{tl} = 1.713 \pm 0.015$. Errors are least square fit error.

the γ exponents. It can be seen that the conditional expectation values scale with their respective arguments as assumed in Eq. 2.6. From the slope of the best fitted straight lines through the data points in Fig. 2.7, the values of the exponents are estimated as: $\gamma_{al} = 2.002 \pm 0.002$, $\gamma_{at} = 1.167 \pm 0.005$, $\gamma_{sa} = 1.453 \pm 0.003$, and $\gamma_{tl} = 1.715 \pm 0.005$. In Table 2.1, the values of γ_{xy} of RSM are listed and compared with those of BTW and SSM. There are few things to notice. First, the exponent γ_{al} is found ≈ 2 since the avalanche clusters are almost compact with a few holes here and there. Second, γ_{sa} is found greater than one. This is expected because in this model, a site topples many times in an avalanche due to rotational constraint. Moreover the value of γ_{sa} for the RSM is higher than that of the BTW and the

$\gamma_{sa} = \frac{\tau_a - 1}{\tau_s - 1}$	$\gamma_{at} = \frac{\tau_t - 1}{\tau_a - 1}$	$\gamma_{al} = \frac{\tau_l - 1}{\tau_a - 1}$	$\gamma_{tl} = \frac{\tau_l - 1}{\tau_t - 1}$
1.491 ± 0.010	1.165 ± 0.010	1.997 ± 0.010	1.715 ± 0.014

Table 2.2: Critical exponents associated with conditional expectation values for RSM are estimated from the scaling relation $\gamma_{xy} = \frac{\tau_y - 1}{\tau_x - 1}$. The τ and γ exponents are found to obey the above scaling relation among them within error bars.

SSM. Third, the value of the dynamical exponent γ_{tl} is the highest in the RSM and it is lowest in the BTW. Because, due to the rotational constraint the sand grains whirl around several maximal zones inside the avalanche and take a longer time to complete an avalanche. Fourth, according to the scaling function form given in Eq. 2.6, the exponents should satisfy the scaling relation $\gamma_{xz} = \gamma_{xy}\gamma_{yz}$. It can be seen that the scaling relation $\gamma_{al} = \gamma_{at}\gamma_{tl}$ is satisfied within error bars. Fifth, the values of γ_{sa}, γ_{at} and γ_{tl} are found different from that of the BTW as well as the SSM except γ_{al}. The exponents γ_{xy}, τ_x and τ_y are connected via the following scaling relation

$$\gamma_{xy} = (\tau_y - 1)/(\tau_x - 1). \tag{2.7}$$

as derived in chapter 1. The above scaling relation is satisfied within error bars for $x, y \in \{s, a, l, t\}$. Thus, the extended set of exponents obtained here in the RSM from both power law analysis and conditional probabilities are consistent with the scaling relations. Note that the values of the critical exponents obtained here should remain invariant under the reversal of rotational symmetry. Though some of the exponents are close to that of the BTW, the RSM belongs to a new universality class because the extended set of exponents are not identical. It can be noted that, because of their anisotropic character DSM and DFES are already found to belong to different universality classes.

2.5.3 Finite size scaling study

Singularities of thermodynamic quantities in equilibrium critical phenomena are characterized by well defined critical exponents. The set of critical exponents and the form of the scaling function determine the universality class of a system in the thermodynamic limit[2]. In numerical simulations, the results are very often limited by the finite system size L. There is rounding and shifting of critical singularities in finite systems depending on the ratio of correlation length to the linear dimension L of a system. In order to obtain the behaviour of a macroscopic system in the thermodynamic limit, results of finite systems are often extrapolated using finite-

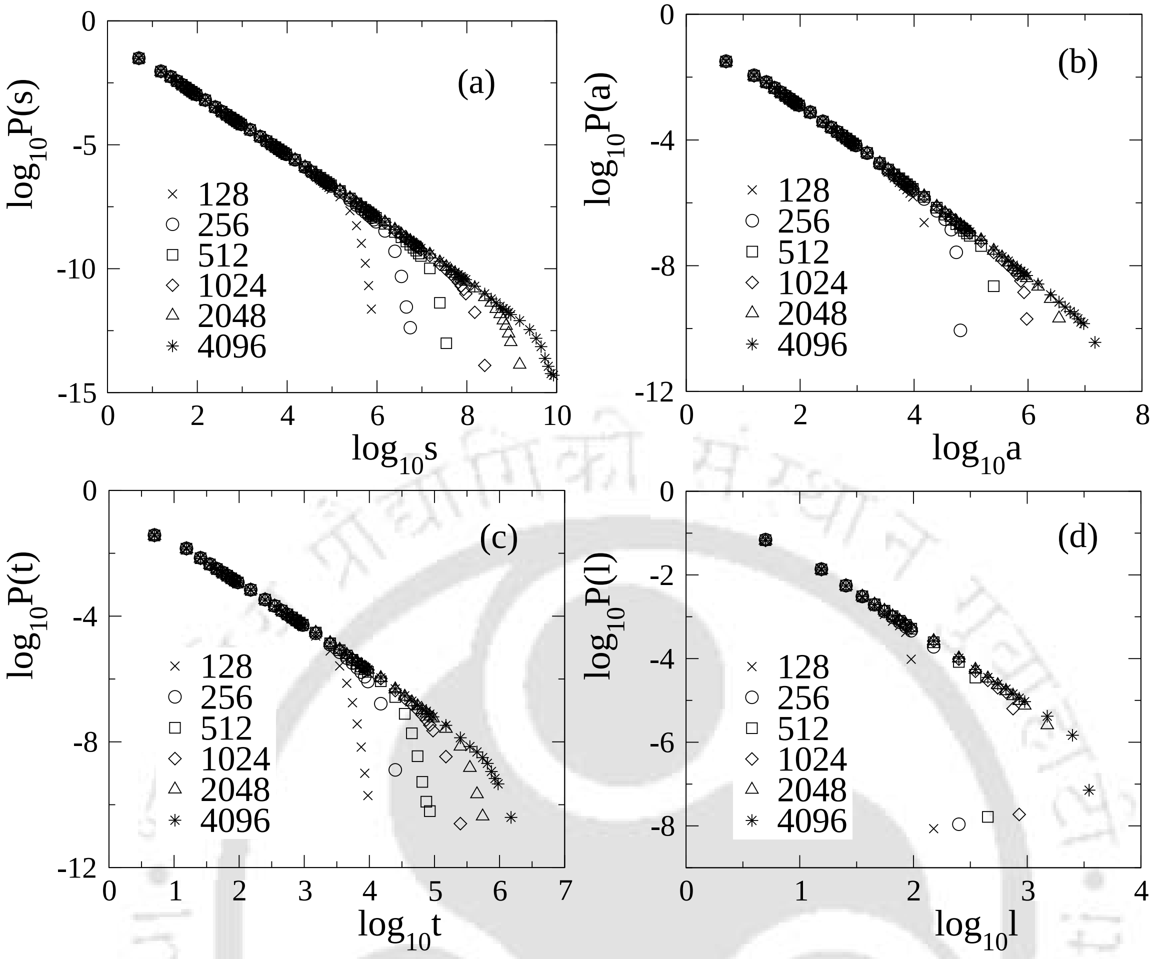

Figure 2.8: (a) $P(s)$, (b) $P(a)$, (c) $P(t)$ and (d) $P(l)$ are plotted against s, a, t and l respectively for different systems of sizes $L = 128$ (×), 256 (○), 512 (□), 1024 (◇), 2048 (△) and 4096 (✳). All the four distributions have power law correlation with cutoff that increases with system size L.

size scaling (FSS) ansatz[83]. The critical properties of sandpile models exhibiting SOC at the non-equilibrium steady state is expected to follow the usual FSS ansatz as observed in equilibrium critical phenomena. Surprisingly, the scaling behavior of the BTW sandpile model[4,114,115], is found to obey a peculiar multiscaling[79,80,81] rather than FSS whereas SSM follows FSS. Since the RSM has features of both the BTW and the SSM, it is interesting to study the FSS behaviour of the probability distribution functions.

In an infinite system though the probability distribution of the avalanche related quantities follow power law scaling as given in Eq. 2.4. However, for a finite system, the probability distributions terminates at a well defined cutoff as observed in Fig. 2.8. The cutoff of the distributions are expected to depend on the system size

L. The cutoff s_{max} of the probability distribution $P(s)$ is assumed to scale with finite system size L as $s_{max} \sim L^{D_s}$, where D_s is the capacity dimension of toppling size. Similarly, the cutoffs of the probability distributions of area a_{max}, life time t_{max} and extension l_{max} are also expected to scale with L as $a_{max} \sim L^{D_a}$, $t_{max} \sim L^{D_t}$ and $l_{max} \sim L^{D_l}$ where D_a, D_t and D_l are capacity dimensions of area, life time and extension respectively. Thus, the probability distribution $P(x, L)$ of an avalanche related quantity x for a given L is expected to obey a scaling function form given by

$$P(x, L) = s^{-\tau_x} \mathsf{f}(x/L^{D_x}) \quad x \in s, a, t, l \tag{2.8}$$

where $\mathsf{f}(x/L^{D_x})$ is the finite size scaling function. In the $L \to \infty$ limit, the scaling function $\mathsf{f}(0)$ becomes a constant and the power law behaviour given in Eq. 2.8 can be approximated as $P(x) \sim x^{-\tau_x}$ for $x \in s, a, t, l$.

Extensive numerical simulation has been performed on the square lattice of different lattice sizes starting from $L = 128$ to $L = 4096$ in multiples of 2. For each lattice size, a large number of avalanches are collected for averaging, ranging from a total 64×10^6 avalanches for $L = 128$ down to 2×10^6 avalanches for $L = 4096$. In Fig. 2.8, distributions of toppling size $P(s)$, area $P(a)$, life time $P(t)$ and extension $P(l)$ are plotted for different systems of sizes ranging from $L = 128$ to 4096. It can be seen that the probability distributions of all four avalanche related quantities on smaller system sizes are also following the same power law scaling of the largest system size $L = 4096$. Hence the power law scaling exponent τ_x can be taken as that of the system size $L = 4096$ given in section 1.5.1. However, the distributions are found to have sharp cutoffs corresponding to different system sizes. The cutoffs x_{max} of the distributions $P(x)$ are found to increase with increase in L as expected. As already mentioned, the cutoff value of a property x on a given system size L will be determined by the capacity dimension D_x of that quantity.

Moment analysis: In order to estimate the values of D_xs as well as to verify FSS form of the distribution functions, the avalanche properties are analyzed following the method of moment analysis[79,80,81,82]. The q moments of a property x is defined as

$$\langle x^q \rangle = \int_0^{x_{max}} x^q P(x, L) dx \sim L^{\sigma_x(q)} \tag{2.9}$$

where $\sigma_x(q) = (q+1-\tau_x)D_x$. Thus, if the probability distributions obey FSS then the moment exponent $\sigma_x(q)$ should have a constant gap between two successive values and the gap is defined as $\delta\sigma_x(q, q+1) = \sigma_x(q+1) - \sigma_x(q)$ which should be equal to

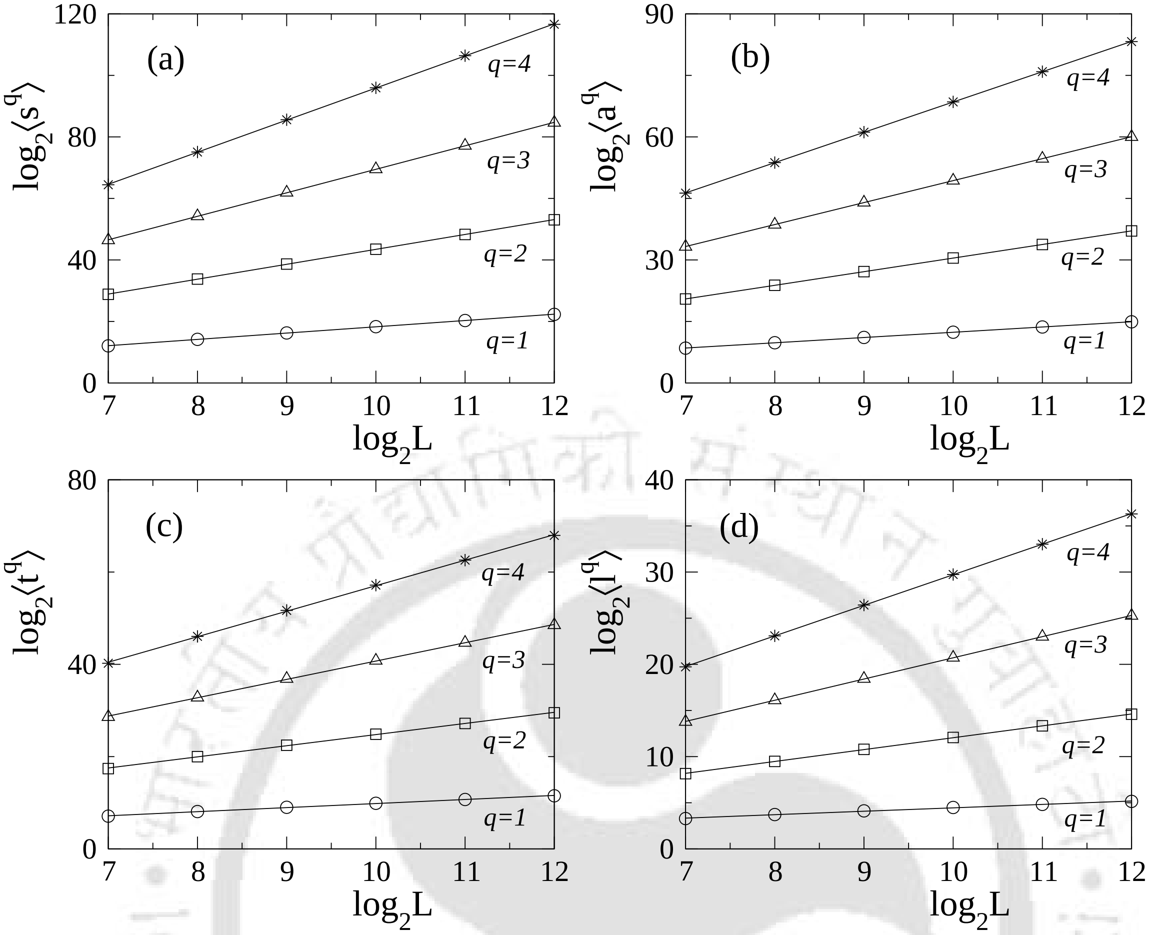

Figure 2.9: Plot of (a) $\langle s^q(L)\rangle$, (b) $\langle a^q(L)\rangle$, (c) $\langle t^q(L)\rangle$, (d) $\langle l^q(L)\rangle$ versus L for $q = 1$ (○), 2 (□), 3 (△), 4 (✻). Solid lines are the linear least square fitted lines.

D_x. On the other hand, if they obey multiscaling, $\sigma_x(q)$ should have a continuous dependence on q. In Fig. 2.9, $\langle x^q(L)\rangle$ is plotted against L in double logarithmic scale for $x \in s, a, t, l$ for $q = 1, 2, 3$ and 4. The lattice size is varied from $L = 128$ to 4096 in multiples of 2. It can be seen that different moments of the avalanche related quantities follow the FSS with L as it is given in Eq. 2.9. For a given q, the value of $\sigma_x(q)$ has been obtained from the slope of the plot of $\log_2\langle x^q(L)\rangle$ versus $\log_2 L$ and their values are listed in Table 2.3. Two important things are to notice. First, $\langle s(L)\rangle$ is equivalent to the number of steps by a random walker required to reach the lattice boundary[119]. In an avalanche, a sand grain moves unit distance in each toppling and the sand grains diffuse over a certain distance in a time exactly equal to the number of toppling occurred in the avalanche. From the FSS analysis it can be seen that $\sigma_s(1) = 2.01 \pm 0.01$. Thus, the growth of average toppling number as a quadratic power of the system size L for RSM represents diffusive transport of

	$\sigma_s(q)$	$\sigma_a(q)$	$\sigma_t(q)$	$\sigma_l(q)$
$q = 1$	2.01 ± 0.01	1.28 ± 0.01	0.88 ± 0.01	0.37 ± 0.01
$q = 2$	4.84 ± 0.02	3.34 ± 0.01	2.41 ± 0.02	1.29 ± 0.01
$q = 3$	7.64 ± 0.02	5.36 ± 0.01	3.98 ± 0.03	2.30 ± 0.01
$q = 3$	10.44 ± 0.03	7.38 ± 0.01	5.53 ± 0.04	3.31 ± 0.01

Table 2.3: Values of $\sigma_X(q)$, $x \in \{s, a, t, l\}$ for $q = 1, 2, 3$ and 4 for the RSM.

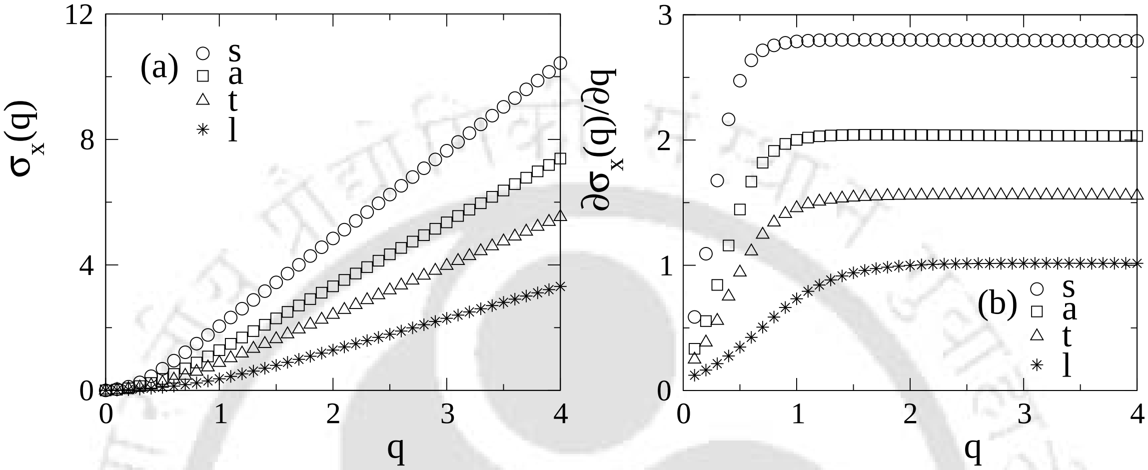

Figure 2.10: (a) Plot of $\sigma_x(q)$ versus q for $x \in \{s, a, t, l\}$. (b) Plot of $\partial\sigma_x(q)/\partial q$ versus q for $x \in \{s, a, t, l\}$. For each $x \in \{s, a, t, l\}$, $\partial\sigma_x(q)/\partial q$ saturates to constant value D_x for large q limit.

sand grains. The diffusive nature of the RSM is in accordance with the fact that spiral random walks are also diffusive[122]. Diffusive nature of sand flow has already been observed for the BTW and the SSM[119]. Second, one could calculate the gap between exponents of successive moments and verify FSS. From the data given in Table 2.3, it could be verified that for a given x the values of $\delta\sigma_x(q, q+1)$ are almost constant within error bars. Thus, it may be concluded from the above analysis that the RSM is following FSS.

Capacity dimensions: In order to obtain a better estimate of the capacity dimension D_x, sequences of exponents $\sigma_x(q)$, $x \in \{s, a, t, l\}$, are obtained for 400 values of q between 0 and 4 with equal interval. In Fig. 2.10(a), the exponents $\sigma_x(q)$ for $x \in \{s, a, t, l\}$ are plotted against the moment q. It can be seen that for higher values of q, the slopes of different curves are fairly constant. It has been verified by estimating the slopes $\partial\sigma_x/\partial q$ using finite difference method. In Fig. 2.10(b), $\partial\sigma_x/\partial q$ is plotted against q. It can be seen that the slopes converge to a fixed value for large values of q. The limiting values of the slopes are the respective capacity

Exponent	Models		
	BTW	SSM	RSM
D_a	2.00	2.00	2.03 ± 0.02
D_s	$\cdots$	2.74	2.86 ± 0.02
D_t	$\cdots$	1.56	1.60 ± 0.02
D_l	1.00	1.00	1.00 ± 0.02

Table 2.4: Critical exponents related to diffusivity and capacity dimensions of avalanche related quantities of the RSM are compared with that of the BTW and the SSM.

dimensions D_x. The values of capacity dimensions of several quantities are obtained as $D_s = 2.86 \pm 0.01$, $D_a = 2.03 \pm 0.01$, $D_t = 1.60 \pm 0.01$ and $D_l = 1.00 \pm 0.01$ for the RSM. The errors are due to the finite difference method adopted for differentiation of the $\sigma(q)$ sequence. These values are consistent with those measured in Ref.[113] considering lower system sizes. The values of D_x are listed in Table 2.4 and compared with those of the BTW and the SSM. It can be seen that D_a for all three models is approximately 2, which signifies the compactness of the avalanche clusters in all three models. Since the maximum linear extension of the avalanche clusters are proportional to the system size, the value of D_l is found to be 1 for all the three models. The values of D_t in SSM and in RSM are found close whereas the values of D_s in these models are different. From the moment analysis, it was already observed that $\partial\sigma_a(q)/\partial q$ do not saturate in BTW[81], hence numerical values of these exponents were not possible to estimate. Since the values of D_s and D_t did not saturate to a definite value, it was concluded that BTW does not follow FSS ansatz rather follows a peculiar multiscaling. On the other hand, SSM follows FSS ansatz and the exponent values saturates to a definite value in the limit of large q. In order to compare the probability distribution functions of the RSM and that of the BTW with respect to that of the SSM a quantity $\Delta_{x,m}(q)$ is defined as

$$\Delta_{x,m}(q) = \left| 1 - \frac{\sigma'_{x,m}(q)}{\sigma'_{x,\mathrm{SSM}}(q)} \right|, \tag{2.10}$$

where $\sigma'(q) = \partial\sigma/\partial q$ and m stands for the models BTW or RSM. $\Delta_{x,\mathrm{BTW}}$ and $\Delta_{x,\mathrm{RSM}}$ are plotted against q in Fig. 2.11(a) for $x = s$ and in Fig. 2.11(a) for $x = t$. The dotted line corresponds to $\Delta_{x,\mathrm{BTW}}$ and the solid line corresponds to $\Delta_{x,\mathrm{RSM}}$. It can be seen that the value of $\Delta_{x,\mathrm{RSM}}(q)$ for toppling size and lifetime remains constant with respect to the SSM whereas in the case of the BTW, they increases slowly with

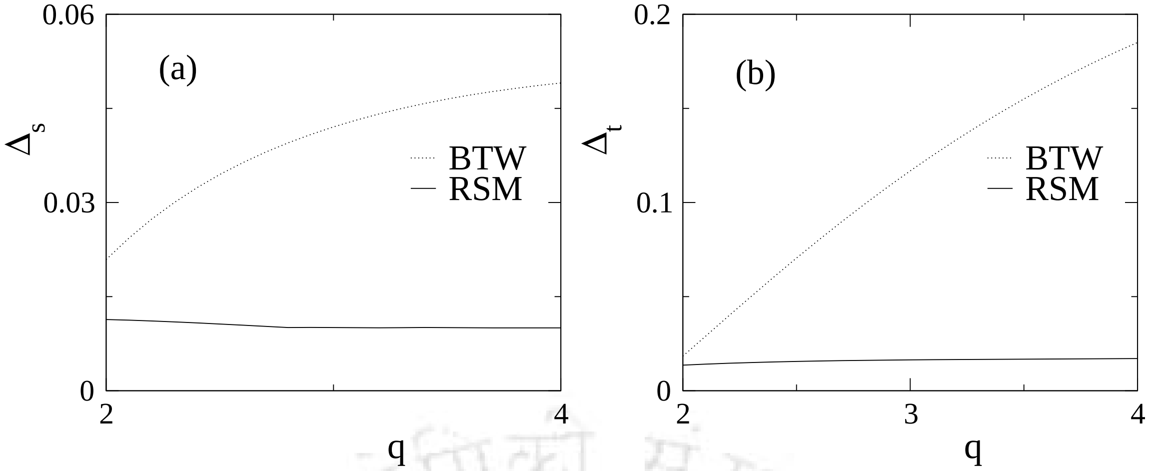

Figure 2.11: (a) Plot of $\Delta_{s,\mathrm{BTW}}$ and $\Delta_{s,\mathrm{RSM}}$ versus q. (b) Plot of $\Delta_{t,\mathrm{BTW}}$ and $\Delta_{t,\mathrm{RSM}}$ versus q. In both the case of toppling size and lifetime $\Delta_{x,\mathrm{BTW}}$ increases with q with respect to SSM whereas for RSM they remain unchanged with q with respect to SSM.

respect to the SSM. Thus, the scaling functions of the avalanche properties in the RSM follow FSS as in SSM rather than multiscaling as in the BTW.

The capacity dimensions D_x extracted from the moment analysis are not independent but they can be related to the distribution exponents τ_x. Since for a given system size L the sum of the probabilities of appearance of any avalanche related quantity must be equal to one, the integrated probabilities for any two avalanche properties x and y can be written as,

$$\int P(x)dx = \int P(y)dy \tag{2.11}$$

$$\int x^{-\tau_x}\mathsf{f}_x(x/L^{D_x})dx = \int y^{-\tau_y}\mathsf{f}_y(y/L^{D_y})dy \tag{2.12}$$

Defining a scaled variable $z_x = x/L^{D_x}$ and $z_y = y/L^{D_y}$ the above equation can be written in terms of z_x and z_y as

$$L^{(1-\tau_x)D_x}\int z_x^{-\tau_x}\mathsf{f}_x(z_x)dz_x = L^{(1-\tau_y)D_y}\int z_y^{-\tau_y}\mathsf{f}_y(z_y)dz_y \tag{2.13}$$

Since the integral will contribute to a constant one can write

$$\frac{D_x}{D_y} = \frac{1-\tau_y}{1-\tau_x} = \gamma_{xy} \tag{2.14}$$

Therefore, taking $D_l = 1$, one should have $D_x = \gamma_{xl}$. Such a scaling relation is known to be valid for the SSM. In the case of RSM one can verify the relation as

$\gamma_{al} = 2.002 \pm 0.002$ (Table 2.1) and $D_a = 2.03 \pm 0.02$ (Table 2.4). Thus, the above scaling relations are also valid for the RSM.

It has already been established that all these models are diffusive in nature. Hence, one may assume that $\sigma_s(1)$ is exactly equal to 2 and a scaling relation among the capacity dimension D_s and the distribution exponent τ_s can be obtained as

$$D_s(2-\tau_s) = 2 \quad \text{or} \quad \tau_s = 2 - \frac{2}{D_s}. \tag{2.15}$$

In the case of SSM, the above scaling relation is well verified. However, for the RSM the estimated value of τ_s is found little lower than what is expected from the above scaling relation.

Data collapse: Since the values of the capacity dimensions are known, it is now possible to check the scaling function form given in Eq. (2.8). The scaling function form is checked by plotting a scaled distribution $P(x)L^{D_x\tau_x}$ against the scaled variable x/L^{D_x} for $x \in \{s,a,t,l\}$ in Fig. 2.12 following Chessa *et al.*[73]. In Fig. 2.12 the scaled distributions $P(x)L^{D_x\tau_x}$ are plotted against the scaled variables x/L^{D_x} for $x \in \{s,a,t,l\}$ for different systems of size $L = 512, 1024, 2048$ and 4096. It can be seen that, using the measured critical exponents, data for different system sizes collapse on a single curve representing the FSS function assumed in Eq. 2.8 for all the four properties s, a, t and l. The FSS forms assumed here for the probability distribution functions for the avalanche properties in RSM are then correct. It is interesting to note that though RSM has locally deterministic rule for grain distribution, it is conservative, its avalanche cluster morphology is almost compact, it is diffusive, and some of the critical exponents are similar to that of BTW, the scaling functions in RSM do not follow multiscaling as in BTW. This has happened due to the nature of the rotational constraint which incorporates "internal stochasticity" by changing the state of the critical sites in a time step during time evolution of the system. Note that, due to the presence of rotational constraint on the sand flow the toppling balance is also broken as already mentioned. Recently, it is demonstrated by Karmakar *et al.*[82] that the scaling functions obey FSS rather than multi-scaling if toppling imbalance is introduced in the BTW sandpile model. Existence of FSS in RSM is possibly due to toppling imbalance as well as "internal stochasticity" in the model.

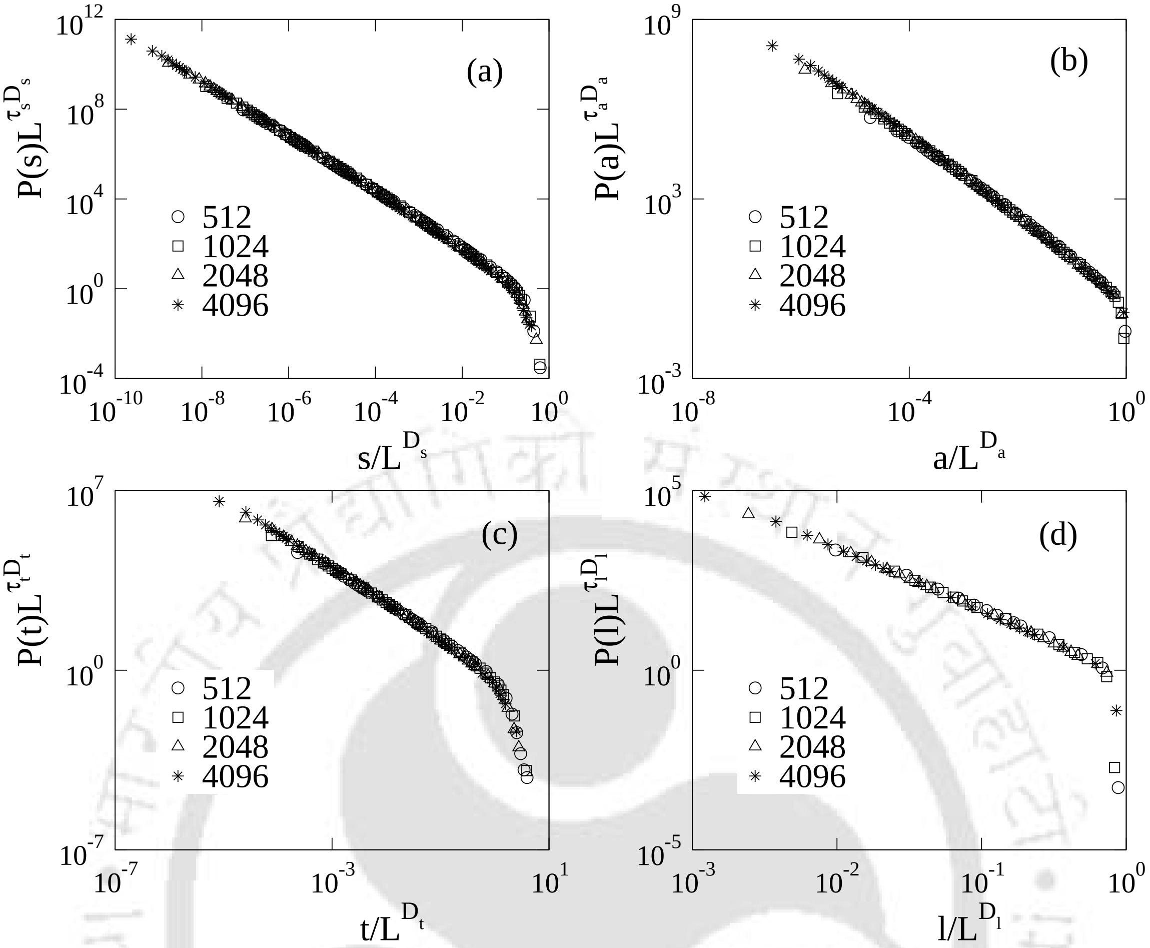

Figure 2.12: Plot of the scaled distribution $P(x)L^{D_x\tau_x}$ against the scaled variable x/L^{D_x} for $x \in \{s, a, t, l\}$. System sizes are taken as $L = 512$ (○), $L = 1024$ (□), 2048 (△) and 4096 (✻). A reasonable data collapse occurs for (a) toppling size s, (b) the area a, (c) lifetime t and (d) spatial extension l of the avalanche.

2.5.4 Toppling waves and time auto-correlation

In order to understand the microscopic reason behind FSS to be followed by certain sandpile models at out of equilibrium situations, a coarse grained study of the time evolution of the avalanches were performed by decomposing avalanches into waves of toppling[86,87,88]. The same technique has been applied for the RSM and the RSM toppling waves are generated. The generation of RSM toppling waves is demonstrated on a 15 × 15 square lattice in Fig. 2.13. The toppling wave is generated from the first active site where the sand grain is added. In Fig. 2.13(a), the central site, marked by ×, is made active by adding sand grains. The central active site is toppled and it generates a cascade of toppling. During the toppling the central site may become active again but it is not allowed to topple until the avalanche once trig-

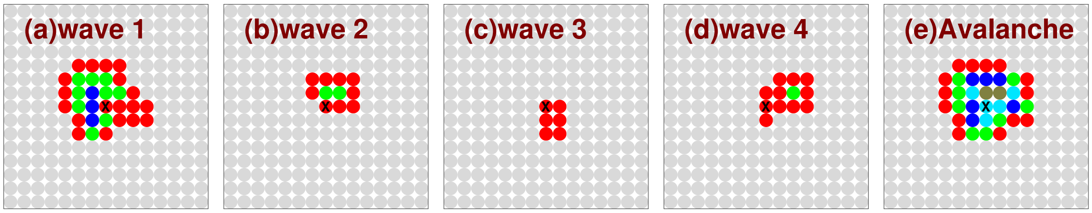

Figure 2.13: Typical waves of an avalanche generated at the steady state of RSM is shown for a square lattice of size 15 × 15. The site marked with × corresponds to the site where the sand grain is added. The four waves of toppling together constitute the avalanche. Different colours in a wave correspond to toppling number of a site in the wave. Different colours in the avalanche corresponds to toppling number of a site in the avalanche. Different colours represent different toppling numbers as grey (●) for 0, red (●) for 1, green (●) for 2, blue (●) for 3, sky-blue (●) for 4 and dark green (●) for 5.

gered is not over. The number of toppling during the propagation of an avalanche starting from an active site without allowing further toppling of the same, constitute the first wave of toppling. The lattice sites toppled in the first toppling wave generated from central active site (×) are shown in Fig. 2.13(a). Different colours associated with the lattice sites represent the number of times a site toppled during the propagation of the wave as: grey (●) for 0, red (●) for 1, green (●) for 2, blue (●) for 3, sky-blue (●) for 4 and dark green (●) for 5. It can be seen that the lattice sites toppled multiple times in the wave and the central active site ×, the origin, topples only ones. After the completion of first toppling wave the central active site × is toppled again and a sequence of toppling activity occurs to become all the sites under critical except the central site. This constitutes the second wave of toppling and is shown in Fig. 2.13(b) using the same colour code of the first toppling wave. Thus, each toppling of the central active site (×) creates a new toppling wave and the generation of waves will stop when the central site (×) becomes under critical. In the example considered here, the avalanche initiated by the central active site (×) is consisting of four toppling waves as shown in Fig. 2.13. An avalanche cluster can be constructed by superimposing these toppling waves. Such an avalanche cluster by superimposing all four toppling waves is shown in Fig. 2.13(e). The colour of a toppled site in the avalanche cluster represents the total number of toppling of that site in all four toppling waves.

The total number of toppling s in an avalanche is then the sum of toppling occurred in individual toppling wave to create such an avalanche. If there are m toppling waves to create an avalanche, the total toppling number s can be obtained as

$$s = \sum_{k=1}^{m} s_k \tag{2.16}$$

where s_k is the number of toppling in the kth wave. Taking each toppling wave as a time unit, a wave time series $\{s_k\}$ is generated by keeping sequentially the toppling numbers of all the toppling waves generated in a large number of avalanches. Following Menech and Stella[89,90,91], a time auto-correlation function is defined as

$$C(t) = \frac{\langle s_{k+t} s_k \rangle - \langle s_k \rangle^2}{\langle s_k^2 \rangle - \langle s_k \rangle^2}, \tag{2.17}$$

where $t = 1, 2, \cdots$ and $\langle \cdots \rangle$ represents the time average. It has already been

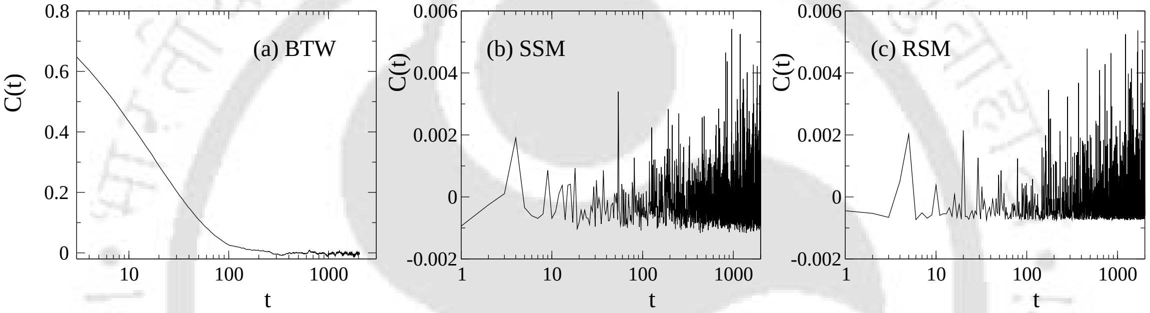

Figure 2.14: Time auto-correlation function $C(t)$ is plotted against time t for (a) the BTW, (b) the SSM and (c) the RSM. There is a long range correlation for BTW. The toppling waves are uncorrelated for both the SSM and the RSM.

demonstrated by Menech and Stella[89,90,91] and Karmakar *et al.*[82] that there is long range correlation in $C(t)$ for the BTW whereas $C(t)$ remains negative initially and then becomes zero in the case of SSM. Thus, the waves in the BTW have correlation over a longer period of time whereas they are uncorrelated in case of the SSM. It can be mentioned here that the probability distribution of sizes of individual toppling waves follow FSS for both the BTW and the SSM[88,89,90,91]. It was argued by Menech and Stella[89,90,91] that since the toppling waves in SSM are uncorrelated, the scaling behaviour of the probability distribution of sizes of the toppling waves must be the same as that of the toppling sizes of the avalanches. Thus, negative auto-correlation in the SSM toppling wave is consistent with the FSS of its avalanche sizes. On the other hand, because of the long range correlation in BTW toppling waves, it was observed that the probability distribution of the sum of sizes of n successive toppling waves changes with increase in n and the distribution approaches the avalanche size distribution in the $n \to \infty$ limit. Further they have established that the presence of long range positive auto-correlation in the BTW toppling wave time series leads to multiscaling in the avalanche size distribution. The time auto-correlation function $C(t)$ for the toppling waves has also been calculated here for the RSM for a system of size $L = 2048$ taking time average over 10^6 toppling waves and are compared with that of the BTW and the SSM. In Fig. 2.14(a), (b) and (c) $C(t)$ is plotted against t for the BTW, the SSM and the RSM. It can be seen that toppling waves have correlation over long range for the BTW whereas they are anti-correlated for the SSM as expected. The toppling waves are also uncorrelated here in the RSM as in the case of the SSM. $C(t)$ is found negative initially and then becomes zero. It is then consistent with the fact that the toppling size distribution follow FSS rather than multiscaling. The origin of negative auto-correlation in SSM is the stochasticity. In the RSM, the local deterministic toppling rule picks up certain randomness during the evolution and as a consequence the toppling wave shows negative auto-correlation. Though the rotational constraint has local correlation, the toppling waves become uncorrelated because of the "hidden stochasticity." It should be mentioned here that in the cases of the SSM and the RSM, the sites involved in a toppling wave may topple more than once unlike in the case of the BTW. Moreover, the toppling numbers as well as the final configurations of the SSM and the RSM strongly depend on the sequence of toppling. As a consequence, Eq. 2.16 may not always be satisfied in the RSM and the SSM. However, on an average the collection of toppling waves can be considered as a representation of an avalanche in these models.

2.6 Conclusion

A two state "quasi-deterministic" rotational sandpile model, the RSM, is defined on a $2d$ square lattice imposing rotational constraint on the sand flow. The model has microscopic properties such as mass conservation, open boundary, and local deterministic rule in sand grain distribution at the time of toppling as that of BTW. On the other hand, the rotational bias introduces toppling imbalance and certain internal stochasticity in the toppling dynamics. Stochasticity and toppling imbalance are the properties of the SSM. The avalanche cluster morphology in the steady state exhibits characteristics of both BTW as well as SSM. The critical properties of the non-equilibrium steady state of RSM is studied by measuring probability distribution of several avalanche properties and performing FSS study of those properties.

Avalanche properties in the steady state exhibit power law distributions with specific critical exponents. Therefore, the steady state of the RSM represents a SOC state. RSM is found to be diffusive in character like BTW and SSM. An extended set of critical exponents is calculated. It is observed that some of them are close to that of BTW but different from SSM. The values of the exponents satisfy the scaling relations among them within error bars. RSM then belongs to a new universality class. The scaling function forms are determined. It is found that the scaling functions of the RSM obey the usual FSS as in the case of SSM rather than multiscaling as in the case of BTW. This has been confirmed by negative time auto-correlation of toppling waves constituting an avalanche. The appearance of FSS as well as negative time auto-correlation in the RSM may be due to the local toppling imbalance and the "internal stochasticity" caused by the imposed rotational constraint on the model.

Chapter 3

Variants of RSM and their characterization

The RSM described in previous chapter was found to belong to a new universality class than that of the BTW and the stochastic SSM. Interestingly, the RSM has some microscopic as well as macroscopic characteristics of both the deterministic BTW and the SSM. The RSM was found to be non-Abelian and does not have toppling balance. As a consequence of toppling imbalance and negative auto-correlation in the toppling waves, the RSM follows FSS ansatz as in the case of SSM. These observations are all related to the fact that the local correlation due to the rotational constraint in the toppling rule does not propagate upto the system size due to appearance of internal stochasticity during time evolution. The appearance of internal stochasticity in the RSM is due to the fact that the direction of flow of sand grains from an active site may change from the expected direction of flow due to toppling of its neighbouring sites. It is then interesting to explore the effect of change in internal stochasticity in the RSM by controlling the direction of sand flow at the time of toppling. In the RSM, the sand flow was governed by the direction from which the last sand grain was received by the active site. The flow of sands can be controlled in the following two different manners. First, the sand flow can occur according to the direction from which the sand grain was received to make the site active for the first time. Second, the sand flow can occur according to a randomly selected direction from which the sands were received by an active site, above or equal to the critical height. In the first case, it is expected that the internal stochasticity will decrease and the local correlation will be stronger. As a consequence the model will be more deterministic in nature and closer to the BTW. On the other hand the internal stochasticity would increase and the local correlation should reduce due to the second condition. As a consequence the model will be more stochastic and closer to the SSM. The effect of decrease or increase in internal stochasticity in the critical behaviour of the RSM will be explored here constructing two variants of the RSM by controlling the direction of sand flow.

3.1 The models: RSM1 and RSM2

Two different versions of the original RSM[113] namely the RSM1 and the RSM2 are presented here. These two models are constructed by changing the toppling rules of the RSM in such a way that in one the internal stochasticity as compared to the RSM will be decreased and that will be called as RSM1. In the other, the internal stochasticity will be increased and that will be called as RSM2. The models are defined on a two dimensional ($2d$) square lattice of size $L \times L$ as it was done for the RSM. Both the models are developed in the similar way as that of the RSM starting from an empty lattice and adding sand grains to the randomly chosen lattice sites one at a time. The critical height is also taken as $h_c = 2$ for both the models. A site becomes active if the height of the sand column at that site becomes greater than or equal to h_c. On the very first toppling of the active site, two sand grains are distributed to two randomly chosen nearest neighbours as in the case of the RSM. As soon as a site receives a sand grain, its height h_i is increased by 1 and the direction d_i from which the sand is received is noted. The information from which direction the sand grain was received by a site is kept at all heights $h \geq h_c$. The next active sites with $h_i \geq h_c$ in the avalanche will topple and two sand grains will be taken away. The rotational toppling rule for the RSM1 and the RSM2 is given below:

Toppling rule of RSM1: On the event of toppling of an active site, one sand grain from the active site flows in the forward direction and the other will flow in a clockwise rotational direction with respect to the forward direction. The forward direction in RSM1 corresponds to the direction from which a site received sand grain to become critical or active ($h = h_c$) for the first time. The toppling rule of the RSM1 is given by

$$\begin{aligned} h_i &\rightarrow h_i - 2 \\ h_j &\rightarrow h_j + 1, \quad j = d_c, \;\; d_c + 1 \end{aligned} \tag{3.1}$$

where d_c is the direction from which the sand grain was received at $h = h_c$.

Toppling rule of RSM2: The forward direction of sand flow in RSM2 corresponds to the direction of the sand grain received by the site at an arbitrary height on, or above the critical height $h \geq h_c$. The toppling rule of the RSM2 is given by

$$\begin{aligned} h_i &\rightarrow h_i - 2 \\ h_j &\rightarrow h_j + 1, \quad j = d_r, \;\; d_r + 1 \end{aligned} \tag{3.2}$$

where d_r is a randomly chosen direction from which a sand grain was received at a height $h \geq h_c$.

In both the RSM1 and the RSM2, toppling of an active site may trigger a cascade of toppling activities which constitutes an avalanche. Toppling of the first active site in an avalanche is considered as the first time step. The NN sites which become active at the end of the first time step are kept sequentially as they appear. All those active sites are toppled in the sequence as they are stored in the second time step. This is called a parallel update. The sites which become active at the end of the second time step are relaxed by the next parallel update, the third time step. The process of parallel update continues until an avalanche stops when height of all the sand columns are less than h_c. The number of parallel updates required to make the system under critical is taken as the lifetime of an avalanche. During an avalanche no sand grain is added and the avalanche dynamics is studied with open boundary condition as it was followed for the RSM.

3.2 Steady state

As observed in the RSM, the non-equilibrium steady state of sandpile model is characterized by the constant average height of the sand columns in the lattice. In order to identify the steady states of the RSM1 and the RSM2, the average height $\langle h \rangle$ of the sand columns is measured adding a large number of sand grains to randomly chosen lattice sites one at a time starting from an empty lattice of size 2048×2048. The average height of the sand columns is defined as

$$\langle h \rangle = \frac{1}{L^2} \sum_{i=1}^{L^2} h_i. \tag{3.3}$$

The average height $\langle h \rangle$ is measured after every $10,000$ sand grains added. Measurement of $\langle h \rangle$ is always performed after the avalanche is completed. In Fig.3.1, $\langle h \rangle$s are plotted against the number of sand grains added for both RSM1 and RSM2 and is compared with the RSM. It can be seen that $\langle h \rangle$ attains a constant value for both the RSM1 and the RSM2. The steady state value of $\langle h \rangle$ for the RSM1 is found to

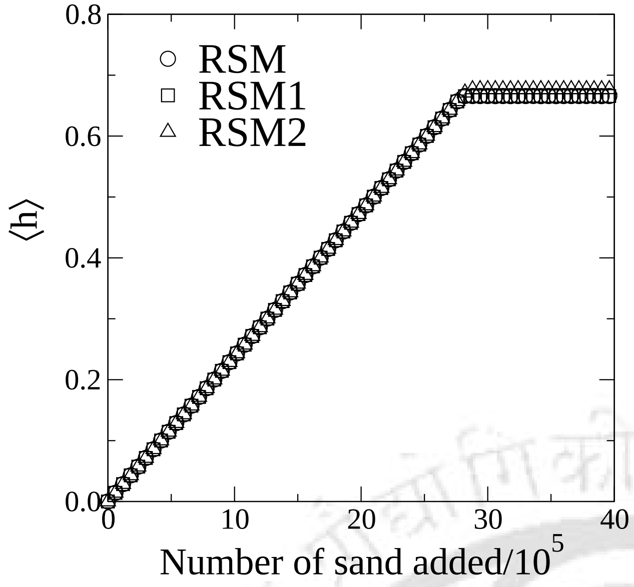

Figure 3.1: Plot of average height $\langle h \rangle$ against the number of sand grains added for the RSM, the RSM1 and the RSM2 for $L = 2048$. The value of $\langle h \rangle$ remains constant after a large number of sand grains added. The steady state value of $\langle h \rangle$ for the RSM1 is close to that of the RSM but it is slightly higher for the RSM2.

be close to that of the RSM but it is slightly different for the RSM2. Total number of sand grains added to the system of size $L = 2048$ is 4×10^6. For smaller lattice sizes the constant average height is reached earlier than that of $L = 2048$.

3.3 Salient features of RSM1 and RSM2

The toppling rules followed in the RSM1 and the RSM2 incorporate certain non-trivial features in the models. First, both the RSM1 and the RSM2 are found to be a non-Abelian model and the final state depends on the sequence of toppling. However, it is observed that the RSM1 produces more Abelian configurations whereas the RSM2 produces more non-Abelian configurations in comparison to the original RSM. As a consequence, the RSM1 is more closer to the BTW in which all configurations are Abelian and RSM2 is more closer to the SSM in which most of the configurations are non-Abelian. This is demonstrated in Fig.3.2 applying different toppling rules on the same initial configuration. Second, for both the RSM1 and the RSM2 the number of sand grains outgoing from an active site after toppling is not necessarily equal to the number of sand grains incoming to the same site after toppling of its NNs once each. Thus there is no precise toppling balance for both the RSM1 and RSM2. Third, in the RSM1 the internal stochasticity of the model is expected to be less in comparison to the original RSM in which toppling rule was governed by the direction of the last sand grain received whereas the RSM2 will incorporate more stochasticity into the model in comparison to the original one. As a consequence, the RSM1 is expected to be more closer to a BTW like model on the

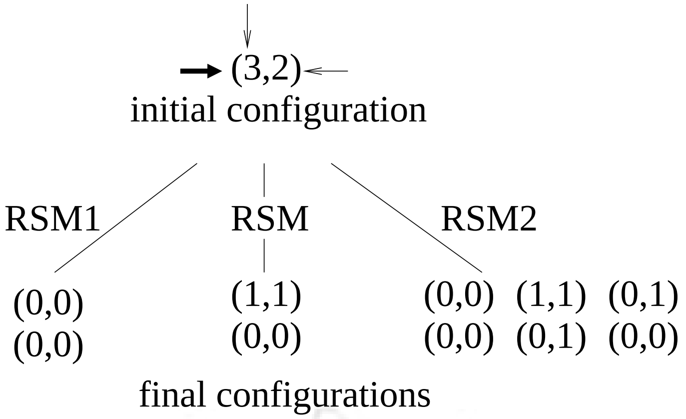

Figure 3.2: Toppling rules of the RSM, the RSM1 and the RSM2 are applied on a two state initial configuration shown. In a state the numbers represent the height of the columns. For this initial configuration, the RSM produces non-Abelian configurations whereas the RSM1 produces Abelian configurations. The RSM2 produces Abelian as well as non-Abelian configurations. The first row of the states are obtained by toppling the site with 3 grains first and the second row corresponds to the states obtained by toppling the site with 2 grains first. The thin arrows represent the direction from which the site received a grain to become critical for the first time. The thick arrow represents the direction of the next sand grain received.

other hand the RSM2 is expected to be more closer to the SSM. The stochasticity in the RSM1 and the RSM2 appear from the fact that the sand flow in a given direction is changed by the direction of the sand grain received by the same site to become critical. The stochasticity in these models is thus internal and originates from the implementation of the deterministic rotational rule of sand propagation as observed in the RSM. Fourth, applying the toppling rules of the RSM1 and the RSM2 on a same initial configuration leads to different final configurations. It can be seen in Fig.3.2 that application of toppling rules of the RSM1 and the RSM2 on a same initial configuration leads to different final configurations. It has also been checked for a larger lattice that different final height configuration can be obtained from the same initial configuration after applying the toppling rule of both the RSM1 and the RSM2. Though it is still possible to generate the same final configuration starting from different initial states, one may eventually generate ensemble of considerably different avalanche clusters than that of the RSM with the new toppling rules. This has been demonstrated here by generating a pair of avalanche clusters for the RSM1 and the RSM2 from the same initial steady state height configuration on a 128 × 128 square lattice and are shown in Fig.3.3. The initial configuration taken is a steady state configuration of the RSM1. However, in order to generate the final configurations, rules of both the RSM1 and the RSM2 are applied to the same

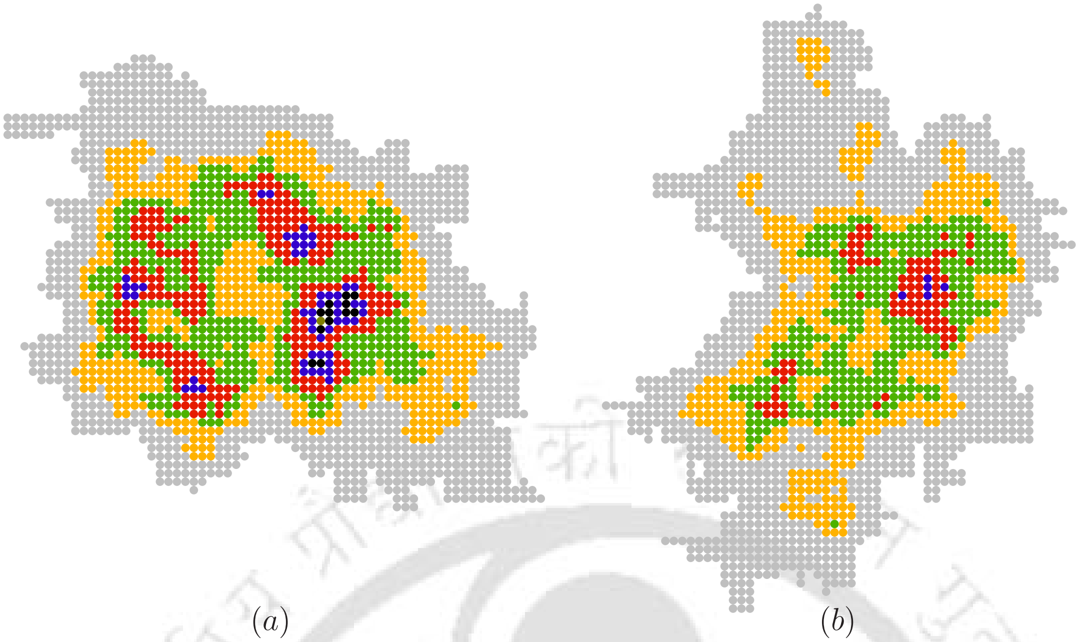

(a) (b)

Figure 3.3: Avalanche clusters for (a) the RSM1 and (b) the RSM2 are generated on a 128×128 square lattice starting from the same initial configuration. The toppling numbers are binned into six equal groups. Different colours assigned to each bin as: grey (●) for $1 \leq S_i \leq 8$, yellow (●) for $9 \leq S_i \leq 16$, green (●) for $17 \leq S_i \leq 24$, red (●) for $25 \leq S_i \leq 32$, blue (●) for $33 \leq S_i \leq 40$ and black (●) for $41 \leq S_i \leq 50$. White space inside the avalanche corresponds to the sites that did not topple at all during the avalanche.

initial configuration assuming that it could also be a possible configuration of the RSM2. Though the clusters are generated from the same initial configuration the final avalanche clusters obtained for RSM1 and RSM2 are different and have total number of toppling 27862 and 19322, number of distinct sites toppled 2215 and 2045, and have duration of 899 and 690 time steps respectively. However, both the clusters are found isotropic and almost compact except few holes here and there. Different colours assigned to a range of toppling numbers are: grey (●) for $1 \leq S_i \leq 8$, yellow (●) for $9 \leq S_i \leq 16$, green (●) for $17 \leq S_i \leq 24$, red (●) for $25 \leq S_i \leq 32$, blue (●) for $33 \leq S_i \leq 40$ and black (●) for $41 \leq S_i \leq 50$. It can be seen that the clusters consist of several maximal toppling zones, the black or blue zones. The clusters also has concentric zones of lower and lower numbers of toppling sites appearing around the maximal toppling zones. The avalanche clusters then look like random superposition of several BTW type avalanche clusters[60,117,118]. These clusters look like the RSM avalanche clusters but are different from the SSM avalanche clusters[75,77].

3.4 Characterization of the steady states

In order to study the critical behaviour of avalanches and FSS of the RSM1 and the RSM2, different physical properties are studied as a function of the system size L. Avalanche clusters are generated at the respective non-equilibrium steady states of these models on $2d$ square lattices of different linear dimension $L = 128$ to $L = 2048$ in multiples of 2. After reaching the steady state extensive data collection has been made for each lattice size for averaging in a similar way as mentioned for the RSM in the previous chapter. Number of avalanches for ensemble averaging ranges from 32×10^6 for $L = 128$ down to 2×10^6 for $L = 2048$.

3.4.1 Probability distributions

In the steady state of both the RSM1 and the RSM2, critical properties of three different avalanche quantities: toppling size (s), area (a), and lifetime (t) are studied for different system sizes L. The probability distributions of avalanche properties in the steady state are expected to follow power law scaling behaviour as given by

$$P(s) \sim s^{-\tau_s}, \quad P(a) \sim a^{-\tau_a}, \quad P(t) \sim t^{-\tau_t} \tag{3.4}$$

where τ_s, τ_a and τ_t are the associated critical exponents. The probability distributions of s, a, and t obtained in the RSM1 and the RSM2 are shown in Fig.3.4(a) for the system size $L = 2048$. The probability distributions of all three properties are found to obey power law behavior for both the models for the given system size. The power law scaling of these properties are also verified for the RSM1 and the RSM2 on smaller system sizes. Since there is power law distribution, no typical toppling size, area or lifetime of an avalanche exists at the non-equilibrium steady state of these models and hence they exhibit SOC. The values of the critical exponents obtained for the system size $L = 2048$ are: $\tau_s = 1.225 \pm 0.005$, $\tau_a = 1.333 \pm 0.006$, and $\tau_t = 1.389 \pm 0.006$ for both the variants[123,124]. These exponent values are also found within error bars of the exponents obtained in the original RSM. The errors are due to the least square fitting taking into account the statistical error of each data point. Therefore, the critical behaviour of the probability distributions remain unaltered under the modifications of toppling rules of the original RSM. Neither the exponents of the RSM1 become closer to that of the BTW nor the exponents of the RSM2 become closer to that of the SSM. Though the RSM1 and the RSM2 exhibit similar critical behaviour at their respective non-equilibrium steady state as that of

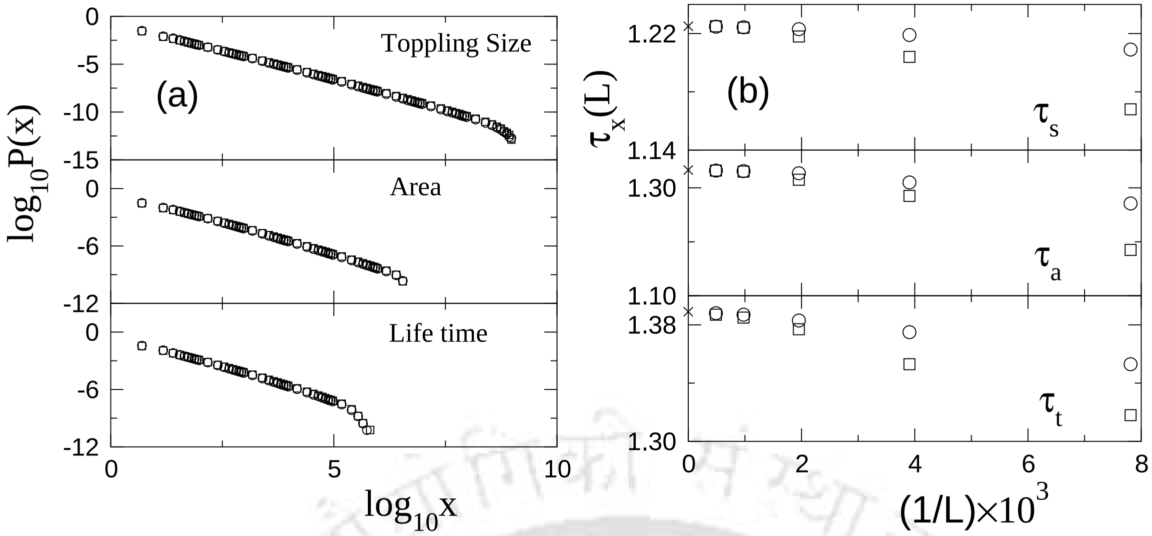

Figure 3.4: (a) $P(x)$ is plotted against x,$x \in \{s, a, t\}$ for the system size $L = 2048$ for the RSM1 (circles) and the RSM2 (squares). $P(x)$ demonstrates power law correlation at the steady state of both the models. (b) The size dependent critical exponents $\tau_x(L)$ is plotted against $1/L$ for the RSM1 (circles) and the RSM2 (squares). As $L \to \infty$, the avalanche properties are characterized by the same critical exponents for both the models. The crosses on the y-axis represent the exponent values obtained for the original RSM on a 2048×2048 square lattice.

the original RSM, the absolute values of the avalanche properties are found different with different cutoff of the probability distributions. This implies that though different models generate ensembles of different avalanche clusters their scaling behaviour remains the same. It is therefore important to note that change in toppling rule does not lead to any different scaling behaviour in the case of the RSM. This may be due to the robustness of the broken mirror symmetry present in these models. In order to study the effect of finite system size on critical exponents associated with the probability distributions, the values of critical exponents for different L are estimated determining the probability distributions of these properties for the respective system size L. The values of the critical exponents obtained for different system sizes on the RSM1 and the RSM2 are presented in Fig.3.4(b) by plotting $\tau_x(L)$ against $1/L$. The values of the critical exponents are obtained from the best fitted part of the distributions for a given system size as shown in Fig.3.4(a). It can be seen that though the exponent values depend on the system size at smaller L, they converge to a single value at large system size. The values of the exponents obtained in the original RSM are represented by crosses on the y-axis and are found to be the same with the extrapolated values of the critical exponents of the RSM1 and the RSM2. The toppling size s and the lifetime t in the BTW model follow

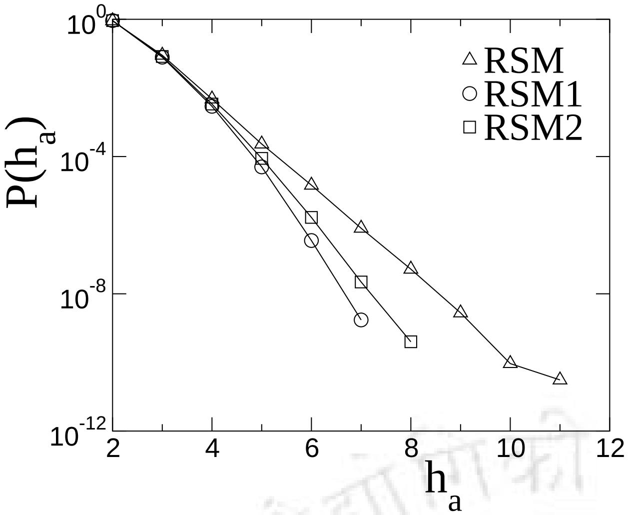

Figure 3.5: Plot of $P(h_a)$ against h_a for $h_a \geq h_c$ obtained on a 1024×1024 lattice generating 10^5 avalanches in the steady state for the RSM, the RSM1 and the RSM2.

multiscaling and accordingly the slope of these distributions are found to depend on the system size L and no convergence can be achieved in the $L \to \infty$ limit. On the other hand, the size dependent critical exponents in the RSM1 and the RSM2 are due to numerical errors, smaller linear region of probability distribution in double logarithmic scale and finally they found to converge to a single value as $L \to \infty$. This indicates that the distribution functions of the RSM1 and the RSM2 should not obey multiscaling as in the BTW. The values of the critical exponents in the RSM1 and the RSM2 are that of the original RSM but different from that of the BTW and the SSM. Consequently, they belong to the same universality class of the RSM which is different from the SSM and the BTW. The change in toppling rule is unable to change the universality class of these models. This may be due to a typical height distribution of the active sites in the rotational models. The probability of appearance of an active site with height h_a ($h_a \geq h_c$) before toppling in an avalanche can be written as

$$P(h_a) = \frac{n(h_a)}{N_a}, \tag{3.5}$$

where $n(h_a)$ is the number of active sites with sand column having height h_a before toppling in an avalanche and N_a is the total number of active sites. In Fig.3.5, $P(h_a)$ is plotted against the height of the active site h_a. It can be seen that not only the distributions are different in different models but also, only a few active sites with height $h >> h_c$ appear in all these models. If the height is not much greater than h_c, the change in toppling rule at different heights will not be that effective. Eventually at the thermodynamic limit, these minority events did not contribute sufficiently to change the universality class.

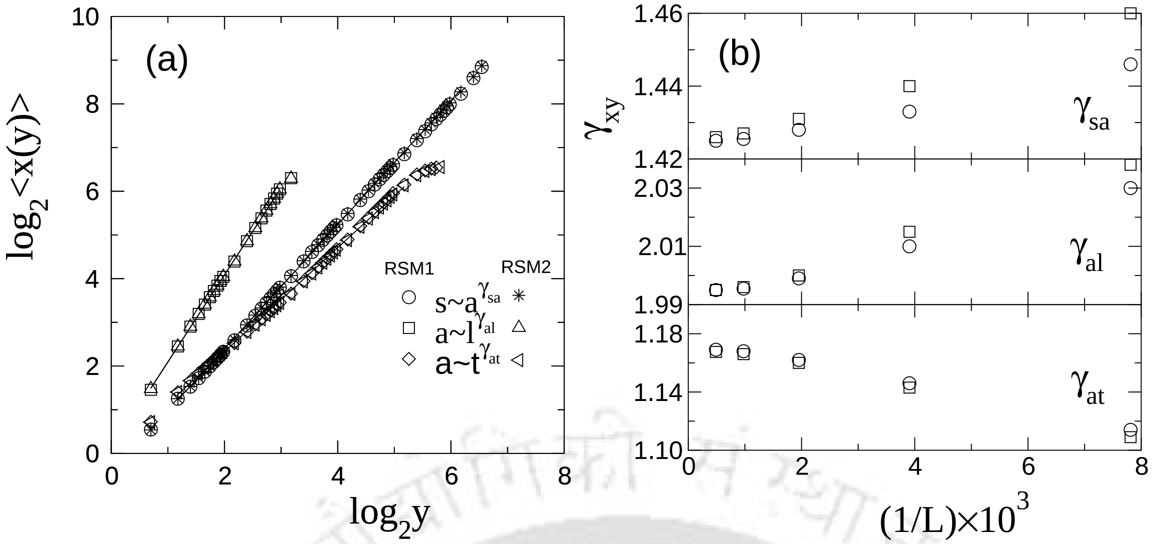

Figure 3.6: (a) Plot of conditional expectation value of avalanche properties: toppling s versus area a (○) and (✻), area a versus extension l (□) and (△), area a versus time t (◇) and (◁∗) for the RSM1 and the RSM2 respectively. The solid lines show the best fitted straight line parts. (b) Plot of γ_{xy} against $1/L$ for the RSM1 (○) and the RSM2 (□). As $L \to \infty$, the exponents for both the models have the same value.

3.4.2 Conditional expectations

In order to further characterize the critical behaviour of the avalanches of the RSM1 and the RSM2, the conditional expectation values of the avalanche properties are also studied for different system sizes L. The conditional expectation value of three different avalanche properties $\langle s(a)\rangle$, $\langle a(l)\rangle$ and $\langle a(t)\rangle$ are considered here. In the steady state, the expectation values scale with its argument as

$$\langle s(a)\rangle \sim a^{\gamma_{sa}}, \quad \langle a(l)\rangle \sim l^{\gamma_{al}}, \quad \langle a(t)\rangle \sim t^{\gamma_{at}} \tag{3.6}$$

where γ_{sa}, γ_{al} and γ_{at} are the critical exponents. An extended set of critical exponents[75,77] are obtained from the conditional expectation values as given in Eq.3.6 for both the models. In Fig.3.6, the conditional expectation values $\langle s(a)\rangle, \langle a(l)\rangle$ and $\langle a(t)\rangle$ are plotted against their respective arguments a, l and t for system of size $L = 2048$ in double logarithmic scale. The conditional expectation values scale with their respective arguments as it was assumed in Eq.3.6. For smaller system sizes the conditional expectation values follow the same scaling behaviour. For a given system size L, the associated exponents γ_{sa}, γ_{al} and γ_{at} (Eq.3.6) are obtained by least square fitting to the data points. The exponent values for different system sizes are plotted in Fig.3.6. It is observed that the values of the critical exponents at small finite lattices differ from each other but converge to a single value in the asymptotic $L \to \infty$ limit. The asymptotic large L values of the critical exponents are: $\gamma_{sa} \approx 1.425$,$\gamma_{al} \approx 1.995$, $\gamma_{at} \approx 1.169$ for both the RSM1 and the RSM2 within ± 0.005[123,124]. The exponents obtained in the original version are found close to these values and within error bars. Once again, the RSM1 and the RSM2 are found to belong to the same universality class of the RSM. The critical exponents γ_{xy}, τ_x and τ_y obtained in these models satisfy usual scaling relation among them $\gamma_{xy} = (\tau_y - 1)/(\tau_x - 1)$. It can be noted that $\gamma_{al}(\approx 2)$ for these models as that of the original RSM. The values of τ_x and γ_{xy} are listed in Table 3.1 and are compared with that of the RSM. It can be seen that the exponents of the RSM1 and the RSM2 are same with that of the RSM within error bars. The same critical behaviour of the RSM1 and the RSM2 with the RSM is due to the robustness of the rotational rule present in these models.

3.4.3 Capacity dimensions

It is observed in the case of both the RSM1 and the RSM2 that there is a cutoff in the probability distributions of the avalanche related quantities x at x_{max} due to the finite system size L. The cutoff $x_{max}(L)$ is expected to scale with L as $x_{max}(L) \sim L^{D_x}$, where D_x is capacity dimension of the quantity. The probability distribution function for a quantity x for a system of size L is expected to obey the scaling function form given by

$$P(x, L) = x^{-\tau_x} \mathsf{f}(x/L^{D_x}) \quad x \in \{s, a, t\} \tag{3.7}$$

where $\mathsf{f}(x/L^{D_x})$ is the finite size scaling function. In order to verify the scaling function form $\mathsf{f}(x/L^{D_x})$ given in Eq.3.7, one needs to know the capacity dimensions D_x. To estimate D_x, q moments of a property x are estimated as

$$\langle x^q \rangle = \int_0^{x_{max}} x^q P(x, L) dx \sim L^{\sigma_x(q)} \tag{3.8}$$

where $\sigma_x(q) = (q + 1 - \tau_x)D_x$. The value of D_x can be determined taking partial derivative of the $\sigma_x(q)$ series in the large q limit. If $P(x, L)$ obey FSS then the moment exponent $\sigma_x(q)$ should have a constant gap between two successive values. On the other hand, if $P(x, L)$ obey multiscaling, $\sigma_x(q)$ should have a continuous nonlinear dependence on q. For a given q, the value of σ_x has been obtained here from the slope of the plot in double logarithmic scale of $\langle x^q(L) \rangle$ versus L changing

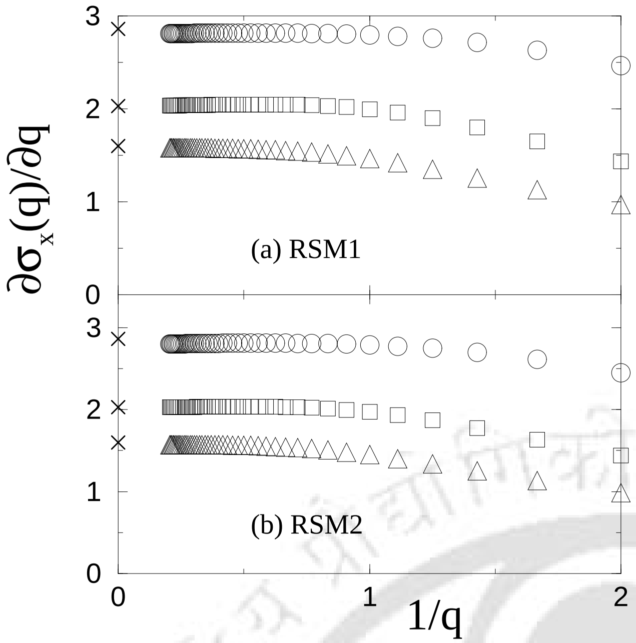

Figure 3.7: Plot of $\partial\sigma_x(q)/\partial q$ versus $1/q$ where $x \in \{s, a, t\}$ for (a) the RSM1 and (b) the RSM2. Data of s, a and t are represented by circles, squares and triangles respectively. All the properties converge to a single value as $q \rightarrow \infty$.

lattice size from $L = 128$ to 2048 in multiples of 2. A sequence of exponents $\sigma_x(q)$, $x \in \{s, a, t\}$, is obtained for 400 values of q between 0 and 4 at equal intervals. It can be noted here that the values of $\sigma_s(1)$ are 2.01 ± 0.01 for both the RSM1 and the RSM2 which indicates that the RSM1 and the RSM2 are diffusive in accordance with the fact that spiral random walks are diffusive[122]. In order to verify the functional dependence of $\sigma_x(q)$ on q, the derivative $\partial\sigma_x(q)/\partial q$ is calculated following the finite difference method and it is plotted against $1/q$ in Fig.3.7 for (a) the RSM1 and (b) the RSM2. It can be seen that $\partial\sigma_x(q)/\partial q$ converges to the corresponding capacity dimensions D_x in the large q limit for all three properties for both the RSM1 and the RSM2. The linearly extrapolated values to the $q \rightarrow \infty$ limit are marked by the crosses. Therefore, $\sigma_x(q)$ maintains a constant gap between two successive values for q and $q+1$ in the $q \rightarrow \infty$ limit for both the RSM1 and the RSM2 as in the original RSM. This is another indication that FSS is valid for the RSM1 and the RSM2 independent of the toppling rules. The values of D_x obtained are: $D_s = 2.86 \pm 0.01$, $D_a = 2.03 \pm 0.01$ and $D_t = 1.60 \pm 0.01$ for both models[123,124]. The errors are due to the finite difference method adopted for differentiation of the $\sigma(q)$ sequence. The values of D_x are listed in Table 3.1 and are compared with that of the RSM.

Exponent	Models		
	RSM	RSM1	RSM2
τ_s	1.224 ± 0.005	1.225 ± 0.005	1.224 ± 0.005
τ_a	1.334 ± 0.005	1.333 ± 0.005	1.333 ± 0.005
τ_t	1.389 ± 0.005	1.389 ± 0.005	1.389 ± 0.005
τ_l	1.667 ± 0.007	1.667 ± 0.007	1.667 ± 0.007
γ_{sa}	1.453 ± 0.003	1.425 ± 0.003	1.425 ± 0.003
γ_{at}	1.167 ± 0.005	1.169 ± 0.005	1.169 ± 0.005
γ_{al}	2.002 ± 0.002	1.995 ± 0.002	1.995 ± 0.002
γ_{tl}	1.715 ± 0.005	1.715 ± 0.005	1.715 ± 0.005
D_a	2.03 ± 0.02	2.03 ± 0.02	2.03 ± 0.02
D_s	2.86 ± 0.02	2.86 ± 0.02	2.86 ± 0.02
D_t	1.60 ± 0.02	1.60 ± 0.02	1.60 ± 0.02

Table 3.1: Comparison of critical exponents obtained for the RSM, the RSM1 and the RSM2. Critical exponents of the RSM1 and the RSM2 are almost equal to that of the RSM.

3.4.4 Data collapse

Finally the scaling function forms $\mathsf{f}(x/L^{D_x})$ of the RSM1 and the RSM2 are verified by studying a scaled distribution $P(x)x^{\tau_x}$ as a function of the scaled variable x/L^{D_x}[73]. $P(x)x^{\tau_x}$ is plotted against x/L^{D_x} for $x \in \{s, a, t\}$ for the RSM1 and the RSM2 in Fig.3.8. The data of the RSM2 is shifted down and leftwards in the plot for clarity. For all three properties, s, a and t, a good collapse of data are observed for $L = 256, 512, 1024$ and 2048 in support of the finite size scaling function form for both the RSM1 and the RSM2 as it was observed in the original RSM. It can be noticed that, though the RSM1 and the RSM2 have locally deterministic rule for sand grain distribution, it is conservative and diffusive, its avalanche cluster morphology is almost compact with concentric toppling zones, some of the critical exponents are similar to that of the BTW, yet, the scaling functions for all three properties s, a and t in these models obey FSS. It should be emphasized that the RSM1 which generates large number of Abelian configurations and is believed to be the more closer to the BTW, do not follow multiscaling as in the BTW. This has happened due to the nature of the rotational constraint which incorporates internal as well as imposed stochasticity during time evolution of the system which in effect breaks the correlation in toppling sequence generated by the rotational toppling rules. The correlation between the toppling sequence can be verified by generating a toppling wave[86,87,88] time series for the number of toppling $\{s_k\}$ in the kth wave and defining

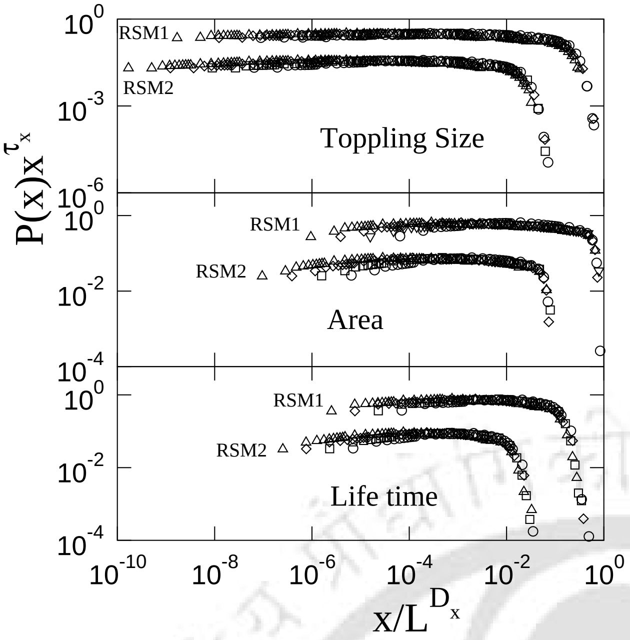

Figure 3.8: Plot of the scaled distribution $P(x)x^{\tau_x}$ against the scaled variable x/L^{D_x} for $x \in \{s, a, t\}$ for both the RSM1 and the RSM2. System sizes are taken as $L = 256$ (○), $L = 512$ (□), 1024 (◇) and 2048 (△). A reasonable data collapse occurs for all three properties. Data of the RSM2 is shifted down and leftwards for clarity.

a time auto-correlation function[89,90,91] as $C(t) = (\langle s_{k+t}s_k\rangle - \langle s_k\rangle^2)/(\langle s_k^2\rangle - \langle s_k\rangle^2)$. Time auto-correlation of the toppling waves for the RSM has already been studied in previous chapter and no correlation was observed between the toppling waves in contrast to large positive correlation in the BTW[82,89,90,91]. The similar analysis is also performed for the RSM1 and the RSM2. In Fig.3.9 $C(t)$ is plotted against t and absence of time auto correlation between the toppling waves is observed as expected for both the models. Negative auto-correlation suggests that the local correlation in the rotational toppling rule does not propagate upto the system size because of superposition of toppling waves from different directions. Existence of FSS in the RSM1 and the RSM2 is then possibly due to toppling imbalance as well as internal stochasticity and negative auto-correlation in the toppling waves.

3.5 Conclusion

Two variants of the original RSM, the RSM1 and the RSM2, are constructed. The toppling rule in the RSM1 is such that the internal stochasticity present in the original RSM reduces and it becomes closer to the BTW. In the case of the RSM2 the toppling rule increases the internal stochasticity and makes it closer to the SSM. The RSM1 incorporates less randomness and produces more Abelian configurations whereas the RSM2 incorporates more randomness and produces more non-Abelian configurations. Both these models have same microscopic properties such as mass

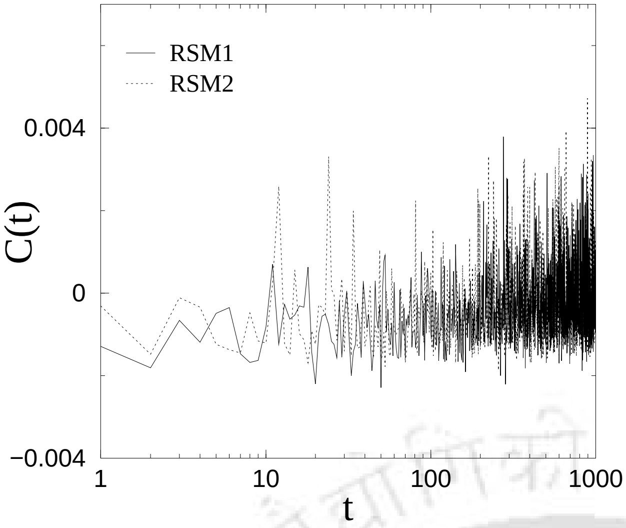

Figure 3.9: Time auto-correlation function $C(t)$ is plotted against time t for the RSM1 and the RSM2. The toppling waves are uncorrelated for both the RSM1 and the RSM2 as in the RSM.

conservation, toppling imbalance, internal stochasticity etc. as that of the RSM. The values of most of the critical exponents obtained numerically are found different from those of the BTW as well as the SSM but are identical to that of the original RSM. Consequently, all rotational models belong to the same universality class. Neither the RSM1 is found in the BTW universality class nor the RSM2 is found in the SSM universality class. This may be due to the robustness of broken mirror symmetry present in the rotational models as well as due to a typical height distribution of the active sites. Knowing the fact that FSS ansatz is obeyed by the SSM whereas a multiscaling is obeyed by the BTW, attempt has been made to resolve whether the RSM1 and the RSM2 obey FSS ansatz or not. FSS ansatz has been verified by moment analysis and data collapse of the probability distribution functions of the avalanche properties. Interestingly, both the analysis indicate that the scaling functions describing the avalanche properties of these rotational models obey usual FSS ansatz as in equilibrium critical phenomena. The existence of FSS in these rotational models is possibly due to toppling imbalance, non-Abelian property, internal stochasticity and the negative auto-correlation in the toppling waves.

Chapter 4

Sandpile avalanches: Multifractality and multi-affinity

Fractals are characterized geometrically by a single fractal dimension while multifractals are characterized by a set of fractal dimensions. Multifractals appear in a wide range of situations like energy dissipation in turbulent flows[125], electronic eigenstates at metal insulator transition[126,127,128], diffusion in porous structures[129], diffusion limited aggregation[130], fluctuations in finance[131,132], dynamics of human heartbeat[133,134] and many others. On the other hand, self-affine fractal surfaces often appear in nature as well as in many physio-chemical processes[99]. For example: the Earth's relief, mountains[135], clouds[136,137], etc. in nature, the crack fronts in materials[138], fractured surfaces[139,140], crumpled paper[141,142], ripple wave turbulence[143], flame front surfaces[144] etc. appeared in different physio-chemical processes are found to be self-affine lines or surfaces. A simple self-affine surface is characterized by a single Hurst exponent whereas a multi-affine surface[145,146,147,148,149,150,151,152,153,154,155,156] is characterized by a set of Hurst exponents.

Sandpile avalanches are usually characterized by studying certain "macroscopic" avalanche properties such as toppling size s, area a, lifetime t, etc. In this chapter the multifractal and the multi-affine aspects of the sandpile avalanches are investigated introducing a new microscopic parameter S, the number of times a sand column toppled during an avalanche. Little attention has been paid to this new microscopic parameter S, the toppling numbers of individual sand columns, in the literature. Negligible effort has been made to characterize the critical properties of sandpile avalanches in terms of S which keeps more detailed information of the avalanche dynamics than what is kept by the heights $h(x)$ of the sand columns after the avalanche. The parameter S is used here to define a suitable multifractal measure to study the multifractal aspect of the sandpile avalanches. At the same time, the parameter S is also used to define a toppling surface to study the self-affinity as well as multi-affinity of the toppling surfaces associated with the avalanches. It should be noted here that the toppling surface is very different from that of the sandiple surface[157,158,159] defined by the heights $h(x)$ of the sand columns after the avalanche. The study of sandpile models in terms of this newly introduced "microscopic" avalanche parameter S provides deeper insight to the avalanche dynamics as well as it is able to classify the sandpile models distinctly.

Simulations are performed on $2d$ square lattices of size $L \times L$. The system size L considered are 128, 256, 512, 1024 and 2048. The steady states correspond to the constant average height of these models and are achieved after 10^6 avalanches. Another 10^5 avalanches are rejected before collecting data. 1000 large spanning (touching opposite sides of the lattice) avalanche clusters are collected generating another $10^6 - 10^7$ avalanches and averages are made over these spanning avalanche clusters. The toppling number S during an avalanche is stored in an array. Several new "macroscopic" avalanche properties such as distribution of S, density distribution of S as multifractal measure, fluctuation and correlation in the toppling surface, etc.; are defined in terms of S and they are analyzed numerically. All these properties are evaluated for all the three models, the BTW, the SSM and the RSM, and the results are compared at the suitable places.

4.1 Toppling number distribution

In this section, the toppling number S of individual sand column is first characterized by calculating the probability distribution function $P(S)$. $P(S)$ is the probability of finding a sand column having toppling number S and it is defined as

$$P(S) = \frac{n(S)}{a}, \tag{4.1}$$

where $n(S)$ is the number of sand columns that toppled S times and a is the area of an avalanche defined by the number of distinct lattice sites (sand columns) toppled. In Fig.4.1(a), $P(S)$s are plotted against S for the BTW, the SSM and the RSM. The distributions are found very different in different models. All of them decreasing with the increasing toppling number S and have different cut-off. The distribution of S then provides new information about the microscopic structure of the avalanches

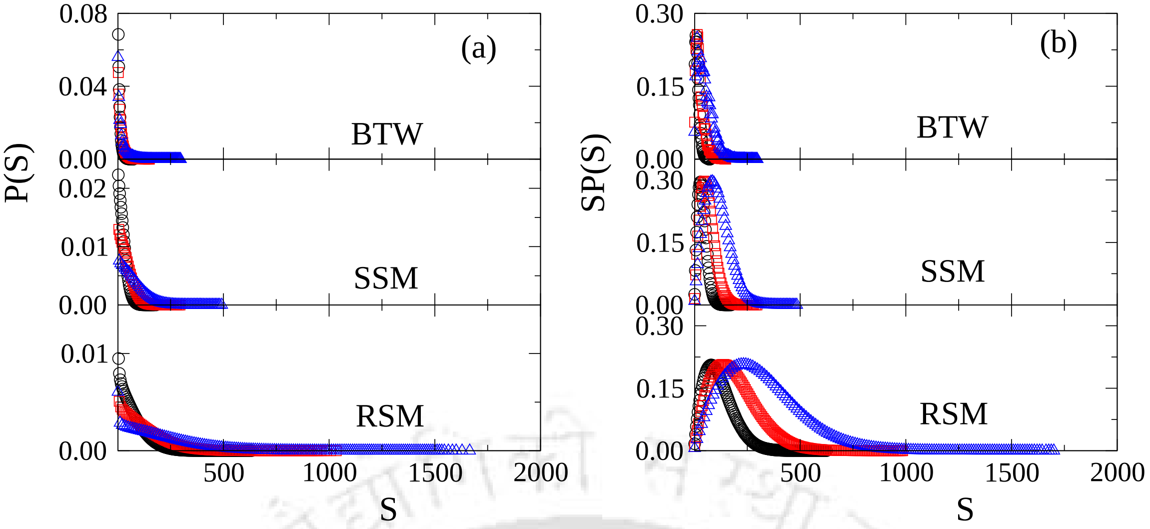

Figure 4.1: (a) Plot of $P(S)$ against S for the BTW, the SSM and the RSM for system of size $L = 512$ (○), $L = 1024$ (□) and $L = 2048$ (△). The distributions have different cutoffs for different system sizes. (b) Plot of $SP(S)$ against S for the BTW, the SSM and the RSM for the same set of system sizes with same symbol code. The distribution is similar to that of the Poisson distribution.

in different models. Note that, the distribution considered here is different from that of the total toppling number $s = \sum_i S_i$. The later is known to have a power law distribution in all three models as $P(s) \sim s^{-\tau_s}$ with $\tau_S = 1.293$ (BTW), 1.275 (SSM) and 1.224 (RSM)[47,75,113]. However, no power law decay of $P(S)$ is observed in the double logarithmic scale. Since the functional form of the distribution $P(S)$ is difficult to determine, the distribution of the first moment of toppling number $SP(S)$ is studied with S. In Fig.4.1(b), $SP(S)$s are plotted against S for the BTW, the SSM and the RSM for different system sizes L. The distributions are found Poissonian in nature in all three models. However, they have different height and width for different models for a given system size L. The cutoff in the distributions or the maximum toppling number S_{max} is largest in the RSM and it is smallest in the BTW. For the SSM, S_{max} is found between the RSM and the BTW. For a given model, the cutoff of the distributions depends on the system size L. The average S_{max} is expected to scale with L as

$$\langle S_{max} \rangle \sim L^{\theta} \tag{4.2}$$

where θ is an exponent. In Fig.4.2(a), $\langle S_{max} \rangle$ is plotted against L for the BTW, the SSM and the RSM. It can be seen that the scaling law assumed in Eq.4.2 is valid for all three models. The values of the exponent θ are obtained as 0.72 ± 0.02,

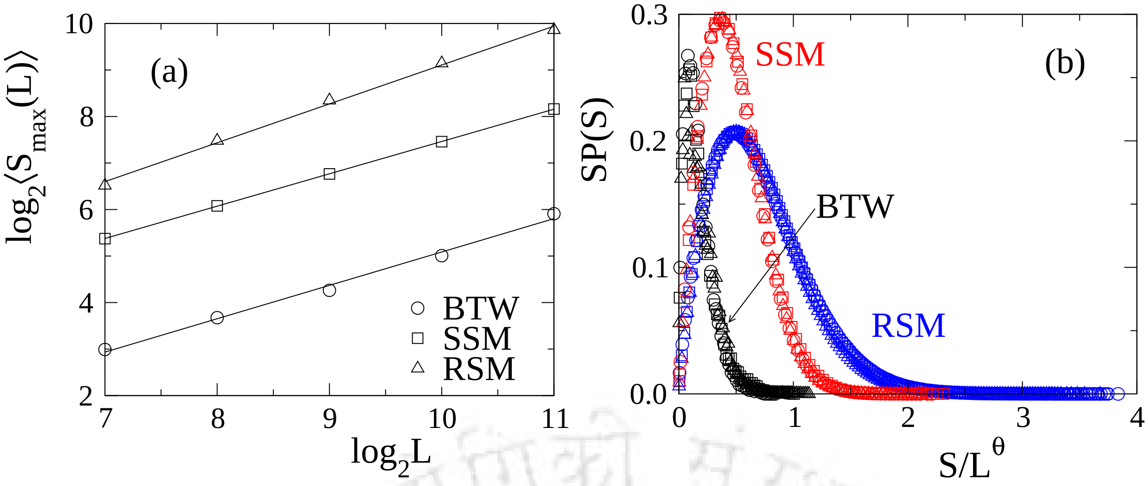

Figure 4.2: (a) Plot of $\langle S_{max}(L)\rangle$ against L for the BTW (○), the SSM (□) and the RSM (△). (b) Plot of $SP(S)$ against S/L^θ for the BTW, the SSM and the RSM for different system of sizes $L = 512$ (○), 1024 (□) and 2048 (△). For the the BTW, the SSM and the RSM a reasonable collapse of data is observed.

0.70 ± 0.02 and 0.82 ± 0.02 for the BTW, the SSM and the RSM respectively. For a given model, the distribution $SP(S)$ is also expected to scale with L as $\langle S_{max}\rangle$ scales with the system size. Hence a scaling form for $SP(S)$ can be assumed as

$$SP(S) = f(S/L^\theta). \tag{4.3}$$

In Fig.4.2(b), the probabilities $SP(S)$ are plotted against the scaled toppling number S/L^θ. A reasonable data collapse is observed for all the models with their respective values of θ. The distribution $SP(S)$ then scales with system size in these models and is found consistent with usual FSS characteristics of these models[73,113]. It is interesting to note that the individual toppling numbers in the BTW are also following the usual FSS ansatz but the total toppling size does not follow FSS ansatz[80,81]. It can be noted here that the individual toppling waves in the BTW also follow FSS[80]. The parameter S then can be considered as an useful microscopic parameter to quantify microscopic differences in different sandpile models.

4.2 Multifractal analysis

The concept of multifractal was originally introduced by Mandelbrot in the context of turbulence[125,160]. The concept was extended to other fields by Grassberger[149] Hentschel and Procaccia[161], Grassberger and Procaccia[162]. The distribution of currents in fractal resistor network was found to be multifractal in nature[163,164,165,166]. Meakin *et al.*[167,168] studied multifractal aspects of diffusion limited aggregation and related growth processes. In order to study multifractality of an object one needs to define a multifractal measure which is usually the distribution of a physical quantity on a geometrical support[145]. Having a suitable measure, one performs box counting analysis of different moments of the measure in order to estimate the variation of fractal dimension with the moments. In the following, a suitable multifractal measure will be defined for the sandpile avalanches and that would be analyzed to explore the multifractal aspects of them.

4.2.1 Toppling number density as multifractal measure

Spanning avalanche clusters are considered here as geometrical supports. A multifractal measure is defined in terms of the toppling number density distribution over a spanning avalanche cluster, the geometrical support. The toppling number density μ_i is defined as

$$\mu_i = \frac{S_i}{\sum_{i=1}^{L^2} S_i} \tag{4.4}$$

where $\sum_{i=1}^{L^2} S_i$ is the total toppling size s. Before going to investigate the multifractal aspects of μ_i, it would be interesting to look at the avalanche clusters in terms of μ_i. In Fig.4.3(a), the distribution of μ_i over the entire square lattice of size 128×128 is shown for the RSM with a continuous variation of colours. The white colour corresponds to the maximum of μ_i and the black colour corresponds to $\mu_i = 0$. In Fig.4.3(b) and (c), the distribution of μ_i on the same system size as that of the RSM is shown for the BTW and SSM respectively with the same colour code and compared with that of the RSM. The maximum value of μ_i is the largest in the case of RSM whereas it is the smallest for the BTW. It has an intermediate value for the SSM. In the RSM, there are several bright spots around which whirling of sand occurred. As a consequence, around a large toppling number smaller and smaller number of toppling happened during the avalanche. It is then possible to define different subsets of lattice sites, connected by nearest neighbour bonds, those of which toppled only once, only twice, only thrice, up to a maximum number of times of toppling occurred in that avalanche. An avalanche cluster then consists of several such subsets of lattice sites with specific number of toppling. Each of these subsets are found to be irregular with holes inside. A particular subset is found to appear randomly at many different places in an avalanche cluster. These subsets may have appeared at different stages of time evolution of the avalanche

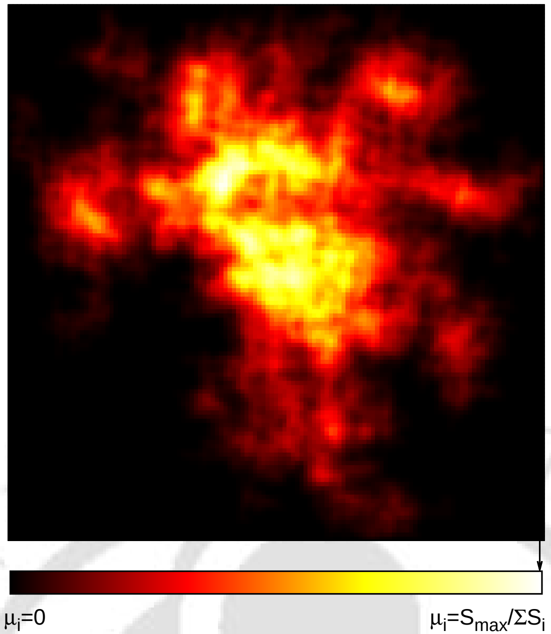

(a) RSM

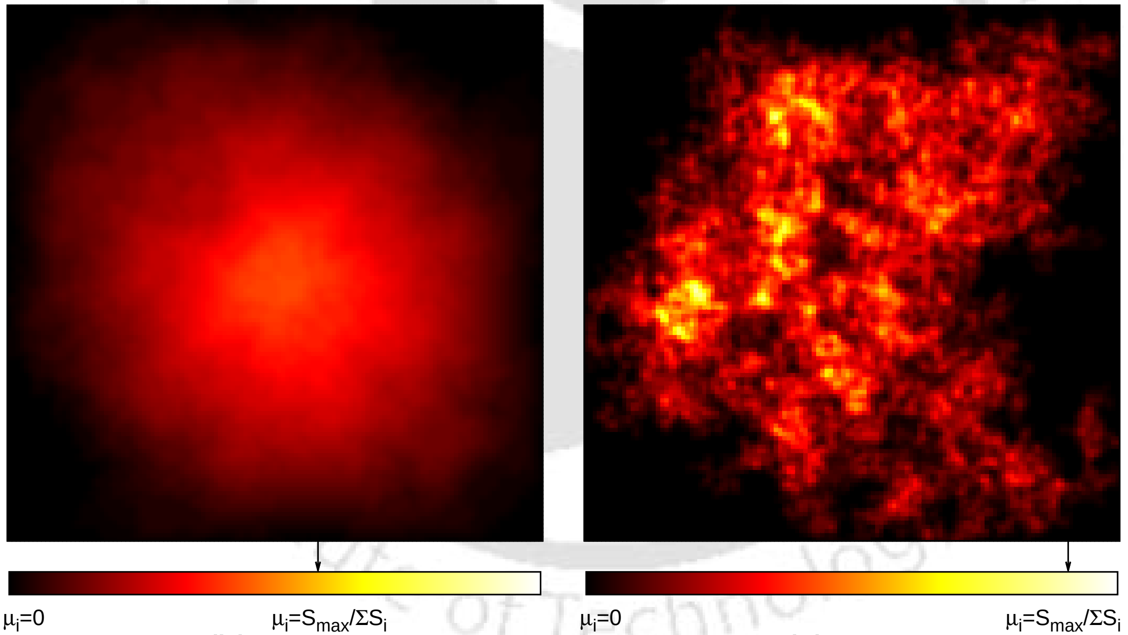

(b) BTW (c) SSM

Figure 4.3: Distribution of toppling number density on spanning avalanche clusters generated on a 128 × 128 square lattice for (a) the RSM, (b) the BTW and (c) the SSM are shown. The toppling numbers form ring like structure around a maximal toppling zone in the BTW, in the RSM it looks like random superposition of several BTW type structure and in the SSM several large toppling numbers are scattered randomly here and there.

cluster. A multiplicative cascade of these subsets is then formed in a complicated manner during the growth of the avalanche. This is very similar to the situation of mass distribution on a geometrical support generally considered for multifractal study[145]. The distribution of S_i over the lattice sites for the avalanche of the SSM also consists of several such subsets of lattice sites of toppling number one, two etc. These subsets are also found to be irregular with holes inside. Moreover, they are more randomly scattered over the lattice in comparison to the RSM. However, in the case of the BTW, the distribution of S_i over the lattice is found to have a single maximal region surrounded by lower and lower number of toppling. The subset of lattice sites consisting of specific toppling number is found to be circular rings of decreasing radii with increasing toppling number. The subsets are found to be regular and compact. As a consequence, the manifold of toppling numbers looks like a superposition of regular circular discs. Thus the μ_i distribution on the avalanche clusters of the RSM and the SSM have random manifolds whereas the same distribution for the BTW avalanche clusters have regular manifolds. It is therefore interesting to investigate the distribution of different moments of μ_i and perform a multifractal analysis for the avalanche clusters of these models. It is already known that the base of the avalanche cluster is compact and is characterized by a single fractal dimension $D_a = 2$, the capacity dimension of the avalanche area. Therefore, the multifractal measure considered here is distributed over a geometrical support of fractal dimension 2. In the following it will be demonstrated that only one fractal dimension is not sufficient to characterize the distribution of μ_i over such a geometrical support rather it requires a sequence of fractal dimensions to characterize the distribution.

4.2.2 Moment analysis

The dimensionality of a fractal object is characterized by the fractal dimension d_f which is defined as,

$$M(r) \sim r^{d_f} \tag{4.5}$$

where, $M(r)$ is the mass of the object with lateral extension r. The box-counting method is widely used to determine the fractal dimension of many physical systems[145,146,147,148,149,150,151,152,153,154,155,156] and will be employed here to determine the multifractal dimensions of measure μ_i. The box-counting algorithm is briefly discussed here taking an avalanche cluster of RSM on a 8×8 square lattice. In the box counting algorithm, the spanning avalanche cluster at the steady state is

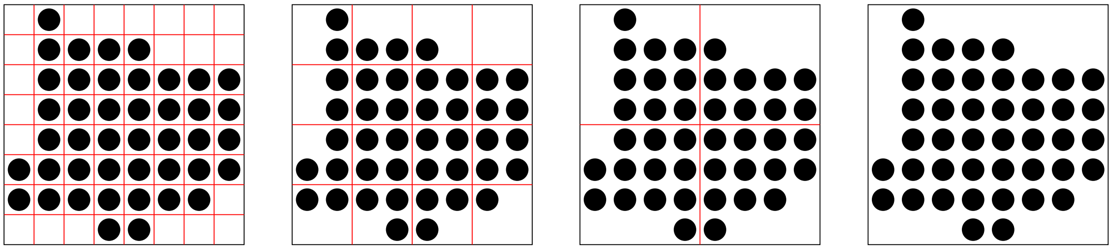

$\epsilon = 1$
$N_B(\epsilon) = 43$

$\epsilon = 2$
$N_B(\epsilon) = 15$

$\epsilon = 4$
$N_B(\epsilon) = 4$

$\epsilon = 8$
$N_B(\epsilon) = 1$

Figure 4.4: Demonstration of box counting method for the determination of fractal dimension. The black circles represent the occupied sites of a spanning cluster generated on a 8×8 square lattice. The lattice is divided into smaller boxes of linear size $\epsilon = 1$, 2, 4 and 8, as shown by red lines. Corresponding number of occupied boxes are $N_B(\epsilon) = 43$, 15, 4 and 1 respectively.

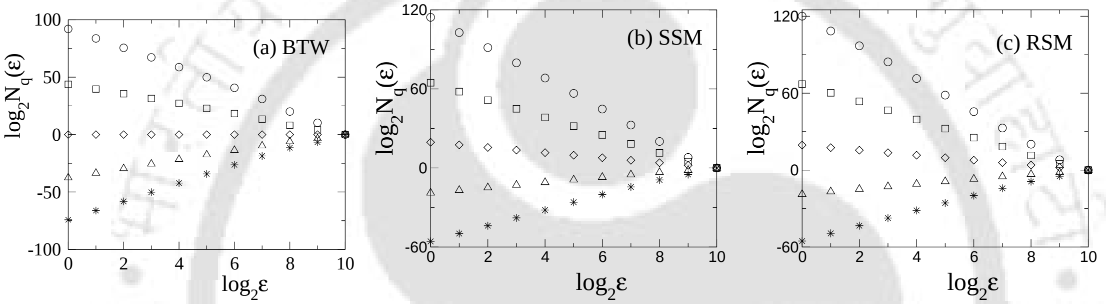

Figure 4.5: Plot of $N(q, \epsilon)$ versus ϵ for (a) the BTW, (b) the SSM and (c) the RSM for $q = -4$ (○), -2 (□), 0 (◇), 2 (△) and 4 (✻).

considered on a single large lattice. The $2d$ square lattice of linear size L, which contains the cluster, is then divided into $(L/\epsilon)^2$ number of smaller boxes of linear size ϵ. The number of boxes $N_B(\epsilon)$, which contain at least one occupied site of the cluster is then counted for a given box of dimension ϵ. The linear size ϵ of the box is then varied and the number of the occupied boxes $N_B(\epsilon)$ is counted as a function of the box size ϵ. The method is demonstrated in Fig.4.4 for a spanning avalanche cluster generated on a square lattice of size 8×8. The fractal dimension d_f can then be calculated using the scaling relation,

$$N_B(\epsilon) \sim \epsilon^{-d_f} \tag{4.6}$$

which is equivalent to the definition in Eq.4.5.

In order to obtain multifractal dimensions of μ_i, one needs to study the scaling of the q-moments of the measure over different length scales. Analysis has been made for $q = -5$ to $q = 15$ in steps of 0.01 for lattice size $L = 1024$. The lattice is divided into n_ϵ boxes of length ϵ as mentioned above and placed on the avalanche. To estimate the appropriate dimension of μ_i corresponding to the qth moment, the weighted number of box $N(q, \epsilon)$ is required to be determined. The weighted number of box is given by

$$N(q, \epsilon) = \sum_{j=1}^{n_\epsilon} \mu_j^q \quad \text{where} \quad \mu_j = \sum_{\epsilon} \mu_i. \tag{4.7}$$

The weighted number of box $N(q, \epsilon)$ is expected to scale with the box size ϵ as

$$N(q, \epsilon) \sim \epsilon^{-\tau(q)} \tag{4.8}$$

where $\tau(q)$ is called a "toppling exponent". Note that $\tau(0)$ is essentially the capacity dimension D_a of the avalanches. $N(q, \epsilon)$ is determined as a function of box size ϵ using box counting method, as described above, for a given q and it is studied against ϵ taking q as a parameter. In Fig.4.5, $N(q, \epsilon)$ for certain q values are plotted against ϵ in double logarithmic scale for all three models. A reasonable power law behaviour is observed for different q for all the models. A sequence of toppling exponents $\tau(q)$ has been determined from the slope of the plots for all three models. The toppling exponent $\tau(q)$ is plotted against q for BTW, RSM and SSM in Fig.4.6. A new set of toppling exponents $\tau(q)$ is obtained. The functional dependence of $\tau(q)$ on q is found linear for BTW whereas it is non-linear for SSM and RSM. Note that $\tau(1) = 0$ for all three models because the measure for all of them is normalized to 1. However, $\tau(0) \approx 2$ for all three models. The moment $q = 0$ of the measure corresponds to the lattice points which had toppled during the avalanche. Therefore, $\tau(0)$ corresponds to the base fractal dimension of the avalanches. The exponent $\tau(0)$ can be associated with the sandpile probability distribution exponents for the area. Since the area distribution is given by $P(a, L) = a^{-\tau_a} f(a/L^{D_a})$, $\tau(0)$ corresponds to the capacity dimension D_a. If the measure μ_i is characterized by a single fractal dimension D_a, the toppling exponent $\tau(q)$ should have a constant gap between two consecutive exponents and consequently should have a linear dependence on q. In that case, $\tau(q)$ can be written as

$$\tau(q) = -(q - 1)D_a. \tag{4.9}$$

Such a linear dependence of $\tau(q)$ on q is observed in the case of the BTW only and

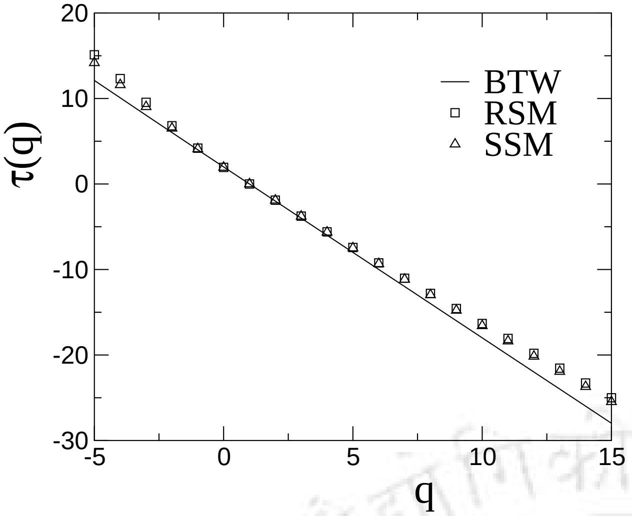

Figure 4.6: Plot of toppling exponent $\tau(q)$ versus q for the BTW (line), the SSM ($\triangle$) and the RSM ($\square$) for the system size $L = 1024$. $\tau(q)$ has linear dependence on q for the BTW whereas it has non-linear dependence on q for both the SSM and the RSM.

is represented by a solid line in Fig.4.6(a). Thus, the measure distribution in the BTW is monofractal which is contrary to the fact that the probability distributions in the BTW exhibit multifractal character[80,90]. For the RSM and the SSM, $\tau(q)$ has a nonlinear dependence on q. Thus, each moment of μ_i needs a new exponent to characterize the measure distribution and consequently the measure distributions in these models are multifractal. However, the probability distributions of avalanche sizes follow usual FSS rather than multiscaling in both the SSM and the RSM[81,113]. The monofractal nature in the BTW and multifractal nature in the RSM and the SSM of the same measure can be understood qualitatively in terms of the manifolds occurred in these models. In the case of BTW, the manifolds in the measure can be considered as a stack of regular compact discs with reducing radii as one goes from the bottom to the top. The regular compact discs will definitely have the same fractal dimensions at all level of manifold. On the other hand, in the case of the RSM and the SSM, these manifolds are irregular and random in nature. Random, irregular structures at different levels of manifold correspond to different fractal dimensions in these models. Different universality classes of the BTW, the RSM and the SSM are then merely a consequence of multifractal analysis of a suitable measure, μ_i the toppling number density, in this method.

4.2.3 $f(\alpha)$ spectrum

The associated fractal dimensions $f(\alpha)$ with the measure and the corresponding Lipschitz-Hölder exponent α are obtained through a Legendre transformation[145] of

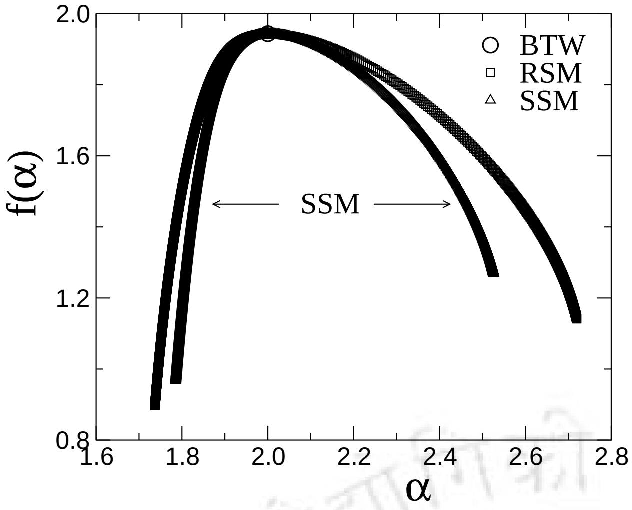

Figure 4.7: Plot of $f(\alpha)$ against α for the BTW (○), the SSM (△) and the RSM (□). Data of the BTW is represented by a single point whereas the SSM and the RSM are characterized by two different sets of fractal dimensions.

the toppling exponent sequence $\tau(q)$ given by

$$f(\alpha) = q\alpha(q) + \tau(q), \quad \alpha(q) = -d\tau(q)/dq. \tag{4.10}$$

The values of $f(\alpha)$ obtained for the system size $L = 1024$ are plotted against α in Fig.4.7. Since $\tau(q)$ follows a constant gap equation with q for the BTW, it is expected that $f(\alpha)$ versus α will be represented by a single point for this model. This is shown by an open circle in Fig.4.7. On the other hand, since $\tau(q)$ has nonlinear dependence on q for the RSM and the SSM, the spectra of $f(\alpha)$ against α are obtained for these models. In Fig.4.7, the squares represent $f(\alpha)$ for the RSM and the triangles represent the same for the SSM. A number of important features are to be noted. First, the maximum value of $f(\alpha)$ corresponds to $q = 0$ and it is obtained as ≈ 2 for all three models. The maximum value of $f(\alpha)$ then corresponds to the capacity dimension D_a of the avalanche clusters of the respective models (D_a is obtain little less than 2 as an artifact of box counting method). Since the whole spectrum has to be below $f(\alpha) = \alpha$, then α corresponding to the maximum $f(\alpha)$ is also equal to the capacity dimension D_a. Second, α_{min} corresponds to $q \to +\infty$ and α_{max} corresponds to $q \to -\infty$. Therefore, large toppling numbers will contribute toward α_{min} whereas small toppling numbers will contribute toward α_{max}[145]. The numerical values of α_{min} and α_{max} are obtained in the limit $f(\alpha) \to 0$. The finite size effect on the values of α_{min} and α_{max} has been verified by calculating $f(\alpha)$ spectrum for several lower system sizes than $L = 1024$ and it was found that the spectrum remains unaltered for both the models. It is observed that $\alpha_{min}(\text{SSM}) > \alpha_{min}(\text{RSM})$ and $\alpha_{max}(\text{SSM}) < \alpha_{max}(\text{RSM})$. $\alpha_{min}(\text{SSM})$ is higher because of the fact that the number of peaks appearing in the measure is much higher on the

SSM avalanche clusters than that of the RSM as it can be seen in Fig.4.3. On the other hand, α_{max}(SSM) is smaller than that of the RSM because of the fact that the number of smaller toppling numbers appearing in the measure is smaller on the SSM avalanche clusters than that of the RSM. Third, the values of $f(\alpha_{min})$ and $f(\alpha_{max})$ for the SSM are greater than those of the RSM. $f(\alpha_{max})$ corresponds to the fractal dimension of the region covered by small S_i and $f(\alpha_{min})$ correspond to that of the region covered by large S_i. In $q \to -\infty$ limit, the RSM will have ring like structure made up of mostly by the singly toppled sites and the fractal dimension would be close to one as it is observed. On the other hand, in the $q \to +\infty$ limit, lesser number of large S_i are expected in the RSM than in the SSM and consequently the corresponding fractal dimension would be small in the RSM in comparison to the SSM. Finally, it can be seen that the $f(\alpha)$ spectra for the RSM and the SSM are entirely different. The RSM and the SSM thus require different sets of fractal dimensions to characterize their respective toppling number density distributions. Thus, the density distribution in the BTW is monofractal whereas it corresponds to different multifractal distributions for the RSM and the SSM. The manifolds generated by the toppling waves then correspond to multifractal toppling distribution in the case of sandpile models with toppling imbalance and stochasticity. These observations not only represent a clear distinction of the universality classes of these models but also provide deep insight to the avalanche dynamics.

4.3 Multi-affinity of the toppling surfaces

The height of a surface can be defined by the z-coordinate of a set of points in 3 dimension. A surface is called self-affine if the heights of the surface obey the scaling given by

$$z(r) \approx \lambda^{-H} z(\lambda r) \tag{4.11}$$

where r is the position of a point, λ is a parameter and H is the Hurst exponent[99] of the surface. If the surface is self-affine, then it can be characterized by a single exponent H. However if the surface is multi-affine one requires a sequence of exponents to characterize it. For a sandpile avalanche a surface can be defined by the toppling numbers S_i of individual sand columns. Such a surface can be called a “toppling surface”. In this section the morphology of the toppling surfaces of all three sandpile models will be characterized performing height-height correlation and roughness study.

4.3.1 The toppling surface

A toppling surface corresponding to an avalanche is defined here in terms of the toppling number S_i at each lattice site. Typical toppling surfaces obtained in the BTW, the SSM and the RSM at their respective steady states are shown in Fig.4.8. These surfaces are generated on a 128×128 square lattice. Light brown colour represents higher toppling number whereas dark brown colour represents lower toppling number and the intensity is varied continuously. First of all it should be emphasized here that the toppling surface defined is very different from that of the sandpile surface defined in the earlier literature by the height of the sand columns $h(x)$[157,158,159]. This simple representation of an avalanche by a toppling surface in terms of S_i provides more insight to the structure of toppling occurred during the avalanche. As a first observation, it can be noticed that the structure of the toppling surfaces in three models are vividly different. Such details of toppling surface were not explored before except obtaining $2d$ morphology of avalanche clusters[47,75]. The BTW toppling surface has only one centrally located maximum toppling zone with concentric zones of lower and lower toppling numbers without intersection as already observed in $2d$[47,75]. The SSM toppling surface is highly fluctuating and rough. Several large toppling numbers appear randomly here and there. On the other hand, the RSM toppling surface is neither fully consisting of concentric zones as in BTW nor it is totally random as the SSM. The RSM toppling surface is less fluctuating than that of the SSM but consists of several BTW type structures around different maximal toppling zones. It is important to note that the local correlation in rotational constraint does not lead to long range correlation generating BTW like correlated structure.

In terms of interface, the toppling dynamics of the Oslo sandpile model was first mapped into avalanching interface by Paczuski and Boettcher[101] where the height profile of the interface is the accumulated number of topplings. In the context of absorbing state phase transition[84,92], sandpile models are also described as a growing interface defined by the toppling numbers upto certain time t in a disordered medium[93,94,95,96,97]. The toppling surface defined above may correspond to one of the final configuration of these growing interfaces in the absorbed state.

4.3.2 Roughness of toppling surfaces

Toppling surfaces can be characterized by studying the scaling of roughness or width $W(L)$ of the surface with the system size L. $W(L)$ of the toppling surface is defined

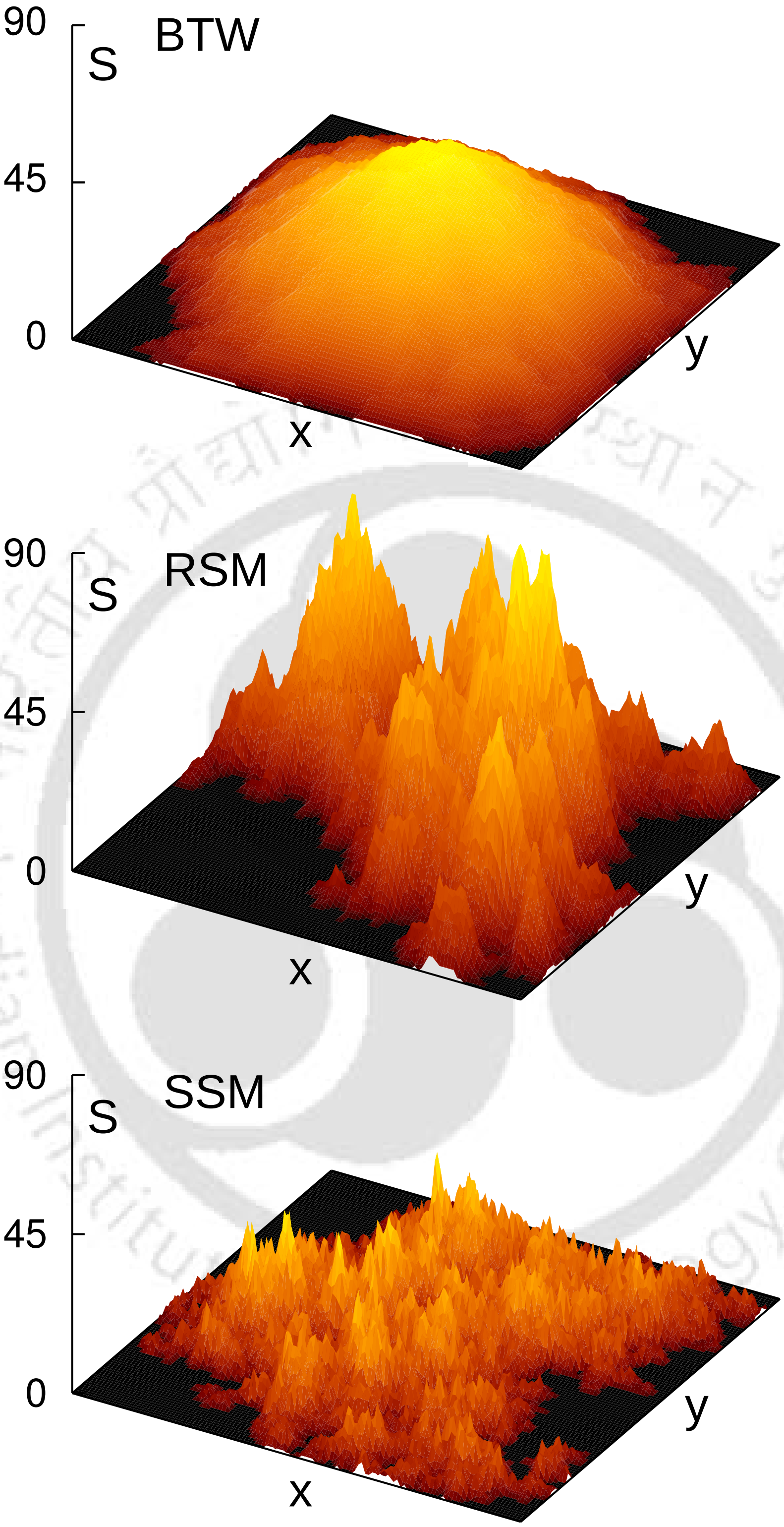

Figure 4.8: Toppling surfaces generated on a 128 × 128 square lattice for the BTW, the RSM and the SSM are shown. The toppling surface of the BTW is found smooth, in the SSM it is rough. In the RSM it looks like a collection of several BTW type toppling zones.

as

$$W^2(L) = \left\langle \frac{1}{L^2} \sum_{i=1}^{L^2} (S_i - \bar{S})^2 \right\rangle \tag{4.12}$$

where $\bar{S} = \sum_{i=1}^{L^2} S_i/L^2$ is the average height of the surface. The width $W(L)$ is expected to scale with the system size L as

$$W(L) \sim L^{\chi} \tag{4.13}$$

where χ is the roughness exponent, similar to that of the saturated width of the growing interfaces in the absorbing state phase transition[95,96]. The scaling of $W(L)$ of the toppling surfaces with L is shown in Fig.4.9 for all three models. It can be seen that the scaling given in Eq.4.13 is satisfied for all three models. The exponent χ is found as $\chi = 0.69 \pm 0.03$ for the BTW, 0.82 ± 0.03 for the RSM and 0.73 ± 0.03 for the SSM. It can be noted here that the value of χ obtained for the saturated width of the growing interfaces in the absorbing state phase transition for the Manna model is 0.80(3)[93]. It can be noted here that the values of χ and θ are almost equal for the BTW, the RSM and the SSM within error bars. The roughness exponent χ is known to be related to the exponents describing macroscopic quantity like toppling size $s = \sum_{i=1}^{L^2} S_i$. The toppling size distribution is given by $P(s, L) = s^{-\tau_s} f_s(s/L^{D_s})$ where τ_s is a critical exponent and D_s is the capacity dimension of avalanche size. Since the avalanche areas are compact having fractal dimension $D_a = 2$ and fluctuation in toppling numbers $W(L)$ scale with system size as $W(L) \sim L^{\chi}$, the sum of D_a and χ then give the capacity dimension if the avalanche size. As in the case of growing interfaces[95,96,101], a scaling relation

$$D_s = 2 + \chi \tag{4.14}$$

is then expected to be valid in the case of toppling surfaces. For RSM and SSM the values of D_s were known to be 2.86[113] and 2.74[73] respectively and thus the above scaling relation is satisfied for both the RSM and the SSM within the error bars. It can be noted that D_s obtained from the roughness exponent ($\chi \approx 0.8$) measured in Ref.[93] is slightly higher than the measured value for the Manna model.

4.3.3 Hurst exponent of the toppling surfaces

Wrinkle rough surfaces are usually characterized by the height difference correlation function or structure function $C(r)$. In the case of toppling surfaces, the toppling

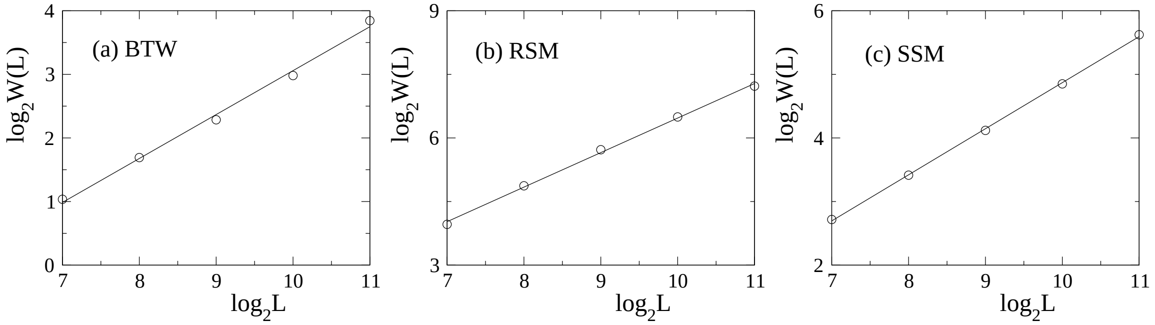

Figure 4.9: Plot of $W(L)$ against L for (a) the BTW, (b) the RSM and (c) the SSM. The straight lines are linear least square fitted lines. The values of χ for the BTW, the RSM and the SSM are obtained as $\chi = 0.69 \pm 0.03$, 0.82 ± 0.03 and 0.73 ± 0.03 respectively.

numbers are assumed to represent a self-affine function

$$S(r) \approx \lambda^{-H} S(\lambda r) \tag{4.15}$$

where λ is a parameter and H is the Hurst exponent[99] of the surface. The correlation between toppling numbers of two sand columns separated by a distance r is then given by

$$C(r) = \langle |S(r_0 + r) - S(r_0)|^2 \rangle \sim r^{2H} \tag{4.16}$$

where r_0 is a reference point and $S(r_0 + r)$ and $S(r_0)$ are the toppling numbers of the sand columns at $(r_0 + r)$ and r_0 respectively. The $\langle \cdots \rangle$ represents the ensemble average. The integrated correlation function $I(R)$ defined as

$$I(R) = \int_0^R C(r) dr \tag{4.17}$$

should scale as

$$I(R) \sim R^{1+2H}. \tag{4.18}$$

In Fig.4.10, the integrated correlation function $I(R)$ is plotted against distance R in double logarithmic scale for different systems of size L for the toppling surfaces of all three models. It can be seen that $I(R)$ follows a power law scaling with R for all L. It can be noted that $I(R)$ for different L are shifted upwards with increasing L for the RSM and the SSM. For different L, $I(R)$ scales with R in a similar fashion. The slopes of the power law scaling are obtained by least square fit to the data of largest linear region of each model for $L = 2048$ and they are found as $2.32 \pm 0.02, 1.70 \pm 0.02$ and 1.42 ± 0.02 for the BTW, the RSM and the SSM respectively and are shown using straight lines in Fig.4.10. The Hurst exponent

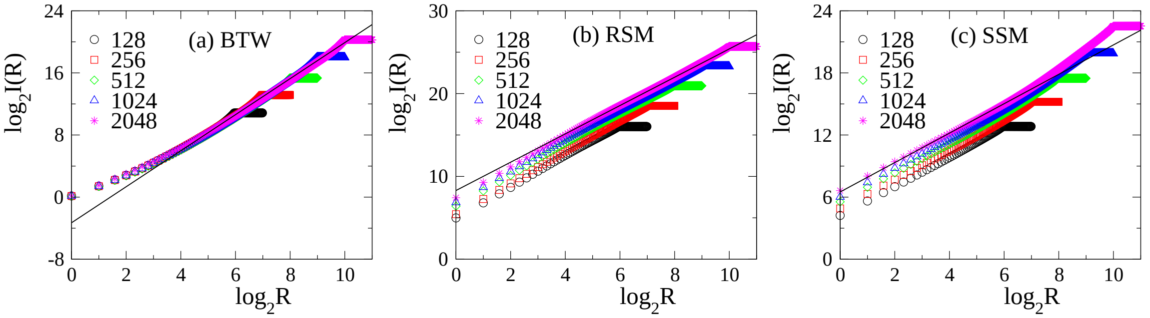

Figure 4.10: Plot of $I(R)$ against R for different systems of size $L = 128$ (○), 256 (□), 512 (◇), 1024 (△) and 2048 (✻) for (a) the BTW, (b) the RSM and (c) the SSM. The straight lines have slopes $2.32, 1.70$ and 1.42 for the BTW, the RSM and the SSM respectively. The values of the Hurst exponents are then $0.66, 0.35$ and 0.21 for the BTW, the RSM and the SSM respectively.

H is then obtained as $H = 0.21 \pm 0.02$ for the SSM, 0.35 ± 0.02 for the RSM and 0.66 ± 0.02 for the BTW[169]. The value of the Hurst exponent H ranges from 0 to 1. The values $H > 0.5$, $H = 0.5$, $H < 0.5$ correspond to correlated, uncorrelated and anti-correlated Brownian functions respectively[99]. Since the Hurst exponents for the RSM and the SSM are below 0.5, their toppling surfaces are self-affine and anti-correlated surfaces with different Hurst exponents. On the other hand, the BTW toppling surface is expected to be smooth and less fluctuating. Consequently, the Hurst exponent of the BTW toppling surface is found greater than 0.5 corresponding to a correlated surface. It can be noted that time auto-correlation of toppling waves also suggested that the BTW exhibits correlation in the toppling sequence whereas the SSM and the RSM exhibit anti-correlation in the toppling sequence[82,89,90,91,113]. The values of the Hurst exponents of these models are clearly different and once again confirm different universality classes of the BTW, the SSM and the RSM.

The Hurst exponent of the toppling surface can also be estimated by obtaining the power spectrum of the toppling surface

$$S(\mathbf{k}) = \langle \left|\tilde{S}(\mathbf{k})\right|^2 \rangle \tag{4.19}$$

in terms of the Fourier transformed toppling number

$$\tilde{S}(\mathbf{k}) = \int S(\mathbf{r}) e^{-i\mathbf{k}\cdot\mathbf{r}} d^2\mathbf{r}. \tag{4.20}$$

The toppling number correlation function $C(\mathbf{r})$ can now be obtained in terms of the

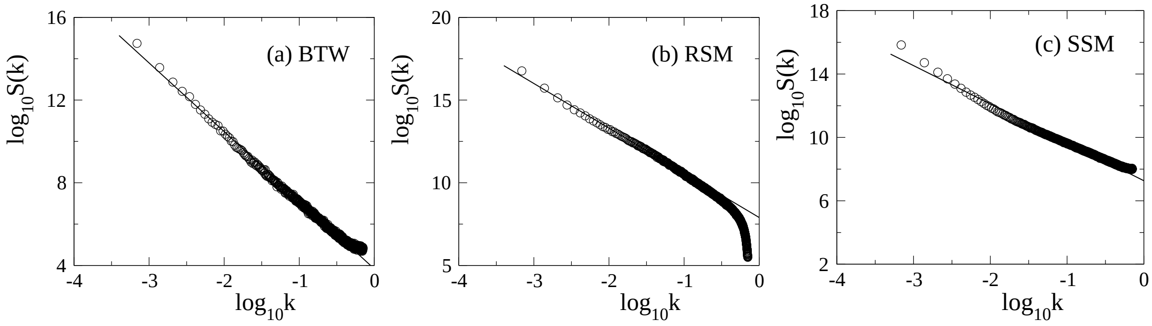

Figure 4.11: Power spectral density $S(k)$ against wave number k for toppling surfaces of (a) the BTW, (b) the RSM and (c) the SSM for a system of size $L = 2048$.

power spectrum as

$$C(\mathbf{r}) = 2\int d^2\mathbf{k}S(\mathbf{k})[1-\cos(\mathbf{k}\cdot\mathbf{r})] \tag{4.21}$$

replacing $S(\mathbf{r})$ in Eq.4.16 by its inverse Fourier transform. Since $C(\mathbf{r})$ is linearly related to $S(\mathbf{k})$, one may obtain a scaling of $S(\mathbf{k})$ with $\mathbf{k}$ as

$$S(\mathbf{k}) \sim |\mathbf{k}|^{-2(1+H)}. \tag{4.22}$$

In Fig.4.11, the power spectrum $S(\mathbf{k})$ is plotted against $\mathbf{k}$ in double logarithmic scale for a system size $L = 2048$ for all three models. The slope of the distributions are obtained from linear least square fit to the data points. The Hurst exponents are determined from the slope of the distributions as: $H(\text{BTW}) = 0.66 \pm 0.01$, $H(\text{RSM}) = 0.35 \pm 0.01$ and $H(\text{SSM}) = 0.21 \pm 0.01$ and are found consistent with the values of the Hurst exponents obtained from the direct measurement of $I(R)$ as a function of R.

It would now be interesting to obtain the critical exponents describing the macroscopic avalanche properties such as toppling size in terms of H. In order to obtain the macroscopic exponents in terms of H, one needs to relate H and χ. A relation between χ and H can be obtained by calculating the width $W(L)$ of the toppling surface in terms of the toppling number correlation function $C_L(r)$, where $C_L(r)$ is the correlation function obtained for a given system size L. The scaling of $C_L(r)$ can be assumed as

$$C_L(r) = A(L)r^{2H} \tag{4.23}$$

where $A(L)$ is a system size dependent prefactor. In order to determine the prefactor $A(L)$ as a function of L, the integrated correlation function I_L is calculated and is

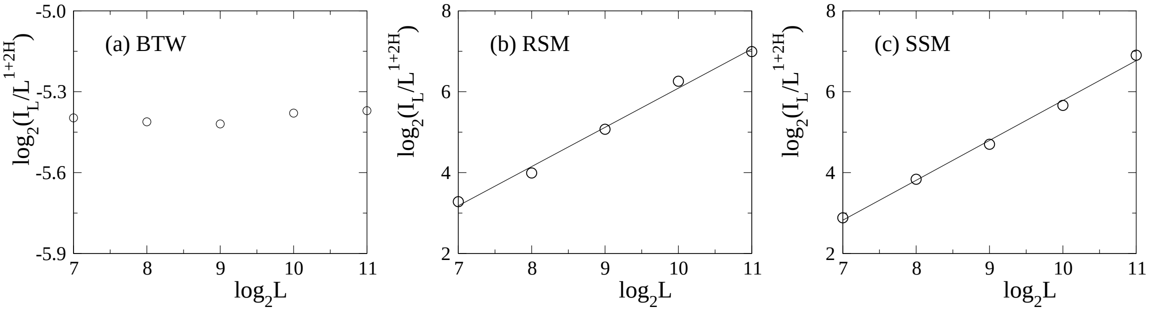

Figure 4.12: Plot of I_L/L^{1+2H} against L for (a) the BTW, (b) the RSM and (c) the SSM. It can be seen that for the BTW, $A(L)$ is independent of system size L whereas $A(L) \sim L$ for the RSM and the SSM.

given by

$$I_L = \int_0^L C_L(r)dr = A(L)L^{1+2H}. \tag{4.24}$$

The values of I_L correspond to the saturated value of $I(R)$ at $R = L$ for different system size L. Hence, the prefactor is given by $A(L) = I_L/L^{1+2H}$. In Fig.4.12 $A(L)$ is plotted against L for the BTW, the RSM and the SSM. It can be seen that $A(L)$ remains independent of L in the case of BTW. However, for the RSM and the SSM, $A(L)$ increases with L and is not a constant prefactor. From the linear least square fitting of the data points of the RSM and the SSM, it is observed that $A(L) \sim L$.

The square of the width of the toppling surface $W^2(L)$ for a system of size L is then given by

$$W^2(L) = \frac{1}{L^2}\int_0^L rC_L(r)dr = \frac{A(L)}{L^2}L^{2+2H}. \tag{4.25}$$

Since $A(L)$ is independent of L for the BTW, $W^2(L) \sim L^{2H}$. Therefore, $\chi = H$ for the BTW surface. The numerical values of $\chi = 0.69$ and $H = 0.66$ are found equal within error bars. Roughness of the BTW surfaces then follow the usual Family-Vicsek scaling[98]. However for the RSM and the SSM, $A(L) \sim L$ and consequently $W^2(L) \sim L^{1+2H}$. Hence, the roughness exponent

$$\chi = 1/2 + H \quad \text{or} \quad H = \chi - 1/2 \tag{4.26}$$

for the RSM and the SSM. Since the values of H are 0.35 for the RSM and 0.21 for the SSM, one has $\chi = 0.85$ and 0.71 for these models respectively. It can be noted that these values are close to the measured values 0.82 and 0.73 respectively for the RSM and the SSM. The capacity dimension then can be obtained as $D_s = 2+\chi = 5/2+H$. The values of D_s obtained from the Hurst exponent, $D_s = 2.85$ and 2.71 for the RSM and the SSM respectively, are very close to the measured values of D_s (2.86 and 2.74) of the respective models. Note that the surface roughness is not following the usual Family-Vicsek scaling[98] rather it is following an anomalous scaling[170,171]. Such an anomalous scaling is resulted here due to the system size dependent correlation function $C_L(r)$ as given in Ref.[172]. Anomalous scaling of Hurst exponent was also observed in the cases of growing interfaces in random media and self-affine fracture surfaces[173,174,175,176,177].

4.3.4 Multi-affinity

The toppling number correlation function $C(r)$ alone can not characterize an ensemble of self-affine surfaces. In principle, it requires proper scaling of qth moments of toppling number difference $\delta S_q(r) = |S(r_0 + r) - S(r)|^q$ through the qth order correlation function

$$C_q(r) = \langle \delta S_q(r) \rangle \sim r^{H_q}. \tag{4.27}$$

If the scaling exponent H_q is found to be a linear function of q as $H_q = qH$, the ensemble of surfaces are called simple self-affine surfaces. On the other hand, if H_q becomes a non-linear function of the moment q, the surfaces are termed as multi-affine. In Fig.4.13(a), $C_q(r)$ for toppling surfaces of RSM is plotted against distance r in double logarithmic scale for a system of size $L = 2048$ for $q = 1, 2, 3, 4$ and 5. It can be seen that $C_q(r)$ follows a power law scaling with r for all q. The values of H_q are calculated from least square fitting to the linear region of the data points. The values of H_q for the RSM is plotted against q in Fig.4.13(b) and are compared with that of the BTW and the SSM. It can be seen that H_q increases linearly with q and the gap between the two consecutive values of H_q are found q independent for the BTW. On the other hand H_q has a non-linear behaviour with q for both the RSM and the SSM and the gap between the two consecutive values of H_q depend on q. The values of H_q are found to be a quadratic function of q as

$$H_q = qH - \Phi q^2. \tag{4.28}$$

The solid lines in Fig.4.13(b) represents the Eq.4.28 corresponding to the RSM and the SSM. The values of Φ for the RSM and and the SSM were found approximately 6×10^{-3} and 4×10^{-3} respectively. The RSM and the SSM toppling surfaces thus require different sequence of roughness exponents to characterize them. Consequently, they are multi-affine surfaces unlike the toppling surfaces of the BTW[169].

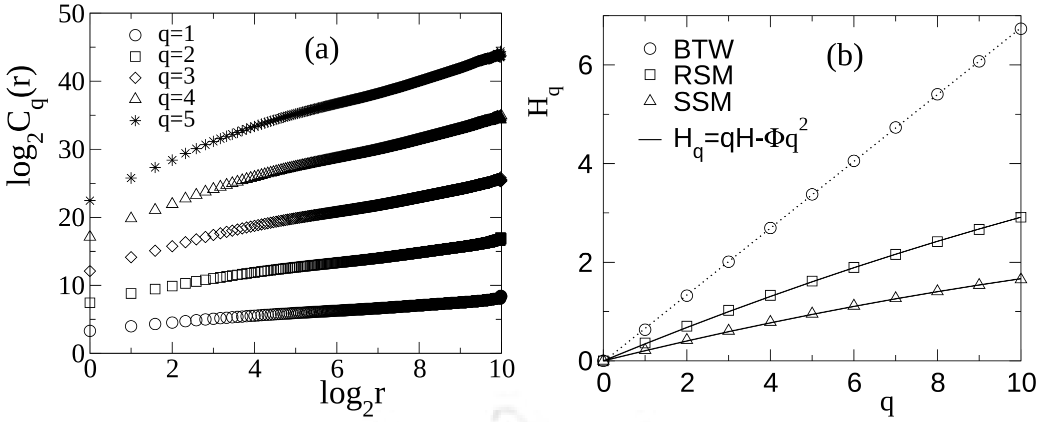

Figure 4.13: (*a*) Plot of $C_q(r)$ for the RSM against r for different moments q with symbols: (○) for $q = 1$, (□) for $q = 2$, (⋄) for $q = 3$, (△) for $q = 4$ and (✻) for $q = 5$. (*b*) Plot of H_q against the moment q for the BTW (∘), the SSM (△) and the RSM (□). Data for the RSM and the SSM are fitted with equation $H_q = qH - \Phi q^2$ and are represented by the solid lines. The values of Φ are 6×10^{-3} and 4×10^{-3} for the RSM and the SSM respectively. The dotted line represents the linear behaviour of H_q with q.

The multi-affinity of these toppling surfaces can also be verified by studying the scaling function form of the probability distribution $P[\delta S_q(r)]$ for different fixed values of r. The qth order correlation function $C_q(r)$ can be written in terms of $P[\delta S_q(r)]$ as

$$C_q(r) = \int \delta S_q(r) P[\delta S_q(r)] d(\delta S_q(r)). \tag{4.29}$$

$P[\delta S_q(r)]$ is expected to have the scaling form given by

$$P[\delta S_q(r)] = r^{-H_q} \mathsf{f}_\mathsf{q}[\delta S_q(r)/r_q^H]. \tag{4.30}$$

Since $C_q(r) \sim r^{H_q}$ and H_q is a non-linear function of q for multi-affine surfaces, the probability distribution $P[\delta S_q(r)]$ for different length scale r will collapse onto a single curve by a rescaling of the length scales with the exponent H_q. The distributions of $\delta S_q(r)$ for different r are calculated for 10^9 pair of lattice sites for the surfaces generated on a square lattice of size $L = 2048$ for all three models. In Fig.4.14, the scaled distributions $P[\delta S_q(r)] r_q^H$ are plotted against the scaled variable $\delta S_q(r)/r_q^H$ for different r values for all three models for $q = 1, 2$ and 3. There are two things to observe. First, there is reasonable data collapse for all q for all the models. This indicates that the probability distribution function $P[\delta S_q(r)]$ can be scaled by the exponents H_q. Second, the scaling functions $\mathsf{f}_\mathsf{q}[\delta S_q(r)/r_q^H]$ of the probability distribution $P[\delta S_q(r)]$ are found to be different for different q for the RSM and the SSM, whereas they are almost same for different q for the BTW. Moreover the scaling

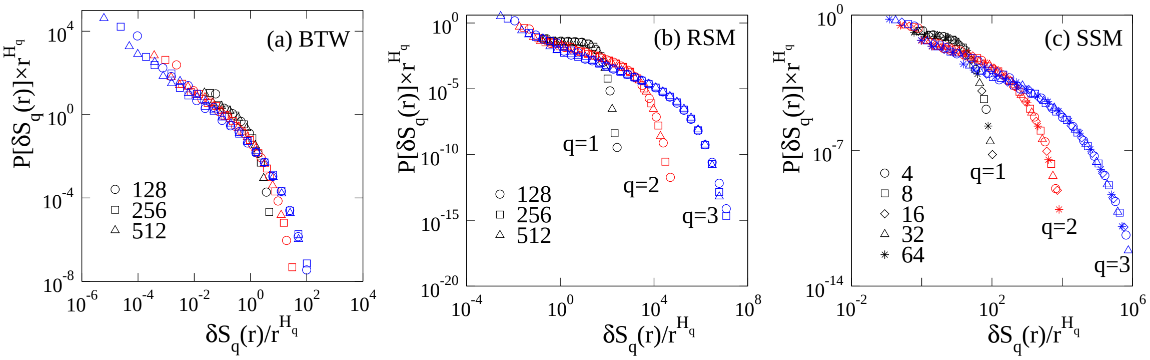

Figure 4.14: Plot of scaled distributions $P[\delta S_q(r)]r_q^H$ against the scaled variable $\delta S_q(r)/r_q^H$ for different r values for $q = 1$(black), 2(red) and 3(blue) for (a) the BTW, (b) the RSM and (c) the SSM. The surfaces considered here are generated on system of $L = 2048$. A reasonable collapse is observed for all three models and for all three q values.

functions for a given q are also different for all three models. This means that not only the whole sequence of H_q is different for the BTW, the RSM and the SSM but also the scaling functions associated with the distribution of $\delta S_q(r)$ are different. This clearly indicates the different universality classes of these models.

4.4 Conclusion

Avalanche cluster properties of the BTW, the RSM and the SSM at their respective non-equilibrium steady states are characterized by introducing a microscopic avalanche parameter S_i, the toppling number of an individual sand column. Different physical quantities such as probability distribution of S_i, multifractality of toppling number density μ_i, roughness and correlation in toppling surface are defined. Multifractal analysis of μ_i reveals that the distribution of μ_i over the avalanche cluster can be characterized by a single fractal dimension for the BTW whereas it requires a spectrum of multifractal dimensions to characterize it in the case of the RSM and the SSM. Toppling surfaces defined by the S_is are found vividly different for the BTW, the RSM and the SSM. These surfaces are found self-affine with distinctly different Hurst exponents. Moreover, the toppling surfaces of the RSM and the SSM are also found to be not only self-affine but also multi-affine in nature. Analysis of avalanche clusters in terms of the microscopic avalanche parameter S_i reveals a rich phenomenology and provides deep understanding of the avalanche properties. A set of new critical exponents and scaling relations are obtained which are able to demonstrate the scaling behaviour of the above properties distinctly in different models.

Chapter 5

Flooding transition in the toppling surface

Percolation is a continuous geometric phase transition where the system undergoes a transition from global disconnectivity to a global connectivity at a sharply defined occupation probability of the lattice sites[42,178,179,180]. Percolation process is well studied and well documented in the literature. It has a wide range of applications in a variety of physical systems such as, oil recovery from porous media[181,182], epidemics[183], networks[184,185], fragmentation[186], conductivity of DNA[187] etc. The study of percolation process in the topography of synthetically generated self-affine surfaces[188,189,190,191,192] revealed a new type of continuous phase transition with no sharply defined critical point. The technique has recently been applied to characterize fluid flow and conduction in rough surfaces[193], X-ray tomography[194], metal oxide surfaces[195], etc.

In the previous chapter, it was observed that the toppling surfaces associated with the avalanches in the RSM[113] and the SSM[50] sandpile models are rough, wrinkled and self-affine with $H < 0.5$ whereas that of the deterministic BTW sandpile model[4,114] was found to be a smooth correlated surface with $H > 0.5$[169]. In search of further in-depth information hidden in a sandpile avalanche, the toppling surface can be flooded with a liquid, say water, and flooding transition through the topography of toppling surfaces can be studied. During flooding, at each level of water, the surface points whose heights are grater than the water level form islands. If the water level is high, there will be a few small islands whereas if the water level is low there will be a few small lakes. It is then expected that there exists a critical height at which for the first time water will be able to flood the landscape from one side to the other creating a large number of islands. This is called flooding transition.

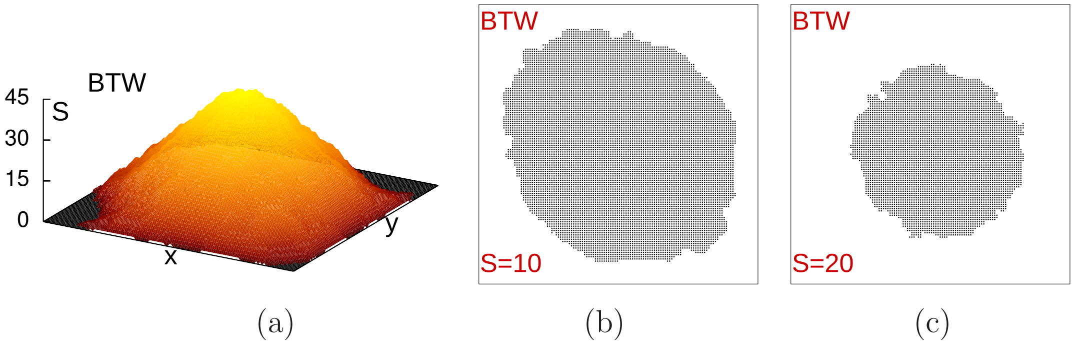

(a) (b) (c)

Figure 5.1: (a) The BTW toppling surface generated on a 128 × 128 square lattice. Islands obtained at different levels of flooding: (b) $S = 10$ and (c) $S = 20$ for the BTW. The black dots represent the islands and water is represented by white. At every level of flooding only one island can be extracted and hence no flooding transition is observed.

However, such a transition is not possible in the smooth toppling surface of BTW sandpile model where at every level of flooding only one island can be extracted as it is demonstrated in Fig.5.1. It is then intriguing to characterize the flooding transition in the toppling surface topography of the stochastic sandpile models RSM and the SSM.

5.1 Flooding transition in the toppling surface

The flooding transition is studied in the topography of toppling surfaces of sandpile models of two different classes, the RSM[113] and the SSM[50]. Toppling surfaces of the RSM and the SSM are shown in the upper panel of Fig.5.2. For studying the flooding transition, these surfaces are flooded with a liquid, say water. At each level of water, the surface points whose heights are grater than the water level form islands. Points belonging to the same island are connected by nearest neighbor bonds. In Fig.5.2, the island morphologies at three different levels of flooding are shown below the respective toppling surfaces. It can be seen that if the water level is high, there appears a few small islands whereas if the water level is low a large island appears covering most of the space of the lattice. At an intermediate level of flooding, there exists a critical height S_c (25 for the RSM and 10 for the SSM) at which a maximum number of islands appear. Below S_c, water is confined locally whereas above S_c water is found to be connected from all sides, flooding the surface for the first time. It is then interesting to study the properties of these islands at the critical transition and verify whether there exits another continuous phase transition through the toppling surface topography which were yielded at the steady

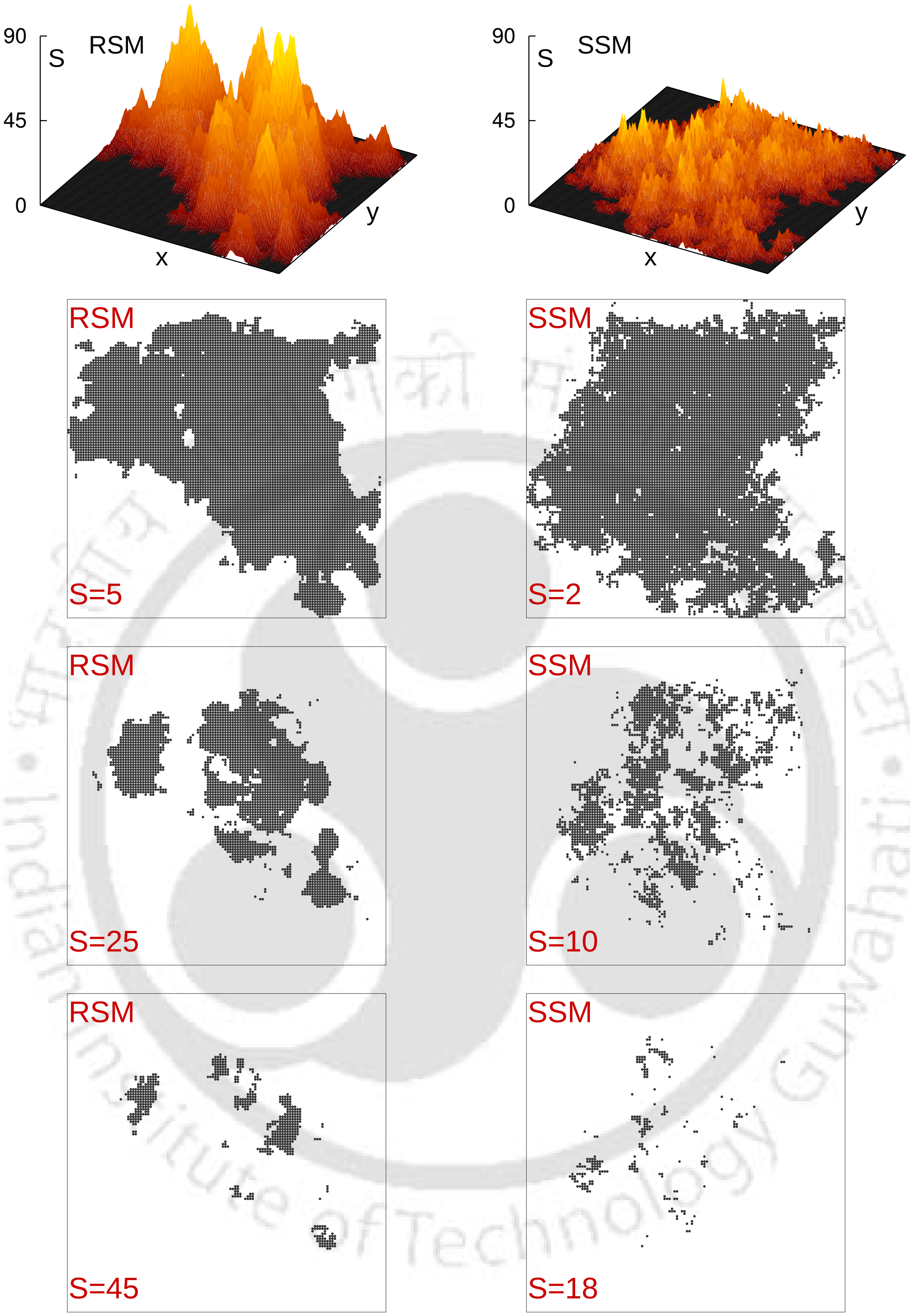

Figure 5.2: Toppling surfaces generated on a 128 × 128 square lattice for the RSM and the SSM are shown on the top. Islands are shown for three different levels of flooding: $S = 5, 25,$ & 45 for the RSM and $S = 2, 10$ & 18 for the SSM. The black dots represent the islands and water is represented by white. Flooding transition occurs at the intermediate level of flooding.

state of the respective dynamical models. Moreover, it is intriguing to see whether flooding transition could shine light on the origin of different universality classes of two stochastic sandpile models.

In order to study the flooding transition, extensive computer simulations are performed on the $2d$ square lattices of different sizes L. The system size L varies form 128 to 2048 in multiple of 2. 10^3 toppling surfaces were generated from the spanning (touching opposite sides of the lattice) avalanche clusters obtained at the steady states of the RSM and the SSM for each system size L. The toppling surfaces are then flooded at every height of the surface. At each level of flooding the number of islands appeared is counted and their areas (number of lattice points present in an island) are recorded.

5.2 Flooding threshold

In case of percolation (or generally in continuous phase transitions), the transition occurs at a sharply defined percolation threshold p_c at which the system percolates for the first time if the occupation probability is increased from below p_c[178]. In the flooding transition, the flooding threshold corresponds to the critical height S_c at which maximum number of islands appear. In the case of flooding transition, a wide distribution of the critical height S_c is observed for both RSM and SSM. In Figs.5.3(a) and 5.3(b), distributions of the critical heights S_c are plotted for different lattice sizes for the toppling surface of the RSM and the SSM respectively. It can be noticed that the width of the distribution of S_c is increasing with the system size L for both models in contrary to the observation in usual second order phase transition in which one expects a sharper and sharper distribution with increasing system size. As a consequence, in the $L \to \infty$ limit, there will be critical flooding at all possible heights.

The critical height for flooding is expected to be directly related to the width $W(L)$ of the toppling surface which scales with L as

$$W(L) \sim L^{\chi} \tag{5.1}$$

where χ is the roughness exponent. The exponent χ was found approximately $\chi = 0.82$ for the RSM and 0.73 for the SSM as mentioned in Chapter 4. It is then expected that the critical height S_c should scale with the system size as L^{χ}. Since the probability of appearing a critical height decreases with increasing system size,

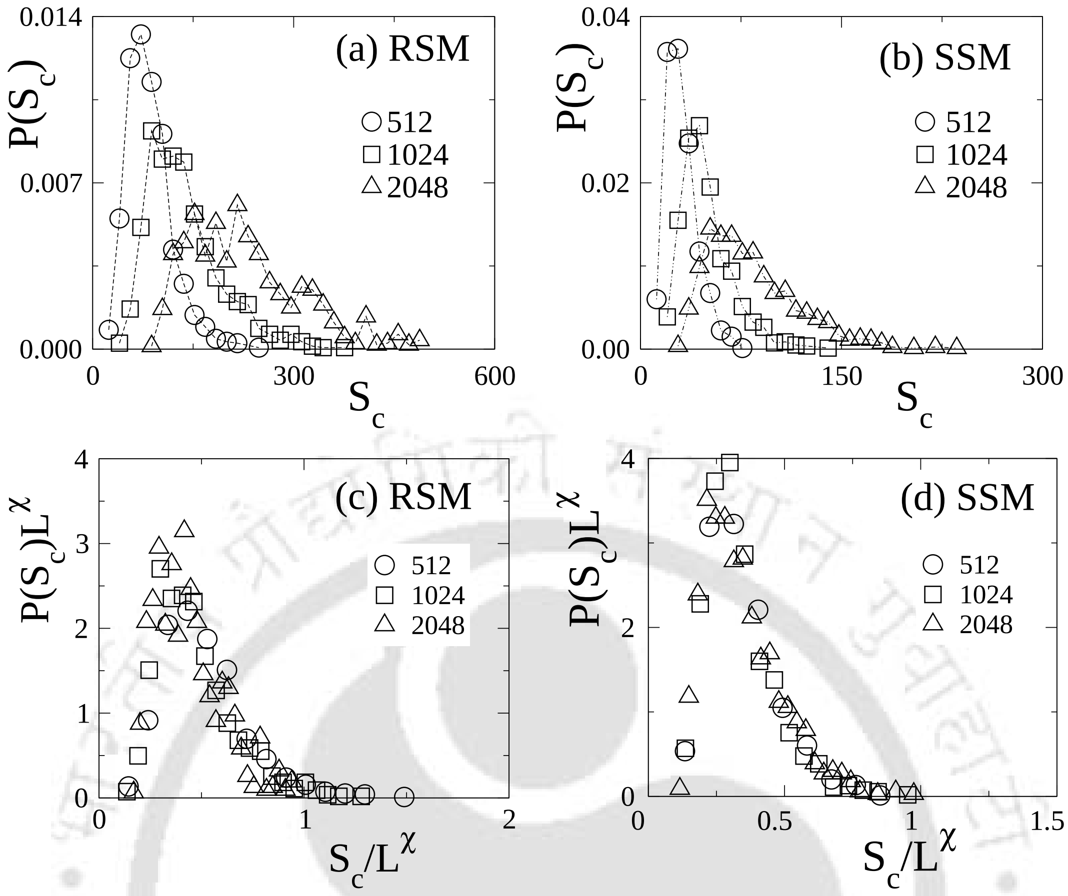

Figure 5.3: Plot of $P(S_c)$ against S_c for the toppling surface of (a) the RSM and (b) the SSM for system sizes $L = 512$ ($\bigcirc$), 1024 ($\Box$) and 2048 ($\triangle$). $P(S_c)L^{\chi}$ is plotted against S_c/L^{χ} for (c) the RSM and (d) the SSM. A reasonable collapse is observed for both the RSM and the SSM.

$P(S_c)$ is assumed to scale with the system size as $L^{-\chi}$. The scaled distribution $P(S_c)L^{\chi}$ is plotted against the scaled variable S_c/L^{χ} in Figs.5.3 (c) and (d) for the RSM and the SSM respectively. For both the RSM and the SSM a reasonable collapse of data is obtained taking $\chi = 0.82$ and 0.73 respectively.

The flooding threshold can also be identified in terms of area fraction p, the ratio of the total island area to L^2, as in percolation. The area fraction corresponding to the critical height is taken as the critical area fraction p_c. It is observed that the critical area fraction p_c also has a wide distribution $P(p_c)$ as shown in the Figs.5.4(a) and (b) for the RSM and the SSM respectively. Note that the width of $P(p_c)$ is almost independent of L as it is seen for the scaled distribution $P(S_c)L^{\chi}$ against the scaled variable S_c/L^{χ} in Figs.5.3(c) and (d). The existence of finite variance in the threshold distribution in the limit $L \to \infty$ was also observed in the contour cuts of

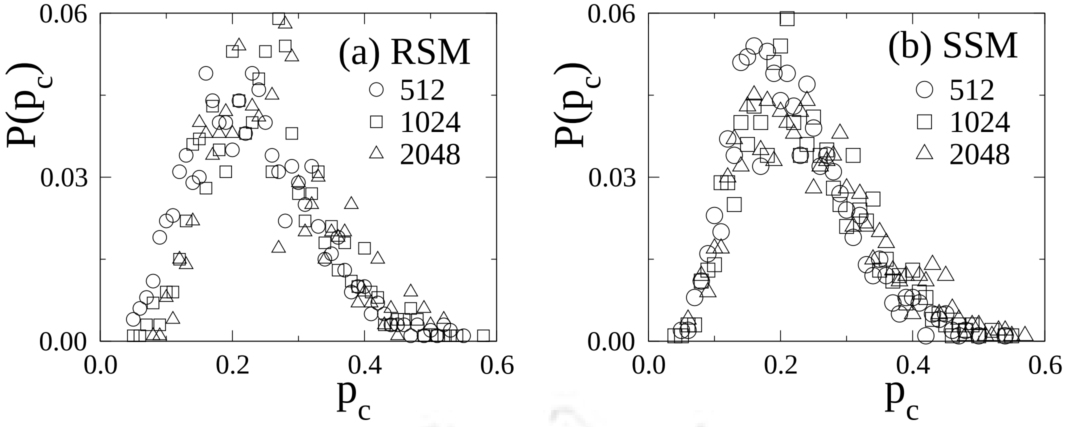

Figure 5.4: Plot of $P(p_c)$ against the critical area fraction p_c for the toppling surface of (a) the RSM and (b) the SSM for system sizes $L = 512$ (○), 1024 (□) and 2048 (△).

self-affine wrinkled surfaces[189,190].

Since there is a wide distribution of critical heights for an ensemble of toppling surfaces, the critical point or the flooding threshold is defined as $\Delta S = S - S_c = 0$ for each surface. Data is collected for the same value of ΔS of different surfaces and averaging of a physical quantity is made corresponding to the same ΔS value. In terms of area fraction, one may define the critical point as $\Delta p = p - p_c = 0$. Though the distribution of critical heights in RSM and SSM are different, the critical points of these models are defined identically at $\Delta S = 0$ (or $\Delta p = 0$). The parameter ΔS can be considered as change in the external field in the system with respect to the critical field.

5.3 Order parameter

In order to identify the order parameter of the flooding transition, one needs to define a spanning island connecting opposite sides of a lattice as in percolation theory. In this transition, such a spanning island appears only at the zero level of flooding. However, there exists a critical flooding level S_c at which maximum number of islands appear. Therefore, a concept of "critical spanning island" is defined as the largest island $a_{max}(S_c)$ present at the criticality for a given surface. Since for the ensemble of surfaces, the critical point is define by $\Delta S = 0$, the area of the critical spanning island for the ensemble of surfaces is taken as the $\langle a_{max}(S_c)\rangle$, where $\langle \cdots \rangle$ represents the ensemble average. The order parameter P_∞ then can be defined as the probability to find a surface point in an island of area $a \geq \langle a_{max}(S_c)\rangle$ at a given

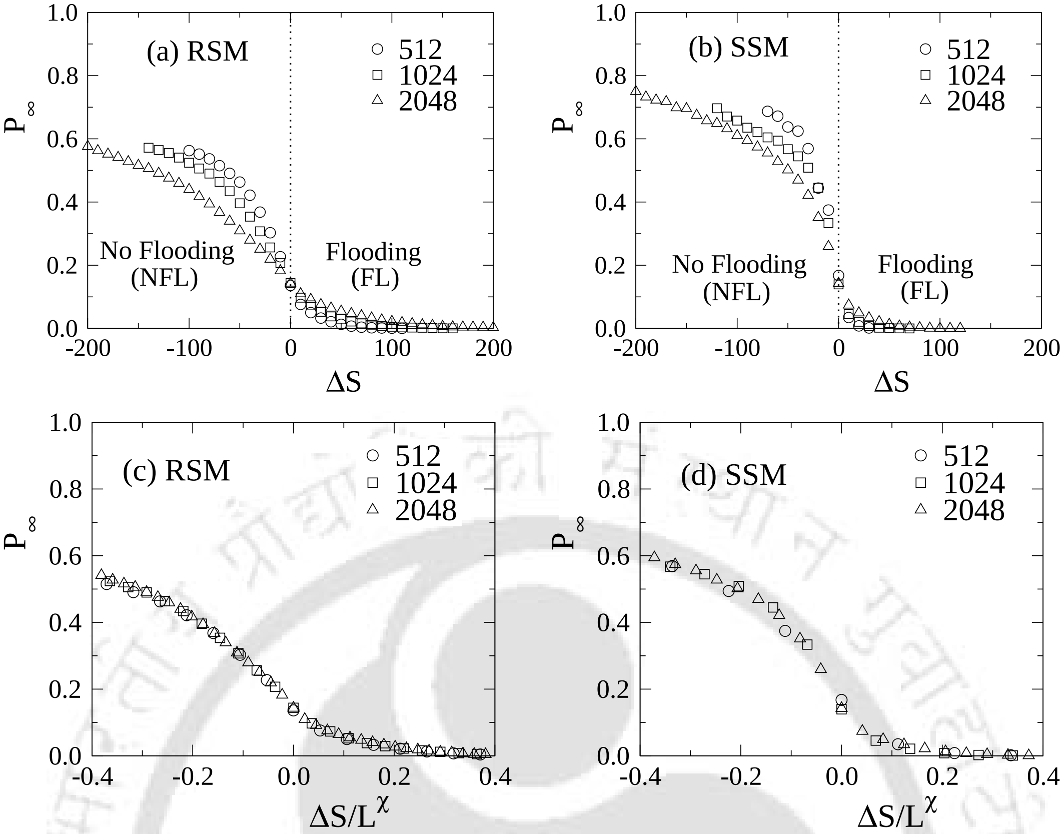

Figure 5.5: Plot of P_∞ against ΔS for the toppling surfaces of (a) the RSM and (b) the SSM for system sizes $L = 512$ (○), 1024 (□) and 2048 (△). Plot of P_∞ against the scaled variable $\Delta S/L^\chi$ for (c) the RSM and (d) the SSM. A reasonable collapse is observed for both the models.

level of flooding. It can be written as

$$P_\infty = 1 - P(a), \quad P(a) = \sum_a{}' a n_a \tag{5.2}$$

where n_a is the number of islands of area a per lattice site at a given ΔS, primed sum denotes exclusion of the critical spanning island. P_∞ is calculated as a function of ΔS for three different lattice sizes $L = 512, 1024$ & 2048 for both the models. In Figs.5.5(a) and (b) P_∞ is plotted against ΔS for the RSM and the SSM respectively. Two things are to be noticed. First, all the curves are crossing at $\Delta S = 0$ indicating $\Delta S = 0$ as the critical point separating two phases, no flooding and flooding for both the models. Second, for both the RSM and the SSM, the plot of P_∞ becomes flatter and flatter as L is increased than sharper and sharper for higher L as expected in a second order phase transition. However, this is related to the fact that the critical flooding height has wider distribution at a larger L than at a smaller L.

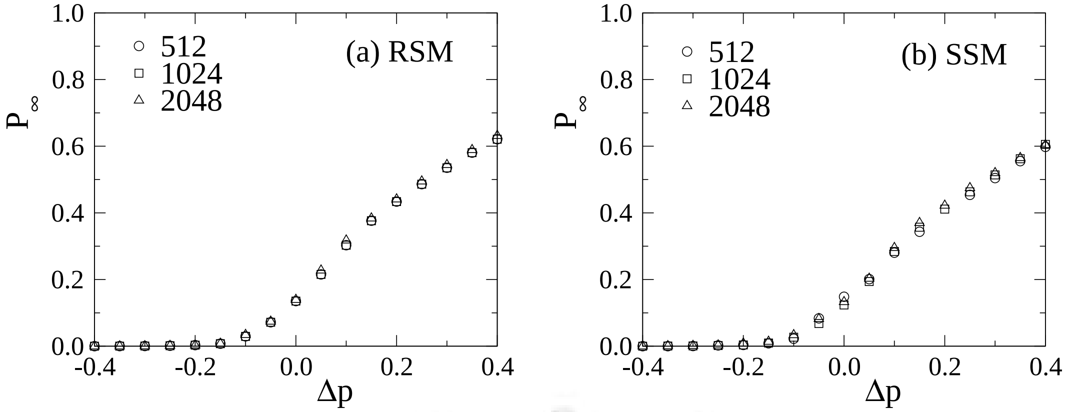

Figure 5.6: Plot of P_∞ against $\Delta p = p - p_c$ for (a) the RSM and (b) the SSM.

In order to verify the finite size dependence of P_∞, a finite size scaling (FSS) analysis has been performed. P_∞ is assumed as a generalized homogeneous function of ΔS and L as given by

$$\lambda P_\infty = F[\lambda^a \Delta S, \lambda^b L] \tag{5.3}$$

where λ is a parameter. Taking $\lambda = L^{-1/b}$, one has

$$P_\infty = L^A F[\Delta S/L^B] \tag{5.4}$$

where $A = 1/b$ and $B = a/b$. Since at $L \to \infty$ limit P_∞ is expected to be L independent, the FSS function should have a value $(\Delta S/L^B)^{A/B}$ in the same limit. Inserting the value of $F(\Delta S/L^B)$ in Eq.5.4, one has $P_\infty \approx (\Delta S)^{A/B}$. Since ΔS is like an external field in the problem, a scaling form for P_∞ with ΔS is assumed as

$$P_\infty \approx (\Delta S)^{1/\delta} \tag{5.5}$$

where $\delta = B/A$. On the other hand, at $\Delta S = 0$, $P_\infty \approx L^A$ assuming $F(0)$ is a constant. It is also expected that $\Delta S \sim L^\chi$ as $W(L)$ scales with L. One then has,

$$P_\infty \approx (\Delta S)^{A/\chi}, \quad A/\chi = 1/\delta. \tag{5.6}$$

Since $A\delta = \chi$ and $B = A\delta$, one has $B = \chi$. At the same time, by definition $P_\infty = L^{(D_f - d)}$ where D_f is the fractal dimension of the critical spanning islands and d is the space dimension. Thus, $A = D_f - d$. Knowing A and B, the FSS form of P_∞ is given by

$$P_\infty = L^{(D_f - d)} F[\Delta S/L^\chi]. \tag{5.7}$$

Since the islands here are almost compact, one has $D_f = d = 2$ and consequently it is expected that $P_\infty \approx F[\Delta S/L^\chi]$. In Figs.5.5(c) and (d), P_∞ is plotted against the scaled variable $\Delta S/L^\chi$ for the RSM and the SSM. Taking the values of $\chi = 0.82$ and 0.73 for the RSM and the SSM, respectively, a collapse of data is obtained as expected for both the models. It not only confirms the scaling theory for P_∞ but also verifies the scaling form of ΔS with L. The problem can also be studied in terms of the area fraction p. In Figs.5.6(a) and (b), P_∞ is plotted against $\Delta p = p - p_c$ for the RSM and the SSM respectively for system sizes $L = 512, 1024$ and 2048. It can be seen that for both the models, data for all three L collapse onto a single curve and no rescaling is required. As per percolation theory, the finite size scaling of P_∞ in terms of area fraction is given by $P_\infty = L^{-\beta/\nu} G[\Delta p L^{1/\nu}]$ where β is order parameter exponent, ν is correlation length exponent and $\beta = \nu(d - D_f)$[178]. Since the argument $\Delta p L^{1/\nu}$ of the scaling function G is found L independent, it seems that the correlation length exponent $\nu \to \infty$. That is what was also one of the conclusion of the study of percolation on the synthetic self-affine surfaces[189,192]. As $\nu \to \infty$ and $(d - D_f) \to 0$, then the exponent $\beta = \nu(d - D_f)$, must be finite. One may also note that $A = \chi/\delta = (D_f - d) \to 0$, then $\delta \to \infty$. Hence, in the $L \to \infty$ limit, as per Eq.5.5, the probability of appearance of a critical spanning island would be uniform at all possible level of flooding (consistent with Figs.5.5(a) and (b)). The order parameter then confirms $\Delta S = 0$ (or $\Delta p = 0$) as a critical point at which no flooding to flooding transition occurs in the topography of the sandpile toppling surfaces.

5.4 Island area distribution

In order to verify the criticality at $\Delta S = 0$ (or $\Delta p = 0$) the probability $P(a_0)$ of appearing an island of area a_0 in an ensemble of islands collected from all the surfaces at their respective critical heights S_c is determined for a system of size $L = 2048$. In Fig.5.7, the distribution $P(a_0)$ is plotted against a_0 in double logarithmic scale for (a) the RSM and (b) the SSM . It can be seen that $P(a_0)$ follows a power law distribution for both the RSM and the SSM. For a given lattice size L, the island area distribution $P(a_0)$ then should be given by

$$P(a_0) = a_0^{-\eta_0} f_0(a_0/L^{D_f}) \tag{5.8}$$

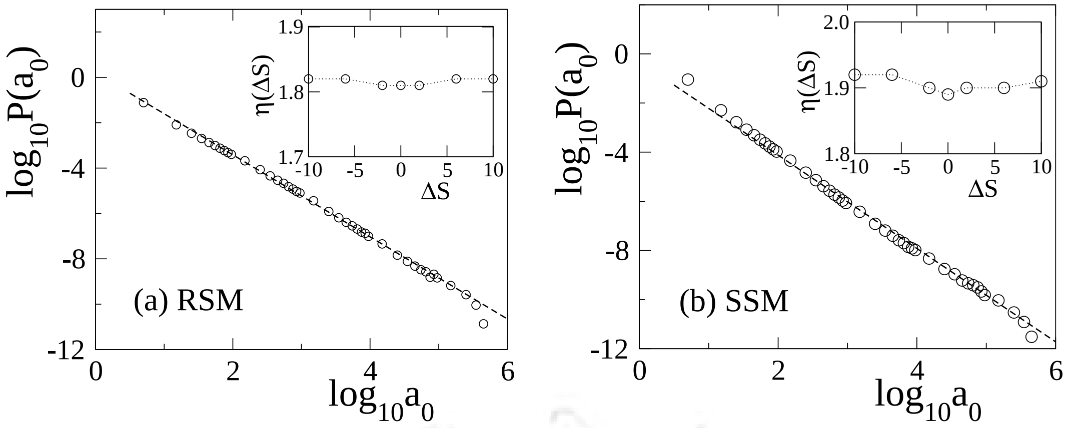

Figure 5.7: Plot of island area distribution $P(a_0)$ against a_0 for (a) the RSM and (b) the SSM at $\Delta S = 0$ for the system size $L = 2048$. The solid lines represent the best fitted lines. In the respective insets $\eta(\Delta S)$ is plotted against ΔS for the RSM and the SSM. The exponents are found close to that of η_0.

where D_f is the fractal dimension of the islands at $\Delta S = 0$ (or $\Delta p = 0$). The best estimate of the exponent η_0 is obtained as 1.81 ± 0.01 for the RSM and 1.90 ± 0.01 for the SSM[171]. The error bars are the linear least square fit errors. It should be noted that η_0 is a new exponent. It is neither equal to the cluster size distribution exponent of percolation $187/91 \approx 2.05$[178] nor it is equal to the avalanche area distribution exponent τ_a of the respective sandpile models ($\tau_a = 1.334$ for the RSM[113] and $\tau_a = 1.373$ for the SSM[74,75,76,113]). These exponents are also different from those recently obtained for the island area distribution at average height of Kardar-Parisi-Zhang and Edwards-Wilkinson interfaces by Saberi *et al.*[196]. Thus, the flooding transition is a novel continuous phase transition in the topography of the toppling surfaces of stochastic and rotational sandpile models and does not belong to the percolation universality class. However, the flooding transition will be equivalent to classical percolation transition for uncorrelated surfaces[189,190]. Though the flooding transition is able to characterize the RSM and the SSM distinctly, such a transition does not exists in the smooth toppling surface of the BTW sandpile model[4,114] for which at every level of flooding a single island will appear. Interestingly, the power law distribution of island area $P(a)$ is not restricted to $\Delta S = 0$ only, rather it is extended over a wide range of ΔS. The corresponding exponents $\eta(\Delta S)$ are extracted and plotted against ΔS in the respective insets of Fig.5.7. The values of $\eta(\Delta S)$s are found close (within error bars) to that of η_0 within $\Delta S = \pm 10$. For large values of ΔS (beyond ± 10), the distributions are found to deviate from the critical distribution with different critical exponents. The power law distribution is observed upto $\Delta S = \pm 100$ on a system of size $L = 2048$. It can be noted here that the area fraction p is ≈ 0.25 corresponding to $\Delta S = 0$ for both the models. Criticality over a wide range of area fraction is also observed in the synthetically generated self-affine surface by Olami[190]. Though the power law distribution occurs over a wide range of ΔS (or Δp), it is observed that the distribution extends for a longest possible range of area in the case of $\Delta S = 0$. This again indicates that $\Delta S = 0$ (or $\Delta p = 0$) is the critical point.

5.5 Scaling relations

It is interesting to explore the relationship between the criticality of flooding transition and the roughness or self-affinity of toppling surface topography. The criticality of flooding transition is characterized by the distribution exponent η_0 whereas the self-affinity of the toppling surface is characterized by the Hurst exponent H. The value of H can be calculated from the variation of correlation $C(r)$ between toppling numbers of two sand columns separated by a distance r with r as $C(r) \sim r^{2H}$ as mentioned in Chapter 4. The Hurst exponents of the RSM and the SSM are $H(\text{RSM}) = 0.35 \pm 0.01$ and $H(\text{SSM}) = 0.21 \pm 0.01$ respectively as mentioned in Chapter 4. A scaling inequality can now be developed to obtain an upper bound for the critical exponent η_0 in terms of the Hurst exponent H following Ref.[190]. The scaling inequality in the critical exponents is developed based on the fact that the number of islands N_0 must be less than the total contour length of all the islands at a given level of flooding. If N_0 is the number of islands at $\Delta S = 0$, the total area of all the islands should be

$$N_0 \int a_0^{-\eta_0+1} f_0(a_0/L^{D_f}) da_0 \approx N_0 L^{D_f(2-\eta_0)}. \tag{5.9}$$

At the same time, total island area at $\Delta S = 0$ flooding should also be L^{D_f} where D_f is the fractal dimension of the islands. The number of islands N_0 then can be obtained as $N_0 = L^{D_f(\eta_0-1)}$. On the other hand, total perimeter length of all the islands at the criticality should go as L^D where $D = 2 - H$ is the Mandelbrot exponent[146]. Thus the inequality in island numbers and the perimeter length can be written as

$$L^{D_f(\eta_0-1)} \leq L^{2-H}. \tag{5.10}$$

The scaling inequality then can be obtained as

$$\eta_0 \leq 2 - H/2 \tag{5.11}$$

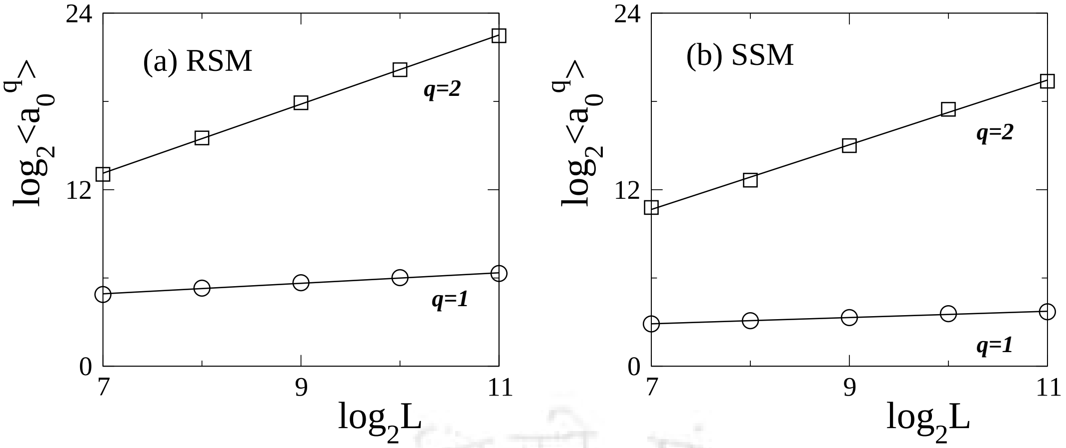

Figure 5.8: Plot of $\langle a_0^q \rangle$ against L for (a) the RSM and (b) the SSM for $q = 1$ (○) and 2 (□). The straight lines are the linear least square fit lines.

assuming $D_f = 2$ for the compact islands. Since $2 - H/2$ is equal to 1.825 ± 0.010 and 1.895 ± 0.010 for the RSM and the SSM respectively and the values of η_0 for these models are 1.81 and 1.90 respectively, the scaling relation holds as equality for a wide range of ΔS (± 10) within error bars. Such scaling equality is also found to be valid for the auto correlation function for the island areas on self-affine surfaces[197]. The universality class of the flooding transition is thus directly related to the roughness of the toppling surfaces and the fractal dimension of critical spanning islands. Since the toppling size distribution exponent τ_s is related to the roughness exponent $\chi = 1/2 + H$ the island area distribution exponent η_0 can also be connected to τ_s.

5.6 Moment analysis and finite size scaling

A FSS theory is developed by calculating the qth moment $\langle a_0^q \rangle$ of the island area as a function of system size L at $\Delta S = 0$. The qth moment of area distribution is defined as

$$\langle a_0^q \rangle = \int a_0^{-\eta_0 + q} f_0(a_0/L^{D_f}) da_0 \sim L^{\sigma_q} \tag{5.12}$$

where $\sigma_q = (q + 1 - \eta_0)D_f$. For FSS to be valid, $\sigma_{q+1} - \sigma_q = D_f$ should be satisfied for any q. $\langle a_0^q \rangle$ are calculated excluding the critical spanning islands upto $q = 4$. In Figs.5.8(a) and (b), $\langle a_0^q \rangle$ for $q = 1$ and 2 are plotted against L in double logarithmic scale for the RSM and the SSM respectively. The values of the exponents are estimated as $\sigma_1 = 0.35 \pm 0.02$ and $\sigma_2 = 2.35 \pm 0.03$ for the RSM and $\sigma_1 = 0.21 \pm 0.02$ and $\sigma_2 = 2.20 \pm 0.03$ for the SSM by linear least square fit to the data points. A few important things are to be noticed. First, $\sigma_2 - \sigma_1 \approx 2$ for both the models.

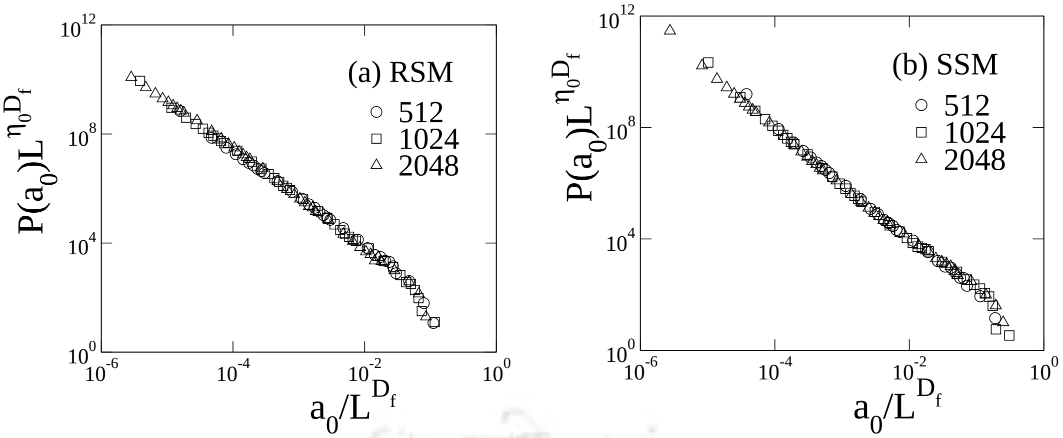

Figure 5.9: Plot of scaled island area distribution at the flooding threshold $P(a_0)L^{\eta_0 D_f}$ against scaled variable a_0/L^{D_f} for $L = 512$ (○), 1024 (□) and 2048 (△) for (a) the RSM and (b) the SSM. A reasonable data collapse is observed for both the models.

It is also verified for two more higher moments. Thus $P(a_0)$ follows FSS. Second, σ_1 and σ_2 both are different for the RSM and the SSM and are then characteristic exponents of these models. Third, the scaling relation $\sigma_q = (q+1-\eta_0)D_f$ is satisfied within error bars for both the models assuming $D_f = 2$. Fourth, assuming equality in Eq.5.11, $\eta_0 = 2 - H/2$, and $D_f = 2$, one has $\sigma_q = 2(q-1+H/2)$. Hence, $\sigma_1 = H$ and $\sigma_2 = 2+H$. It is important to note that the measured values of σ_1 and σ_2 are equal to H and $2+H$ respectively for both the models. Therefore, all the exponents of flooding transition can be defined in terms of the Hurst exponent H alone taking $D_f = 2$ for the compact islands. The FSS form of $P(a_0)$ is verified by studying the scaled distributions $P(a_0)L^{\eta_0 D_f}$ as a function of the scaled variable a_0/L^{D_f}. In Fig.5.9 $P(a_0)L^{\eta_0 D_f}$ is plotted against the scaled variable a_0/L^{D_f} for (a) the RSM and (b) the SSM for $L = 512, 1024$ and 2048. A reasonable data collapse is obtained for the distribution functions using the respective values of η_0 and D_f for both the models. Thus, the FSS form assumed for the island area distribution at the flooding threshold is correct for these models.

In the above, FSS of the island area distribution function is verified at the critical flooding threshold $\Delta S = 0$ only. It is important to verify the FSS form of the distribution function with ΔS or with $\Delta p = p - p_c$, where p is the area fraction (total island area per lattice site at a given level of flooding) and p_c is the area fraction at the flooding threshold. This has been verified by studying the average island area $\langle a \rangle$ as a function of ΔS and Δp for different L. In Fig.5.10, $\langle a(\Delta S, L)\rangle$ is plotted against ΔS for (a) the RSM and (b) the SSM. It can be seen that $\langle a(\Delta S, L)\rangle$ increases with L at the criticality $\Delta S = 0$ for both the models as expected and shown

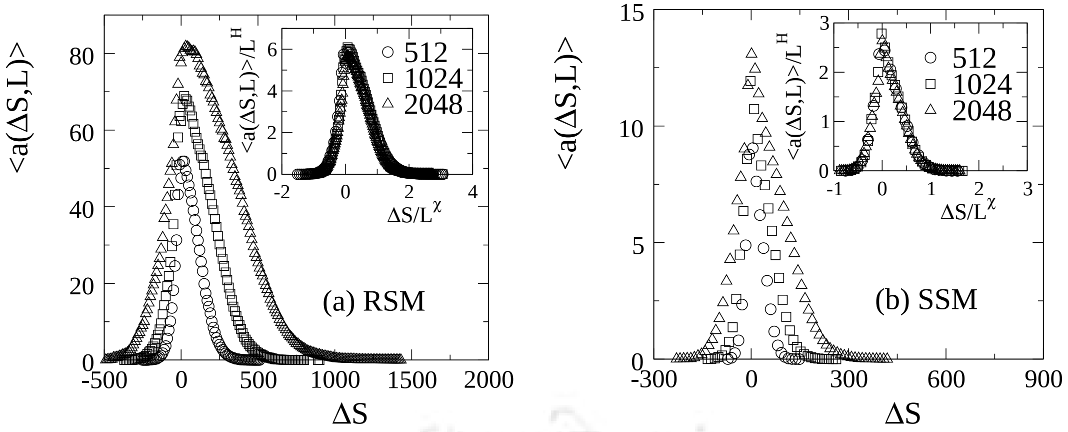

Figure 5.10: Plot of $\langle a(\Delta S, L)\rangle$ against ΔS for $L = 512$ (○), 1024 (□) and 2048 (△) for (a) the RSM and (b) the SSM. In the respective insets, $\langle a(\Delta S, L)\rangle/L^H$ is plotted against $\Delta S/L^\chi$ for the same set of L. A reasonable collapse is observed for both the RSM and the SSM.

in Fig.5.8. On the other hand, ΔS should scale in a similar fashion as the toppling surface width $W(L)$ scales with the system size as L^χ. FSS form of $\langle a(\Delta S, L)\rangle$ is then expected to be

$$\langle a(\Delta S, L)\rangle = L^H f_a[\Delta S/L^\chi]. \tag{5.13}$$

In the insets of Fig.5.10(a) and (b), $\langle a(\Delta S, L)\rangle/L^H$ is plotted against $\Delta S/L^\chi$ for the RSM and the SSM respectively. A reasonable data collapse is obtained for both the RSM and the SSM. FSS form of $\langle a\rangle$ as a function of Δp and L is is expected to be

$$\langle a(\Delta p, L)\rangle = L^H g_a(\Delta p L^{1/\nu}) \tag{5.14}$$

where ν is the correlation length exponent. $\langle a\rangle$ is estimated for different Δp and L and is plotted in Fig.5.11 for (a) the RSM and (b) the SSM. Interestingly, on one hand the value of $\langle a\rangle$ for both the models diverge at $\Delta p = 0$ as expected in a continuous phase transition and on the other hand, the distribution is becoming broader and broader with increasing L in contradiction to a continuous phase transition. In the insets of the respective plots, the scaled average area $\langle a(\Delta p, L)\rangle/L^H$ is plotted against Δp for both the RSM and the SSM. It can be seen that a good collapse of data is obtained taking $H = 0.35$ and 0.21 for the RSM and the SSM respectively. Note that for both the models, Δp itself is the scaled variable since $\nu \to \infty$ in these cases. As per percolation theory, H is also equal to γ/ν, where γ is the critical exponent describing the singularity of $\langle a\rangle$ at $\Delta p = 0$. Since the ratio of γ to ν is finite and $\nu \to \infty$, the exponent γ must be very large. It seems that most

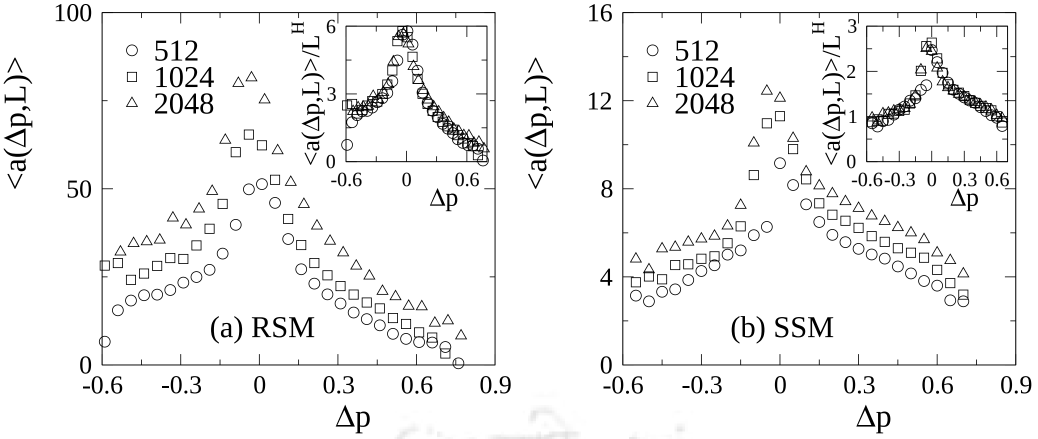

Figure 5.11: Plot of $\langle a(\Delta p, L)\rangle$ against Δp for $L = 512$ (○), 1024 (□) and 2048 (△) for (a) the RSM and (b) the SSM. In the respective insets, $\langle a(\Delta p, L)\rangle / L^H$ is plotted against Δp for the same set of L. Here Δp itself a scaled variable as $\nu \to \infty$. A reasonable collapse is observed for both the RSM and the SSM.

of the percolation exponents are infinitely large. But the ratio of these exponents to the correlation length exponent is found to be finite[171]. Therefore, there exists a critical point where the island related quantities will diverge in the $L \to \infty$ limit with appropriate FSS exponents. In that sense, FSS is the most appropriate theory to study this type of phase transition.

In a continuous phase transition, it is also expected that the fluctuation in island area should diverge at the criticality. Therefore it is interesting to study the fluctuation in island area $\langle \delta a^2(\Delta S, L)\rangle$ as a function of ΔS for a given system of size L. $\langle \delta a^2(\Delta S, L)\rangle$ is defined as

$$\langle \delta a^2(\Delta S, L)\rangle = \frac{\langle a^2(\Delta S, L)\rangle - \langle a(\Delta S, L)\rangle^2}{\langle a(\Delta S, L)\rangle^2}. \tag{5.15}$$

$\langle \delta a^2(\Delta S, L)\rangle$ is calculated at different ΔS for different L and plotted against ΔS for the RSM and the SSM in Figs.5.12 (a) and (b) respectively. It can be seen that maximum in island fluctuation $\langle \delta a^2(\Delta S, L)\rangle$ appears at the criticality $\Delta S = 0$ for both the models. The fluctuation in island area at criticality $\langle \delta a^2(L)\rangle_0$ is given by

$$\langle \delta a^2(L)\rangle_0 = \frac{\langle a_0^2(L)\rangle - \langle a_0(L)\rangle^2}{\langle a_0(L)\rangle^2} \tag{5.16}$$

and it is expected to diverge with L as

$$\langle \delta a^2(L)\rangle_0 \sim L^{\Delta\sigma} \tag{5.17}$$

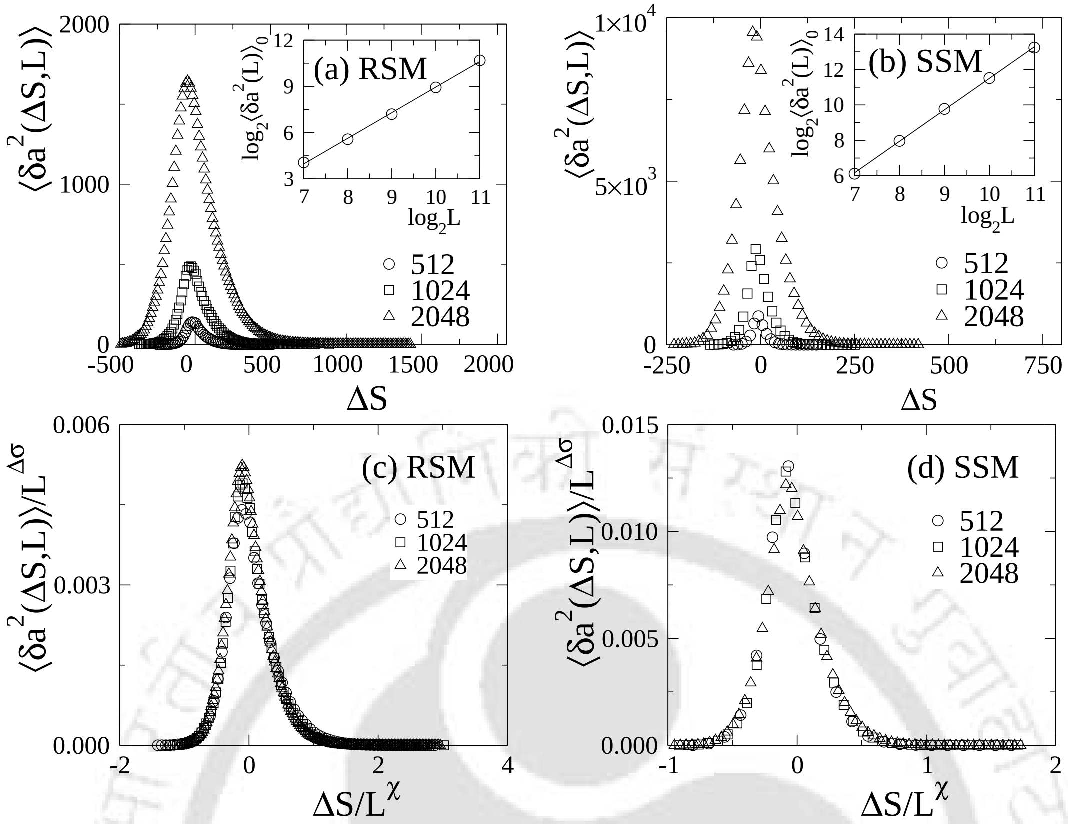

Figure 5.12: Plot of $\langle \delta a^2(\Delta S, L)\rangle$ against ΔS for $L = 512$ (○), 1024 (□) and 2048 (△) for (a) the RSM and (b) the SSM. In the insets of (a) and (b) $\langle \delta a^2(L)\rangle_0$ is plotted against L in double logarithmic scale for the respective models. Plot of $\langle \delta a^2(\Delta S, L)\rangle / L^{\Delta\sigma}$ against $\Delta S/L^{\chi}$ for both (c) the RSM and (d) the SSM for the same set of L. A reasonable collapse of data is obtained for both the models.

where $\Delta\sigma = \sigma_2 - 2\sigma_1 = 2 - H$. It can be seen from Figs.5.12(a) and (b) that $\langle \delta a^2(L)\rangle_0$ increases with L at the criticality for both the models. In the insets of Figs.5.12 (a) and (b) values of $\langle \delta a^2(L)\rangle_0$ are plotted against L in double logarithmic scale for both the models and they follow the scaling law assumed in Eq.5.17. The values of $\Delta\sigma$, obtained from the linear least square fitting to the data points, are $\Delta\sigma = 1.65 \pm 0.01$ for the RSM and $\Delta\sigma = 1.78 \pm 0.01$ for the SSM. The values of $\Delta\sigma$ obtained are also satisfying the scaling relation among σ_2, σ_1 and the Hurst exponent H within the error bars. Numerical values of the critical exponents associated with island area distribution, different moments of island area distribution and fluctuation in island area for the RSM and the SSM are listed in Table 5.1 and the scaling relations are verified. Since ΔS scales with L with exponent χ, the scaling of $\langle \delta a^2(\Delta S, L)\rangle$ is expected to be

$$\langle \delta a^2(\Delta S, L)\rangle = L^{\Delta\sigma} f_{af}[\Delta S/L^{\chi}]. \tag{5.18}$$

Model	H	$2-H/2$	η_0	σ_1^a	σ_2^a	$\Delta\sigma$	$\sigma_2^a - 2\sigma_1^a$
			$=(2-H/2)$	$=(H)$	$=(2+H)$	$=(2-H)$	$=(2-H)$
RSM:	0.35	1.825	1.81	0.35	2.35	1.65	1.65
	±0.01	±0.01	±0.01	±0.02	±0.03	±0.01	±0.05
SSM:	0.21	1.895	1.90	0.21	2.20	1.78	1.78
	±0.01	±0.01	±0.01	±0.02	±0.03	±0.01	±0.05

Table 5.1: Numerical values of the critical exponents associated with the flooding transition for the SSM and the RSM are listed here. Errors quoted with the critical exponents obtained through the scaling relations are propagation errors. The scaling relations are found valid within error bars.

In Figs.5.12(c) and (d), the scaled fluctuation $\langle \delta a^2(\Delta S, L)\rangle / L^{\Delta\sigma}$ is plotted against the scaled variable $\Delta S/L^{\chi}$ for the RSM and the SSM respectively. A reasonable data collapse is obtained using the values of $\Delta\sigma$ and χ for the respective models. Thus, the FSS form of island area distribution is again found to be correct scaling forms.

5.7 Conclusion

A continuous phase transition, called flooding transition, is found to occur in the toppling surface topography of stochastic and rotational sandpile models. Such a transition is not possible to occur in the smooth topography of the deterministic BTW type sandpile toppling surfaces. Though there exists a wide distribution of flooding threshold, a critical point is defined by merging the flooding thresholds of all the toppling surfaces. The width of critical height distribution for a given system size is found to scale with the roughness exponent of the toppling surface. The singularity of several island related quantities are explored at the critical point. A number of important observations are noted in the study of flooding transition. An order parameter for the flooding transition is defined in terms of the probability to find a surface point in the critical spanning island. Power law distribution of island area is found to exist over a wide range of area fraction. A set of new critical exponents are determined. A FSS theory for the island related quantities is developed and verified. Most of the percolation type exponents are found to be infinitely large though their ratio to the correlation length exponent are found finite. The flooding transition is found to be a novel continuous phase transition and does not belong to the percolation universality class. Not only the critical exponents of flooding transition are obtained in terms of the Hurst exponent H of the toppling surfaces and the fractal dimension D_f of the critical islands but also the exponents describing the avalanche size distribution are also obtained.

Chapter 6

Critical properties of island perimeters

In the previous chapter, a novel continuous phase transition called flooding transition through the self-affine toppling surfaces of the RSM and the SSM was described. At the flooding threshold the islands exhibits nontrivial critical behaviour which depends on the Hurst exponent H of the toppling surfaces. It is then expected that the properties of the external perimeters of these islands should exhibit a non-trivial critical behaviour at the same flooding threshold. In the case of synthetically generated self-affine surfaces, an ensemble of contour loops were generated by intersection of horizontal planes with the surface and its geometrical properties were found useful to characterize these surfaces[198,199,200,201]. Study of contour loop properties were also extended to the Kardar-Parisi-Zhang (KPZ) interface[196,202], WO_3 surface[203], discrete scale invariant rough surface[204] as well as multifractal surfaces[205]. Percolation transition and the contour loop properties on the self-affine surfaces were studied independently without enough emphasis on loop properties at the percolation threshold. In this chapter the critical properties of the external perimeter of islands are studied in detail at the flooding threshold performing FSS studies.

6.1 Perimeter extraction

In Chapter 5, flooding transition is studied in the topography of the toppling surfaces of the RSM and the SSM by flooding the toppling surfaces with a liquid, say water. At each level of flooding S, the surface points whose heights are greater than the water level ($S_i > S$) form islands. Points belonging to the same island are connected by NN bonds. The external perimeter of an island is identified by

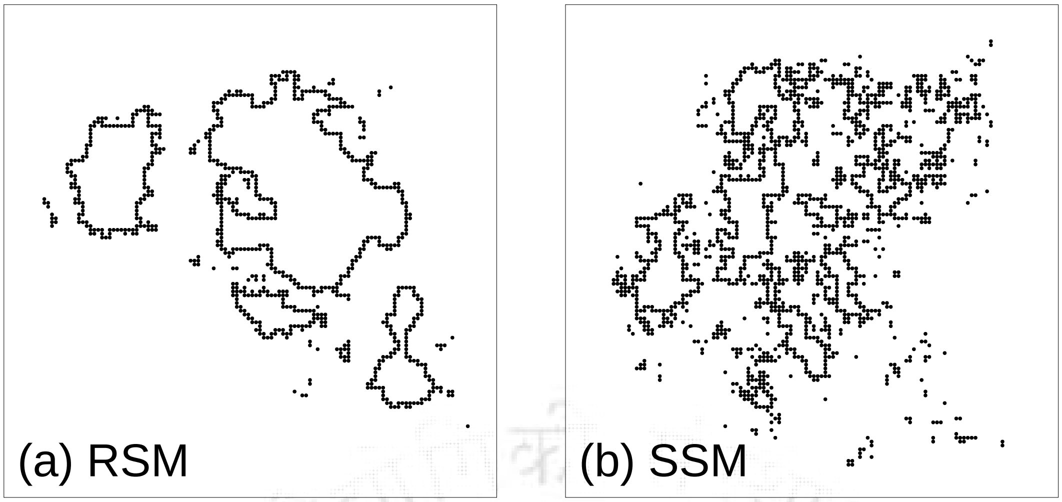

Figure 6.1: Perimeters of the islands obtained at the flooding threshold of the toppling surfaces of (a) the RSM and (b) the SSM (given in Chapter 4) are shown by black dots. The flooding thresholds are $S = 25$ for the RSM and $S = 10$ for the SSM.

performing a kinetic random walk, an algorithm developed by Ziff *et al.*[206]. Such an algorithm had been extensively used to determine the external hull of percolation clusters[207,208,209,210,211,212,213]. In this algorithm, one starts from a pair of occupied and empty NN sites at one point on the perimeter. The walker then moves to the occupied site from the empty site and the direction of occupation from the empty site to the occupied site, is noted. Facing the direction of occupation, a search is made for an occupied nearest neighbour in the same island from the left following the sequence left, front, right and back. As soon as an occupied site is encountered the direction of occupation of the new site, from the old occupied to the new occupied site, is again noted. The walker moves to the new occupied site and keeps on moving until it encounters a pair of occupied sites which had already been occupied in the same direction. However, a site could be visited from different directions during this walk. All the distinct occupied sites encountered during the walk are listed in an array and they define the external perimeter of the island. Typical perimeters of the islands obtained by flooding the toppling surfaces of the SSM and the RSM are shown in the lower panel of Fig.6.1. It can be seen that the island perimeters are not only tortuous but also have different geometries for the SSM and the RSM toppling surfaces. In the study of flooding transition, the critical properties of islands were found to be characterized by the Hurst exponent H of the toppling surface. It is then intriguing to study the critical properties of external perimeters of these islands for further information relating the avalanche properties and the toppling surface of sandpile models.

It may be noted here that the toppling surface of the Bak, Tang and Wiesenfeld (BTW) sandpile model[4,114] is a single Gaussian surface around the maximum toppling number. During flooding through the smooth toppling surface of BTW, only one island can be obtained at every level of flooding and no flooding transition can occur. Hence, its properties are not studied.

For each lattice size L, 10^3 toppling surfaces corresponding to large spanning avalanche clusters are collected and perimeters of islands are extracted for each level of flooding of all these surfaces. Since it was observed for flooding transition that there exists a wide distribution of flooding thresholds the island perimeters are collected for different values of $\Delta S = S - S_c$ at and around the flooding threshold $\Delta S = 0$. In the following, several geometrical properties of the island perimeters will be analyzed.

6.2 Critical properties of island perimeters

6.2.1 Fractal dimension of island perimeter

During flooding of the toppling surface of the SSM and the RSM, the perimeter of the islands appeared at the flooding threshold are found highly tortuous. They are expected to be a self similar random object and hence, it is useful to measure their fractal dimension. An island perimeter is consist of the occupied lattice sites at the perimeter of an island whose coordinates are given by (x_i, y_i). The mass (size) m of a perimeter is then the number of sites present on the island perimeter. The lateral extension r of an island perimeter is taken as $r = max\{\Delta x, \Delta y\}$ where $\Delta x = (x_{max} - x_{min})$ and $\Delta y = (y_{max} - y_{min})$. The perimeter mass m is expected to scale with its extension r as

$$m \sim r^{d_\ell} \tag{6.1}$$

where d_ℓ is fractal dimension of the island perimeter. At the flooding threshold, mass m of the island perimeters are collected as a function of their lateral extension r, dividing r in logarithmic bins of base 2. In Fig.6.2(a), $\langle m \rangle_r$ is plotted against r in double logarithmic scale for both models for the system of size $L = 2048$. Data for the largest bin is dropped to avoid the lattice boundary effect. Fractal dimensions d_ℓ of island perimeters of both models are calculated by linear least square fitting to the data points in Fig.6.2(a). The values of d_ℓ are found different for the RSM and the SSM as 1.33 ± 0.01 and 1.41 ± 0.01 respectively[170]. Since $d_\ell(\text{SSM}) > d_\ell(\text{RSM})$,

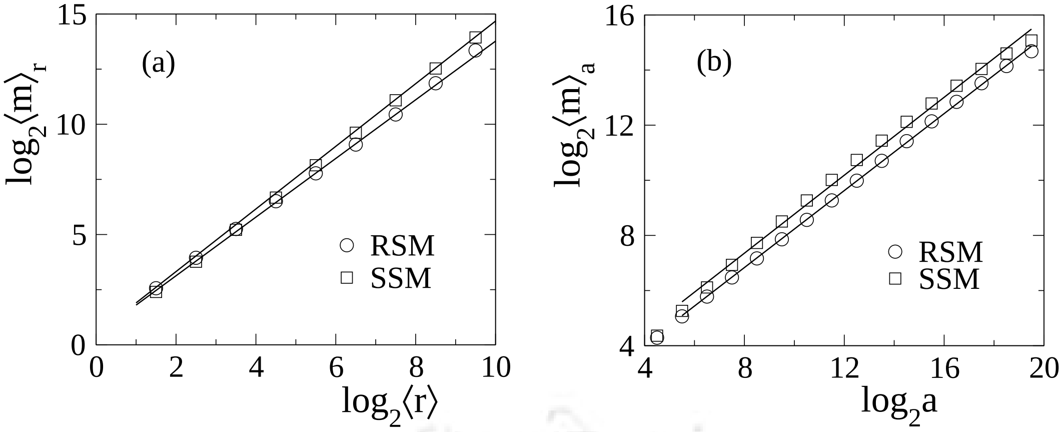

Figure 6.2: (a) Plot of perimeter mass $\langle m\rangle_r$ against the lateral extension r of the corresponding island perimeters for the RSM (circle) and the SSM (square) for a system of size $L = 2048$. The perimeter fractal dimensions are obtained as: 1.33±0.01 for the RSM and 1.41 ± 0.01 for the SSM. (b) Plot of perimeter mass $\langle m\rangle_a$ against the corresponding island area a for the RSM (circle) and the SSM (square) for the same system size. It is found that $\langle m\rangle_a$ scales with a with an exponent 0.68 ± 0.01 for the RSM and 0.71 ± 0.01 for the SSM.

the SSM island perimeters are more tortuous than the RSM island perimeters as it can be seen in Fig.6.1. Note that, the values of d_ℓ obtained here are consistent with that obtained for the ensemble of perimeters obtained by flooding the toppling surfaces at all possible levels on a lower lattice size[169]. It can also be noted that the percolation hull dimension is 4/3[178,179,214].

Since the islands obtained in the flooding transition are compact, the island area a is expected to scale with the extension r of the island as $a \sim r^2$. Therefore, the mass m of the island perimeter of area a should scale as

$$m \sim a^{d_\ell/2}. \tag{6.2}$$

In Fig.6.2(b), $\langle m\rangle_a$ is plotted against island area a in double logarithmic scale for both models for the system of size $L = 2048$. The slopes of the plots are calculated by linear least square fitting to the data points in Fig.6.2(b) and the values of slopes are obtained as 0.68 ± 0.01 for the RSM and 0.71 ± 0.01 for the SSM. The values obtained here are equal to $d_\ell/2$ within the error bars. It is not only confirming the compactness of the islands but is also verifying the correctness of the measured value of d_ℓ.

6.2.2 Perimeter mass and extension distributions

During the flooding transition it was observed that the island area distribution follows a power law scaling behaviour at the flooding threshold $\Delta S = 0$ and the distribution exponent was found to depend only on the Hurst exponent H of the toppling surfaces[171]. It is thus important to obtain the scaling behaviour of the probability distributions of perimeter mass m and its extension r at $\Delta S = 0$. As the island perimeters are self-similar with fractal dimension d_ℓ, the number of island perimeter $n(m,r)$ of size m and lateral extension r is expected to scale as

$$n(m,r) = m^{-\zeta} f_\ell(m/r^{d_\ell}) \tag{6.3}$$

where ζ is an unknown exponent. If the total number of islands appeared at $\Delta S = 0$ is N, the probability $\tilde{n}(m)$ of finding an island perimeter of mass m for any extension r is given by

$$\tilde{n}(m) = \frac{1}{N}\int m^{-\zeta} f_\ell(m/r^{d_\ell})dr \sim m^{-\eta_m}. \tag{6.4}$$

Defining a scaled variable $z = m/r^{d_\ell}$, $\tilde{n}(m)$ can be written in terms of z as

$$\tilde{n}(m) = m^{-\zeta+1/d_\ell}\left(\frac{-1}{Nd_\ell}\right)\int_z z^{-2} f_\ell(z)dz. \tag{6.5}$$

Since the integral will contribute to a constant, the scaling behavior of $\tilde{n}(m)$ with m can be written as

$$\tilde{n}(m) \sim m^{-\zeta+1/d_\ell} \sim m^{-\eta_m}. \tag{6.6}$$

Therefore the scaling relation among η_m, ζ, and d_ℓ is given by

$$\eta_m = \zeta - 1/d_\ell. \tag{6.7}$$

Similarly, the probability $\tilde{n}(r)$ of finding an island perimeter of extension r for any masses m is given by

$$\tilde{n}(r) = \frac{1}{N}\int m^{-\zeta} f_\ell(m/r^{d_\ell})dm \sim r^{-\eta_r} \tag{6.8}$$

Defining a scaled variable $z = m/r^{d_\ell}$, $\tilde{n}(r)$ can be written in terms of z as

$$\tilde{n}(r) = r^{(-\zeta+1)d_\ell}\left(\frac{1}{N}\right)\int_z f_\ell(z)dz. \tag{6.9}$$

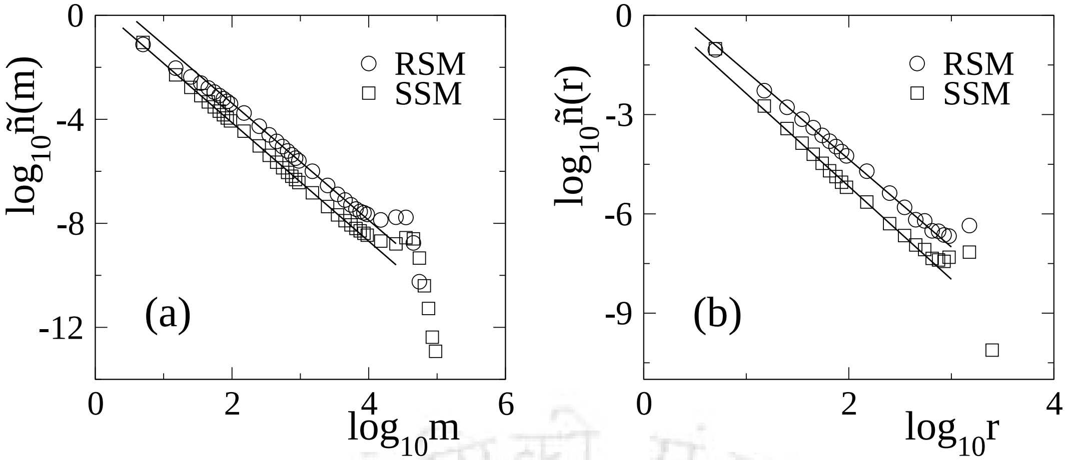

Figure 6.3: (a) Plot of $\tilde{n}(m)$ against the perimeter mass m for the RSM (○) and the SSM (□), (b) plot of $\tilde{n}(r)$ against the perimeter extension r for the RSM (○) and the SSM (□). The solid lines are the best fitted lines through the data points.

The integral can be taken as a constant and consiquently, the scaling behavior of $\tilde{n}(r)$ with r can be written as

$$\tilde{n}(r) \sim r^{(-\zeta+1)d_\ell} \sim r^{-\eta_r}. \tag{6.10}$$

Therefore the scaling relation among η_r, ζ, and d_ℓ is given by

$$\eta_r = d_\ell(\zeta - 1). \tag{6.11}$$

Eliminating ζ from the Eqs.6.7 and 6.11, a scaling relation between η_r and η_m can be obtained as

$$\eta_r = 1 + d_\ell(\eta_m - 1). \tag{6.12}$$

The probability distributions $\tilde{n}(m)$ and $\tilde{n}(r)$ are calculated at $\Delta S = 0$ for a system of size $L = 2048$. Data are collected in bins of intervals of 10s, 100s, 1000s, and so on. Finally, they are normalized by the respective bin widths. In Fig.6.3(a), $\tilde{n}(m)$ is plotted against m and in Fig.6.3(b), $\tilde{n}(r)$ is plotted against r in double logarithmic scale for both the RSM (circle) and the SSM (square). It can be seen that both $\tilde{n}(m)$ and $\tilde{n}(r)$ follow power law scaling for both models as expected. The power law scaling signifies the criticality of the system at the flooding threshold. The slopes of the distributions are calculated from the linear least square fitting to the linear part of the distribution. From the slope of the best fitted straight lines, the values of the exponents η_m and η_r are obtained as: $\eta_m = 2.25 \pm 0.01$, $\eta_r = 2.65 \pm 0.01$ for the RSM and $\eta_m = 2.28 \pm 0.01$, $\eta_r = 2.79 \pm 0.01$ for the SSM[170]. It can be seen that the values of η_r are different for both the RSM and the SSM but the values of η_m are close for both models. Moreover, the scaling relation $\eta_r = 1 + d_\ell(\eta_m - 1)$ is satisfied within error bars by the values of the critical exponents η_m and η_r obtained for both models.

6.2.3 Hyperscaling

The critical exponents associated with the properties of island perimeters such as d_ℓ, η_r and η_m can be related to roughness or the self-affinity of the toppling surface by studying hyperscaling. Through hyperscaling, these exponents can be obtained in terms of the roughness exponent χ that describes the width of the toppling surface or in terms of the Hurst exponent H that describes the toppling number (height) correlation in the toppling surface. The hyperscaling relations is obtained here in terms of H following Ref.[198,199]. It can be noted that an island perimeter consists of sites of different toppling numbers (or heights) at a given level of flooding. In order to confine island perimeters of extensions r to $r + dr$ along with toppling numbers associated with perimeter sites in a box of side ϵ, the vertical height of the box is needed to be Δ, say. Similarly, to confine island perimeters of extensions r/b to $r/b + d(r/b)$ in a box of side ϵ/b, the vertical height of the box is needed to be Δ', say. Since in continuum, the toppling number (height of the surface at a given point) $S(r) \approx \lambda^{-H} S(\lambda r)$, Δ should scale as $\Delta' \sim b^{-H}\Delta$ for $\lambda = 1/b$. The number of island perimeters per unit height in a box of side ϵ is then statistically equivalent to the number of island perimeters per unit height in a box of side ϵ/b. Therefore,

$$\frac{\epsilon^2 \tilde{n}(r)dr}{\Delta} \approx \frac{(\epsilon/b)^2 \tilde{n}(r/b)d(r/b)}{\Delta'} = \frac{\epsilon^2 b^{H-3} \tilde{n}(r/b)dr}{\Delta}. \tag{6.13}$$

From this hyperscaling, it can be seen that

$$\tilde{n}(r/b) = b^{(3-H)}\tilde{n}(r/b). \tag{6.14}$$

This is possible if

$$\tilde{n}(r) \sim r^{-(3-H)}. \tag{6.15}$$

Since $\tilde{n}(r) \sim r^{-\eta_r}$ the hyperscaling relation between η_r and H can be obtained as

$$\eta_r = 3 - H. \tag{6.16}$$

Knowing that $\eta_r = 1 + d_\ell(\eta_m - 1)$ from Eq.6.12, by eliminating η_r the hyperscaling relation between η_m and H can then obtained as

$$d_\ell(\eta_m - 1) = 2 - H. \tag{6.17}$$

Both the hyperscaling relations are found satisfied within error bars for the measured values of d_ℓ, η_r, η_m and H for the island perimeters of both models. The critical exponents obtained here are listed in Table 6.1 and different scaling relations are verified.

It may be noted here that the above scaling theory is obtained here considering the island perimeters only at the flooding threshold. Such scaling relations were also obtained for a contour loop ensemble constructed by horizontal cuts of synthetically generated Gaussian random surfaces at all possible levels by Kondev *et el.*[198,199]. In the case of flooding transition on the sandpile toppling surfaces as well as percolation transition on the synthetically generated self-affine surfaces, the flooding threshold (percolation threshold) was found to have a wide distribution and the width of the distribution diverges in the thermodynamic limit[171]. This is why the scaling relations obtained at the flooding threshold are found identical to those obtained for the contour loop ensemble.

6.2.4 Perimeter site-site correlation function

A direct scaling relation between perimeter fractal dimension d_ℓ and Hurst exponent H of the toppling surface can be obtained by studying perimeter site-site correlation function $G_m(r)$ following Ref.[198,199]. The correlation function $G_m(r)$ is defined as the probability to find a pair of sites separated by a distance r on the same perimeter of mass m and assumed to scale with m and r as

$$G_m(r) = \frac{m^{x_m}}{r^{x_r}} g_\ell\left(\frac{r}{m^{1/d_\ell}}\right) \tag{6.18}$$

where x_m and x_r are two unknown exponents. The perimeter mass m can be obtained by summing $G_m(r)$ for perimeters of all possible extensions r in the critical regime and is given by

$$m = \int d^2 r G_m(r) \sim m^{x_m + (2 - x_r)/d_\ell}. \tag{6.19}$$

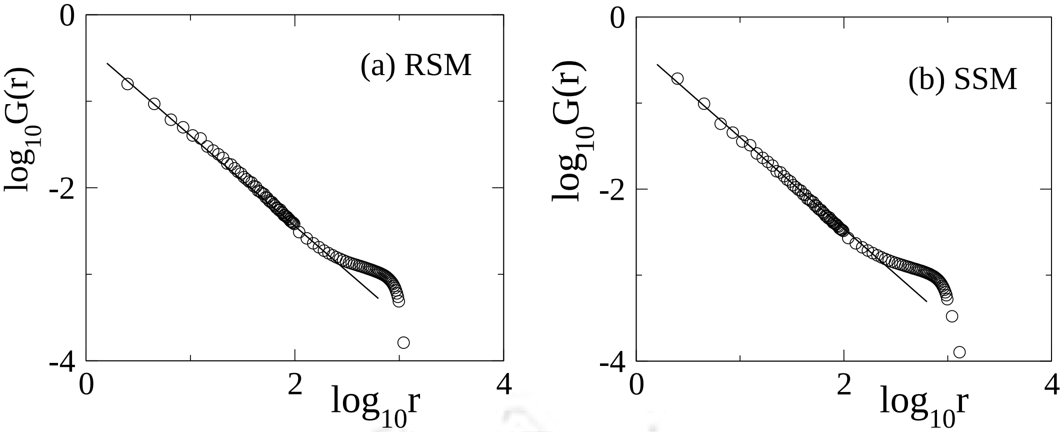

Figure 6.4: Plot of perimeter site-site correlation function $G(r)$ against r, distance between two points on the same perimeter, for (a) the RSM and (b) the SSM for system size $L = 1024$. Solid lines are the best fitted lines through the data points. For the RSM and the SSM, $x_l \approx 1$ and is independent of the Hurst exponent H.

This provides a relation between the exponents x_m and x_r as $2-x_r = d_\ell(1-x_m)$. On the other hand, the total correlation function $G(r)$ can be obtained by integrating $G_m(r)$ for the perimeters of all possible masses m at the flooding transition. $G(r)$ is then given by

$$G(r) = \int m\tilde{n}(m)G_m(r)dm = \int m^{-\eta_m+1}\frac{m^{x_m}}{r^{x_r}}g_\ell\left(\frac{r}{m^{1/d_\ell}}\right)dm. \tag{6.20}$$

Defining a scaled variable $z = r/m^{1/d_\ell}$, $G(r)$ can be written in terms of z as

$$G(r) = r^{d_\ell(x_m-\eta_m+2)-x_r}\left(-d_\ell\right)\int_z g_\ell(z)dz. \tag{6.21}$$

The integral can be taken as a constant and therefoe, the $G(r)$ is assumed to scale with r as $G(r) \sim r^{x_l}$ then the perimeter site-site correlation exponent x_l can be written as

$$x_l = d_\ell(x_m - \eta_m + 2) - x_r. \tag{6.22}$$

Since, $2 - x_r = d_\ell(1 - x_m)$, x_l can be obtained as

$$x_l = 2 - d_\ell(3 - \eta_m) \tag{6.23}$$

after eliminating x_m and x_r. The total correlation function $G(r)$ is calculated at the flooding threshold. During calculation of $G(r)$, values of r are collected in bins of width 2 for $0 \leq r < 100$, 20 for $100 \leq r < 1000$ and so on and finally the values

Model	H	d_ℓ	η_m	η_r	d_ℓ	η_m	η_r	d_ℓ
					$(\frac{\eta_r-1}{\eta_m-1})$	$(1+\frac{2-H}{d_\ell})$	$(3-H)$	$(\frac{3-H}{2})$
RSM:	0.35	1.33	2.25	2.65	1.32	2.24	2.65	1.33
	±0.01	±0.01	±0.01	±0.01	±0.02	±0.02	±0.01	±0.01
SSM:	0.21	1.41	2.28	2.79	1.40	2.27	2.79	1.40
	±0.01	±0.01	±0.01	±0.01	±0.02	±0.02	±0.01	±0.01

Table 6.1: Numerical values of the critical exponents associated with properties of island perimeters for the RSM and the SSM are listed here. The exponent values are compared with those obtained from the scaling relations. Errors quoted with the critical exponents obtained through the scaling relations are propagation errors. The scaling relations are found valid within error bars. The values of H are taken from Chapter 4.

are normalized by the respective bin widths. $G(r)$ is plotted against r for (a) the RSM and (b) the SSM in Fig.6.4. The correlation exponent x_l is found ≈ 1 for both models and is independent of the Hurst exponent H of the toppling surfaces of these models[170]. The value of x_l satisfies the scaling relation Eq.6.23 within error bars for both the RSM and the SSM for their respective values of d_ℓ and η_m. Assuming x_l exactly equal to 1 and knowing $d_\ell(\eta_m - 1) = 2 - H$ (Eq.6.17), a scaling relation between d_ℓ and H can be obtained as

$$d_\ell = (3 - H)/2. \tag{6.24}$$

The scaling relation holds true within error bars for the values of d_ℓ and H obtained here for both the RSM and the SSM. Note that d_ℓ is the fractal dimension of a single perimeter at the flooding threshold. However, fractal dimension of all island perimeters at the flooding threshold should be $2 - H$, the Mandelbrot exponent[146] and the fractal dimension of a surface in three dimensions would be $3 - H$[215].

6.2.5 Sandpile avalanche exponents in terms of perimeter exponents

It is now important to obtain the critical exponents describing the macroscopic avalanche properties such as avalanche size distribution in terms of the critical exponents obtained here. The distribution of toppling size $s = \sum_{i=1}^{L^2} S_i$ is given by

$$P(s, L) = s^{-\tau_s} f_s(s/L^{D_s}) \tag{6.25}$$

where τ_s is a critical exponent and D_s is the capacity dimension. Since the avalanches in these sandpile models are compact and the base fractal dimension is 2, a scaling relation $D_s = 2+\chi$[95,96] and consequently $D_s = 5/2+H$ is expected to be valid connecting the exponents describing the surface properties and the capacity dimension. For the RSM and the SSM the values of D_s were known to be 2.86[113] and 2.74[73] respectively. Since the values of H for the RSM and the SSM are 0.35 and 0.21 respectively, the above scaling relations are satisfied for both models within the error bars. The distribution exponent τ_s is also known to be connected to the capacity dimension by a scaling relation $\tau_s = 2 - 2/D_s$[95,96] and hence τ_s can also be expressed in terms of χ or H. Since all the critical exponents describing the properties of island perimeters are also related to χ or H, avalanche size distribution exponents can also be obtained in terms of these exponents. It is interesting to note that the non-equilibrium steady state of sandpile models were usually characterized by studying the probability distributions of certain "macroscopic" avalanche properties such as toppling size s, toppling area a, lifetime t of an avalanche, etc[47,74,75,76,113,123] and performing moment analysis of those probability distributions[73,81,85]. On the other hand, a toppling surface corresponding to an avalanche is defined in terms of a microscopic parameter S_i, the toppling number of individual sand columns. The critical exponents obtained here describe the properties of the island perimeters that appeared at the flooding transition on the toppling surfaces of different sandpile models. The set of critical exponents obtained here are distinctly different for the RSM and SSM as well as they are new exponents in the literature of sandpile models.

6.3 Moment analysis and finite size scaling

Different moments of distributions of the perimeter mass $\tilde{n}(m, L)$ and extension $\tilde{n}(r, L)$ are studied here as a function of the system size L. Since mass m of the largest perimeter should scale as L^{d_ℓ}, the finite size scaling (FSS) form of the distribution $\tilde{n}(m, L)$ for a given system size L is expected to be

$$\tilde{n}(m, L) = m^{-\eta_m} f_\ell(m/L^{d_\ell}). \tag{6.26}$$

Similarly, extension r of the largest perimeter scales as L, the distribution $\tilde{n}(r, L)$ should be given by

$$\tilde{n}(r, L) = r^{-\eta_r} f_\ell(r/L). \tag{6.27}$$

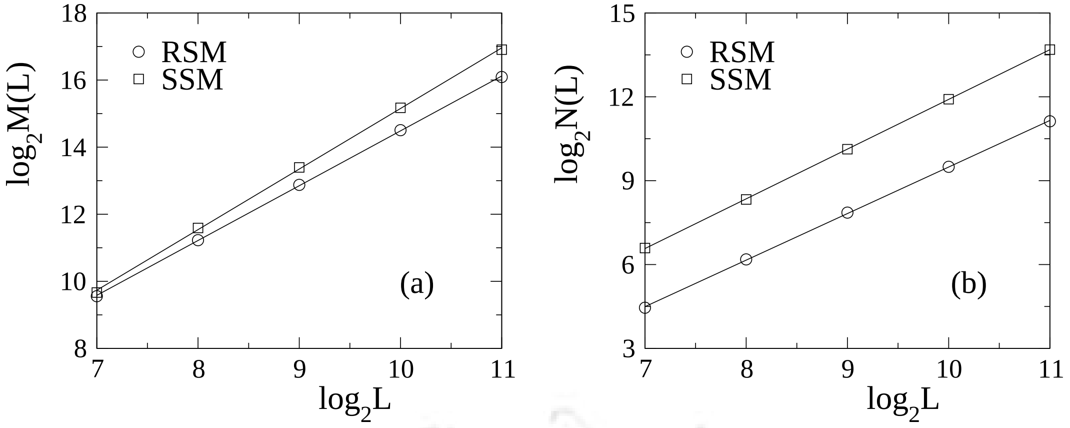

Figure 6.5: (a) Plot of total perimeter mass $M(L)$ at the flooding threshold against system size L for the RSM (○) and the SSM (□). (b) Plot of total number of island perimeters $N(L)$ at flooding threshold against system size L for the RSM (○) and the SSM (□). Solid lines are the best fitted lines through the data points.

The qth moments $\langle m^q(L)\rangle$ and $\langle r^q(L)\rangle$ are defined as

$$\langle m^q(L)\rangle = \frac{\int m^q \tilde{n}(m, L) dm}{\int m \tilde{n}(m, L) dm} \tag{6.28}$$

and

$$\langle r^q(L)\rangle = \frac{\int r^q \tilde{n}(r, L) dr}{\int r \tilde{n}(r, L) dr}. \tag{6.29}$$

Note that the island perimeters are not generated by pinning any site of the perimeter with unit probability and such definitions for calculating the moments of the distributions are appropriate. As per this definition, the first moment is going to be system size independent and the second moment will represent the average of the respective quantities.

The L independence of the first moment is verified by measuring the total perimeter mass $M(L)$ as well as the total number of perimeters $N(L)$ present at the critical flooding threshold for a system of size L. The values of $M(L)$ and $N(L)$ are plotted against the system size L for both the models in Fig.6.5(a) and Fig.6.5(b) respectively. It can be seen that $M(L)$ scales with the system size L with exponents 1.64 ± 0.02 and 1.80 ± 0.02, respectively for the RSM and the SSM. The number of perimeters (or islands) $N(L)$ also scales with the system size L with exponents 1.66 ± 0.02 and 1.78 ± 0.02 for the RSM and the SSM, respectively. It can be noticed that the exponents characterizing the scaling behavior of $M(L)$ and $N(L)$ with L are not only close but also they are approximately $2 - H$ for both models, where H is the Hurst exponent of the respective toppling surfaces. The scaling of $M(L)$ with L at a given flooding level, $M(L) \sim L^{(2-H)}$, is expected and confirms the Mandelbrot scaling[146] as mentioned in the previous section. The scaling of the number of island perimeters $N(L) \sim L^{(2-H)}$, confirms the already observed scaling behaviour for the island numbers at the flooding threshold in the study of flooding transition[171]. The average mass then remains independent of L for both models as expected.

Since the first moment of these distributions are constant, the qth moment of m for $q \geq 2$ is then given by

$$\langle m^q(L)\rangle \approx \int m^{-\eta_m+q} f_\ell(m/L^{d_\ell})dm. \tag{6.30}$$

Defining a scaled variable $z = m/L^{1/d_\ell}$, $\langle m^q(L)\rangle$ can be written in terms of z as

$$\langle m^q(L)\rangle \approx L^{(q+1-\eta_m)d_\ell} \int_0^{z_{max}} f_\ell(z)dz \sim L^{\sigma_q^m}. \tag{6.31}$$

Therefore, σ_q^m can be written as $\sigma_q^m = (q+1-\eta_m)d_\ell$. Since $\eta_m = 1 + (2-H)/d_\ell$ and $d_\ell = (3-H)/2$, the value of σ_q^m is given by

$$\sigma_q^m = \frac{(2-q)H + 3q - 4}{2}. \tag{6.32}$$

Similarly, the qth moment of r for $q \geq 2$ can be defined as

$$\langle r^q(L)\rangle \approx \int r^{-\eta_r+q} f_\ell(r/L)dr. \sim L^{\sigma_q^r} \tag{6.33}$$

Defining a scaled variable $z = r/L$, $\langle r^q(L)\rangle$ can be written in terms of z as

$$\langle r^q(L)\rangle \approx L^{-\eta_r+q} \int_0^{z_{max}} f_\ell(z)dz \sim L^{\sigma_q^r}. \tag{6.34}$$

As the intergral will contribute to a constant, σ_q^r can be written as $\sigma_q^r = q + 1 - \eta_r$. Since $\eta_r = 3 - H$, the value of σ_q^r is given by

$$\sigma_q^r = q - 2 + H. \tag{6.35}$$

Eqs.6.32 and 6.35 represent new scaling relations in terms of the Hurst exponent H of the toppling surface for sandpile models. It can be noted that $\sigma_2^m = 1$, $\sigma_3^m = 1 + d_\ell = (5-H)/2$ and $\sigma_2^r = H$, $\sigma_3^r = 1 + H$. For FSS to be valid, $\sigma_{q+1}^m - \sigma_q^m$

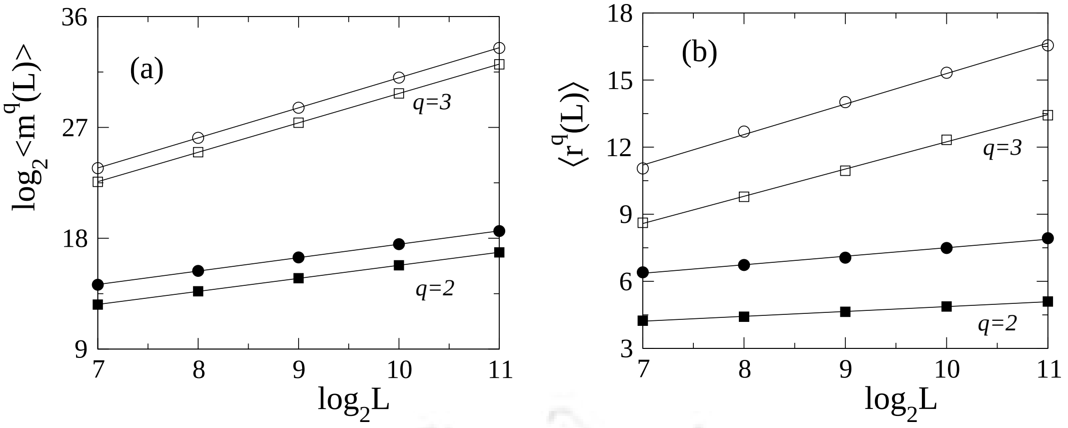

Figure 6.6: (a) Plot of $\langle m^q(L)\rangle$ against L for the RSM and the SSM for $q = 2$ and 3. Symbols used are: (●) and (○) for the RSM and (■), and (□) for the SSM. (b) Plot of $\langle r^q(L)\rangle$ against L for the RSM and the SSM for $q = 2$ and 3. The same symbol set is used for different moments of the respective models. The straight lines are the linear least-square-fit lines.

and $\sigma^r_{q+1} - \sigma^r_q$ must be equal to d_ℓ and 1 respectively for any $q \geq 2$. The values of $\langle m^q(L)\rangle$ and $\langle r^q(L)\rangle$ are measured for $q = 2$ and 3 for both the RSM and the SSM for different system sizes L. In Figs.6.6(a) and (b), $\langle m^q(L)\rangle$ and $\langle r^q(L)\rangle$ are respectively plotted as a function of L in double logarithmic scale for $q = 2$ and 3 for the RSM (circle) and the SSM (square). The values of the exponents σ^m_q and σ^r_q are obtained by linear least square fit to the data points. The values of the exponents are obtained as $\sigma^m_2 = 1.06\pm0.02$, $\sigma^m_3 = 2.38\pm0.03$ and $\sigma^r_2 = 0.37\pm0.02$, $\sigma^r_3 = 1.36\pm0.02$ for the RSM. For the SSM, they are found as $\sigma^m_2 = 1.06 \pm 0.02$, $\sigma^m_3 = 2.48 \pm 0.03$ and $\sigma^r_2 = 0.22 \pm 0.02$, $\sigma^r_3 = 1.22 \pm 0.02$. Numerical values of the critical exponents associated with different moments of perimeter mass and extension distributions for the RSM and the SSM are listed in Table 6.2 and the scaling relations are verified. There are few things to notice. First, for both the RSM and the SSM $\sigma^m_2 \approx 1$ and $\sigma^r_2 \approx H$. They are found to satisfy the scaling relations given in Eqs.6.32 and 6.35. Second, the values of σ^m_3 as well as σ^r_2 are found different for the RSM and the SSM. These exponents then can be taken as characteristic exponents of these sandpile models. Third, since the difference $\sigma^m_3 - \sigma^m_2 \approx d_\ell$ and $\sigma^r_3 - \sigma^r_2 \approx 1$ for the RSM and the SSM, the perimeter mass and extension distribution functions $\tilde{n}(m, L)$ and $\tilde{n}(r, L)$ respectively follow FSS for these models. The FSS form of $\tilde{n}(m, L)$ and $\tilde{n}(r, L)$ are verified by studying the scaled distributions $\tilde{n}(m, L)L^{\eta_m d_\ell}$ and $\tilde{n}(r, L)L^{\eta_r}$ as function of the scaled variables m/L^{d_ℓ} and r/L respectively. In Fig.6.7(a), $\tilde{n}(m, L)L^{\eta_m d_\ell}$ is plotted against the scaled variable m/L^{d_ℓ} for the RSM and the SSM. Similarly, in Fig.6.7(b), $\tilde{n}(r, L)L^{\eta_r}$ is plotted against the scaled variable

Model	σ_2^m	σ_3^m	$\sigma_3^m - \sigma_2^m$	σ_2^r	σ_3^r	$\sigma_3^r - \sigma_2^r$
	(≈ 1)	$(\approx 1 + d_\ell)$	$(\approx d_\ell)$	$(\approx H)$	$(\approx 1 + H)$	(≈ 1)
RSM:	1.06	2.38	1.32	0.37	1.36	0.99
	±0.02	±0.03	±0.05	±0.02	±0.02	±0.04
SSM:	1.06	2.48	1.42	0.22	1.22	1.00
	±0.02	±0.03	±0.05	±0.02	±0.02	±0.04

Table 6.2: Numerical values of the critical exponents associated with different moments of perimeter mass and extension distributions for the RSM and the SSM are listed here. Errors quoted with the critical exponents obtained through the scaling relations are propagation errors. The scaling relations are found valid within error bars.

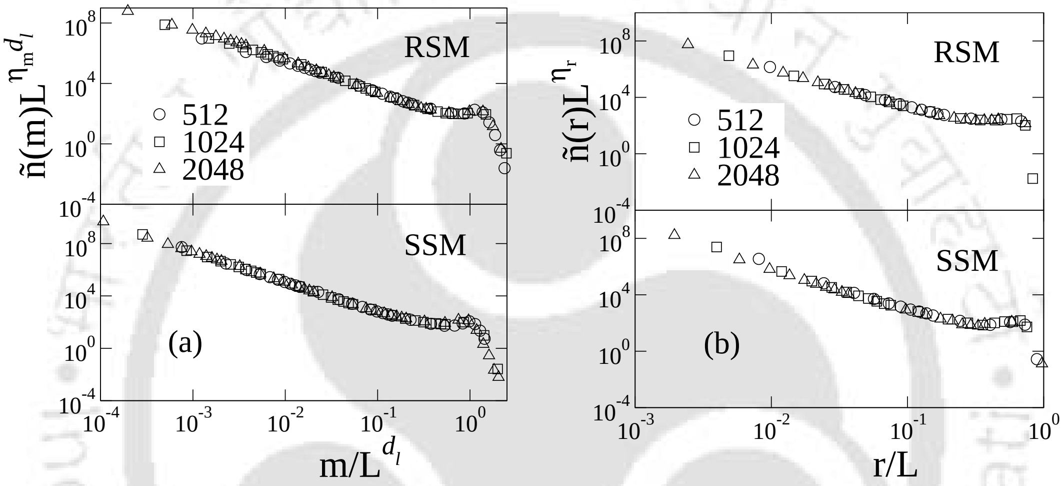

Figure 6.7: (a) Plot of scaled perimeter mass distribution $\tilde{n}(m, L)L^{\eta_m d_\ell}$ against scaled variable m/L_ℓ^d, for the RSM and the SSM for system sizes $L = 512$ (○), 1024 (□) and 2048 (△). A reasonable collapse is observed. (b) Plot of scaled perimeter extension distribution $\tilde{n}(r, L)L^{\eta_r}$ against scaled variable r/L, for the RSM and the SSM for the same system sizes using same symbols. A reasonable data collapse is observed.

r/L for these models. A reasonable data collapse is obtained for both the distribution functions for both models. Thus, the FSS forms assumed for the perimeter mass and extension distributions are correct for these models.

In the above, FSS of the distribution functions are verified at the critical flooding threshold $\Delta S = 0$ only. It is important to verify the FSS form of these distribution functions with ΔS or with $\Delta p = p - p_c$, where p is the area fraction (total island area per lattice site at a given level of flooding) and p_c is the area fraction at the flooding threshold. This has been verified by studying the second moments of m and r as a function of ΔS and Δp for different L. In Figs.6.8(a) and (b), $\langle m^2(\Delta S, L)\rangle$ is plotted against ΔS for the RSM and the SSM respectively. It can be seen that

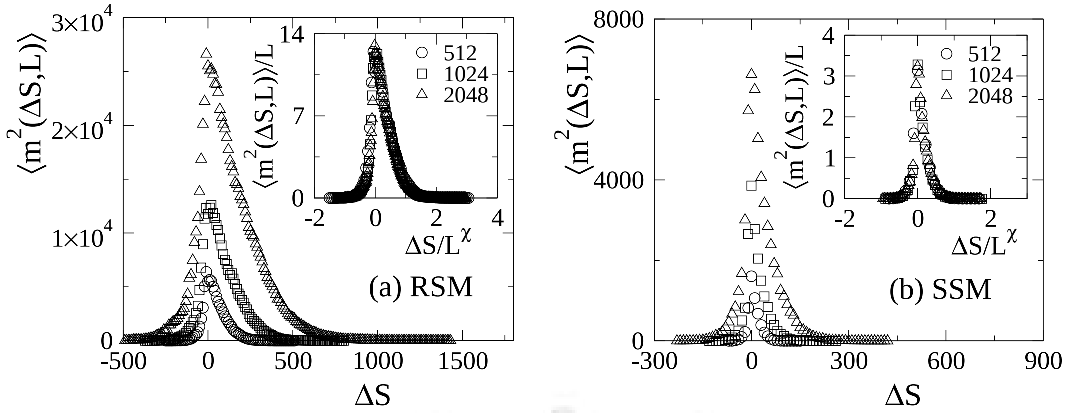

Figure 6.8: Plot of $\langle m^2(\Delta S, L)\rangle$ against ΔS, for (a) the RSM and (b) the SSM for system sizes $L = 512$ (○), 1024 (□) and 2048 (△). In the insets of the respective plots, $\langle m^2(\Delta S, L)\rangle/L$ is plotted against $\Delta S/L^\chi$ and a reasonable collapse is observed for both models.

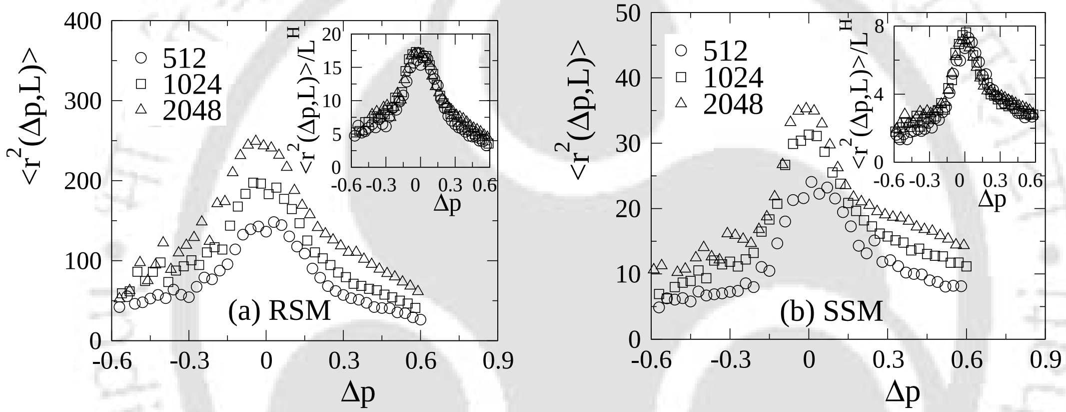

Figure 6.9: Plot of $\langle r^2(\Delta p, L)\rangle$ against Δp, for (a) the RSM and (b) the SSM for system sizes $L = 512$ (○), 1024 (□) and 2048 (△). In the insets of respective plots, $\langle r^2(\Delta p, L)\rangle/L^H$ is plotted against Δp and a reasonable collapse is observed for both models.

$\langle m^2(\Delta S, L)\rangle$ increases with L at the criticality $\Delta S = 0$ for both models as expected and shown in Fig.6.6(a). On the other hand, ΔS should scale in a similar fashion that the toppling surface width $W(L)$ scales with the system size as L^χ. The scaling of $\langle m^2(\Delta S, L)\rangle$ is then expected to be

$$\langle m^2(\Delta S, L)\rangle = L f_m[\Delta S/L^\chi]. \tag{6.36}$$

In the insets of Figs.6.8(a) and (b), $\langle m^2(\Delta S, L)\rangle/L$ is plotted against $\Delta S/L^\chi$ for the RSM and the SSM respectively. A reasonable data collapse is obtained for both models. Similarly, the second moments of r is studied as a function of Δp and L. In Figs.6.9(a) and (b), $\langle r^2(\Delta p, L)\rangle$ is plotted against Δp for different system sizes L

for the RSM and the SSM respectively. It is found that $\langle r^2(\Delta p, L)\rangle$ increases with the system size as L^H for both models as it is shown in Fig.6.6(b) for $\Delta S = 0$. Since in the flooding transition the correlation length exponent $\nu \to \infty$, Δp should be independent of L. Hence, the scaling of $\langle r^2(\Delta p, L)\rangle$ is expected to be

$$\langle r^2(\Delta p, L)\rangle = L^H f_r[\Delta p]. \tag{6.37}$$

In the insets of Figs.6.9(a) and (b), $\langle r^2(\Delta p, L)\rangle / L^H$ is plotted against Δp for the RSM and the SSM respectively. A reasonable data collapse is obtained for both models. Thus, the FSS forms given in Eqs.6.36 and 6.37 are the correct scaling forms. Two important things are to notice. First, the width of the distribution of $\langle m^2\rangle$ and $\langle r^2\rangle$ are increasing with the system size L in contradiction with percolation transition or any other second order phase transition in which one expects a delta function distribution in the thermodynamic limit of the system size. However, this is in agreement with the observation of flooding transition and related to the fact that the flooding thresholds have a wide distribution as $L \to \infty$. Second, if the singularities of $\langle m^2\rangle$ and $\langle r^2\rangle$ at $\Delta p = 0$ is given by $\langle m^2\rangle \sim |\Delta p|^{-\gamma_m}$ and $\langle r^2\rangle \sim |\Delta p|^{-\gamma_r}$, then from the above FSS theory one has $\gamma_m/\nu = 1$ and $\gamma_r/\nu = H$ where ν is the correlation length exponent. Since the ratios are finite and $\nu \to \infty$, both γ_m and γ_r are also expected to be infinitely large as it was observed for the island area exponent[171] in the flooding transition.

6.4 Conclusion

The flooding transition, a continuous phase transition from non-flooding to flooding, can be realized by flooding the self-affine toppling surfaces of stochastic and rotational sandpile models. The critical properties of external perimeters of the islands are studied here in the critical regime of the flooding transition. The island perimeters of the RSM and the SSM are found tortuous, self-similar fractal objects with different fractal dimensions d_ℓ. The probability distributions of perimeter mass and extension are found to exhibit power law scaling at the flooding threshold which corresponds to the criticality of flooding transition. A set of new critical exponents describing the properties of island perimeters are estimated and they have been connected to the roughness exponent χ as well as Hurst exponent H of the toppling surfaces via a hyperscaling. The scaling relations among the critical exponents are found satisfied by the numerical values of the exponents obtained here within error bars. The exponents describing the macroscopic avalanche properties such as avalanche size distribution, capacity dimension of avalanche size, etc are found related to the island perimeter critical exponents through χ or H. The values of the critical exponents are found different for the RSM and the SSM. The scaling forms assumed for the contour loop properties are verified by FSS at the flooding threshold as well as with ΔS and Δp. The width of the distribution of certain perimeter properties are found increasing with the system size L in contradiction with percolation transition in which one expects a delta function distribution in $L \to \infty$ limit. The percolation type critical exponents are found infinitely large but their ratio to the correlation length exponent ν is found finite. Thus, the universality class of island perimeters not only different from the percolation hull universality class but also different for sandpile models with different symmetries in the toppling rules.

Chapter 7

Symmetry, crossover and universality

In the equilibrium critical phenomena, the universality class of thermodynamic systems in the same spatial dimension is independent of the lattice structure or type of interactions. The universality class is determined by the symmetry of the order parameter or the number of components present in the order parameter in a given space dimension. However, it was interestingly observed that whenever there is an external constraint applied on the equilibrium lattice statistical model, the universality class of the model has changed. For example, self-avoiding walk (SAW)[216], directed SAW[103,104], and spiral SAW[106,107] belong to different universality classes. Percolation[178], directed percolation[102], spiral percolation[110], directed-spiral percolation[111,112] all belong to different universality classes. This is also the case for non-equilibrium lattice models. BTW sandpile model, directed sandpile model[51], SSM[50], RSM[113] all belong to different universality classes. It is always important to know how the universality classes are determined for a given set of equilibrium or non-equilibrium models. In a recent field theoretic study by Rossi *et al.*[217] in the context of absorbing state phase transitions, it was shown that the universality class of a sandpile model is determined by the underlying symmetry present in the system. In this chapter, an effort has been made to classify the sandpile models studied here according to their inherent symmetry and verify their corresponding universality class. It was observed that such a classification is possible for a group of rotational and a group of stochastic models. Since the rotational models are intrinsically stochastic and the stochastic models are extrinsically stochastic, it is expected that a cross over form one model to the other should be possible in a suitable parameter space. Finally such a parameter space is identified tuning which a crossover from RSM to SSM is obtained.

7.1 Symmetries in different sandpile models

It was observed that the universality classes of certain sandpile models remain unaffected even if the details of these models are changed within the same symmetry of the model. For example, different versions of BTW models[4,47,78], different SSMs[48,50] or different RSMs[113,123] preserve their own universality classes. In the following, sandpile models of two different symmetries such as stochastic and rotational are considered. The universality classes of two stochastic models, MSM and SSM, and three rotational models, RSM, RSM1 and RSM2, will be classified as per their symmetries present in the toppling rule. The differences in the stochastic models and the rotational models are briefly mentioned here. In the MSM, all the sand grains of the active site are randomly given to all its NNs whereas in the SSM only two sand grains are given to two randomly selected NNs until it becomes under critical. In the RSM, the rotational direction was determined by the direction from which the last sand grain arrived to the active site. In the RSM1 it was decided by the direction from which a sand grain arrived to a site to make it active whereas in the RSM2, it was decided by a randomly selected direction from which sand grains arrived to the active site above and equal to the critical height.

7.1.1 Critical exponents of different sandpile models

In last few chapters, a large number of critical exponents for the sandpile models are defined and estimated. Some of them are already known and available in the literature. For example, the critical exponents describing the distributions of avalanche related quantities for the MSM and the SSM are already known[50,75,76,77]. In Chapter 3, the values of the critical exponents describing the distributions of avalanche related quantities were estimated for the RSM1 and RSM2[123]. From Chapter 4 onwards, several new critical exponents were introduced such as the roughness exponent χ describing the scaling of the width of the toppling surface $W(L)$ with the system size L, the Hurst exponent H describing the two point height-height correlation function, the critical exponents related to the flooding transition as well as to the island perimeters for the SSM and RSM. However, such exponents were not estimated either for the stochastic MSM or for the rotational RSM1 and RSM2. In this section, these new exponents will be determined for the MSM, RSM1 and RSM2 and their universality classes will be classified as per the symmetry present in their toppling rules.

Roughness exponent: The width, $W(L)$ of the toppling surface is defined in

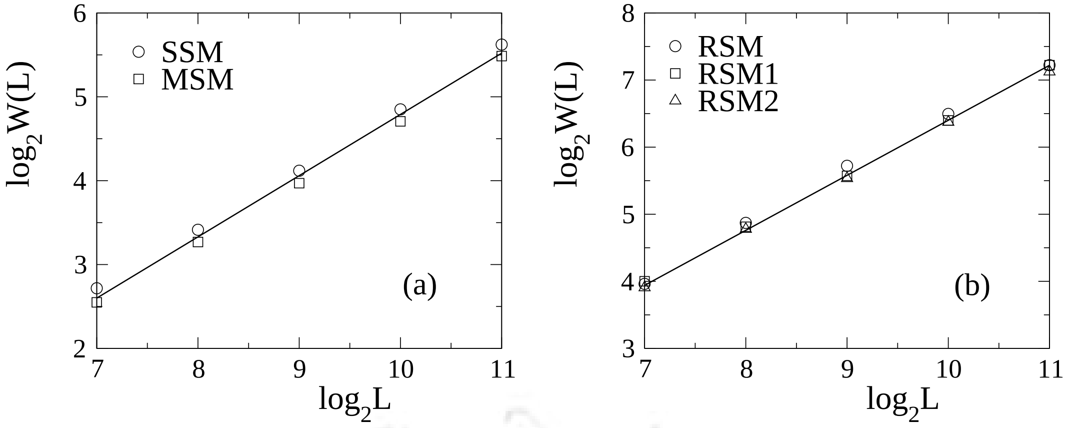

Figure 7.1: (a) Plot of $W(L)$ against L for the SSM (○) and the MSM (□). (b) Plot of $W(L)$ against L for the RSM (○), the RSM1 (□) and the RSM2 (△). The solid lines in the plots (a) and (b) have slopes 0.73 and 0.82 respectively.

Chapter 4 and scales with the system size L as

$$W(L) \sim L^{\chi} \tag{7.1}$$

where χ is the roughness exponent. In Fig.7.1(a), $W(L)$ is plotted against L for the MSM and the data are compared with that of SSM. In Fig.7.1(b), $W(L)$ is plotted against L for the RSM1 and the RSM2 and the data are compared with that of the RSM. It can be seen that the scaling given in Eq.7.1 is satisfied for all the models. The value of χ obtained for the MSM $\chi = 0.73 \pm 0.02$ is same as that of the SSM. Similarly, the value of χ obtained for both RSM1 and RSM2 0.81 ± 0.02 is same as that of the RSM. Therefor, the values of χ for the stochastic models the SSM and the MSM are same within error bars. Similarly, for the rotational models the values of χ are also same within error bars. The minute details in the toppling rule under the same symmetry does not able to change the scaling behaviour of the roughness of the toppling surfaces though the absolute values may differ.

Hurst exponent: The toppling surfaces of the RSM and the SSM were found to be self-affine with distinctly different Hurst exponent H. The toppling surfaces of the stochastic models the MSM and the SSM must have the same H in order to belong to the same universality class. Similarly the toppling surfaces of the RSM1 and the RSM2 should have the same H as that of the RSM. The Hurst exponents of the toppling surfaces are determined by obtaining the power spectrum $S(\mathbf{k})$ of

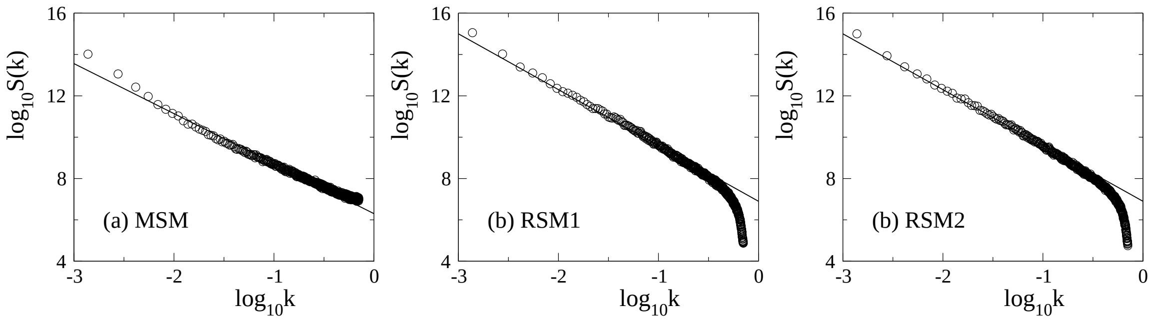

Figure 7.2: Plot of $S(k)$ against k for (a) the MSM, (b) the RSM1 and (c) the RSM2 for $L = 2048$. The straight lines are the best fitted lines.

the toppling surface which scales with the wave vector $\mathbf{k}$ as

$$S(\mathbf{k}) \sim |\mathbf{k}|^{-2(1+H)} \tag{7.2}$$

as given in chapter 4. In Fig.7.2, $S(\mathbf{k})$ is plotted against $|\mathbf{k}|$ for the MSM, the RSM1 and the RSM2 for their respective toppling surfaces extracted from the spanning avalanches on $L = 2048$. It can be seen that the scaling given in Eq.7.2 is satisfied for all the models. The values of the Hurst exponents H obtained are 0.21 ± 0.01 for the MSM, 0.35 ± 0.01 for the RSM1 and 0.35 ± 0.01 for the RSM2. It can be noticed that the values of H are same for the MSM and the SSM and similarly they are same for all the rotational models the RSM, the RSM1 and the RSM2. Consequently, the stochastic models belong to same universality class and the rotational models belong to the RSM universality class.

Scaling of average island area: As seen in Chapter 5, the critical exponents of flooding transition[171] are possible to define in terms of the Hurst exponent H of the toppling surface and the fractal dimension D_f of islands at the critical flooding. Since the islands are compact and $D_f \approx 2$ for all the models considered here, then the value of H will define the universality class of a model. It is just now observed that the value of H is able to distinguish the universality class of the stochastic and rotational models distinctly. The average island area $\langle a_0 \rangle$ at the flooding transition point $\Delta S = 0$ also scales with the system size L as

$$\langle a_0 \rangle \sim L^H \tag{7.3}$$

as discussed in Section 5.6. Hence, measuring the average island area $\langle a_0 \rangle$ as a function of the system size L at $\Delta S = 0$, the scaling given in Eq.7.3 as well as the value of Hurst will be reconfirmed for these models. In Fig.7.3(a), $\langle a_0 \rangle$ is plotted

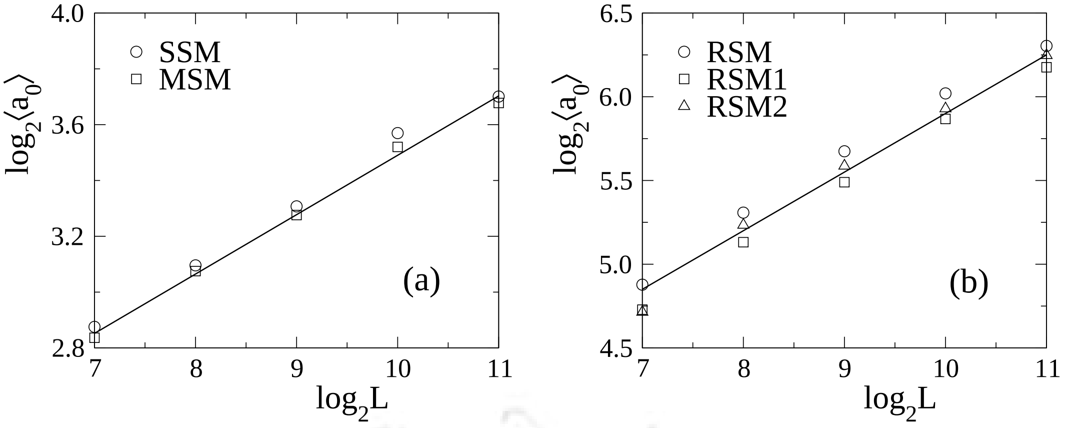

Figure 7.3: (a) Plot of $\langle a_0\rangle$ against L for the SSM (○) and the MSM (□). (b) Plot of $\langle a_0\rangle$ against L for the RSM (○), the RSM1 (□) and the RSM2 (△). The solid lines in the plots (a) and (b) have slopes 0.21 and 0.35 respectively.

against L for the MSM and compared with that of the SSM. The straight line with a slope of 0.21 in this plot is guide to eye. In Fig.7.3(b), $\langle a_0\rangle$ is plotted against L for the RSM1 and the RSM2 and compared with that of the RSM. The straight line with slope 0.35 in this plot is guide to eye. It can be seen that $\langle a_0\rangle$ for all models follow the scaling given in Eq.7.3 almost with the same Hurst exponent of the model of respective symmetries. Thus, the values of the Hurst exponents do not depend on the minute details of the toppling dynamics within the same symmetry of the models. Since all the critical exponents related to the flooding transition depend on the Hurst exponent H of the toppling surface and the fractal dimension $D_f(\approx 2)$ of critical spanning islands, the universality class of flooding transition as well as that of the sandpile models should remain unchanged within the same symmetry of the model.

Fractal dimension of island perimeter: Though the island area is compact, the perimeter of an island is found to be fractal. The critical properties of the island perimeters at the flooding threshold are also found to be determined by the perimeter fractal dimension d_ℓ and the Hurst exponent H of the toppling surfaces as seen in Chapter 6. Since the value of H is already found to classify the universality class of these models as per their symmetries in the toppling rule, the perimeter fractal dimension d_ℓ is expected to do the same. The perimeter mass m scales with its extension r as

$$m \sim r^{d_\ell} \tag{7.4}$$

where d_ℓ is fractal dimension of the island perimeter as given in Chapter 6. In order to obtain d_ℓ, $\langle m\rangle_r$ is studied as a function of r for the system size $L = 2048$. In

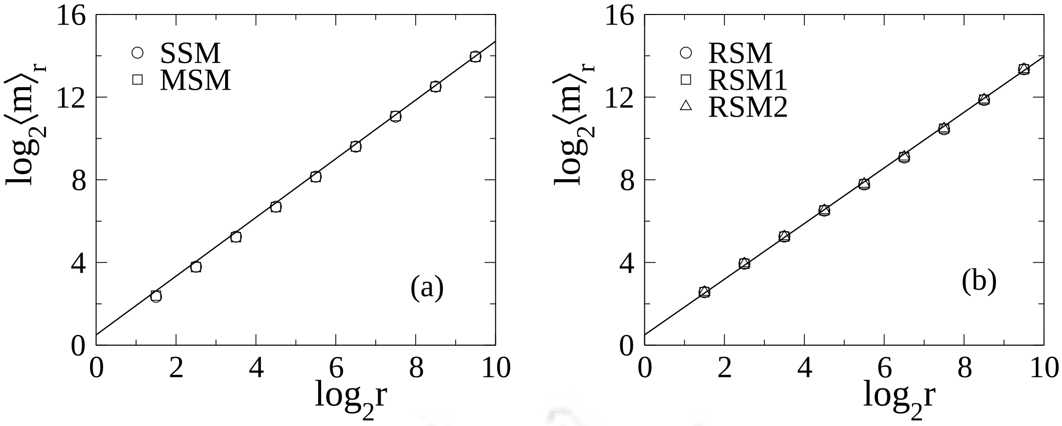

Figure 7.4: (a) Plot of $\langle m\rangle_r$ against r for the SSM (○) and the MSM (□). (b) Plot of $\langle m\rangle_r$ against r for the RSM (○), the RSM1 (□) and the RSM2 (△). The solid lines in the plots (a) and (b) have slopes 1.42 and 1.33 respectively.

Fig.7.4(a), $\langle m\rangle_r$ is plotted against r in double logarithmic scale for the MSM and compared with that of the SSM. The value of d_ℓ for the MSM obtained from the linear least square fitting to the data points is 1.42 ± 0.01 which is same as that of the SSM and shown by a line in Fig.7.4(a). In Fig.7.4(b), $\langle m\rangle_r$ is plotted against r for the RSM1 and the RSM2 and compared with that of the RSM. For both the RSM1 and the RSM2, the values of d_ℓ obtained are 1.33 ± 0.01 which is equal to that of the RSM and a line of the same slope is placed on the data points. For all these models the values of d_ℓ and H obtained here follow the scaling relation relation $d_\ell = \frac{3-H}{2}$ within error bars.

The stochastic models, MSM and SSM, have one set of critical exponents whereas the rotational models, RSM, RSM1 and RSM2, have another set of critical exponents. Therefore, the values of the critical exponents obtained for a group of sandpile models classify them into two universality classes according to their underlaying symmetries present in the toppling rule and do not depend of the minute details of toppling rules under the same symmetry. Universality class of sandpile models exhibiting self-organized criticality then can be classified as per the underlying symmetry present in the toppling rules as it was demonstrated by Rossi *et al.*[217].

7.2 Study of crossover: RSM to SSM to RSM

Since the universality class of sandpile models are determined by the symmetries present in the toppling rule, it is intriguing to study the possibility of crossover form one universality class to another in a suitable parameter space. In the literature of sandpile models, crossover from one sandpile universality class to other was already reported. For example, a crossover from BTW to Zhang model was observed by O. Biham *et al.*[47] by controlling the fraction of energy to be distributed to the NNs in a toppling. A crossover from Zhang model to MSM was studied by Lübeck[81] by controlling the threshold condition. Crossover from DSM to DP (directed percolation) class was observed by Tadić and Dhar introducing a stickiness parameter in the DSM[218]. It is therefore interesting to look for a suitable parameter to study a crossover from the RSM to the SSM. In the RSM, as described in Chapter 2, a clockwise rotational filed (CRF) is assigned to all lattice sites. A quenched-randomness can be introduced in the RSM under CRF by adding an anti-clockwise rotational field (ACRF) to certain randomly chosen sites. A quenched-random rotational sandpile model (QRRSM) is constructed by introducing ACRF to a fraction p of sites of original RSM. The critical properties of QRRSM are studied as a function of p to explore the possibility of a crossover from the RSM to the SSM.

7.2.1 The model QRRSM

QRRSM[219,220] is defined on a two dimensional ($2d$) square lattice of size $L \times L$. Randomness in rotational field is introduced by randomly assigning a fraction p of total sites in a lattice with anti-clockwise rotational field and rest of the sites (fraction $q = (1 - p)$ of total sites) with clockwise rotational field. The distribution of ACRF remains unchanged during the time evolution and hence this can be considered as a quenched random configuration. As in RSM, each lattice site is assigned with a positive integer h_i representing the height of the sand column. Initially, all h_is are set to zero. The system is driven by adding sand grains, one at a time, to randomly chosen lattice sites i. The critical height is taken as $h_c = 2$. As the height of the sand column of a site $h_i \geq h_c$, the site become active and bursts into a toppling activity. The first toppling rule remains the same as that of RSM. The successive rotational toppling rule depends on the nature of the active site whether it is assigned to CRF or ACRF. For the CRF active site the toppling rule is given by

$$h_i \to h_i - 2, h_j \to h_j + 1 \text{ and } j = d_i, d_{i+1} \tag{7.5}$$

and for the ACRF active site the toppling rule is given by

$$h_i \to h_i - 2, h_j \to h_j + 1 \text{ and } j = d_i, d_{i-1} \tag{7.6}$$

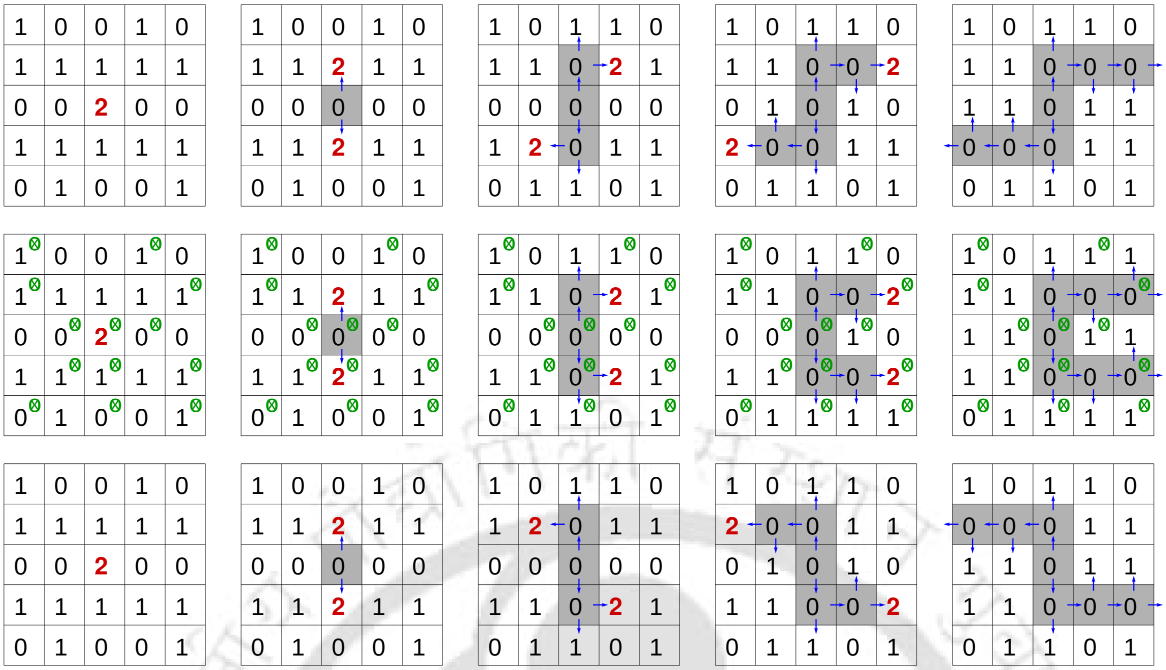

Figure 7.5: QRRSM is demonstrated on a 5×5 square lattice taking an arbitrary initial configuration with the central site as an active site for $p = 0$ in top panel, $p = 0.5$ in middle panel and $p = 1$ in bottom panel. The active sites with height 2 are represented by red bold numbers. In the middle panel, squares containing encircled cross in green have the anti-clockwise rotational field and others have clockwise rotational field. In the top and bottom panels all the lattice sites have clockwise and anti-clockwise rotational field respectively. The blue arrows represent the flow of sand grain during avalanche. The propagation of the avalanches is shown using the grey shade. For all three cases the toppling sizes are 7 and the number of parallel updates required to complete the avalanche are 4.

where d_i is the direction from which the last grain was received by the active site. If the index j becomes greater than 4 it is taken to be 1 and if it becomes 0 it is taken to be 4. The toppling rule of QRRSM is demonstrated in Fig.7.5 for three different values $p = 0$, $p = 1/2$, and $p = 1$ on a 5×5 square lattice with the central site as the initial active site. The directions of sand flow are represented by arrows. The fraction $p = 0$ corresponds to the original RSM under CRF shown in the top panel of Fig.7.5 and $p = 1$ corresponds to a RSM under completely ACRF shown in the bottom panel of Fig.7.5. Whereas, $p = 1/2$ corresponds to a disorder situation where half of the sites are assigned with opposite field and it is shown in the middle panel of Fig.7.5. The active sites with ACRF are marked by encircled crosses in green. In all three cases, the system becomes under critical after four parallel updates. The final configurations of the toppled sites (shown under shadow) are different for different

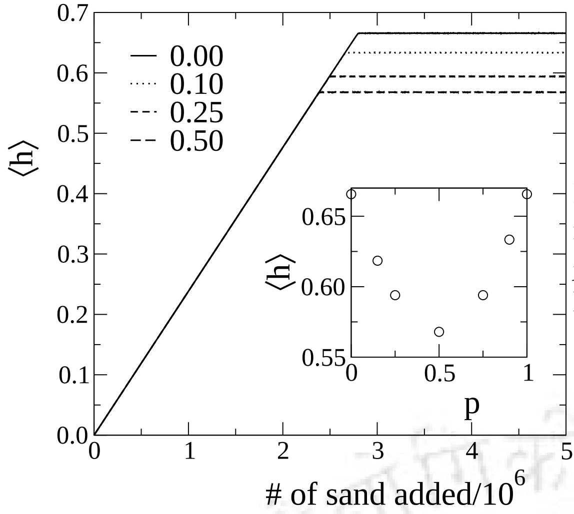

Figure 7.6: Plot of $\langle h \rangle$ as a function of number of sand grains added for QRRSM for $p = 0.00, 0.10, 0.25$ and 0.50 for $L = 2048$. In the inset, the steady state $\langle h \rangle$ is plotted against p for $L = 2048$.

p values. The final configuration changes from a structure with clockwisely rotated arms for $p = 0$ to a structure with anti-clockwisely rotated arms for $p = 1$. However, the structure corresponding to $p = 1/2$ is different from both the structures obtained for $p = 0$ and $p = 1$. As RSM, the QRRSM is non-abelian and it has no toppling balance.

QRRSM is studied for different system sizes starting form $L = 128$ to 2048 in multiple of 2 for $p = 0.00, 0.10, 0.25, 0.50, 0.75, 0.90$ and 1.00. The steady state of the QRRSM is also defined as the constant average height $\langle h \rangle = \frac{1}{L^2}\sum_i^{L^2} h_i$ of the sand columns. In Fig.7.6 $\langle h \rangle$ is plotted against number of sand grains added for $L = 2048$ for different p. For all different p the systems reach their respective stable steady state after adding a sufficiently large number of sand grains. The average steady state height of the sand columns are calculated when the system reaches a steady state. In the inset of Fig.7.6, $\langle h \rangle$ is plotted against p for $L = 2048$. It can be seen that the steady state average height of the sand columns decreases as p is increased from 0 to 0.5 and attains a minimum value at $p = 0.5$ and then increases with increasing p. The value of $\langle h \rangle$ at $p = 1$ attains the same value as that of $p = 0$ and it is found symmetric about $p = 0.5$.

7.2.2 Avalanche cluster morphology and toppling surface

Typical avalanche clusters obtained in the QRRSM for $p = 0.0, 0.5$ and 1.0 at their respective steady states are shown in the top panel of Fig.7.7. The avalanche clusters are generated on a 128×128 square lattice. Toppling numbers are binned into 6 equal intervals and the different colours represent the different bins of toppling

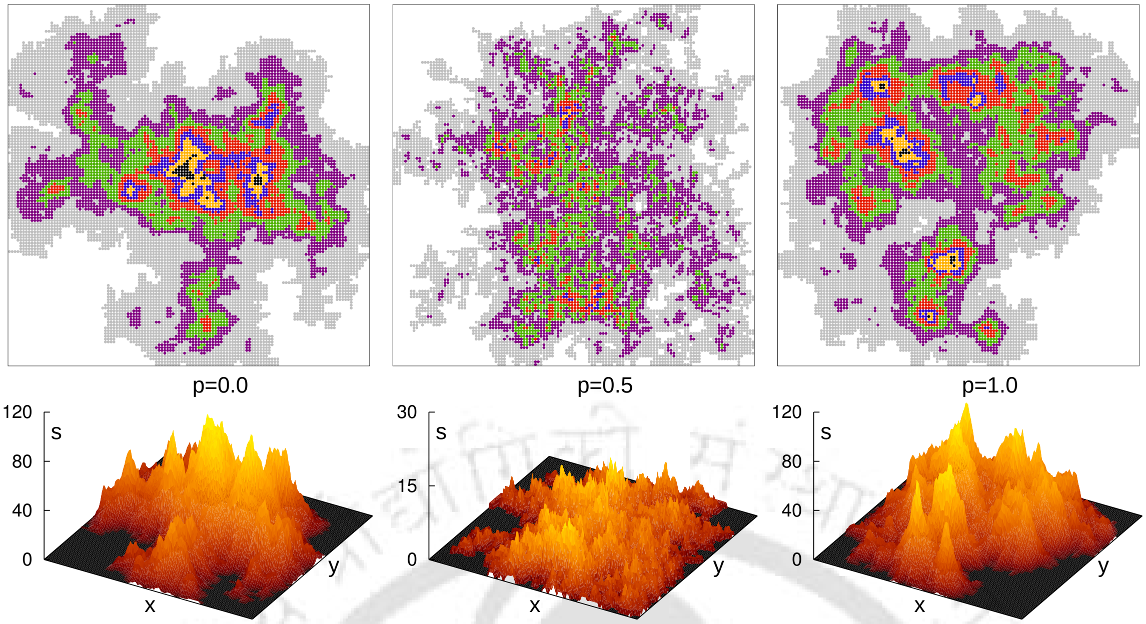

Figure 7.7: In the top panel, typical avalanche clusters generated on a square lattice of size $L = 128$ are shown for $p = 0.0, 0.5$ and 1.0. Toppling numbers are binned into 6 equal intervals and the different colours represent the different bins of toppling numbers. The lowest bin of toppling numbers is represented by grey colour, whereas maroon, green, red, blue, yellow and black colour represent the next higher bins. In the lower panel, toppling surfaces corresponding to the above avalanche clusters are presented. The highest toppling number corresponds to light brown colour and the lower toppling numbers are represented by darker and darker brown colours.

numbers. Grey colour represent the lowest bin of toppling numbers, maroon, green, red, blue, yellow and black colours represent the next higher bins. The avalanche cluster corresponding to $p = 0.0$ and 1.0 consists of random superposition several BTW type concentric zones of lower and lower toppling numbers around different maximal toppling zones whereas the avalanche cluster of QRRSM for $p = 0.5$ is highly fluctuating and several large toppling numbers appear randomly here and there in the avalanche cluster. It can also be seen from the $2d$ structure that the avalanche cluster for $p = 0.5$ is random like the SSM avalanche clusters. Thus as p is increased from 0 the avalanche structure changes and becomes that of the SSM at $p = 0.5$. As p is further increased to 1.0 the avalanche structure become that of the RSM. The toppling surfaces corresponding to the avalanches shown above for $p = 0.0, 0.5$ and 1.0 are given in the lower panel of Fig.7.7. Light brown colour represents higher toppling number whereas dark brown colour represents lower toppling number and the intensity is varied continuously. It can be seen that the toppling surfaces at $p = 0$ and $p = 1$ are very similar and corresponds to the

RSM toppling surface whereas that corresponding to $p = 0.5$ is very different. The toppling surfaces for $p = 0.5$ is similar to that of the SSM except the toppling heights which are less than that of the SSM.

It is now important to characterize the toppling surfaces of QRRSM for different values of p in order to understand the effect of quenched randomness in the rotational field. One thousand spanning avalanche clusters are collected at the steady state for each p value for every system sizes following the same procedure of data collection mentioned in the previous chapters. In the following, the toppling surface will be characterized and the probability distribution functions of several avalanche properties will be studied.

7.2.3 Characterization of toppling surfaces

The toppling surfaces are characterized by studying the roughness and the self-affine properties.

Roughness exponent: The roughness of toppling surfaces can be characterized by studying the width $W(L)$ defined in Eq.4.12 as a function of system size L. The scaling of $W(L)$ with L is given as

$$W(L) \sim L^{\chi} \tag{7.7}$$

where χ is the roughness exponent. Surfaces width $W(L)$ is calculated for different system sizes $L = 128$ to 2048 for different values of p between 0 and 1. In Fig.7.8, $W(L)$ is plotted against the system size L in double logarithmic scale for QRRSM for $p = 0.0, 0.5$ and 1.0. It can be seen that the surface roughness scales with system size L as expected. The values of χ are obtained by linear least square fitting to the data points. The values of χ are plotted as a function of p in Fig.7.9. It can be seen that the values of χ for both $p = 0.0$ and 1.0 are found as 0.82 ± 0.02 which is same as that of the RSM. However the value of χ for $p = 0.5$ is obtained as 0.70 ± 0.02 which is equal to that of the SSM within error bar. Moreover, a continuous change in the values of χ is observed with p.

Hurst exponent: Wrinkle rough toppling surfaces can also be characterized by $C(r)$, the correlation between toppling numbers of two sand columns separated by a distance r. The scaling of $C(r)$ with r is given by

$$C(r) \sim r^{2H} \tag{7.8}$$

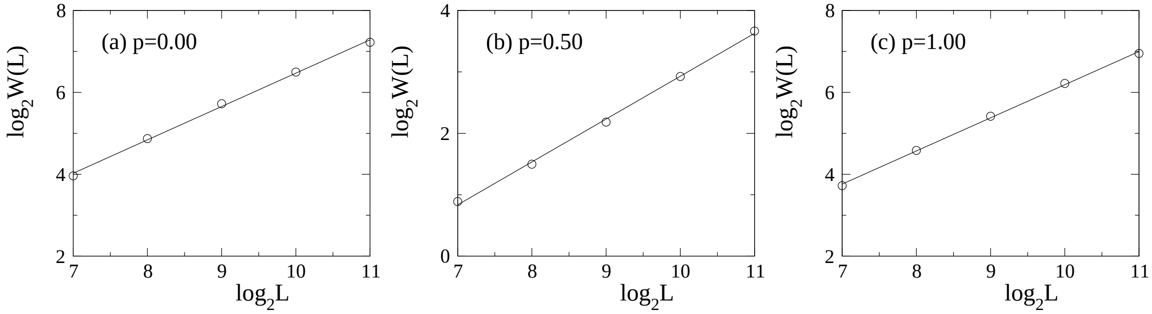

Figure 7.8: Plot of $W(L)$ against L for the QRRSM for (a) $p = 0.0$, (b) $p = 0.5$ and (c) $p = 1.0$. The straight lines are the linear least square fitted lines through the data points.

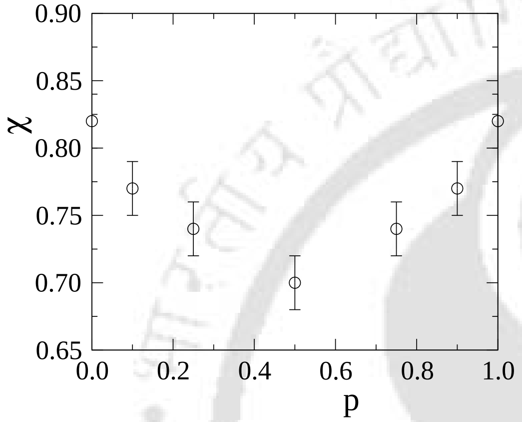

Figure 7.9: Plot of χ against p for the QRRSM. The value of χ continuously changes from the RSM value at $p = 0.0$ and 1.0 to the SSM value at $p = 0.5$.

where H is the Hurst exponent. The integrated correlation function $I(R)$ should scale as

$$I(R) = \int_0^R C(r)dr \sim R^{1+2H} \tag{7.9}$$

as mentioned in Chapter 4. In Fig.7.10, the integrated correlation function $I(R)$ is plotted against distance R in double logarithmic scale for toppling surfaces of the QRRSM for $p = 0.0, 0.5$ and 1.0 for different system sizes L. It can be seen that $I(R)$ follows a power law scaling with R. For a given p, $I(R)$ scales with R in a similar way for different system sizes L. Plots of $I(R)$ for different L are vertically shifted because it has some L dependent prefactor $A(L)$ which was found to scale linearly with L as it was discussed in Chapter 4. The slopes of the power law scaling are obtained by least square fit to the data of largest linear region for each values of p. The values of the Hurst exponent H obtained from the values of the slopes of $I(R)$ versus R plot, are plotted against p in Fig.7.11. It can be seen that the values of H of the toppling surfaces for both $p = 0$ and 1 are approximately 0.35 which is equal to that of the RSM. However, the value of H for toppling surfaces of the QRRSM for $p = 0.5$ is approximately 0.21 which is equal to that of the SSM. As $p \to 0.5$,

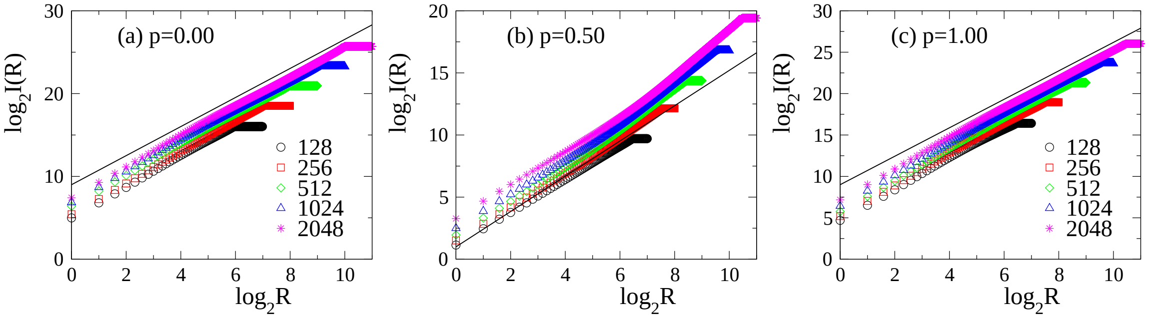

Figure 7.10: Plot of $I(R)$ against R for system sizes $L = 128$ (○), 256 (□), 512 (◇), 1024 (△) and 2048 (✻) for QRRSM for (a) $p = 0.0$, (b) $p = 0.5$ and (c) $p = 1.0$. The straight lines have slopes in plots (a), (b) and (c) are 1.70, 1.42 and 1.70 respectively.

the values of H continuously changes from the RSM value at $p = 0$ and $p = 1$ to the SSM value at $p = 0.5$. Since the values of $H < 0.5$ for the toppling surfaces of the QRRSM for any value of p, the surfaces are self-affine and anti-correlated. The scaling relation $\chi = \frac{1}{2} + H$ is verified for all p and found satisfied within error bars.

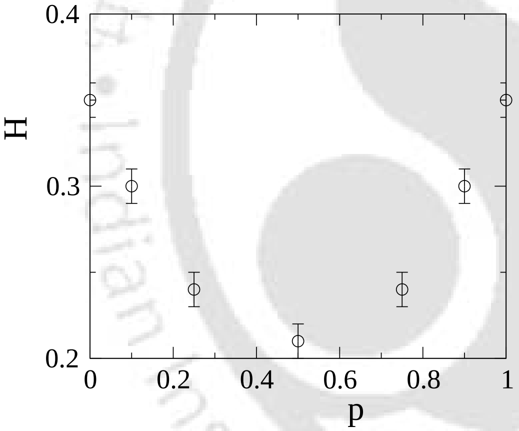

Figure 7.11: Plot of H against p for the QRRSM. The value of H continuously changes from the RSM value at $p = 0.0$ and 1.0 to the SSM value at $p = 0.5$.

Hence, it is observed that the values of χ as well as H change continuously as the fraction of ACRF, p, is changed. The values of these exponents at $p = 0$ and $p = 1$ correspond to that of the RSM and at $p = 0.5$ they correspond to that of the SSM. Since χ and H define all the critical exponents of the flooding transition and island perimeters, the critical exponents of the flooding transition and that of the island perimeters are also expected to have continuous crossover from the RSM at $p = 0$ to the SSM at $p = 0.5$. Therefore, a continuous crossover from RSM universality class at $p = 0$ and $p = 1$ to the SSM universality class at $p = 0.5$ is possible, controlling the ACRF fraction p.

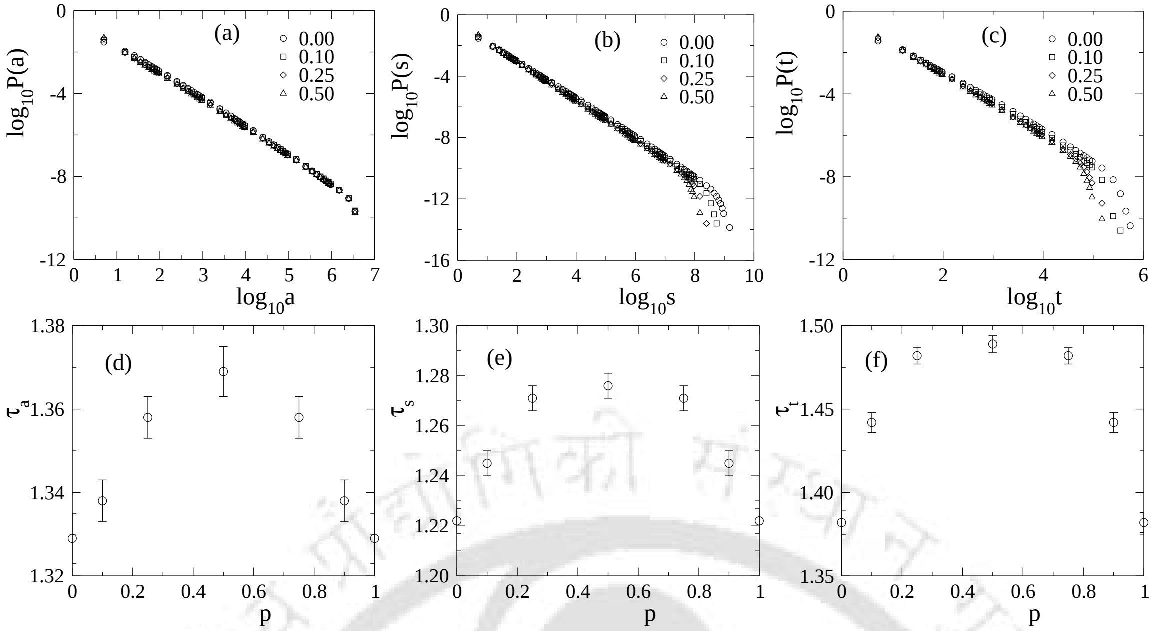

Figure 7.12: Plot of (a) $P(a)$, (b) $P(s)$ and (c) $P(t)$ against a, s and t in double logarithmic scale for the QRRSM with $p = 0.0(\bigcirc)$, $p = 0.1(\Box)$, $p = 0.25(\diamond)$ and $p = 0.50(\triangle)$ for system size $L = 2048$. All three distributions $P(a), P(s)$ and $P(t)$ demonstrate power law scaling at the steady state of the QRRSM with different p. Plot of (d) τ_a, (e) τ_s and (f) τ_t against p. The value of τ_a, τ_s and τ_t continuously changes from the RSM value at $p = 0.0$ and 1.0 to the SSM value at $p = 0.5$.

7.2.4 Probability distribution of avalanche properties

Probability distribution : As the roughness exponent χ and Hurst exponent H show a continuous crossover from the RSM to the SSM with p, the distribution exponents of the avalanche related quantities such as toppling size (s), area (a), and lifetime (t) are also expected to exhibit the same crossover. The probability distribution of s, a and t are studied for different p values on different system sizes L and they are expected to scale as

$$P(x, L) \sim x^{-\tau_x} \mathsf{f}(x/L^{D_x}) \tag{7.10}$$

where τ_x is the corresponding critical exponent and $x \in \{s, a, t\}$. The function $\mathsf{f}(x/L^{D_x})$ is the finite size scaling function where D_x is the capacity dimension. The probability distributions of s, a and t obtained for the QRRSM for different values of p for the system size $L = 2048$ are shown in Figs.7.12(a), (b) and (c) respectively. These distributions are found to obey power law scaling for all p and consequently the QRRSM exhibit SOC for all p. The characteristic exponents τ_a, τ_s and τ_t for

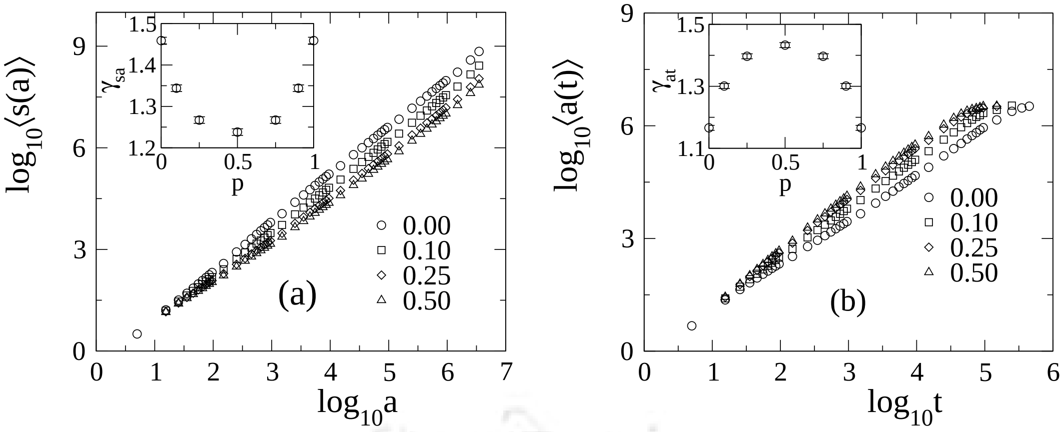

Figure 7.13: (a) $\langle s(a)\rangle$ and (b) $\langle a(t)\rangle$ are plotted against a and t respectively in double logarithmic scale for the QRRSM with $p = 0.0(\bigcirc)$, $p = 0.1(\Box)$, $p = 0.25(\diamond)$ and $p = 0.50(\triangle)$ for system size $L = 2048$. The values of γ_{sa} and γ_{at} are plotted against p in the respective insets. The values of γ_{sa} and γ_{at} continuously changes from the RSM value at $p = 0.0$ and 1.0 to the SSM value at $p = 0.5$.

different p are determined from the linear part of the respective distributions through linear least square fitting of the data points. The values of τ_a, τ_s and τ_t are plotted against p in Figs.7.12(d), (e) and (f) respectively. The error bar associated with each exponent values include both statistical and fitting error. It can be noticed that the exponent values continuously change from the exponent values of the RSM[113] at $p = 0$ or $p = 1$ to the exponent values of the SSM[113] at $p = 0.5$. QRRSM with $p = 0.5$ is then have the same scaling behaviour as that of the SSM. Thus, as the randomness in rotational field $p \to 0.5$ the robustness of the broken mirror symmetry present in the RSM slowly broke down and it completely vanishes at $p = 0.5$ causing a continuous crossover from the RSM ($p = 0$ or $p = 1$) to SSM ($p = 0.5$)[219,220].

Conditional expectations : In order to further confirm the continuous crossover from the RSM to the SSM as $p \to 0.5$ from 0 or 1, the critical exponents describing the conditional expectation values[121] of the avalanche properties as a function of p are determined. As observed in Chapter 2, the conditional expectation values $\langle s(a)\rangle$ and $\langle a(t)\rangle$ scale with their arguments a and t as

$$\langle s(a)\rangle \sim a^{\gamma_{sa}}, \quad \langle a(t)\rangle \sim t^{\gamma_{at}} \tag{7.11}$$

where γ_{sa} and γ_{at} are the critical exponents. In Figs.7.13 (a) and (b), $\langle s(a)\rangle$ and $\langle a(t)\rangle$ are plotted against a and t respectively for $p = 0.0, 0.10, 0.25$ and 0.50 for system size $L = 2048$. The values of the exponents γ_{sa} and γ_{at} for different p are obtained by least square fitting to the linear region of the data points and are

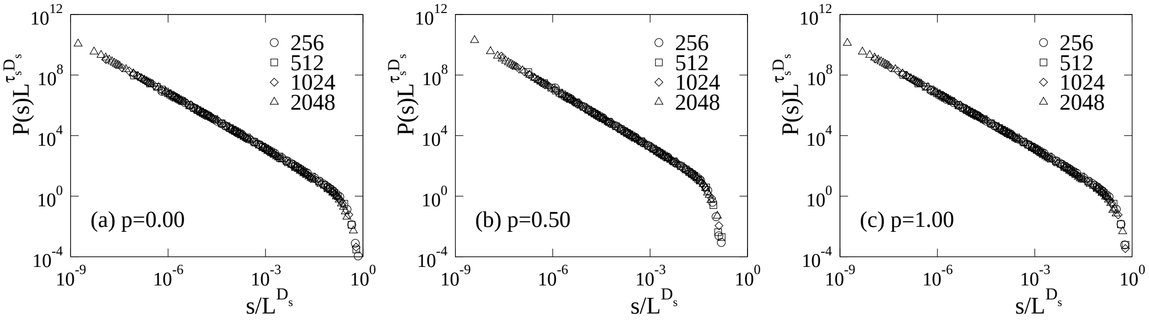

Figure 7.14: Plot of scaled distribution $P(s)L^{\tau_s D_s}$ against the scaled variable s/L^{D_s} for the QRRSM for (a) $p = 0.0$, (b) $p = 0.5$ and (c) $p = 1.0$ for system sizes $L = 256$ (○), 512 (□), 1024 (◇) and 2048 (△). A reasonable collapse is observed for all p.

plotted in Figs.7.13(c), and (d) respectively. It can be seen that the values of the exponents extracted above at $p = 0$ or $p = 1$ are equal to that of RSM whereas the values at $p = 0.5$ are equal to that of the SSM[113]. The exponent values continuously approach to the corresponding values of SSM as $p \rightarrow 0.5$ from 0 or 1 as it is observed in the the case of other exponents estimated above. The critical exponents γ_{sa}, γ_{at}, τ_a, τ_s and τ_t obtained in QRRSM for different values of p satisfy the scaling relations $\gamma_{sa} = (\tau_a - 1)/(\tau_s - 1)$ and $\gamma_{at} = (\tau_t - 1)/(\tau_a - 1)$ among them within error bars. Therefore, a continuous crossover from the RSM to the SSM is observed again.

Finite size scaling : It was already observed that the probability distribution function of avalanche related quantities obey FSS for both the RSM and SSM[73,79,80,81,84,85,113]. In order to study whether the QRRSM for different p follows FSS, a finite size scaling analysis is performed using moment analysis[79,80,81,82] of the toppling size distribution $P(s, L)$ for different values of p and the corresponding capacity dimensions D_s are obtained following the methods described in detail in Chapter 2. In order to verify the scaling function forms $\mathsf{f}(s/L^{D_s})$ of the QRRSM for different p the scaled distribution $P(s)L^{\tau_s D_s}$ are studied as a function of the scaled variable s/L^{D_s}. In Figs.7.14 (a), (b) and (c) $P(s)L^{\tau_s D_s}$ is plotted against s/L^{D_s} respectively for $p = 0.0, 0.5$ and 1.0 using the values of τ_s and D_s obtained at respective p values. A good collapse of data is observed for $L = 128, 256, 512, 1024$ and 2048 in support of the finite size scaling function form for the QRRSM for different p.

7.3 Conclusion

A continuous crossover from the RSM to the SSM universality class is studied by constructing the QRRSM in which a fraction p of the lattice sites are having anti-

	τ_a	τ_s	τ_t	γ_{sa}	γ_{at}	χ	H
$p = 0$	1.329	1.222	1.382	1.459	1.166	0.82	0.35
	0.006	0.005	0.007	0.008	0.008	0.02	0.01
$p = 0.5$	1.369	1.276	1.489	1.238	1.433	0.70	0.21
	0.006	0.005	0.005	0.008	0.008	0.02	0.01
$p = 1$	1.329	1.222	1.382	1.459	1.166	0.82	0.35
	0.006	0.005	0.006	0.008	0.008	0.02	0.01

Table 7.1: Critical exponents associated with several avalanche properties are listed for the QRRSM for three different values of $p = 0, 0.5$ and 1. The values of exponents for $p = 0$ and 1 correspond to that of the RSM whereas for $p = 0.5$ they correspond to that of the SSM.

clockwise rotational field. The values of critical exponents obtained for different values of p are listed in Table 7.1. It can be seen that the numerical values of the critical exponents for $p = 0$ and $p = 1$ are within the error bars of the critical exponents obtained for the RSM (given in Chapter 2) whereas for $p = 0.5$ they correspond to those of the SSM (given in Chapter 2). Therefore, a continuous crossover is found to occur if the parameter p is varied continuously. The intermediate values of p correspond to different non-universal models. The universality class of a model corresponding to a given p is decided by the deviation $\Delta p = |p - 0.5|$. On the both sides of $p = 0.5$, two models corresponding to the same Δp belong to the same universality class. It should be emphasized here that $p = 0$ corresponds to the RSM under clockwise rotational field whereas $p = 1$ corresponds to the RSM under anti-clockwise rotational field. However, there universality class remains the same. Hence, the direction of the rotational field present in the model can not change the universality class of the rotational models. However, a random mixing of the two rotational direction in a single model leads to a new universality class.

Chapter 8

Summary and conclusion

External bias was found to have non-trivial effect on the critical behaviour of lattice statistical models in equilibrium critical phenomena. For example, models like directed self-avoiding walks[103,104], directed lattice animal[105], directed percolation[102] exhibit different critical behaviour than the respective models without directed bias. Similarly, spiral self-avoiding walks[106,107], spiral lattice animal[108,109], spiral percolation[110], directed spiral percolation[111,112] etc. belongs to new universality classes than their original counter part in absence of rotational field. The application of global directed bias on the sandpile dynamics of the directed sandpile model (DSM) leads to a non-trivial phenomenon as well as anisotropy in the avalanche clusters. Motivated by the fact that, the rotational bias have nontrivial effect on the critical behaviour of many lattice statistical models in equilibrium critical phenomenon, a sandpile model[113] is constructed applying rotational constraint on the toppling dynamics on a BTW type sandpile model in order to study the effect of rotational bias on the critical properties at out of equilibrium situation. The non-equilibrium steady state of this model is studied developing several new statistical methods besides the existing numerical techniques. The results obtained are compared with that of the existing models mostly with the BTW and the SSM.

In order to study the effect of rotational constraint on the critical behaviour of sandpile model, a new sandpile model namely rotational sandpile model (RSM)[113] is introduced in Chapter 2. The toppling rule in RSM is found non-Abelian. The model has several microscopic properties which are similar to that of the BTW. Such microscopic properties are the mass conservation during toppling and local deterministic rule in sand grain distribution at the time of toppling. The rotational bias in RSM introduces toppling imbalance and certain internal stochasticity in the toppling dynamics. Stochasticity and toppling imbalance are the properties of the SSM. Therefore, RSM has microscopic properties of both the BTW and the SSM. The morphology of the avalanche clusters in the steady state also exhibits characteristics of both BTW as well as SSM. The critical behaviour of RSM at the non-equilibrium steady state is studied by measuring probability distribution of several avalanche properties. In the steady state, the probability distribution of avalanche related quantities are found to exhibit power law scaling with specific critical exponents. An extended set of critical exponents is calculated to characterize the steady state[74,75,76,77]. It is observed that some of them are close to that of the BTW but different from the SSM. The values of the exponents satisfy the scaling relations among them within error bars. RSM then belongs to a new universality class. Neither the internal stochasticity makes the RSM to belong to the SSM universality class nor the deterministic toppling rule takes it to the BTW universality class. Therefore, the presence of stochasticity in a model does not necessarily makes the critical behaviour of the system as that of a stochastic system. The finite size effect on the critical exponents are verified performing moment analysis of the distribution functions[79,80,81,82]. The scaling function forms associated with different probability distributions are determined. It is found that the scaling functions of the RSM obey the usual FSS as in the case of SSM rather than multi-scaling as in the case of BTW. The appearance of FSS in RSM is due to the local toppling imbalance as well as negative time auto-correlation of toppling waves[82,87,89,90,91] constituting an avalanche.

The effect of change in internal stochasticity in the RSM by controlling the direction of sand flow at the time of toppling is explored by constructing two variants of the original RSM, the RSM1 and the RSM2 in Chapter 3. The toppling rule in the RSM1 is such that the internal stochasticity present in the original RSM reduces and it produces more Abelian configurations than the RSM. RSM1 thus becomes closer to the BTW. In the case of the RSM2 the toppling rule increases the internal stochasticity and produces more non-Abelian configurations than the RSM. The increase in the internal stochasticity makes RSM2 closer to the SSM. Both these models have same microscopic properties such as mass conservation, toppling imbalance, internal stochasticity etc. as that of the RSM. Interestingly, the critical exponents characterizing the avalanche properties at the steady state are identical to that of the original RSM[123,124]. Neither the RSM1 is found in the BTW universality class nor the RSM2 is found in the SSM universality class. All rotational models belong to the same universality class of RSM. This may be due to the robustness of broken mirror symmetry present in the rotational models. FSS ansatz for the RSM1 and the RSM2 has been verified by moment analysis and data collapse of the probability distribution functions of the avalanche properties. It is found that that the scaling functions describing the avalanche properties of these rotational models obey usual FSS ansatz as in equilibrium critical phenomena and does not follow multiscaling as that of the BTW. Presence of toppling imbalance, internal stochasticity and the negative auto-correlation in the toppling waves in the RSM1 and RSM2 are responsible for the existence of FSS in these models.

In Chapter 4, a new "microscopic" avalanche parameter, toppling number S_i is introduced to characterize the avalanches of sandpile models. The toppling number S_i is the number of times a sand column at site i toppled in an avalanche. Two aspects of the avalanche clusters are looked into in terms of S_i in Chapter 4. One is the multifractal aspect and other is the multi-affine aspect. In order to study the multifractal aspect, a suitable multifractal measure, toppling number density per lattice site $\mu_i = S_i/\sum S_i$ is defined. Performing multifractal analysis it is found that the toppling number density is mono-fractal for BTW but they correspond to different multifractal spectrum of exponents for the RSM and the SSM. The parameter S_i is further used to define a toppling surface associated with the avalanche cluster. Toppling surfaces for the BTW, the RSM and the SSM are found very different. The roughness exponents characterizing the width of these surfaces are found distinctly different. The self-affine[99] property of these surfaces are studied from two point height difference correlation function $C(r)$ as well as power spectral analysis of the surfaces. Toppling surfaces of these models are found self-affine with distinctly different Hurst exponents. Moreover, from the moment analysis of the correlation function $C(r)$ it was found that the toppling surfaces of the RSM and the SSM are not only self-affine but also multi-affine in nature. The Hurst exponents H are further connected to the roughness exponents χ as well as to the capacity dimensions D_s and distribution exponents τ_s of the avalanche size. The scaling relation between χ and H obeys usual Family-Vicsek scaling[98] for the BTW whereas an anomalous scaling is found to obey for the RSM and the SSM. Analysis of avalanche clusters in terms of the microscopic avalanche parameter S_i thus provides deep insight of the avalanche dynamics as well as it is able to classify the sandpile models distinctly[169].

In Chapter 5, a novel continuous phase transition called flooding transition[171] topography of the toppling surfaces is studied. If the topography of toppling surfaces are flooded with a liquid, say water, a path of water connecting the opposite sides of the toppling surface appears for the first time for the critical height of flooding, called flooding threshold S_c. Such a transition is found to occur on the toppling surfaces of RSM and SSM but does not occur on the toppling surface of BTW model. Though there exists a wide distribution of flooding threshold, a critical point is defined by merging the flooding thresholds of all the toppling surfaces. The singularity of several island related quantities are explored at the critical point via a FSS theory developed in this chapter. A set of new critical exponents are determined. It is found that most of the percolation type exponents associated with the flooding transition are infinitely large though their ratio to the correlation length exponent are found finite. The criticality of the transition is also characterized by power law distribution of island area in a wide range of flooding heights. Most of the critical exponents characterizing the flooding transition are obtained in terms of the Hurst exponent H. Not only the exponents of flooding transition but also the exponents describing the singularity of avalanche size, are also obtained in terms of H. Universality class of the flooding transition does not belong to percolation[178] universality class.

The critical properties of the external perimeters of the islands obtained at the critical regime of the flooding transition are studied in Chapter 6. The island perimeters are extracted from the islands obtained at different level of flooding of the toppling surfaces by performing a kinetic random walk[206]. The island perimeters of the RSM and the SSM are found tortuous, self-similar fractal objects with different fractal dimensions d_ℓ. The perimeter mass and extension distributions are found to exhibit power law scaling at the flooding threshold which corresponds to the criticality of flooding transition. The critical exponents associated with the distribution of the perimeter mass and extension are found to be related with the roughness exponent χ as well as Hurst exponent H of the toppling surfaces via a hyperscaling. The values of the critical exponents are found different for the RSM and the SSM. A FSS theory related to the island perimeters are developed and verified at the flooding threshold. The universality class of island perimeters are found not only different from the percolation hull universality class[178,179,214] but also different for sandpile models with different symmetries in the toppling rules.

It has been observed that the universality class of sandpile models depend on the underlying symmetries present in their toppling rules. For example BTW model has deterministic abelian toppling rule, SSM has stochastic toppling rule and RSM has rotational toppling rule with broken mirror symmetry. All these models having different symmetries in their toppling rule and belong to different universality classes. In Chapter 7, the study of toppling surfaces, properties of island area and perimeters at the flooding thresholds was studied. It was observed that different stochastic sandpile models belong to same universality class of SSM whereas different rotational sandpile models belong to the same universality class of the RSM. An attempt has been made in this chapter to explore the possibility of a crossover from the RSM to the SSM in some parameter space. A continuous crossover from the RSM to the SSM is demonstrated by introducing a quenched randomness to the rotational field associated with each lattice site in the RSM. The quenched randomness was introduced by assigning a fraction p of randomly selected sites with anti-clockwise rotational field and rest of the sites have clockwise rotational field. The model corresponds to the SSM at $p \approx 0.5$[219,220]. The breakdown of broken mirror symmetry with increasing randomness in the rotational field is responsible for the crossover to stochastic sandpile universality class.

As a final point, it should be emphasized that the techniques developed here for studying the sandpile avalanches such as construction and characterization of toppling surface, study of critical properties of islands and their perimeters in the flooding transition can also be useful to characterize any dynamical system with threshold in general. In such a system, occurrence of avalanches is inevitable and hence a surface associated with an avalanche will always be possible to define in terms of a suitable microscopic parameter. The characterization of such a surface is expected to provide more indepth information of the dynamical system as it is obtained here.

Bibliography

[1] C. Domb and J. L. Lebowitz, editors, *Phase Transitions and Critical Phenomena*, Academic Press, New York, 1972 onwards. pages 1, 7

[2] H. E. Stanley, *Introduction to Phase Transitions and Critical Phenomena*, Oxford University Press, New York, 1971. pages 1, 7, 31

[3] J. J. Binney, N. J. Dowrick, A. J. Fisher, and M. E. J. Newman, *The Theory of Critical Phenomena*, Oxford University Press, Oxford, 1992. pages 1, 7

[4] P. Bak, C. Tang, and K. Wiesenfeld, Phys. Rev. Lett. **59**, 381 (1987). pages 1, 3, 21, 32, 83, 92, 103, 120

[5] G. A. Held, D. H. Solina, H. Solina, D. T. Keane, W. J. Haag, P. M. Horn, and G. Grinstein, Phys. Rev. Lett. **65**, 1120 (1990). pages 1

[6] H. M. Jaeger, C. H. Liu, and S. R. Nagel, Phys. Rev. Lett. **62**, 40 (1989). pages 2

[7] H. M. Jaeger and S. R. Nagel, Science **255**, 1523 (1992). pages 2

[8] V. Frette, K. Christensen, A. Malthe-Sorenssen, J. Feder, T. Jossang, and P. Meakin, Nature **379**, 49 (1996). pages 2

[9] B. Plourde, F. Nori, and M. Bretz, Phys. Rev. Lett. **71**, 2749 (1993). pages 2

[10] J. R. Claycomb, K. E. Bassler, J. H. Miller, M. Nersesyan, and D. Luss, Phys. Rev. Lett. **87**, 178303 (2001). pages 2

[11] C. M. Aegerter, M. S. Welling, and R. J. Wijngaarden, Europhys. Lett. **65**, 753 (2004). pages 2

[12] E. Altshuler et al., Phys. Rev. B **70**, 140505 (2004). pages 2

[13] M. S. Welling, C. M. Aegerter, and R. J. Wijngaarden, Phys. Rev. B **71**, 104515 (2005). pages 2

[14] P. J. Cote and L. V. Meisel, Phys. Rev. Lett. **67**, 1334 (1991). pages 2

[15] J. S. Urbach, R. C. Madison, and J. T. Markert, Phys. Rev. Lett. **75**, 276 (1995). pages 2

[16] P. Cizeau, S. Zapperi, G. Durin, and H. E. Stanley, Phys. Rev. Lett. **79**, 4669 (1997). pages 2

[17] G. Durin and S. Zapperi, Phys. Rev. Lett. **84**, 4705 (2000). pages 2

[18] D. Kim, S. Choe, and S. Shin, Phys. Rev. Lett. **90**, 087203 (2003). pages 2

[19] J. M. Beggs and D. Plenz, J. Neuroscience **23**, 11167 (2003). pages 2

[20] J. M. Beggs and D. Plenz, J. Neuroscience **24**, 5216 (2004). pages 2

[21] J. O. H. Bakke, A. Hansen, and J. Kertész, Europhys. Lett. **76**, 717 (2006). pages

2

[22] O. Peters, C. Hertlein, and K. Christensen, Phys. Rev. Lett. **88**, 018701 (2001). pages 2

[23] O. Peters and K. Christensen, Phys. Rev. E **66**, 036120 (2002). pages 2

[24] K. Chen, P. Bak, and S. P. Obukhov, Phys. Rev. A **43**, 625 (1991). pages 2

[25] D. Hughes, M. Paczuski, R. O. Dendy, P. Helander, and K. G. McClements, Phys. Rev. Lett. **90**, 131101 (2003). pages 2

[26] M. Paczuski, S. Boettcher, and M. Baiesi, Phys. Rev. Lett. **95**, 181102 (2005). pages 2

[27] M. Baiesi, M. Paczuski, and A. L. Stella, Phys. Rev. Lett. **96**, 051103 (2006). pages 2

[28] Z. Olami, H. J. S. Feder, and K. Christensen, Phys. Rev. Lett. **68**, 1244 (1992). pages 2

[29] K. Christensen and Z. Olami, Phys. Rev. A **46**, 1829 (1992). pages 2

[30] P. Grassberger, Phys. Rev. E **49**, 2436 (1994). pages 2

[31] A. Corral, C. J. Perez, A. Diaz-Guilera, and A. Arenas, Phys. Rev. Lett. **74**, 118 (1995). pages 2

[32] A. A. Middleton and C. Tang, Phys. Rev. Lett. **74**, 742 (1995). pages 2

[33] H. J. Jensen, Phys. Rev. Lett. **64**, 3103 (1990). pages 3

[34] T. Fiig and H. J. Jensen, J. Stat. Phys. **71**, 653 (1993). pages 3

[35] B. Drossel and F. Schwabl, Phys. Rev. Lett. **69**, 1629 (1992). pages 3

[36] B. Drossel, S. Clar, and F. Schwabl, Phys. Rev. Lett. **71**, 3739 (1993). pages 3

[37] B. Drossel, Phys. Rev. Lett. **76**, 936 (1996). pages 3

[38] C. Rhodes and R. Anderson, Nature **381**, 600 (1996). pages 3

[39] P. Bak and K. Sneppen, Phys. Rev. Lett. **71**, 4083 (1993). pages 3

[40] P. Bak, *How Nature Works: The Science of Self-Organized Criticality*, Copernicus, New York, 1996. pages 3

[41] H. J. Jensen, *Self-Organized Criticality*, Cambridge University Press, Cambridge, 1998. pages 3

[42] K. Christensen and N. R. Moloney, *Complexity and Criticality*, Imperial College Press, London, 2005. pages 3, 83

[43] S. Hergarten, *Self organized criticality in earth systems*, Springer-Verlag, Berlin, 2002. pages 3

[44] M. J. Aschwanden, *Self organized criticality in Astrophysics: The Statistics of Nonlinear Processes in the Universe*, Springer-Verlag, Berlin, 2011. pages 3

[45] D. Dhar, Physica A **263**, 4 (1999), and references therein. pages 3

[46] Y. C. Zhang, Phys. Rev. Lett. **63**, 470 (1989). pages 4, 11

[47] O. Biham, E. Milshtein, and O. Malcai, Phys. Rev. E **63**, 061309 (2001). pages 4, 11, 63, 73, 111, 120, 125

[48] S. S. Manna, J. Phys. A **24**, L363 (1991). pages 4, 22, 120

[49] S. S. Manna, Physica A **179**, 249 (1991). pages 4, 22

[50] D. Dhar, Physica A **270**, 69 (1999). pages 5, 22, 83, 84, 119, 120

[51] D. Dhar and R. Ramaswamy, Phys. Rev. Lett. **63**, 1659 (1989). pages 5, 11, 25, 119

[52] P. K. Mohanty and D. Dhar, Phys. Rev. Lett. **89**, 104303 (2002). pages 7, 14

[53] P. Ghaffari, S. Lise, and H. J. Jensen, Phys. Rev. E **56**, 6702 (1997). pages 7, 21

[54] T. Tsuchiya and M. Katori, Phys. Rev. E **61**, 1183 (2000). pages 7, 21

[55] A. Vázquez, Phys. Rev. E **62**, 7797 (2000). pages 7, 21

[56] G. Pruessner and H. J. Jensen, Europhys. Lett. **58**, 250 (2002). pages 7, 21

[57] B. Tadić, U. Nowak, K. D. Usadel, R. Ramaswamy, and S. Padlewski, Phys. Rev. A **45**, 8536 (1992). pages 7

[58] N. Azimi-Tafreshi and S. Moghimi-Araghi, Phys. Rev. E **80**, 046115 (2009). pages 7

[59] O. Malcai, Y. Shilo, and O. Biham, Phys. Rev. E **73**, 056125 (2006). pages 7

[60] S. S. Manna, J. Stat. Phys. **59**, 509 (1990). pages 7, 25, 50

[61] S. S. Manna, A. D. Chakrabarti, and R. Cafiero, Phys. Rev. E **60**, R5005 (1999). pages 7

[62] A. Benyoussef, M. Khfifi, and M. Loulidi, Eur. Phys. J. B **43**, 213 (2005). pages 7

[63] E. Jettestuen and A. Malthe-Sorenssen, Phys. Rev. E **72**, 062302 (2005). pages 7

[64] R. P. Satorras and A. Vespignani, J. Phys. A **33**, L33 (2000). pages 7, 11

[65] M. Kloster, S. Maslov, and C. Tang, Phys. Rev. E **63**, 026111 (2001). pages 7, 11

[66] D. Hughes and M. Paczuski, Phys. Rev. Lett. **88**, 054302 (2002). pages 7

[67] J. M. Yeomans, *Statistical Mechanics of Phase Transitions*, Clarendon Press, Oxford, 1992. pages 7

[68] K. Christensen, H. C. Fogedby, and H. J. Jensen, J. Stat. Phys. **59**, 509 (1990). pages 9

[69] A. Díaz-Guilera, Phys. Rev. A **45**, 8551 (1992). pages 10

[70] A. Díaz-Guilera, Europhys. Lett. **26**, 177 (1994). pages 10

[71] L. Pietronero, A. Vespignani, and S. Zapperi, Phys. Rev. Lett. **72**, 1690 (1994). pages 10

[72] A. Vespignani, S. Zapperi, and L. Pietronero, Phys. Rev. E **51**, 1711 (1995). pages 10

[73] A. Chessa, H. E. Stanley, A. Vespignani, and S. Zapperi, Phys. Rev. E **59**, R12 (1999). pages 10, 12, 13, 38, 57, 64, 75, 111, 134

[74] K. Christensen and Z. Olami, Phys. Rev. E **48**, 3361 (1993). pages 11, 92, 111, 138

[75] A. Ben-Hur and O. Biham, Phys. Rev. E **53**, R1317 (1996). pages 11, 25, 28, 29, 50, 54, 63, 73, 92, 111, 120, 138

[76] S. Lübeck and K. D. Usadel, Phys. Rev. E **55**, 4095 (1997). pages 11, 28, 29, 92, 111, 120, 138

[77] E. Milshtein, O. Biham, and S. Solomon, Phys. Rev. E **58**, 303 (1998). pages 11, 25, 28, 29, 50, 54, 120, 138

[78] S. Lübeck, Phys. Rev. E **56**, 1590 (1997). pages 11, 120

[79] M. DeMenech, A. L. Stella, and C. Tebaldi, Phys. Rev. E **58**, R2677 (1998). pages

11, 12, 13, 32, 33, 134, 138

[80] C. Tebaldi, M. DeMenech, and A. L. Stella, Phys. Rev. Lett. **83**, 3952 (1999). pages 11, 12, 13, 32, 33, 64, 70, 134, 138

[81] S. Lübeck, Phys. Rev. E **61**, 204 (2000). pages 11, 12, 13, 32, 33, 36, 64, 70, 111, 125, 134, 138

[82] R. Karmakar, S. S. Manna, and A. L. Stella, Phys. Rev. Lett. **94**, 088002 (2005). pages 11, 12, 21, 33, 38, 41, 58, 77, 134, 138

[83] J. L. Cardy, in *Finite-size Scaling*, edited by J. L. Cardy, North Holland, Amsterdam, 1988. pages 11, 32

[84] A. Vespignani, R. Dickman, M. A. Muñoz, and S. Zapperi, Phys. Rev. Lett. **81**, 5676 (1998). pages 12, 13, 73, 134

[85] A. Chessa, A. Vespignani, and S. Zapperi, Comput. Phys. Commun. **121-122**, 299 (1999). pages 12, 13, 111, 134

[86] V. B. Priezzhev, D. V. Ktitarev, and E. V. Ivashkevich, Phys. Rev. Lett. **76**, 2093 (1996). pages 13, 39, 57

[87] M. Paczuski and S. Boettcher, Phys. Rev. E **56**, R3745 (1997). pages 13, 39, 57, 138

[88] D. V. Ktitarev, S. Lübeck, P. Grassberger, and V. B. Priezzhev, Phys. Rev. E **61**, 81 (2000). pages 13, 39, 41, 57

[89] M. DeMenech and A. L. Stella, Phys. Rev. E **62**, R4528 (2000). pages 13, 41, 58, 77, 138

[90] A. L. Stella and M. DeMenech, Physica A **295**, 101 (2001). pages 13, 41, 58, 70, 77, 138

[91] M. DeMenech and A. L. Stella, Physica A **309**, 289 (2002). pages 13, 41, 58, 77, 138

[92] R. Dickman, A. Vespignani, and S. Zapperi, Phys. Rev. E **57**, 5095 (1998). pages 13, 73

[93] A. Vespignani, R. Dickman, M. A. Muñoz, and S. Zapperi, Phys. Rev. E **62**, 4564 (2000). pages 13, 14, 73, 75

[94] R. Dickman, M. Alava, M. A. Muñoz, J. Peltola, A. Vespignani, and S. Zapperi, Phys. Rev. E **64**, 056104 (2001). pages 13, 73

[95] M. J. Alava and K. B. Lauritsen, Europhys. Lett. **53**, 563 (2001). pages 13, 14, 73, 75, 111

[96] M. Alava, J. Phys. Condens. Matter **14**, 2353 (2002). pages 13, 14, 73, 75, 111

[97] M. Alava and M. A. Muñoz, Phys. Rev. E **65**, 026145 (2002). pages 13, 73

[98] F. Family and T. Vicsek, J. Phys. A **18**, 75 (1985). pages 13, 79, 80, 139

[99] P. Mealin, *Fractals, scaling and growth far from equilibrium*, Cambridge University Press, Cambridge, 1998. pages 13, 61, 72, 76, 77, 139

[100] A. L. Barabasi and H. E. Stanley, *Fractal concepts of surface growth*, Cambridge University Press, Cambridge, 1995. pages 13

[101] M. Paczuski and S. Boettcher, Phys. Rev. Lett. **77**, 111 (1996). pages 14, 73, 75

[102] H. Hinrichsen, Adv. Phys. **49**, 815 (2000). pages 14, 119, 137

[103] B. K. Chakrabarti and S. S. Manna, J. Phys. A **16**, L113 (1983). pages 14, 119, 137

[104] S. Redner and I. Majid, J. Phys. A **16**, L307 (1983). pages 14, 119, 137

[105] S. Redner and A. Coniglio, J. Phys. A **15**, L273 (1982). pages 14, 137

[106] H. W. J. Blöte and H. J. Hilhorst, J. Phys. A **17**, L111 (1984). pages 14, 119, 137

[107] K. Y. Lin, J. Phys. A **18**, L145 (1985). pages 14, 119, 137

[108] T. C. Li and Z. C. Zhou, J. Phys. A **18**, 67 (1985). pages 14, 17, 137

[109] S. B. Santra and I. Bose, J. Phys. A **22**, 5043 (1989). pages 14, 17, 137

[110] S. B. Santra and I. Bose, J. Phys. A **24**, 2367 (1991). pages 14, 17, 119, 137

[111] S. B. Santra, Eur. Phys. J. B **33**, 75 (2003). pages 14, 119, 137

[112] S. Sinha and S. B. Santra, Eur. Phys. J. B **39**, 513 (2004). pages 14, 119, 137

[113] S. B. Santra, S. R. Chanu, and D. Deb, Phys. Rev. E **75**, 041122 (2007). pages 15, 26, 28, 36, 46, 63, 64, 70, 75, 77, 83, 84, 92, 111, 119, 120, 133, 134, 137

[114] P. Bak, C. Tang, and K. Wiesenfeld, Phys. Rev. A **38**, 364 (1988). pages 21, 32, 83, 92, 103

[115] C. Tang and P. Bak, Phys. Rev. Lett. **60**, 2347 (1988). pages 21, 32

[116] R. Karmakar and S. S. Manna, Phys. Rev. E **69**, 067107 (2004). pages 25

[117] P. Grassberger and S. S. Manna, J. Phys (France) **51**, 1077 (1990). pages 25, 50

[118] S. Banerjee, S. B. Santra, and I. Bose, Z. Phys. B **96**, 571 (1995). pages 25, 50

[119] S. S. Manna and A. L. Stella, Physica A **316**, 135 (2002). pages 26, 34, 35

[120] S. N. Majumdar and D. Dhar, Physica A **185**, 129 (1992). pages 28

[121] K. Christensen, H. C. Fogedby, and H. J. Jensen, J. Stat. Phys. **63**, 653 (1991). pages 29, 133

[122] S. B. Santra and W. A. Seitz, Int. J. Mod. Phys. C **11**, 1357 (2000). pages 35, 56

[123] J. A. Ahmed and S. B. Santra, Eur. Phys. J. B **76**, 13 (2010). pages 51, 55, 56, 111, 120, 138

[124] J. A. Ahmed and S. Santra, Computer Physics Communications **182**, 1851 (2011). pages 51, 55, 56, 138

[125] B. B. Mandelbrot, *Statistical Model of Turbulence*, Springer, New York, 1972. pages 61, 64

[126] F. Milde, R. A. Römer, and M. Schreiber, Phys. Rev. B **55**, 9463 (1997). pages 61

[127] B. Huckestein and R. Klesse, Phil. Mag. B **77**, 1181 (1998). pages 61

[128] S. M. Nishigaki, Phys. Rev. E **59**, 2853 (1999). pages 61

[129] S. B. Santra and B. Sapoval, Fractals **13**, 9 (2005). pages 61

[130] M. H. Jensen, A. Levermann, J. Mathiesen, and I. Procaccia, Phys. Rev. E **65**, 046109 (2002). pages 61

[131] J. P. Bouchaud, M. Potters, and M. Meyer, Eur. Phys. J. B **13**, 595 (2000). pages 61

[132] J.-F. Muzy, D. Sornette, J. Delour, and A. Arneodo, Quantitative Finance **1**, 131 (2001). pages 61

[133] P. C. Ivanov, L. A. N. Amaral, A. L. Goldberger, S. Havlin, M. G. Rosenblum,

Z. R. Struzik, and H. E. Stanley, Nature **399**, 461 (1999). pages 61

[134] P. C. e. a. Ivanov, Chaos **11**, 641 (2001). pages 61

[135] D. L. Turcotte, *Fractals and Chaos in Geology and Geo-physics*, Cambridge University Press, Cambridge, 1992. pages 61

[136] S. Lovejoy, Science **216**, 185 (1982). pages 61

[137] J. D. Pelletier, Phys. Rev. Lett. **78**, 2672 (1997). pages 61

[138] E. Bouchaud, G. Lapasset, and J. Planés, Europhys. Lett. **13**, 73 (1990). pages 61

[139] M. J. Alava, P. K. V. V. Nukala, and S. Zapperi, Adv. Phys. **55**, 349 (2006). pages 61

[140] S. Santucci, M. Grob, R. Toussaint, S. J., A. Hansen, and K. J. Måløy, Europhys. Lett. **92**, 44001 (2010). pages 61

[141] F. Plouraboué and S. Roux, Physica A **227**, 173 (1996). pages 61

[142] D. L. Blair and A. Kudrolli, Phys. Rev. Lett. **94**, 166107 (2005). pages 61

[143] W. B. Wright, R. Budakian, D. J. Pine, and S. J. Putterman, Science **278**, 1609 (1997). pages 61

[144] O. L. Gülder, G. J. Smallwooda, R. Wonga, D. R. Snellinga, R. Smitha, B. M. Deschampsb, and J. C. Sautetc, Combustion and Flame **120**, 407 (2000). pages 61

[145] J. Feder, *Fractals*, Plenum Press, New York, 1998. pages 61, 65, 67, 70, 71

[146] B. B. Mandelbrot, *The fractal Geometry of Nature*, Freeman, New York, 1992. pages 61, 67, 93, 110, 113

[147] A. Giorgilli, D. Casati, L. Sironi, and L. Galgani, Phys. Lett. A **115**, 202 (1986). pages 61, 67

[148] L. S. Liebovitch and T. Toth, Phys. Lett. A **141**, 387 (1989). pages 61, 67

[149] P. Grassberger, Phys. Lett. A **97**, 224 (1983). pages 61, 64, 67

[150] P. Grassberger, Int. J. Mod. Phys. C **4**, 515 (1993). pages 61, 67

[151] A. Block, W. Vonbloh, and H. J. Schellnhuber, Phys. Rev. A **42**, 1869 (1990). pages 61, 67

[152] F. H. Ling and G. Schmidt, J. Comp. Phys. **99**, 196 (1992). pages 61, 67

[153] B. Dubrulle and M. Lachiezerey, Astronomy and Astrophysics **289**, 667 (1994). pages 61, 67

[154] M. Osaka and N. Ito, Int. J. Mod. Phys. C **11**, 1519 (2000). pages 61, 67

[155] M. Tanaka, Y. Kimura, L. Chouanine, R. Kato, and J. Taguchi, J Material Sc. Lett. **22**, 1279 (2003). pages 61, 67

[156] L. Lorenzo and R. A. Mosquera, Journal of Computational Chemistry **24**, 707 (2003). pages 61, 67

[157] S. N. Majumdar and D. Dhar, J. Phys. A **24**, L357 (1991). pages 62, 73

[158] J. Krug, J. E. S. Socolar, and G. Grinstein, Phys. Rev. A **46**, R4479 (1992). pages 62, 73

[159] J. G. Oliveira, J. F. F. Mendes, and G. Tripathy, Phys. Rev. E **69**, 031105 (2004). pages 62, 73

[160] B. B. Mandelbrot, J. Fluid Mech. **62**, 331 (1974). pages 64

[161] H. G. E. Hentschel and I. Procaccia, Physica **8**, 435 (1983). pages 64

[162] P. Grassberger and I. Procaccia, Physica **9**, 189 (1983). pages 64

[163] L. d. Arcangelis, S. Redner, and A. Coniglio, Phys. Rev. B **31**, 4725 (1985). pages 65

[164] R. Rammal, C. Tannous, P. Breton, and A. M. S. Tremblay, Phys. Rev. Lett. **54**, 1718 (1985). pages 65

[165] A. Aharony, in *Directions in Condensed Matter Physics*, edited by G. Grinstein and G. Mazenko, World Scientific, Singapore, pp. 1-50, 1985. pages 65

[166] R. Blumenfeld, Y. Meir, A. Aharony, and A. B. Harris, Phys. Rev. B **35**, 3524 (1987). pages 65

[167] P. Meakin, H. E. Stanley, A. Coniglio, and T. A. Witten, Phys. Rev. A **32**, 2364 (1985). pages 65

[168] P. Meakin, A. Coniglio, H. E. Stanley, and T. A. Witten, Phys. Rev. A **34**, 3325 (1986). pages 65

[169] J. A. Ahmed and S. B. Santra, Europhys. Lett. **90**, 50006 (2010). pages 77, 80, 83, 104, 139

[170] J. A. Ahmed and S. B. Santra, to appear in Physica A. pages 80, 103, 106, 110

[171] J. A. Ahmed and S. B. Santra, Phys. Rev. E **85**, 031111 (2012). pages 80, 92, 97, 105, 108, 113, 117, 122, 139

[172] A. Hansen and J. Mathiesen, in *Modeling Critical and Catastrophic Phenomena in Geoscience: A Statistical Physics Approach*, edited by P. Bhattacharyya and B. K. Chakrabarti, Springer, Berlin, 2006. pages 80

[173] J. M. López, Phys. Rev. E **52**, R1296 (1995). pages 80

[174] J. M. López and M. A. Rodríguez, Phys. Rev. E **54**, R2189 (1996). pages 80

[175] J. M. López and J. Schmittbuhl, Phys. Rev. E **57**, 6405 (1998). pages 80

[176] S. Morel, J. Schmittbuhl, J. M. López, and G. Valentin, Phys. Rev. E **58**, 6999 (1998). pages 80

[177] J. M. López, Phys. Rev. Lett. **83**, 4594 (1999). pages 80

[178] D. Stauffer and A. Aharony, *Introduction to Percolation Theory*, Taylor and Francis, London, 1994. pages 83, 86, 91, 92, 104, 119, 140

[179] A. Bunde and S. Havlin, *Fractals and Disordered Systems*, Springer-Verlag, Berlin, 1991. pages 83, 104, 140

[180] M. Sahimi, *Application of Percolation Theory*, Taylor and Francis, London, 1994. pages 83

[181] P. R. King, S. V. Buldyrev, N. V. Dokholyan, S. Havlin, Y. Lee, G. Paul, and H. E. Stanley, Physica A **274**, 60 (1999). pages 83

[182] P. R. King, S. V. Buldyrev, N. V. Dokholyan, S. Havlin, E. Lopez, G. Paul, and H. E. Stanley, Physica A **314**, 103 (2002). pages 83

[183] J. L. Cardy and P. Grassberger, J. Phys. A **18**, L267 (1985). pages 83

[184] R. Cohen, D. ben Avraham, and S. Havlin, Phys. Rev. E **66**, 036113 (2002). pages 83

[185] A. Acin, J. I. Cirac, and M. Lewenstein, Nature Physics **3**, 256 (2007). pages 83

[186] J. Brzychczyk, Phys. Rev. C **73**, 024601 (2006). pages 83

[187] I. Brovchenko, A. Krukau, A. Oleinikova, and A. K. Mazur, Phys. Rev. Lett. **97**, 137801 (2006). pages 83

[188] S. V. Buldyrev, S. Havlin, and H. E. Stanley, Physica A **200**, 200 (1993). pages 83

[189] J. Schmittbuhl, J. P. Vilotte, and S. Roux, J. Phys. A **26**, 6115 (1993). pages 83, 88, 91, 92

[190] Z. Olami and R. Zeitak, Phys. Rev. Lett. **76**, 247 (1996). pages 83, 88, 92, 93

[191] G. Wagner, P. Meakin, J. Feder, and T. Jøssang, Phys. Rev. E **55**, 1698 (1997). pages 83

[192] V. V. Mourzenko, J. F. Thovert, and P. M. Adler, Phys. Rev. E **59**, 4265 (1999). pages 83, 91

[193] M. Sahimi, AIChE J. **41**, 229 (1995). pages 83

[194] P. Gouze, C. Noiriel, C. Bruderer, D. Loggia, and R. Leprovost, Geophys. Res. Lett. **30**, 1267 (2003). pages 83

[195] A. A. Saberi, Appl. Phys. Lett. **97**, 154102 (2010). pages 83

[196] A. A. Saberi, M. D. Niry, S. M. Fazeli, M. R. Rahimi Tabar, and S. Rouhani, Phys. Rev. E **77**, 051607 (2008). pages 92, 101

[197] S. B. Ramisetti, C. Campañá, G. Anciaux, J. F. Molinari, M. M. H., and M. O. Robbins, J. Phys. Condens. Matter **23**, 215004 (2011). pages 94

[198] J. Kondev and C. L. Henley, Phys. Rev. Lett. **74**, 4580 (1995). pages 101, 107, 108

[199] J. Kondev, C. L. Henley, and D. G. Salinas, Phys. Rev. E **61**, 104 (2000). pages 101, 107, 108

[200] C. Zeng, J. Kondev, D. McNamara, and A. A. Middleton, Phys. Rev. Lett. **80**, 109 (1998). pages 101

[201] M. A. Rajabpour and S. M. Vaez Allaei, Phys. Rev. E **80**, 011115 (2009). pages 101

[202] A. A. Saberi and S. Rouhani, Phys. Rev. E **79**, 036102 (2009). pages 101

[203] A. A. Saberi, M. A. Rajabpour, and S. Rouhani, Phys. Rev. Lett. **100**, 044504 (2008). pages 101

[204] M. G. Nezhadhaghighi and M. A. Rajabpour, Phys. Rev. E **83**, 021122 (2011). pages 101

[205] S. Hosseinabadi, M. A. Rajabpour, M. Sadegh Movahed, and S. M. Vaez Allaei, Phys. Rev. E **85**, 031113 (2012). pages 101

[206] R. M. Ziff, P. T. Cummings, and G. Stell, J. Phys. A **17**, 3009 (1984). pages 102, 140

[207] R. F. Voss, J. Phys. A **17**, L373 (1984). pages 102

[208] S. Roux and E. Guyon, J. Phys. A **24**, 1611 (1991). pages 102

[209] S. B. Santra and I. Bose, J. Phys. A **26**, 3963 (1993). pages 102

[210] S. Schwarzer, S. Havlin, and H. E. Stanley, Phys. Rev. E **49**, 1182 (1994). pages 102

[211] A. L. Owczarek, A. Rechnitzer, R. Brak, and A. J. Guttmann, J. Phys. A **30**, 6679 (1997). pages 102

[212] K. Oerding and F. Wijland, J. Phys. A **31**, 7011 (1998). pages 102

[213] S. Sinha and S. B. Santra, Int. J. Mod. Phys. C **16**, 1251 (2005). pages 102

[214] M. Aizenman, B. Duplantier, and A. Aharony, Phys. Rev. Lett. **83**, 1359 (1999). pages 104, 140

[215] R. J. Adler, *The Geometry of Random Fields*, Wiley, New York, 1981. pages 110

[216] P. G. d. Gennes, *Scaling Concepts in Polymer Physics*, Cornell University Press, NY, 1979. pages 119

[217] M. Rossi, R. P. Satorras, and A. Vespignani, Phys. Rev. Lett. **85**, 1803 (2000). pages 119, 124

[218] B. Tadić and D. Dhar, Phys. Rev. Lett. **79**, 1519 (1997). pages 125

[219] H. Bhaumik, J. A. Ahmed, and S. B. Santra, AIP Conf. Proc. **1349**, 198 (2011). pages 125, 133, 141

[220] J. A. Ahmed, H. Bhaumik, and S. B. Santra, manuscript under preparation. pages 125, 133, 141

List of publications

Journal:

1. *Invasion of a sticky random solid: Self-established potential gradient, phase separation, and criticality*
   S. B. Santra, Santanu Sinha and Jahir Abbas Ahmed, Phys. Rev. E **78**, 061135 (2008).
2. *Finite size scaling in a BTW like sandpile models*
   Jahir Abbas Ahmed and S. B. Santra, Eur. Phys. J. B **76**,13-20 (2010).
3. *Avalanche properties of sandpile models in terms of a microscopic parameter*
   Jahir Abbas Ahmed and S. B. Santra, Europhys. Lett. **90**, 50006 (2010).
4. *Rotational Sandpile Models: A finite size scaling study*
   Jahir Abbas Ahmed and S. B. Santra, Computer Physics Communications, **182**, 1851 (2010).
5. *Flooding transition in the topography of toppling surfaces of rotational and stochastic sandpile models*
   Jahir Abbas Ahmed and S. B. Santra, Phys. Rev. E, **85**, 031111 (2012).
6. *Critical properties of island perimeters in the flooding transition of stochastic and rotational sandpile models*
   Jahir Abbas Ahmed and S. B. Santra, to appear in Physica A.
7. *Effect of quenched and annealed randomness in rotational sandpile model*
   Jahir Abbas Ahmed, Himangsu Bhaumik and S. B. Santra, manuscript under preparation.

Conference Proceeding:

1. *Roughness and contour loop analysis of toppling surfaces of a rotational sandpile model*
   Jahir Abbas Ahmed and S. B. Santra, Proceedings - 54th DAE Solid State Phys. Symp., M. S. Univ of Baroda, Gujarat, India, Dec. 14-18, 2009, page 259.

2. *Finite size scaling in rotational sandpile models*
   S. B. Santra and Jahir Abbas Ahmed, Proceedings - Conference on Computational Physics 2010, Norwegian University of Science and Technology, Trondheim, Norway, June 23-26, 2010, page 107.

3. *Analysis of toppling surfaces of stochastic sandpile models*
   Jahir Abbas Ahmed and S. B. Santra, AIP Conf. Proc. **1349**, 192-193 (2011).

4. *Crossover from rotational to stochastic sandpile*
   Himangsu Bhaumik, Jahir Abbas Ahmed and S. B. Santra, AIP Conf. Proc. **1349**, 198-199 (2011).